Semiconductor Based Architectures for All-Optical 3R Signal Regeneration at 40 Gbit/s

vorgelegt von
Diplom-Ingenieur
Juraj Slovak

von der Fakultät IV für Elektrotechnik und Informatik
der Technischen Universität Berlin
zur Erlangung des akademischen Grades

Doktor der Ingenieurwissenschaften

– Dr.-Ing. –

genehmigte Dissertation

Promotionsausschuss:

Vorsitzender:	Prof. Dr.-Ing. Ch. Boit
Berichter:	Prof. Dr.-Ing. K. Petermann
Berichter:	Prof. Dr. sc. nat. J. Leuthold

Tag der wissenschaftlichen Aussprache: 27. Oktober 2006

Berlin 2006
D 83

Abstract

In framework of this thesis, novel all-optical 3R regenerators for high-speed signal processing (40 Gbit/s and beyond) have been developed. The focus was on a feasible solution for spectrally efficient DWDM networks. In order to guarantee a high integration potential as well as mechanical and thermal stability, the 3R regeneration schemes have to be based on compact semiconductor devices. From the application point of view, two different functionalities of the all-optical 3R architectures have been considered. On the one side, simple pass-through signal regeneration by simultaneous preservation of signal wavelength and phase is attractive especially for long haul point-to-point DWDM links. Such regenerator can basically operate as a 3R regenerative amplifier without the necessity of any wavelength monitoring function. On the other side, signal regeneration combined with wavelength conversion is an attractive functionality for optical cross-connects, in order to avoid wavelength blocking and, in addition, to use the wavelength conversion for degradation-free signal routing in the reconfigurable transparent optical networks.

Two all-optical semiconductor based 3R regenerators have been developed and optimised for operation in 40 Gbit/s PRBS RZ data streams. The key functional components of both proposed architectures are a self-pulsating PhaseCOMB-laser (Phase Controlled Mode Beating) for all-optical clock recovery and an ultra-long semiconductor optical amplifier (UL-SOA) applied in the 3R circuits for effective exploitation of fast nonlinearities. The semiconductor devices were designed and fabricated in the technology of FhG-HHI. In the thesis, the experimental investigations on the device characteristics as well as assembled 3R architectures are supported by detailed numerical analysis. Based on the simulations, the physical background of the exploited novel effects is explained and the optimised operation conditions are identified.

The PhaseCOMB-clock is a compact three-sections laser providing all-optical clock extraction from PRBS signals. In this work, the potential of the optical clock for application in a 3R regeneration scheme is analysed. The system performance and robustness of the selected devices was studied by operation in 40 Gbit/s data streams. The impact of different signal degradations on the timing stability of the recovered clock signal was evaluated in detail. Furthermore, the burst-mode feasibility of the PhaseCOMB-clock was investigated. The results were later used by design of the proposed 3R schemes optimised for processing of asynchronous packet flows.

In case of the UL-SOA, the device length as an important optimisation parameter was systematically studied and exploited in this work for the first time. Semiconductor amplifiers of different lengths between 2 mm and 8 mm were fabricated. The purpose was to exploit more effectively the nonlinearities needed for fast optical signal processing. It could be demonstrated that the impact of ultra-fast (< 1 ps) intra-band cross gain effects on the total gain saturation clearly increases when enhancing the SOA length. Subsequently, it was found that the inter-band transitions are also effectively accelerated in the long devices. Gain recovery time constants down to 10 ps were evaluated for an 8 mm UL-SOA compared to ~100 ps typically measured for conventional SOAs with a length below 1 mm. Hence, the fast inter-band XGM effects make the long devices attractive for high speed (40+ Gbit/s) optical signal processing.

The unique characteristics of the aforementioned semiconductor components have been exploited in a novel configuration (FhG-HHI patent). The combination of the effective and fast gain dynamics of the ultra-long amplifiers together with the high timing stability of the optical clock signal results in regenerative behaviour of periodically modulated UL-SOAs. The periodically modulated UL-SOA is the basis for both all-optical 3R schemes developed in the framework of this thesis: the 'Optically Clocked' 3R regenerator (OC-3R) and the 'Alternating Data-Clock' 3R regenerator (ADC-3R).

The 'Optically Clocked' 3R regenerator is a wavelength-preserving scheme. The signal regeneration is performed by effective carving of degraded data pulses, when propagating through the saturated long amplifier periodically modulated by the stable clock signal. The dominant clock determines the saturation conditions in the long amplifier and, thus, the regeneration efficiency of the proposed scheme. The quality of the weak PRBS data signal is restored without any wavelength conversion. The impact of amplitude fluctuations, timing instabilities as well as reduced data OSNR on the performance of the OC-3R regenerator was investigated in detail in order to define the optimised operation conditions of the proposed 3R scheme. Furthermore, the capability of the OC-3R for mitigation of polarisation mode dispersion (PMD) and residual chromatic dispersion (CD) as well as regeneration of 40 Gbit/s asynchronous PRBS packet flows is demonstrated.

The second 3R architecture introduced in this work, the 'Alternating Data-Clock' 3R regenerator, combines signal regeneration with wavelength conversion. In contrary to conventional 3R circuits, the output wavelength of the regenerated signal is defined by a CW source and, thus, can be flexibly tuned in the whole C-band (e.g. ITU grid). Also in this scheme, the timing position of the converted data pulses is determined by the stable clock signal. In this work, the regenerative ability of the ADC-3R operated in 40 Gbit/s PRBS RZ data streams is studied for different signal degradations and wavelength combinations in order to evaluate the typical features of the proposed compact 3R circuit.

Zusammenfassung

Im Rahmen der Doktorarbeit wurden neuartige rein-optische 3R Regeneratoren für Datenraten von 40 Gbit/s und höher entwickelt. In Hinblick auf eine praktikable Einsetzbarkeit in spektral effizienten WDM Systemen sollten die Regeneratoren ausschließlich auf kompakten Halbleiterkomponenten mit hohem Integrationspotenzial basieren. Dabei werden 3R Architekturen für unterschiedliche Einsatzbereiche im optischen Netz betrachtet. Zum einen ist für „long-haul“ Übertragungsstrecken ein wellenlängen-erhaltender 3R Regenerator interessant, der möglichst auch die Phase der Lichtwelle erhält und der keine aufwendige λ-Überwachung benötigt. Im Prinzip kann ein solcher Regenerator dann als ein 3R regenerativer Verstärker eingesetzt werden. Zweiter wichtiger Einsatzpunkt für den 3R Regenerator ist der optische Schaltknoten. Hier ist die Regeneration vorzugsweise mit einer Wellenlängen-Konversion zu kombinieren, um so in geschalteten optischen Netzen die Wellenlängen-Kollisionen zu vermeiden oder die λ-Umsetzung für Routing zu nutzen. Angesichts dieser Überlegungen wurden zwei modifizierte 3R Schaltkreise entwickelt, die unter Nutzung der gleichen Halbleiter-Funktionselemente realisiert wurden. Diese wurden sowohl anhand numerischer Simulationen als auch experimentell detailliert analysiert. Die Ergebnisse werden vergleichend diskutiert und genutzt, um die Signal-Regeneration von 40 Gbit/s PRBS RZ Daten-Strömen zu optimieren.

Die erste 3R Schlüsselkomponente ist der selbstpulsierende PhaseCOMB-Laser (Phase Controlled Mode Beating), der für rein-optische Taktrückgewinnung genutzt wird. Diese Komponente ist eine bekannte Entwicklung des FhG-HHI. In der Arbeit wird das Potenzial des PhaseCOMB-Lasers für den Einsatz in einem 3R Regenerator evaluiert. Insbesondere wurde der Einfluss von starken Daten-Degradationen verschiedenen Ursprungs auf die Zeitstabilität des Clock-Signals untersucht, um damit die Robustheit der Clock gegenüber Störungen, die typischerweise in realen Übertragungssystemen auftreten, zu verifizieren. Speziell in Hinblick auf den Einsatz in asynchronen Netzen wurde weiterhin die Burst-Fähigkeit der PhaseCOMB-Clock eingehend analysiert. Die Ergebnisse bestimmten das Design der 3R Schaltkreise, die für den asynchronen Betrieb optimiert wurden.

Die zweite Schlüsselkomponente basiert auf Halbleiterverstärkern. Dabei wurde die Länge der Komponente als Optimierungs-Parameter zum ersten Mal systematisch untersucht und ausgenutzt. Hierzu wurden in der FhG-HHI Technologie ultra-lange SOAs (UL-SOA) zwischen 2 mm und 8 mm hergestellt. Das Ziel war es, die Nichtlinearitäten über die Länge eines Halbleiterverstärkers effektiver zu nutzen. Es konnte gezeigt werden, dass die ultra-schnellen (< 1 ps) Intra-Band Cross-Gain Effekte mit der SOA Länge immer stärker zur Gain-Sättigung beitragen und schließlich dominieren. Darüber hinaus wurde erkannt, dass auch bei den Inter-Band Effekten die Erholzeit deutlich beschleunigt wird. Diese geht in einem 8 mm UL-SOA herunter bis zu 10 ps, im Vergleich zu ~100 ps bei einem konventionellen kurzen SOA. Die schnelle Erholzeit ermöglicht es, die UL-SOAs und Inter-Band Effekte für hochratige optische Signal-Verarbeitung bei 40 Gbit/s und höher auszunutzen.

Die Eigenschaften der oben genannten Halbleiter-Funktionselemente wurden in einer neuartigen Anordnung (FhG-HHI Patent) vereint. Die Kombination der effektiven und schnellen Gain-Dynamik der ultra-langen SOAs zusammen mit der hohen zeitlichen Stabilität des optischen Clock-Signals führt zum regenerativen Verhalten der periodisch modulierten UL-SOAs. Der periodisch modulierte UL-SOA bildet die Grundlage der beiden in dieser Arbeit entwickelten optischen 3R Architekturen, dem ‚Optically-Clocked' 3R (OC-3R) Regenerator und dem ‚Alternating Data-Clock' 3R (ADC-3R) Regenerator.

Die Signal-Regeneration im wellenlängen-erhaltenden ‚Optically-Clocked' 3R Regenerator basiert auf einem effektiven Carving der degradierten Datenpulse, die sich gemeinsam mit dem periodischen Taktsignal der Clock durch den gesättigten UL-SOA ausbreiten. Die dominante Clock bestimmt die Sättigungsverhältnisse und dadurch die Regenerationseffizienz des periodisch getakteten Verstärkers, während das schwache Daten-Signal unter Erhalt der Wellenlänge regeneriert wird. Der Einfluss von unterschiedlichen Daten-Degradationen (Amplituden-Fluktuationen, zeitliche Instabilität, OSNR Verringerung) auf die Funktionalität des optischen 3R Regenerators wurde detailliert untersucht, um die optimale Arbeitsbedingungen zu definieren. Anschließend wurde das Einsatzpotenzial des OC-3Rs zur Korrektur der Polarisations-Moden-Dispersion (PMD), der residualen Chromatischen Dispersion (CD) und zur Regeneration von asynchronen 40 Gbit/s Datenströme (kurze PRBS Pakete) evaluiert.

In der zweiten 3R Architektur, dem ‚Alternating Data-Clock' 3R Regenerator, wird die Signal-Regeneration mit einer Wellenlängen-Umsetzung kombiniert. Anders als bei konventionellen 3R Schaltkreisen, wird im ADC-3R die Ausgangswellenlänge des regenerierten Daten-Signals von einem im ganzen C-Band flexibel wählbaren (z. B. ITU Raster) CW Signal definiert. Die Zeitlage der konvertierten Daten-Pulse wird auch in diesem Schema durch das stabile Clock-Signal bestimmt. Das regenerative Potenzial der ADC-3R Architektur wurde sowohl für unterschiedliche Degradationen der 40 Gbit/s PRBS RZ Datenströme als auch für verschiedene Wellenlängen-Kombinationen ausführlich analysiert, um die typischen Eigenschaften dieses kompakten 3R Schaltkreises zu evaluieren.

Contents

1 Introduction

The increased demands on transmission capacities due to the introduction of new Internet services result in continuous growth of data rates as well as more effective utilisation of the optical bandwidth. Increasing the data rates by a factor of four has historically reduced the cost for the transmission of a unit bandwidth by approximately 40 % [1]. The design of the telecommunication networks has been changed several times in the past decades (e.g. transition from single-wavelength to multi-wavelength transmission, introduction of erbium doped fibre amplifiers). During the last network upgrade from 2.5 Gbit/s to 10 Gbit/s, compensation of chromatic dispersion was introduced, in order to preserve the transmission distances without a significant increase of the penalties (optical signal to noise ratio (OSNR) sensitivity, power dynamic range). The implementation of dispersion compensating fibres (DCF) required modifications in installation of the in-line amplifiers in order to compensate for the additional losses. Even due to this major upgrade of installed systems a new approach to the network planning was introduced, resulting in simpler and less expensive networks in the long-term sense [2].

The next logical step in the network evolution will be upgrading the transmission systems to 40 Gbit/s data rate per WDM (wavelength division multiplexing) channel. It is of economical interest to reduce the number of wavelength channels by increasing the bit rate (lower cost per managed bit per km) [1]. The 40 Gbit/s technology is mature enough today. The new systems are currently designed to be hybrid, where 10 Gbit/s and 40 Gbit/s signals can co-exist in one spectral band. The already installed 10 Gbit/s WDM systems can be in-service upgraded to 40 Gbit/s, enabling carriers and service providers to postpone expensive new network installation.

The key to a successful transition from 10 Gbit/s to 40 Gbit/s is the ability to utilise the existing transmission infrastructure. It is of high importance that 40 Gbit/s systems can use the same type of transmission fibres, optical amplifiers, and dispersion compensating fibres as currently deployed 10 Gbit/s systems. Dispersion map compatibility between 10 Gbit/s and 40 Gbit/s as well as robustness against polarisation mode dispersion (PMD) distortions and fibre nonlinearities has to be guaranteed. The 40 Gbit/s transmitter must provide a similar output power and the modulation format has to enable signal transmission through band-pass filters of typical 10 Gbit/s optical MUX/DEMUX without significant filtering penalty.

The modulation formats that provide the largest transmission distances are generally also the most complex to realise, and therefore the most costly to implement [3] – [5]. Spectrally efficient return to zero (RZ) (50 % duty cycle) as well as carrier suppressed RZ (CS-RC) on-off keying modulation formats is a promising alternative for 40 Gbit/s systems. They offer good robustness to non-linear fibre propagation effects and provide higher PMD tolerance in comparison to non-return to zero (NRZ) signals [6], [10]. Furthermore, the RZ modulation shows advantages when performing signal processing in the optical domain. In contrary to the NRZ signals, the clock information can be directly recovered from the RZ PRBS data streams.

However, the influence of system impairments becomes even more critical when increasing the data rates, limiting seriously the total transmission distances. In 10 Gbit/s dispersion managed (DM) networks, the signal degradation is determined predominately

by linear attenuation due to fibre insertion losses and by amplified spontaneous emission (ASE) of the cascaded EDFAs, which reduce the OSNR. In case of the 40 Gbit/s systems, noise accumulation as well as stronger interactions between the fibre dispersion and nonlinear effects results in faster degradation of the PRBS signals in the amplitude domain and time domain. The impact of these impairments is obvious from Fig. 1.1. The simulated eye diagrams show the quality of an ideal 40 Gbit/s RZ PRBS signal (Fig. 1.1a) after propagation through a 320 km SSMF in a single-channel configuration (Fig. 1.1b) and after transmission over 800 km in a four channel DWDM (Dense Wavelength Division Multiplexing) configuration with 100 GHz channel spacing (Fig. 1.1c). Although the transmission link was properly optimised regarding power levels, amplifier spans and dispersion compensation (typical measures for optimisation of a 10 Gbit/s system), the increase of timing and amplitude fluctuations cannot be omitted.

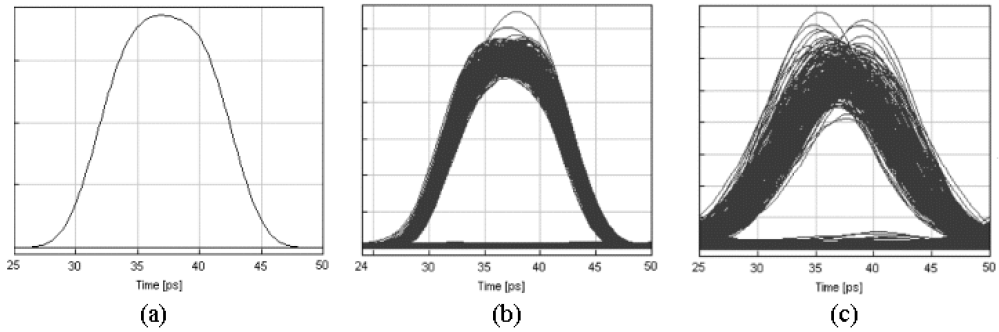

Fig. 1.1: Simulated eye diagrams of a 40 Gbit/s PRBS RZ signal: back-to-back (a), single channel transmission over 320 km SSMF (b), and 4xDWDM channel transmission (100 GHz grid) over 800 km SSMF (c) [11].

The origin of the degradations is related to linear effects (fibre attenuation, chromatic dispersion, polarisation mode dispersion) and nonlinear effects (Kerr nonlinearities, Brillouin scattering, Raman scattering) in fibres [12], as well as to the interactions between the two groups.

The impact of *chromatic dispersion* (CD) is 16-times more critical when increasing the bit rate from 10 Gbit/s to 40 Gbit/s [11]. In this case, the consecutive data bits are four times closer to each other, accelerating the bit-to-bit interactions. Furthermore, the broadened spectrum results in faster walkoff of the spectral components. The consequence is, thus, broadening of the single pulse, resulting in inter-symbol-interference (ISI). With increased channel data rates, the signal degradation caused by *polarisation mode dispersion* (PMD) has to be considered. The origin of PMD distortions is related to the fibre core asymmetry (typical feature of older, already installed fibres) with slow variations in time on the one side and to the mechanical stress (dynamic variations) on the other side. Due to the fibre birefringence, the two orthogonal modes propagate at different velocities, leading to pulse broadening defined by differential group delay (DGD). Because of the statistical behaviour of the PMD, a mitigation technique is inevitable, when the DGD value exceeds one-tenth of the bit-duration [13].

The impact of nonlinear limitations caused by the Kerr-effects in optical fibres is more critical in 40 Gbit/s systems because of stronger influence of the CD and PMD. In case of amplitude modulated data formats, *self-phase modulation* (SPM) results in variations of instantaneous frequency (nonlinear chirp) across the pulse. New frequency components are

generated in the signal spectrum, leading to spectral broadening. Together with CD, the phase modulations are transformed to intensity modulations. Considering a multi-channel transmission system, *cross-phase modulation* (XPM) can lead to signal degradations. In this case, the phase variations are stimulated by power variations in the adjacent channels. The XPM introduces timing jitter as well as amplitude fluctuations to the transmitted optical signals. Additionally, multi-channel systems can suffer from signal distortions due to *four waves mixing* (FWM). The interaction of different frequencies results in generation of new spectral components. Hence, the FWM causes dominant transmission limitation especially in spectral efficient DWDM systems. In case of equal channel spacing (state of the art), the new spectral components overlap directly with signals in adjacent channels.

Due to the relatively fast pulse broadening in 40 Gbit/s systems, nonlinear interactions between adjacent and distant pulses become more significant. Fundamentally, there are two types of distorting effects: *Intra-channel XPM* (IXPM) and *intra-channel FWM* (IFWM). IXPM degrades the signal through phase modulation between two overlapped pulses. The resulted frequency chirp is transformed by fibre dispersion into timing jitter and amplitude fluctuations. The influence of IXPM is most critical for a partial overlap between adjacent pulses. In high bit rate transmission systems with periodical span-by-span dispersion compensation, the IXPM represents the dominant transmission limitation [14]. The anomalous dispersion of standard single mode fibres (SSMF) causes a pulse broadening due to the faster propagation of the blue spectral components. In case of IFWM, the blue components interact with the red spectral components of the adjacent pulses, resulting in amplitude distortions and generation of ghost pulses [11]. The effect of IFWM is most significant in case of nearly completely overlapped pulses.

The 40 Gbit/s systems are thus more sensitive on signal degradations (especially when considering already embedded SSMFs), resulting in even shorter maximum transmission distances compared to the 10 Gbit/s systems. In order to overcome the strong limitations, the signals have to be completely regenerated already during the propagation through the fibre link. Fundamentally, two techniques for signal restoration can be taken into account. The first consist in segmenting the system into independent trunks, which are concatenated by electronic repeater stages. In this case, the transmitted optical signal is converted in the electrical domain, regenerated and then converted back into optical domain. This solution is referred to opto-electronic (o/e) signal regeneration. The second approach is based on an all-optical solution, where the signal restoration is performed in the optical domain. The advantages of the all-optical 3R regeneration are related to higher bandwidth by reduced complexity and enhanced capabilities. The importance of the optical solution grows with increased bit rate per channel (40 Gbit/s and beyond) due to higher costs of o/e/o converters as well as in case of all-optical networks with optical cross-connects (OXC), where the switching and routing functions are incorporated into the optical part of the network. Hence, in a long-term sense, the all-optical signal regeneration becomes more attractive compared to the opto-electronic solution.

2 All-Optical Signal Regeneration

An important issue, which has to be considered when optimising optical networks, is the analogue transmission nature of optical signals (degrading effects that the optical signals undergo during transmission are accumulated). Due to the impact of CD and PMD, the maximum transmission distances in installed point-to-point systems are generally much shorter when increasing the data rates (e.g. up to 40 Gbit/s). In future transparent all-optical networks, the data signals will be optically switched and routed in optical cross-connects. Thus, the signals will be transmitted over different distances, amplified by a different number of optical amplifiers, depending on the path through the network and the number of nodes traversed. In order to preserve the signal quality even in the worst-case scenario, a complete signal restoration will be indispensable.

In this chapter, the principle of optical 3R signal regeneration (re-timing, re-shaping, re-amplification) is discussed and the key requirements for optical regeneration are defined. The regeneration architectures proposed in the literature by other groups are shortly reviewed. Finally, the novel 3R regenerators developed in frame of this work are presented and the outline of the thesis is given.

2.1 Requirements for optical 3R regenerators

A schematic of an optical 3R regenerator is depicted in Fig. 2.1. The operation principle of a 3R regenerator is as follows. The PRBS data signal is amplified in the amplification stage. The clock recovery stage performs extraction of the clock component from the incoming PRBS stream. The clock defines also the shape of the regenerated pulses. A nonlinear gate with a threshold level provides the decision function. The accumulated noise is suppressed and the amplitude fluctuations are equalised. A fully restored signal is obtained behind the optical 3R regenerator.

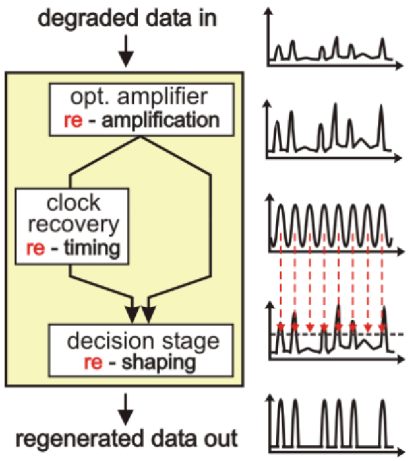

Fig. 2.1: Schematic of an optical 3R regenerator with the main building blocks.

The 3R regenerators have to process data signals of different qualities, leading to request on robust operation of the 3R schemes and high immunity against different system impairments. The main requirements that should be addressed by an all-optical regenerator are given as:

- Suppression of timing jitter and amplitude fluctuations
- OSNR and extinction ratio improvement
- Polarisation independence
- High power dynamic range
- Large optical bandwidth
- Moderate input power requirements
- Low power consumption, compactness and simple implementation

Due to the high requirements for the regeneration schemes, it is difficult to realise an all-optical regeneration circuit providing all functionalities. Generally, each technique has its merits and shortcomings and a compromise in performance has to be found.

2.2 Optical 3R regeneration: State of the art

In the following, several regeneration concepts proposed in the literature are presented. The basic operation principle of the schemes is briefly discussed, pointing out their advantages and limitations. The section focuses on the two most important functionalities of an optical 3R regenerator:

- Clock extraction from PRBS data streams and
- Signal quality restoration in decision gates.

2.2.1 Optical clock recovery techniques

In the 3R scheme, an optical clock extraction circuit has to recover timing information from the incoming optical data signal and to generate a stable periodical pulse trace of the exact frequency and phase of the bit streams. The stability of the recovered clock defines the timing stability of the regenerated PRBS signals. Thus, a low jitter clock signal is a key prerequisite for all-optical signal regeneration. Furthermore, the pulse shape of the data signal at the regenerator output is directly or indirectly determined by the shape of the recovered clock signal. This has to be considered when combining the decision stage with the clock recovery stage in a 3R circuit. In the following, optical clock recovery techniques based on self-pulsating lasers, mode-locked lasers, Fabry-Pérot etalons, and optical phase locked loop are briefly reviewed.

Self-pulsating lasers (SPL) [15] – [19] are compact semiconductor devices comprising generally two laser sections (DFB, FP) and alternatively a passive phase tuning section in-between. In case of high pulsation frequencies, both laser sections are operated at lasing condition. The superposition of the lasing modes produces a beating-type self-pulsation with a frequency given by the spectral distance of the two modes. The nonlinear coupling of the two lasers enables locking of the beating oscillation to external signals. The resulting modulation of the carrier densities due to the injected signal modifies the mode frequencies

and, in turn, the pulsation frequency. The self-pulsation frequency can be tuned nearly continuously in a wide range simply by changing the values of the driving currents. Hence, the same device can be used for clock recovery from different data rates (e.g. 40 Gbit/s and 80 Gbit/s), which is an advantageous feature from an economical point of view. A three section self-pulsating PhaseCOMB-laser (Phase Controlled Mode Beating) for all-optical clock recovery is the key component of the 3R regeneration architectures proposed in this work. The design and basic functionalities of the PhaseCOMB-clock are discussed in Chapter 3.

All-optical clock recovery based on *injection locking of mode-locked lasers (MLL)* was demonstrated in [20] – [24]. Mode-locking is a technique for extraction of optical pulses from a multimode laser oscillator, forcing the optical modes by an active or passive amplitude modulator to defined phase conditions into the laser cavity. Typically, an electro-absorption modulator (EAM) or a saturable absorber (SA) is used to modulate the signal amplitude. The all-optical clock recovery is based on synchronisation and stabilisation of the mode-locking operation by an external optical signal. The recovered clock signal behind the MLL is characterised by short pulses (typically some ps). The pulsation frequency is defined by the length of the laser cavity.

The operation principle of an all-optical clock recovery using a *Fabry-Pérot filter (FPF)* [25] – [27] is based on spectral filtering of the carrier and clock component of the RZ coded data signal. A high finesse value and free spectral range (FSR) exactly matching the clock frequency are the main prerequisites for a stable clock signal behind the FPF. In the time domain, this corresponds to fill the zero slots in the data stream with optical pulses. The pulses are reflected forward and backward in the FPF and partially extracted from the output mirror at each round-trip. The amplitude of the clock pulses depends on number of the consecutive zero bits in the PRBS word (the intensity of the pulses exponentially decays) and, thus, an additional active power equalising function is necessary (e.g. using a saturated SOA). Fine frequency tuning in a limited range can be generally performed when varying the resonator length. The clock extraction by a FPF is basically a very simple technique compared to the other solutions discussed in this section. However, data signal distortions directly influence the timing stability and shape of the clock pulses, which is a disadvantageous feature when considering an optical 3R scheme.

The clock recovery technique based on *optical phase locked loop (OPLL)* [28] – [31] involves a phase comparison in the optical domain. The phase comparator generally exploits nonlinear effects in high dispersive fibres or semiconductor devices (SOA, SA). The extracted error signal is injected into a Voltage Control Oscillator (VCO) that drives an optical pulse source (e.g. MLL). The MLL defines the pulse form and timing stability of the recovered clock signal. The OPLL technique requires a relatively high number of optical and electrical components. Furthermore, expensive RF-electronics is needed when increasing the oscillation frequency.

2.2.2 Schemes for all-optical nonlinear gates

While the clock circuit defines the timing stability of the processed signals, the key function of a decision stage is related to OSNR improvement as well as suppression of signal degradations at the zero and mark power levels. The regenerative performance of the decision circuit is determined by the steepness of the nonlinear transfer function. The steeper the transfer characteristic, the more effective is the signal improvement. Figure 2.2

schematically depicts the impact of the power transfer function on signal improvement. For a linear characteristic (Fig. 2.2a), all input degradations are transferred to the output. On the other hand, an ideal step-like transfer function would completely eliminate the signal distortions (Fig. 2.2b). However, a realistic transfer function of optical decision gates is shown in Fig. 2.2c. In this case, the amplitude fluctuations are only partially suppressed. The efficiency of distortion suppression at the mark (space) level can be controlled when moving the operation point 'P' towards higher (lower) power levels. Generally, the decision gate has to provide high nonlinearities (defining the steepness of the transfer function), which have to be fast enough for performing signal processing at the bit level (exploitation of the whole transfer function).

In the following, the operation principle and main features of decision schemes proposed by different research groups are briefly reviewed.

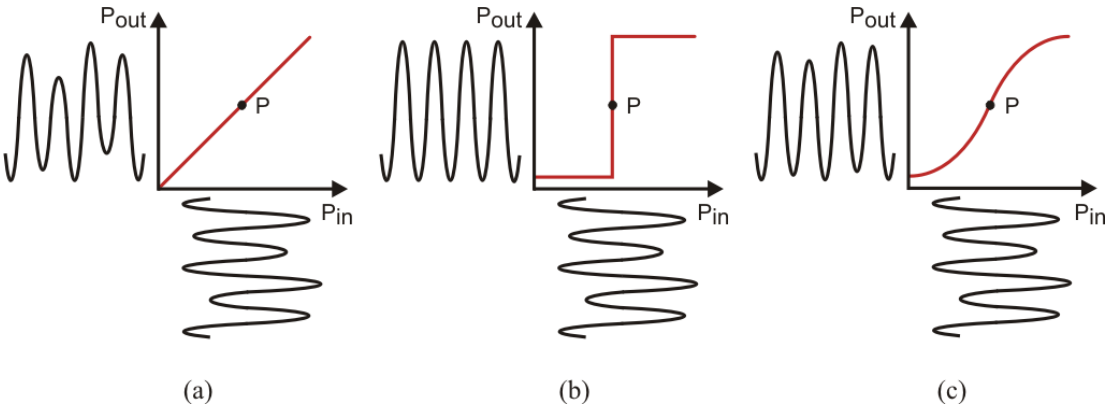

Fig. 2.2: Principle of different power transfer functions indicating their efficiency for suppression of degradations at the signal space and mark levels: (a) linear function, (b) ideal step-like function, (c) typical function of an optical decision gate.

2.2.2.1. All-fibre based decision architectures

The main advantage of fibre based signal processing is related to the inherent high modulation bandwidth (response time of several fs only) and thus to a very high speed potential (beyond 160 Gbit/s). Basically, two different schemes can be exploited for all-optical 3R regeneration, referred as *Kerr Fibre Modulator* (KFM) [33] – [35] and *Nonlinear Optical Loop Mirror* (NOLM) [36] – [38]. Both schemes use phase changes induced by interactions of two modulated signals simultaneously propagating through a highly nonlinear fibre (HNLF). The two decision architectures are sketched in Fig. 2.3. The KFM is simply a transmission fibre itself with simultaneously co-propagating data and clock signals. Two polarisation filters (POL) located in front of and behind the modulator perform the required decision function. The switching effect relies on a polarisation rotation of the clock signal, induced by the data signal in the HNLF. Due to the cross phase modulation between the two signals (a polarisation dependent effect), the component of the data signal parallel to the clock experiences a larger phase shift compared to the orthogonal component. This leads to rotation of the polarisation state for the clock signal that can then pass the second polarisation filter. Thus, the data information is encoded onto the high quality clock signal. The operation principle of the NOLM is similar to the KFM. Here, the

interferometric configuration results in conversion of the phase modulated clock signal into the intensity modulated data signal. If there is no phase difference between the split pulse components of the clock signal ($\Delta\Phi = 0$), all incoming light is reflected. For a phase difference of $\Delta\Phi = \pi$, induced by cross phase modulation in the HNLF through the data signal, the clock pulses are completely transmitted (assuming a 3 dB coupler in the interferometric structure) to the output of the NOLM.

The near instantaneous response of the Kerr nonlinearity makes the fibre based decision gates attractive for high-speed applications. On the other side, major limitations come from environmental instability, strong polarisation dependence, power consumption, and integration difficulty. The shape of the switching window is mainly determined by the shape of the data pulse, as long as chromatic dispersion is neglected [130].

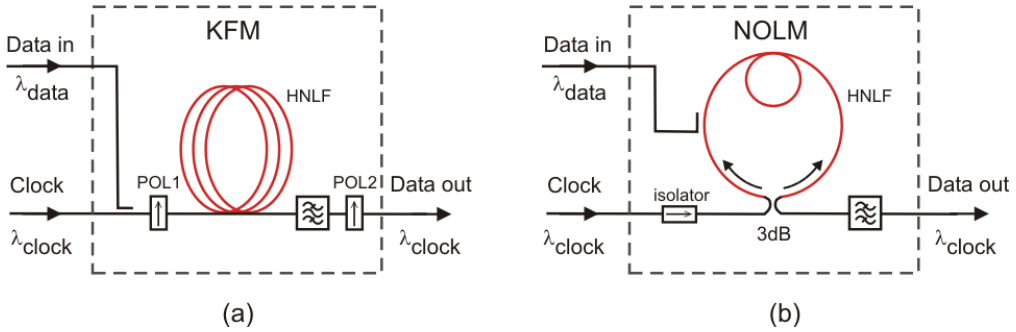

Fig. 2.3: Principle schemes of all-fibre decision gates based on Kerr Fibre Modulator (a) and Nonlinear Optical Loop Mirror (b).

2.2.2.2. Decision elements exploited nonlinearities in semiconductors

In the previous section, the nonlinear function of the optical gates was performed using a fibre with high nonlinearities. In order to obtain the required switching characteristic, a relatively long interaction length is required (several hundred of meters). In this section, decision schemes comprising compact semiconductor devices are discussed. The operation principle exploits gain saturation effects in semiconductor optical amplifiers (SOAs) and absorption saturation effects in saturable absorbers (SAs), respectively.

The decision gate based on *Mach-Zehnder Interferometer* (MZI) [39] – [47] is depicted in Fig. 2.4a. It comprises two SOAs integrated in each interferometer arm. The clock signal is split by a 3 dB coupler and propagates through both SOAs. In the basic configuration, the data signal is inserted into the SOA in the upper branch only. The resulted change of the refractive index due to gain saturation of the SOA induces a phase difference between both interferometer branches. For $\Delta\Phi = \pi$, the clock pulse is switched from the output port 2 to the output port 1. However, the modulation effects in SOAs are intrinsically limited in speed by the relatively slow gain recovery time (100 ps range) that defines the temporal width of the switching window in this case. The switching window can be properly adjusted in a differentially controlled MZI configuration, where the data pulses are injected into both arms of the interferometer, temporally delayed to each other by a delay τ. In this case, the data pulse, which enters the SOA in the lower branch a time τ later, cancels the phase difference between both branches, thus closing the switching window. Hence, the induced phase variation is suppressed after a time τ by the same signal from the second arm. The temporal width of the switching window is directly controlled by the delay τ.

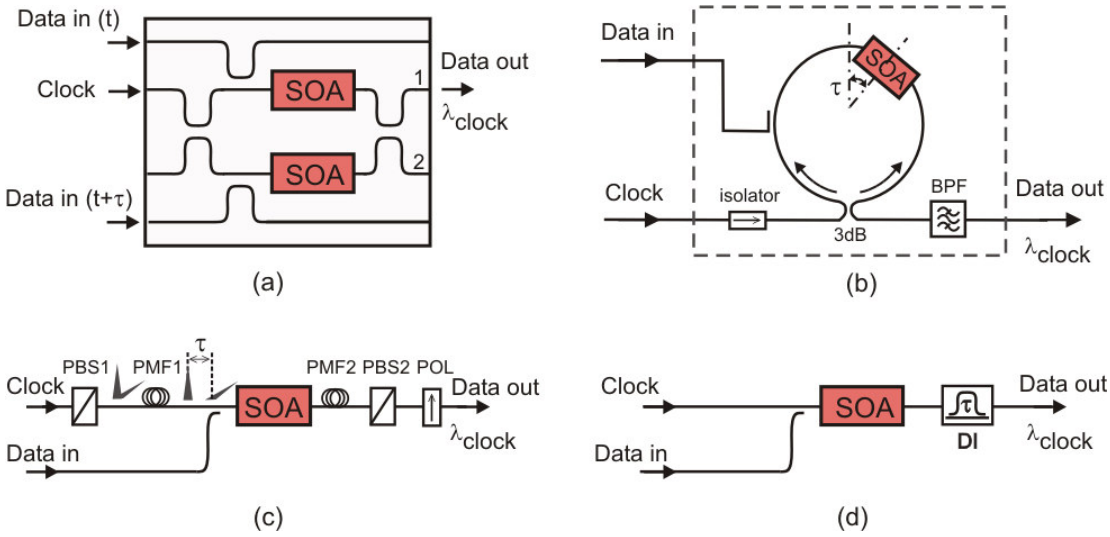

Fig. 2.4: Nonlinear decision gates based on Mach-Zehnder Interferometer (a), Sagnac interferometer (b), ultra-fast nonlinear interferometer (c), and delay interferometer (d).

The principle scheme of a nonlinear decision gate based on *Asymmetric Sagnac Interferometer* [48] – [50] is shown in Fig. 2.4b. The configuration is similar to the NOLM described in the previous section. In this case, however, the nonlinear medium is performed by an SOA instead of the HNLF. A 3 dB coupler splits the incident clock beam into two counter-propagating beams. Both the clockwise and counter-clockwise beams experience a nonlinear phase shift induced in the SOA by the data signal. The SOA is shifted from the centre of the loop by a time delay τ that defines the gating window. The data is encoded onto the clock at the interferometer output.

A semiconductor *Ultrafast Nonlinear Interferometer* (UNI) [51] – [52] has been also used as a decision element in an optical 3R regenerator. The scheme indicating the operation principle is sketched in Fig. 2.4c. The UNI comprises a single SOA as a nonlinear medium. At the input, the clock pulse is split in the polarisation beam splitter (PBS1) into two orthogonal components and propagates through a highly birefringent polarisation maintaining fibre (PMF1). Due to the different propagation velocities of the two orthogonal pulse components, the slow component passes the SOA temporally delayed by τ, which is defined by the differential group delay (DGD) of the PMF. Without a data pulse, the UNI can be balanced such that the clock pulses are blocked at the polarizer (POL) output after passing the PMF2 (delay between the pulse components is cancelled) and PBS2. If a data pulse enters the SOA between the two clock components, the slow component experiences a different phase shift, compared to the fast one. In this case, the clock components recombine to a different polarisation behind the PBS2 and the clock pulse passes through the polarizer.

In a simplified interferometric scheme, the SOA is located outside a passive *Delay Interferometer* (DI) (Fig. 2.4d) [53] – [54]. The data information is encoded onto the clock by means of XPM in the SOA. The relative length difference between the upper and lower brunch of the DI defines the switching window τ and performs gating of the clock signal.

The nonlinearity induced by an SOA can be also effectively exploited in a single *processing filter* [55] – [57]. The basic configuration is depicted in Fig. 2.5a. The filter is

characterised by a sharp frequency response that closely approximates an ideal step-like function. Due to the frequency chirping in the SOA, the probe signal experiences a frequency shift induced by the data signal. If the filter is detuned towards shorter frequencies relatively to the probe wavelength, the degraded ´zeros´ are blocked, while the ´ones´ are blue-shifted and, thus, pass through the filter. As a result, the converted output signal has improved extinction ratio and timing stability of the clock.

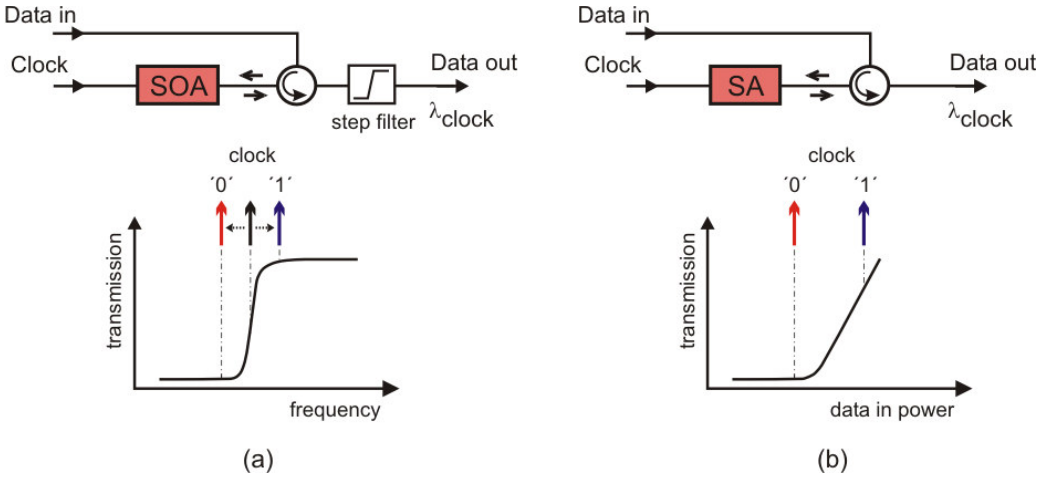

Fig. 2.5: Decision gates exploited frequency chirp in a processing step filter (a) and nonlinear absorption characteristic in a saturable absorber (b).

Lot of interest has been invested on the analysis of *saturable absorbers* (SA) as a nonlinear decision element for optical 3R regeneration [58] – [67]. The major advantage of this scheme is related to its simplicity (Fig. 2.5b). Fundamentally, it comprises only a single component. The effect is based on cross absorption modulation (XAM) in the semiconductor waveguide. In case of low data power (space levels), the photonic absorption of the SA is high (low transparency). However, exceeding the threshold defined by the saturation power (mark levels), the SA transmittance increases rapidly. The clock signal can be thus gated by the contra-propagated PRBS signal, resulting in re-timing and re-shaping function at the SA output.

From the physical point of view, the behaviour of an SOA and SA has inverse character. The SOA provide gain that drops down when exceeding the saturation power level (suppression of amplitude fluctuations). In contrary, the SA provides absorption that can be bleached by an external optical signal (noise suppression at the space level). This is the basic idea of nonlinear decision gates based on an *integrated SOA-SA cascade* [68]. By proper optimisation of the properties of the cascaded SOA and SA structures, a simple pass through 2R regenerator can be obtained [69]. The static characterisation of the SOA-SA structure showed nearly step-like power transfer function. The steepness can be further enhanced when concatenating several cascades on a single chip [70]. The challenges of this concept are related to the difficulty in fabrication. It has to be guaranteed that the signal wavelength is located in the gain spectrum of the SOA and, at the same time, in the absorption spectrum of the SA. Thus, heterostructures with different band gaps have to be monolithically integrated.

2.2.2.3. Decision element based on in-line synchronous modulation

All-optical 3R signal regeneration can be achieved without any wavelength conversion by means of *in-line synchronous modulation* (SM) associated with *narrow-band filtering* (NF) [71] – [77]. Regeneration by SM-NF intrinsically requires nonlinear (soliton) propagation in the trunk fibre. The configuration of the SM-NF decision element is depicted in Fig. 2.6. The narrowband filtering of soliton pulses results in suppression of amplitude fluctuations. An increase in pulse intensity corresponds to both time narrowing and spectral broadening. A decrease in pulse intensity corresponds to time broadening and spectral narrowing. Thus, the filter induces higher loss when the intensity increases, and reduced loss when the intensity decreases. The jitter reduction is performed by self-forming properties of soliton pulses when propagating through the modulator driven by a stable sinusoidal clock signal.

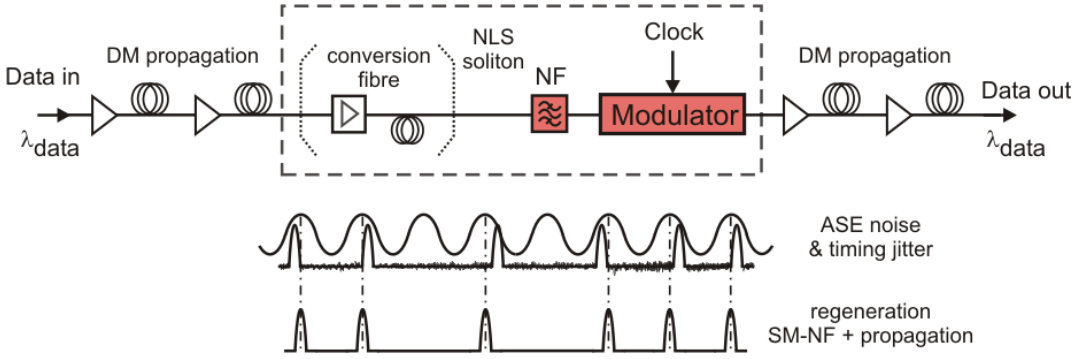

Fig. 2.6: PRBS signal regeneration based on in-line synchronous modulation associated with narrow band filtering.

In summary, a lot of investigations have been already done on optical 3R signal regeneration. The main advantage of fibre based 3R regenerators is related to the high speed potential. However, the large interaction length, strong polarisation sensitivity, high power consumption make them less attractive for system applications. The compact semiconductors provide much higher potential for optical signal processing. Usual architectures are based on interferometric structures exploiting XGM and XPM effects in SOAs. The limiting time constants of inter-band gain dynamics in conventional SOAs (~100 ps) can be overcome using a differential scheme resulting in bit rate enhancement up to 40 Gbit/s. However, the switching window is defined by the shape of the data pulses. In order to effectively use the gating window of interferometers, short pulses are preferable (usually much shorter than the signal bit period). Thus, there is a trade off between the regenerator performance and the spectral efficiency required in DWDM systems. Furthermore, the pattern dependent SOA gain variations induced by the PRBS data signal degrade the exclusively XPM based regenerative efficiency of the interferometers. A relatively steep nonlinear transfer function can be obtained in a cascade of SOA together with a processing filter or in a saturable absorber. The drawback of SAs is related to high power levels needed for XAM and to limited speed potential (usually up to 10 Gbit/s). The processing filters with a steep slope are very attractive for high-speed signal regeneration, when the frequency chirp (high degree of gain saturation and fast gain recovery required) induced by SOAs is sufficiently high.

An optimised all-optical 3R architecture has to overcome physical limits of the optical components used for regenerative high-speed processing of PRBS data streams that are distorted by almost undefined system impairments. Although several of the aforementioned all-optical 3R schemes were successfully applied in high-speed transmission loop experiments, they have not reached a commercial breakthrough up to now. Hence, it is still of high interest to proceed the investigations on all-optical 3R signal regeneration, focusing on a compact and practicable solution for realistic all-optical DWDM networks.

2.3 Novel semiconductor based 3R architectures

The purpose of this work is to develop all-optical 3R regeneration schemes for their implementation in a realistic transmission system. Apart from effective regenerative performance the following aspects are considered:

- Small footprint (thermal and mechanical stability, integration possibility)
- Low power consumption (high nonlinearities at moderate power levels)
- Dense spectral usage (RZ pulses of around 50 % duty cycle)
- High speed potential (40 Gbit/s and beyond)

Two architectures for all-optical 3R signal regeneration were developed in the frame of this thesis:

- A wavelength-preserving scheme, referred as ‘Optically Clocked’ 3R regenerator (OC-3R)
- A wavelength-converting scheme, referred as ‘Alternating Data-Clock’ 3R regenerator (ADC-3R)

Both proposed regeneration architectures are based on two compact semiconductor devices:

- A self-pulsating three-sections PhaseCOMB-laser (Phase Controlled Mode Beating) for all-optical clock recovery and
- An ultra-long semiconductor optical amplifier (UL-SOA) for exploitation of fast gain and phase nonlinearities.

The schematics of the OC-3R and ADC-3R regenerators are sketched in Fig. 2.7a,b. In both architectures, the clock information is extracted all-optically from the PRBS data stream. The signal regeneration is performed by nonlinear data-clock interactions in a periodically modulated semiconductor amplifier. The OC-3R is a wavelength-preserving scheme without necessity of any wavelength controlling during the signal processing. On the other hand, a wavelength conversion is performed in the ADC-3R. In contrary to the conventional 3R schemes, a CW source determines the wavelength of the data signal behind the ADC-3R regenerator (free selectable within the whole C-band), while the timing of the converted pulses is defined by the stable clock signal. The regeneration schemes have been developed and optimised for operation in 40 Gbit/s RZ PRBS data streams. However, the dynamics of the applied semiconductor components provide much higher speed potential and regeneration of data signals up to 160 Gbit/s is fundamentally possible. Both 3R architectures support processing of RZ pulses with a duty cycle of

around 50 %. Thus, they can be directly deployed in current DWDM networks, without any explicit bandwidth modification of the filters used in the transmission system. The advantage of semiconductors is related to low power consumption, high degree of nonlinearities and small footprint. The 3R architectures proposed in this thesis comprises exclusively compact optical devices. Both circuits are thus characterised by mechanical and thermal stability with further integration potential on a common silica motherboard.

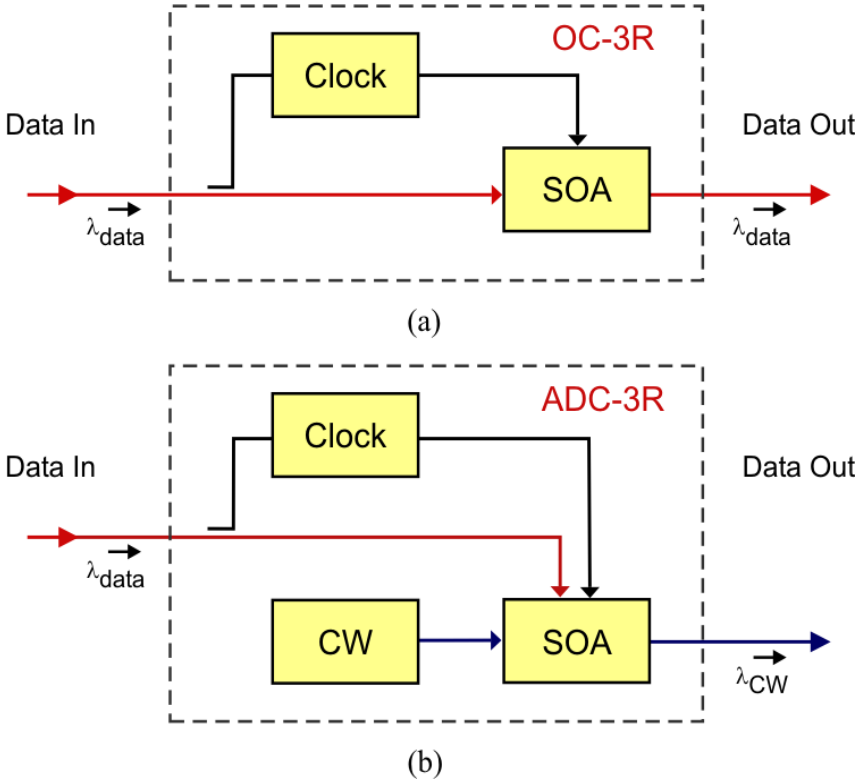

Fig. 2.7: Principle schemes of the wavelength preserving 'Optically Clocked' 3R regenerator, OC-3R (a) and of the 'Alternating Data-Clock' 3R regenerator, ADC-3R, for regenerative wavelength conversion (b).

The advantages, when comparing the two proposed regeneration architectures, depend on the application field in the optical systems. The OC-3R scheme can be deployed as an in-line 3R regenerative amplifier in ultra long-haul point-to-point transmission links for effective enhancing of maximum transmission distances. The ADC-3R regenerator can effectively upgrade the functionality of optical cross-connects in transparent meshed networks. In this case, simultaneous protection against channel blocking and regenerative conversion to a flexible wavelength is performed.

The characteristics of the two building blocks (PhaseCOMB-Clock, UL-SOA) as well as their potential in the proposed all-optical 3R architectures are studied in detail. Furthermore, the optimised operation conditions and regenerative performance of the OC-3R and ADC-3R schemes are analysed. The main results on the numerical and experimental investigations are presented in the following chapters.

2.4 Outline of the Thesis

The contents of this thesis summarises the numerical and experimental analysis on the main building blocks as well as on the assembled all-optical 3R regenerators. The thesis is divided into following chapters:

Chapter 3 demonstrates the potential of the all-optical clock recovery technique exploiting synchronisation of self-pulsating PhaseCOMB-lasers (Phase Controlled Mode Beating). The locking characteristics and the system performance of the PhaseCOMB-clock by operation in 40 Gbit/s degraded PRBS RZ data streams are evaluated.

Chapter 4 analyses the gain dynamics of ultra-long semiconductor optical amplifiers (UL-SOAs). The impact of SOA length on gain suppression and gain recovery processes is studied. The exploitation of nonlinear effects caused by periodical carrier density modulation of UL-SOAs is identified and the conclusions for regenerative potential of the long amplifiers are given.

Chapter 5 investigates the performance of the wavelength preserving 'Optically Clocked' 3R regenerator (OC-3R). The architecture and optimised operation conditions are presented. The regenerative potential of the proposed scheme for different signal degradations is analysed. Mitigation of chromatic dispersion and polarisation mode dispersion as well as operation in 40 Gbit/s asynchronous packet data streams is demonstrated.

Chapter 6 introduces the second optical 3R scheme, the 'Alternating Data-Clock' 3R regenerator (ADC-3R). The principle of regenerative wavelength conversion is described. The importance of XGM and XPM effects in UL-SOAs is pointed out. The performance of the ADC-3R architecture is investigated in degraded 40 Gbit/s PRBS RZ data signals for different wavelength conversions.

Chapter 7 concludes the most important results on the numerical as well as experimental studies and gives an outlook on the potential of the developed novel all-optical 3R schemes.

3 Self-pulsating PhaseCOMB-laser for all-optical clock recovery

The optical clock recovery stage builds an important part of an all-optical 3R regenerator. It defines the timing stability as well as the shape of the regenerated data pulses. Furthermore, the characteristics of the clock recovery stage have to support the functionality of the 3R scheme. In case of the novel 3R regenerators proposed in this thesis, the self-pulsating PhaseCOMB-clock provides a suitable performance, as it will be demonstrated later. The design and theoretical background of the all-optical clock can be found e.g. in [88] – [89], the characterisation of the PhaseCOMB-clock from a system point of view was performed in frame of this work. The target of this chapter is to introduce the typical characteristics of the PhaseCOMB-laser with a focus on the performance analysis of the all-optical clock operated in highly degraded data signals.

First, three types of self-pulsating multi-section lasers developed at FhG-HHI are briefly discussed and compared to each other. In the following, the locking behaviour of the PhaseCOMB-clock is investigated by operation in 40 Gbit/s PRBS RZ data streams. Finally, the regenerative potential of the optical clock is studied for different degradation types of the PRBS signal.

3.1 Basic classification of self-pulsating multi-section lasers

Lot of investigations on generation of optical oscillations in self-pulsating lasers have been already performed (see [79] and references therein). However, only some of the proposed techniques are suited also for high-speed all-optical clock recovery. Self-pulsating multi-section semiconductor lasers provide promising features for application in an all-optical 3R regeneration scheme. At FhG-HHI, three types of self-pulsating lasers have been developed; covering the main classes of SP based clock recovery techniques:

- Dispersive self Q-switching SP lasers (DQS-clock)
- SP-lasers based on beating type oscillations (PhaseCOMB-clock)
- SP-lasers with DFB section and compound feedback cavity (AFL-clock)

The *Dispersive Self Q-Switching* clock [81] is a three-section laser comprising two DFB sections and a passive phase tuning section in-between (Fig. 3.1a). In the DQS-clock, one DFB section is operated at high current (100 mA range). The second DFB section is operated at conditions near the transparency and acts as a reflector with sharp minima in the reflectivity spectrum. The decisive point for generating the self-pulsations is a spectral correlation of the lasing wavelength with a steep slope of the reflector. Here, the threshold conditions are directly correlated with the reflectivity of the resonator. Due to the direct coupling between the carrier density and the refractive index, the laser switches itself off after emitting a short optical pulse and turns on again after a recovery time. Frequency tuning from 5.5 GHz up to 22 GHz has been shown by changing the bias currents of the

laser sections [82]. Up to now, however, higher oscillation frequencies have not been achieved in this type of SP-lasers. Hence, the DQS-clock does not provide sufficient potential for application in high-speed (40 Gbit/s and beyond) 3R schemes.

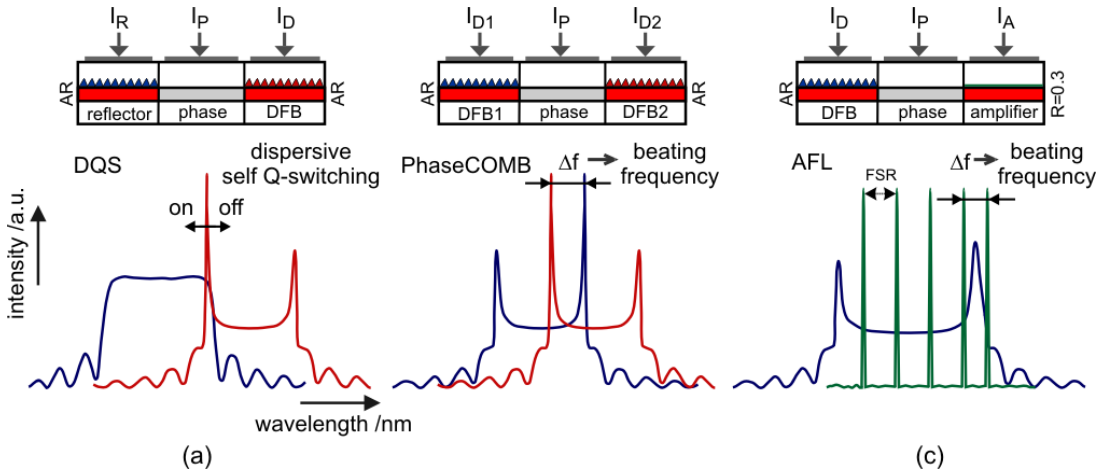

Fig. 3.1: Three-sections self-pulsating lasers for all-optical clock recovery: Dispersive Self Q-Switching (a), Phase Controlled Mode Beating Laser (b), and Laser Active Feedback Laser (c). The principle of the oscillation generation is schematically shown by reflectivity spectra of the corresponding laser sections.

Basically, the same device structure can be used for generation of self-pulsations based on the *Beating Type Oscillations* (Fig. 3.1b) [83]. The main difference is related to the operation of the three-sections laser. In this case, the two DFB lasers are pumped above their threshold level. The DFB gratings are spectrally detuned to each other, as it is obvious from Fig 3.1b. The spectral separation of the DFB modes determines the beating frequency, which can be properly adjusted by the three DC bias currents. The operation of the PhaseCOMB-clock was experimentally demonstrated at 80 GHz [84], a speed potential beyond 160 GHz was theoretically predicted [19].

The DFB laser with short optical feedback (*Active Feedback Laser*) [78], [80] is a three-section laser comprising one DFB section, a passive phase tuning section and an amplifier section (Fig. 3.1c). The pulsation frequency is determined by the spacing of the two compound-cavity modes. Tuning of the oscillation frequency can be performed by changing the driving currents of the DFB section or amplifier section, resulting in spectral shift between the two modes. The role of the phase section is to adjust properly the round trip conditions in the coupled system and, thus, to preserve the mode hopping in the DFB-laser. The feedback strength has a direct impact on the self-pulsation frequencies. Increasing the amplifier current and, thus, increasing the feedback strength results in enhancement of pulsation frequencies. Although the AFL-clock fulfils the prerequisites on high-speed operation, the design of the present generation devices has not been still sufficiently optimised for the high requirements needed by operation in a 3R regenerator.

Thus, the self-pulsating PhaseCOMB-laser was chosen for further application in the novel all-optical 3R regeneration schemes. The typical characteristics of the PhaseCOMB-clock are presented in the following sections.

3.2 Design and locking characteristics of the PhaseCOMB-laser

The PhaseCOMB-laser applied in this work was developed and fabricated in the technology of the FhG-HHI. The self-pulsating laser is a three-section device based on a ridge-waveguide InGaAsP-InP bulk-heterostructure (Fig. 3.2a). It consists of a 1550 nm InGaAsP-layer, which is embedded in an asymmetric InGaAsP optical waveguide. Polarisation independence of the optical gain in the device is achieved by adjustment of the thickness of the layers and the strain of the active layer. The gratings of the two DFB-lasers are detuned by approximately the stop band to each other. After the grating definition, the active layer in the phase tuning section is removed and the p-cladding layers are grown. The wafers are then processed into multi-section ridge-waveguide lasers. The lengths of the two DFB sections and the phase tuning section are around 250 µm and 300µm, respectively. Both facets of the devices are antireflection coated. The laser chips are mounted on a heatsink and packaged into a temperature-controlled module (Fig. 3.2b) for application in system tests.

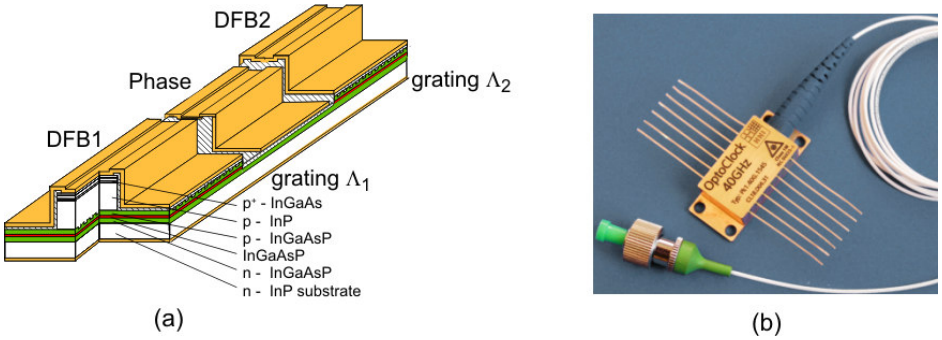

Fig. 3.2: Ridge-waveguide heterostructure of the three-sections self-pulsating laser (a) and the module of the packaged 40 GHz PhaseCOMB-clock (b).

The synchronisation of the self-pulsations in frequency and phase to an injected optical PRBS data signal is the key function needed for optical clock recovery. Figure 3.3a shows the measurement set-up used for the analysis of the locking characteristics of the PhaseCOMB-laser. First, the self-pulsation frequency was properly adjusted by the three DC bias currents and was tuned close to 39.8 GHz (RF-spectrum in Fig. 3.3b: Free running oscillation). The 39.8 Gbit/s (STM-256) PRBS 2^{31}-1 RZ signal (1550 nm) was then launched via a three-port circulator (average P_{data} = +5 dBm) into the PhaseCOMB-clock, stimulating carrier recombination in active layer of the SP-laser. The free-running RF-line shifts to the data frequency and narrows additionally, indicating stable phase conditions of the synchronised pulse trace (Fig. 3.3b). As a result, the clock component is recovered with respect to the frequency and phase of the PRBS data signal.

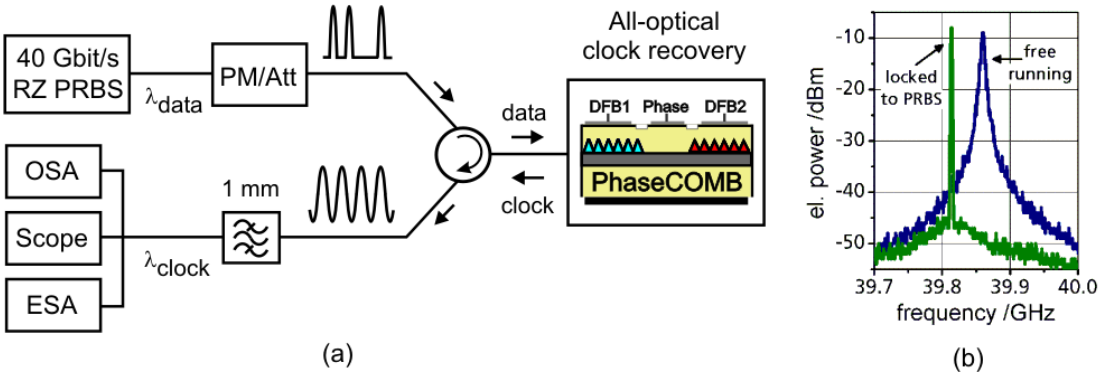

Fig. 3.3: Operation principle and measurement set-up for locking characteristics investigation of the PhaseCOMB-clock (a), RF-spectrum of the free-running clock and synchronised to a 39.8 Gbit/s PRBS RZ signal (1550 nm, P_{data} = +5 dBm) (b).

Basically, the optical locking can be achieved in two different ways. In case of coherent injection, the external wavelength is identical with the DFB lasing mode. The device dynamics is significantly modified already by very low data power levels (µW). However, due to interference effects, the polarisation of the injected signal has to be controlled properly. Alternatively, non-coherent injection can be performed. Here, the injected signal is located arbitrarily within the gain spectrum of the laser. Although the incoherent locking requires higher power levels (mW-range), the polarisation insensitivity and wavelength independence to the external signals are more preferable for system applications. In the following experiments, the non-resonant locking was investigated in more detail.

As mentioned previously, the spectral separation of the two DFB lasing modes determines the oscillation frequency of the self-pulsating PhaseCOMB-laser. The beating type oscillations can be generally tuned in an extremely wide frequency range (Fig. 3.4), simply by changing the driving currents of the laser sections. Hence, a clock recovery from data flows of different bit rates (e.g. 39.8 Gbit/s including all forward error correction (FEC) rates up to 46 Gbit/s) can be performed using the same device. Basically, the PhaseCOMB-clock provides even higher speed potential [19] (pulsation frequencies of 160 GHz and beyond), when optimising the device parameters regarding this operation point.

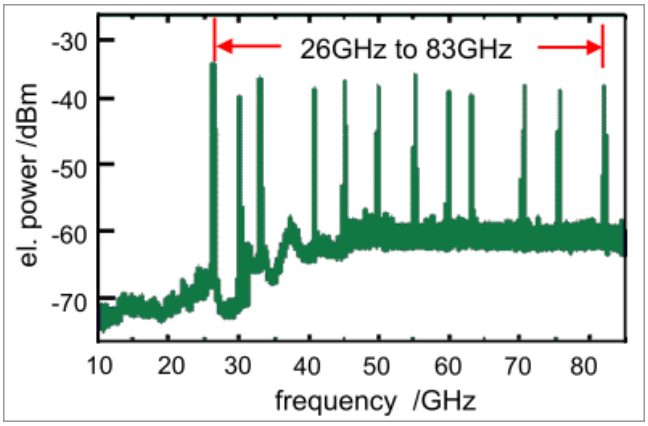

Fig. 3.4: Frequency tuning range of the PhaseCOMB-clock by changing the driving currents of the DFB sections.

In case of 40 GHz pulsation, the spectral distance of the two beating modes corresponds to a wavelength difference of 0.32 nm, as it is obvious from the optical spectrum shown in Fig. 3.5a. The timing jitter of the synchronised clock signal, as one of the most important quality parameter, was measured using an electrical sampling oscilloscope (Agilent 86100B) with a precision time base reference module (Agilent 86107A). The sinusoidal pulse trace behind the PhaseCOMB-clock synchronised to a 40 Gbit/s PRBS RZ signal (λ_{data} = 1550 nm, P_{data} = +5 dBm, 390 fs RMS-jitter) is shown in Fig. 3.5b. The RMS-jitter of 420 fs shows a good timing stability of the recovered clock signal (λ_{clock} = 1562 nm). The zero level (dashed line in Fig. 3.5b) indicates a slightly reduced extinction ratio of the clock signal (ER = 7.8 dB). The ER correlates directly with the relative amplitude of the two DFB modes and can be partially controlled by wavelength detuning of the BP-filter placed behind the clock. The highest extinction corresponds to the equal mode amplitudes. Typically, the clock ER, measured with the electrical sampling oscilloscope (65 GHz modulation bandwidth), is within a range between 6 dB and 8 dB.

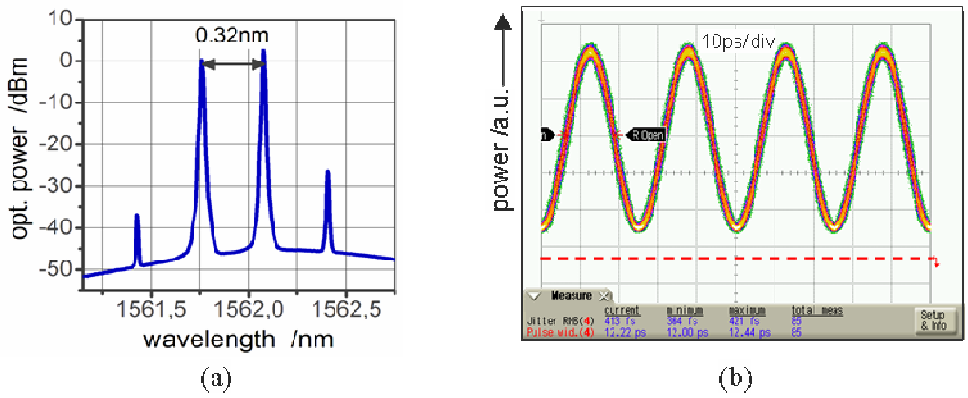

Fig. 3.5: Optical spectrum of the PhaseCOMB-laser operated at 40 GHz (a) and the corresponding sinusoidal pulse trace of the recovered clock signal (420 fs RMS-jitter) synchronised to a 40 Gbit/s PRBS RZ signal (1550 nm, P_{data} = +5 dBm) (b).

3.3 System performance of the PhaseCOMB-clock

The system quality of the all-optical clock was evaluated by comparing it with a proven technique represented by an electrical phase locked loop (PLL). A detailed theoretical analysis on synchronisation behaviour of the optical clock and the analogy to an electrical PLL can be found in [79]. In this section, the system performance of the two clock types is experimentally investigated. A commercially available PLL developed for operation in 40 Gbit/s data streams (SHF Communication Technologies AG, [164]) and successfully applied in several loop experiments was chosen as a reference. The measurement set-up is sketched in Fig. 3.6. A 40 Gbit/s PRBS 2^{31}-1 RZ signal (1550 nm) was injected alternatively into the optical and electrical clock, respectively. The quality of the extracted clock signals was evaluated using an electrical spectrum analyser (Agilent 8565EC), a sampling oscilloscope with precision time base module, and finally by BER measurements (Anritsu MP1776A).

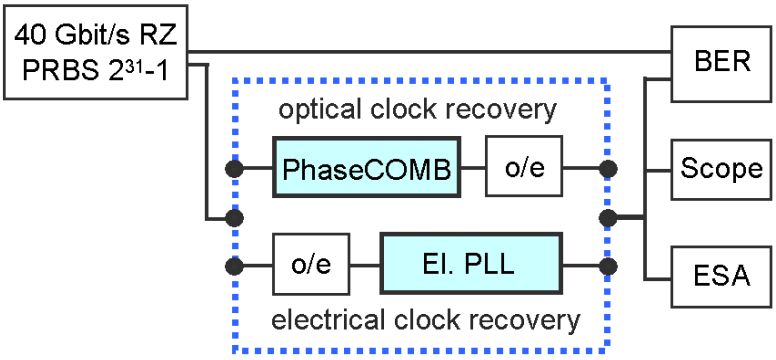

Fig. 3.6: Principle set-up for direct comparison of basic characteristics of the all-optical (PhaseCOMB) and electrical clock recovery (SHF PLL) operated in 40 Gbit/s PRBS 2^{31}-1 RZ data streams.

Phase stability of the recovered clock signals is one of the most critical issues in optical signal processing. Therefore, single side band phase noise measurements (SSB) were performed first (Fig. 3.7). The derived RMS-jitter for three frequency intervals is summarised in the table below. The optical PhaseCOMB-clock shows a jitter of less than 100 fs in the integration range up to 10 MHz, which is lower in comparison to the electrical PLL clock. In contrary, a better performance for the electrical clock was achieved in the integration range up to 1 GHz. In spite of different characteristics in the frequency distribution, both clocks are characterised by a jitter sufficiently low for operation in 40 Gbit/s systems. It should be noted that the jitter calculated by phase noise measurements typically gives lower values than that measured by the sampling oscilloscope. Due to the limited integration range, the phase noise analysis does not take into account the timing jitter correlated with amplitude fluctuations at high frequencies (in GHz range).

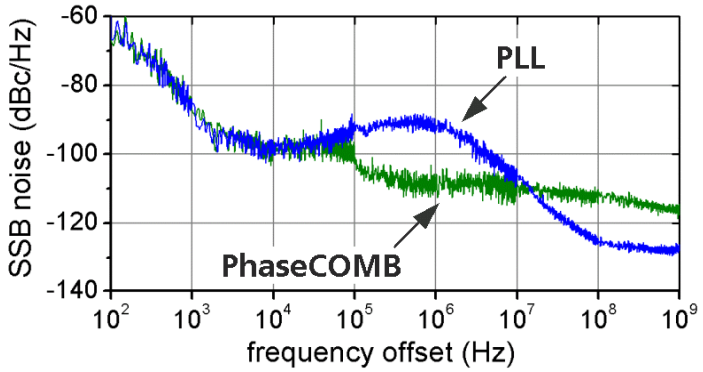

integration range	rms – jitter	
	PLL	PhaseCOMB
100 Hz – 10 MHz	255 fs	98 fs
100 Hz – 100 MHz	264 fs	212 fs
100 Hz – 1 GHz	276 fs	364 fs

Fig. 3.7: Measured single side-band (SSB) phase noise of the synchronised PLL and of the PhaseCOMB-clock and the RMS-jitter calculated from the SSB for different integration ranges.

In the following analysis, the typical average data power levels needed for synchronisation of both clocks were measured. Figure 3.8a shows the RMS-jitter of the extracted clock signals as a function of the input PRBS power. The PLL synchronises to power levels below -4 dBm and remains locked when increasing the input power up to +10 dBm. It should be noted that the extremely large dynamic range is also related to the sensitivity and linearity of the photodiode applied for o/e signal conversion (u^2t Photonics, [122]). The PhaseCOMB-laser partially synchronises to the data signal of around –3 dBm and recovers a stable clock (RMS-jitter below 500 fs) for power levels higher than +3 dBm. Although the dynamic range is much larger in case of the electrical clock, the evaluated range of 6 dB for the optical clock is sufficient, as its jitter performance cannot be influenced by strong power fluctuations in the system. Nevertheless, the minimum power level for locking can be further improved e.g. by reducing the fibre-chip coupling losses or by an additional SOA stage.

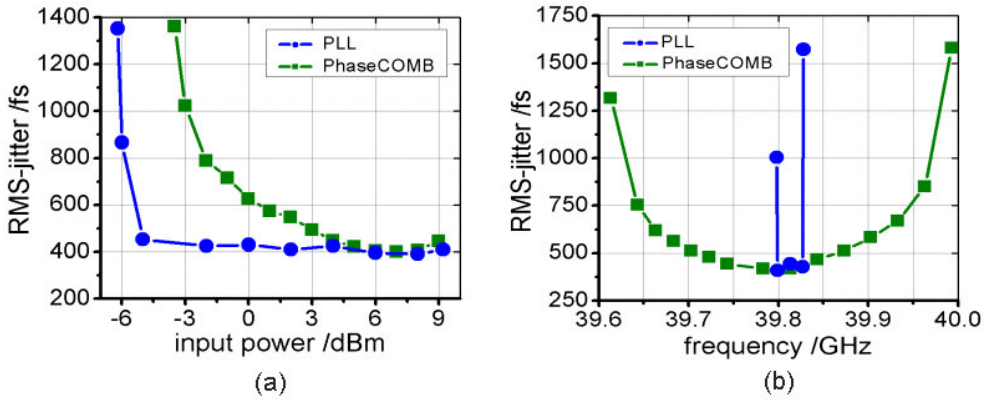

Fig. 3.8: Power dynamic range (a) and frequency locking range (b) of both clocks (PLL, PhaseCOMB) as a function of the RMS-jitter of the recovered clock signals. Input data: 39.8 Gbit/s PRBS 2^{31}-1 RZ, 1550 nm, 390 fs RMS-jitter.

Next, the locking range of both clocks was studied. In the experiment, the system frequency was continuously detuned from the SDH reference (39.81 Gbit/s) and the corresponding timing jitter of the recovered clock signals was evaluated. In case of the PhaseCOMB-clock, the operation point (defined by the DC currents) was optimised for synchronisation to the 39.8 Gbit/s RZ PRBS 2^{31}-1 signal. The average power level of the data signal was kept fixed at +5 dBm. The results are summarised in Fig. 3.8b. It can be seen that the PhaseCOMB-laser remains synchronised to the injected PRBS signal in a much wider frequency range. For an RMS-jitter below 500 fs a locking range of 170 MHz can be identified. In contrary, the electrical clock shows stable synchronisation within a frequency range of 30 MHz only. It should be noted that the small range for the PLL is less critical because of fixed oscillation frequency of the internal VCO. In case of the PhaseCOMB-clock, the pulsation frequency is determined by the three bias currents. Due to the large locking range, only a rough adjustment of the free-running pulsation frequency is required.

Finally, the stability of both clocks was evaluated by BER measurements. Here, the BER receiver was synchronised alternatively by the system clock (reference clock of the pattern generator), the PLL and the PhaseCOMB-clock, respectively. The corresponding BER curves of the 39.8 Gbit/s PRBS 2^{31}-1 are depicted in Fig. 3.9. All BER traces show the

same receiver sensitivity with nearly identical slope. There is no penalty derived from either one of the clock devices with respect to the back-to-back curve. No indication of an error floor down to a BER of 10^{-12} can be noticed, proving the good stability of both clocks.

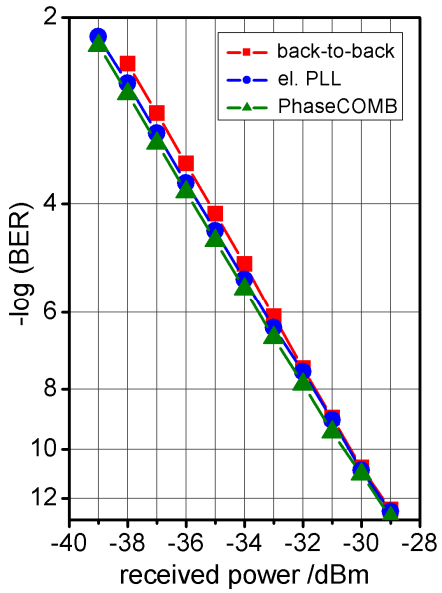

Fig. 3.9: BER measurements of the 39.8 Gbit/s PRBS 2^{31}-1 RZ signal. The error detector was triggered directly by the pattern generator (back-to-back) as well as by the clock signal recovered from the electrical PLL, and PhaseCOMB, respectively.

In summary, the PhaseCOMB-clock shows a good system performance similar to the proved commercially available electrical PLL. The evaluated RMS-jitter (measured using a sampling oscilloscope with high precision time base) of the all-optical clock synchronised to the 40 Gbit/s PRBS 2^{31}-1 RZ data signal was 420 fs. The timing stability of the recovered clock signal remained below 500 fs within a dynamic range of 6 dB and within a 170 MHz locking range. The PhaseCOMB-laser provides bit rate flexible operation with a large tuning range covering all frequencies of a 40 Gbit/s transmission system (e.g. without/with FEC). The high stability of the optical clock was proven by BER measurements.

3.4 Regenerative performance of the PhaseCOMB-clock

In the all-optical 3R regenerator, the clock has to recover a stable pulse trace even from strongly degraded data streams. Hence, the robustness of the PhaseCOMB-clock against signal impairments was investigated. In the following measurements, the 40 Gbit/s PRBS RZ data signal (λ_{data} = 1550 nm, P_{data} = +5 dBm) was intentionally degraded before injecting into the self-pulsating laser. The scheme of the degradation unit used in the experiments for selective generation of data distortions is depicted in Appendix E3. The

impact of the data amplitude and timing fluctuations on synchronisation behaviour of the PhaseCOMB-clock as well as the influence of OSNR degraded data signals was analysed. In order to quantify the influence of the signal impairments on the clock stability, the RMS-jitter of the clock pulse trace was measured using an electrical sampling oscilloscope with precision time base.

It has been shown in the previous section that slow power fluctuations (dynamic range up to 6 dB) have nearly negligible influence on the timing stability of the recovered clock signal. In the following, the PRBS 2^{31}-1 RZ signal was intentionally degraded by patterning effects (1430 fs RMS-jitter). The strong amplitude fluctuations at the bit-to-bit level of 4 dB are clearly visible from Fig. 3.10 (upper trace). The sinusoidal pulse trace of the recovered clock signal remains stable in amplitude and time (Fig. 3.10, lower trace) with an identical RMS-jitter (below 420 fs) as measured for the high quality RZ signal (390 fs RMS-jitter, Fig. 3.5b). Thus, the timing stability of the synchronised PhaseCOMB-clock does not change when increasing the amplitude fluctuations up to 4 dB.

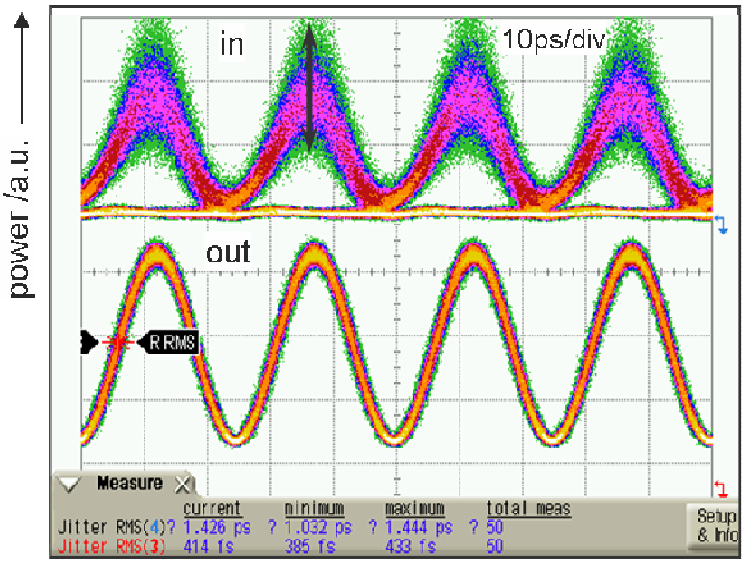

Fig. 3.10: Synchronisation of the PhaseCOMB-clock (λ_{clock} = 1560 nm, 414 fs RMS-jitter) to a 40 Gbit/s PRBS RZ data signal intentionally degraded by patterning effects (P_{data} = +5 dBm, λ_{data} = 1550 nm, 1430 fs RMS-jitter).

One of the most critical distortions in high-speed communication systems is related to the timing jitter caused by nonlinear pulse interactions at the transmission link [14]. In order to separately investigate the impact of the jitter on the clock stability, a gain-switched laser (GSL) was used for generation of the data pulses. The intrinsic turn-on delay of the GSL results in timing fluctuations of the generated pulses. The RMS-jitter of the 40 Gbit/s RZ signal was continuously increased from 970 fs up to 1920 fs by changing the operation point of the GSL by decreasing the bias current and the corresponding RMS-jitter of the recovered clock signal was measured. From the results summarised in Fig. 3.11a is clearly visible that the PhaseCOMB-laser performs an effective jitter reduction function. In the whole measured range, the clock RMS-jitter remains below 600 fs. The eye diagrams of the PRBS signal and of the recovered clock for the worst case are depicted as inset in Fig. 3.11a.

Finally, the influence of the data OSNR on the timing stability of the recovered clock was evaluated. In the experiment, the 40 Gbit/s PRBS RZ signal was first strongly attenuated (power level below –30 dBm) and additionally re-amplified to a constant average power level of +5 dBm. The degree of signal attenuation determines the noise level and, thus, the OSNR of the data signal. The RMS-jitter of the recovered clock signal as a function of the data OSNR is shown in Fig. 3.11b. It is clearly visible that the jitter of the clock signal remains below 500 fs in a wide range down to 14 dB/0.1 nm. Thus, strong degradations up to FEC data quality (BER < 10^{-3}) have only a small influence on the clock stability. The eye diagrams of the distorted data signal and the corresponding stable pulse trace of the extracted clock (inset in Fig. 3.11b) demonstrate robust operation of the PhaseCOMB all-optical clock.

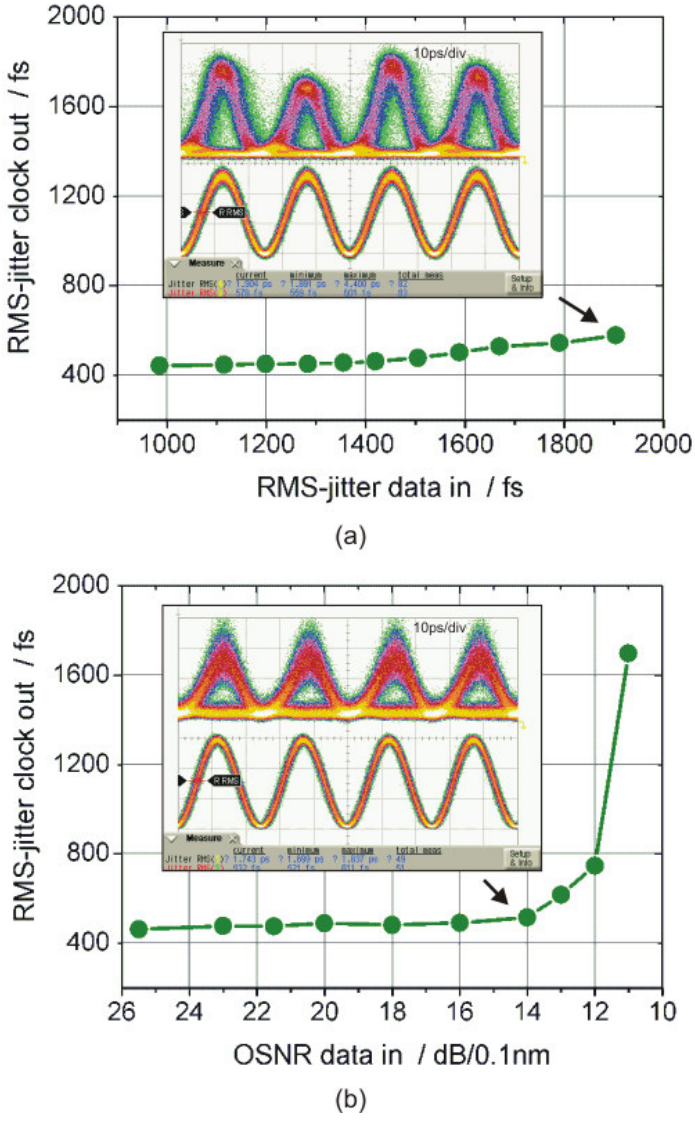

Fig. 3.11: RMS-jitter of the PhaseCOMB-clock (1560 nm) synchronised to the 40 Gbit/s PRBS RZ 2^{31}-1 data signal (1550 nm, P_{data} = +5 dBm) intentionally degraded by timing fluctuations (a) and by reduced OSNR (b).

In summary, the self-pulsating PhaseCOMB-laser recovers a stable sinusoidal pulse trace even in strongly degraded 40 Gbit/s PRBS 2^{31}-1 RZ data streams. The RMS-jitter of the clock signal was evaluated for different types of signal distortions. It was demonstrated that bit-to-bit amplitude fluctuations of 4 dB do not affect the timing stability of the extracted clock signal. A clock RMS-jitter below 500 fs was measured for strongly jittered PRBS signals (1920 fs) as well as in case of reduced data OSNR down to 14 dB/0.1 nm. The measurements prove the robustness of the PhaseCOMB all-optical clock against main distortions in high-speed transmission systems.

3.5 Conclusions

In this chapter, the operation principle and typical characteristics of the all-optical PhaseCOMB-clock were analysed in order to identify suitability of the optical clock for the novel 3R regeneration schemes proposed in this work. The PhaseCOMB-laser synchronises all-optically to the injected PRBS RZ signals and emits a sinusoidal clock pulse trace at the output. The system performance of the optical clock was evaluated by operation in 40 Gbit/s PRBS 2^{31}-1 data streams and compared to the proven electrical PLL-clock (SHF). A stable recovered clock signal was obtained behind the PhaseCOMB-laser in a wide dynamic range (6 dB) and frequency tuning range (170 MHz). The robustness of the PhaseCOMB-clock was studied for selectively controlled data distortions. A high quality clock signal (RMS-jitter below 500 fs) was detected for bit-to-bit power fluctuations of 4 dB, data RMS-jitter up to 2 ps and OSNR reduction down to 14 dB/0.1 nm. The measurements show that the robust operation of the clock recovery stage based on the PhaseCOMB-clock fulfils the key prerequisites for application in an all-optical 3R regenerator.

4 Analysis of XGM effects in ultra-long SOAs

The compact dimension, combined with high nonlinearities at moderate power levels, makes the semiconductor optical amplifiers (SOAs) very attractive for all-optical signal processing. The exploited physical effects are based on cross gain modulation (XGM), cross phase modulation (XPM), and four wave mixing (FWM) between the optical signals, when simultaneously propagating the SOA. A wide application potential of the SOA devices comprising wavelength conversion [144]-[146], signal regeneration [147]-[148], optical switching [149] as well as logic operations [150] has been reported. However, in the most experiments, standard SOAs with a length below 1 mm have been used, originally designed for linear signal amplification.

Effective exploitation of nonlinearities in semiconductor amplifiers is the main prerequisite for proper operation of both 3R regeneration schemes proposed in this work. Although lot of investigations have been performed using short SOAs, the potential of ultra-long SOAs (UL-SOAs, $L \geq 2$ mm) for signal processing has not been sufficiently studied yet. It is therefore of high interest to explicitly analyse the influence of the length on the SOA gain dynamics. For high-speed signal processing, effective gain compression and short recovery time constants are inevitable. In this chapter, the dynamic behaviour of UL-SOAs is studied in detail. The focus is given on the impact of periodical gain modulation of the long amplifiers, which is the key technique exploited in the novel all-optical 3R architectures.

First, the design and basic characteristics of the ultra-long SOAs fabricated in the technology of FhG-HHI are presented. Based on the static characterisation of the long amplifiers, the small signal gain as a function of wavelength and SOA current density is analysed. In the second part, the gain dynamics of the SOAs are investigated by modelling (VPIphotonics^{TM} [156]) and experimentally (high bandwidth optical sampling oscilloscope). The impact of the device length on inter-band and intra-band effects is studied using pump-probe measurements at 10 GHz. The analysis focuses on evaluation of the modulation depth and recovery processes of XGM converted periodical signals for different pulse widths. The re-timing and re-shaping function of 40 GHz sinusoidal signals by periodical modulation of the UL-SOA gain is pointed out. Finally, the behaviour of the ultra-long SOAs operated in PRBS data streams is discussed and the impact of the pattern dependent gain modulation on the data quality is demonstrated.

4.1 Static characterisation of UL-SOAs

The design of the investigated ultra-long SOAs is briefly reviewed, focusing on suppression of internal reflections, as a critical issue in the long devices with high gain. The UL-SOA gain characteristics in 2 mm and 4 mm UL-SOA are statically analysed under different operation conditions including the impact of an additional holding beam on signal amplification.

4.1.1 Design of the ultra-long SOAs

The schematic view of the ultra-long semiconductor optical amplifier investigated in this work is depicted in Fig. 4.1a. The bulk UL-SOAs with buried heterostructure (BH) were fabricated in the technology of FhG-HHI. The layers are epitaxially grown on an n-doped InP substrate. The InGaAsP active layer composition was designed for a gain peak wavelength around 1550 nm. The lateral modes are controlled in a strongly index guided bulk region, which is buried in higher band-gap layers from all sides. The additional p-n blocking inhibits current spreading and forces the carriers to recombine in the active layer. A cross-section photograph of a fabricated semiconductor amplifier is depicted in Fig. 4.1b. The metallisation evaporated on the top of the upper cladding forms the positive electrical contact of the device. The typical parameters of the SOA devices are summarised in Appendix A.

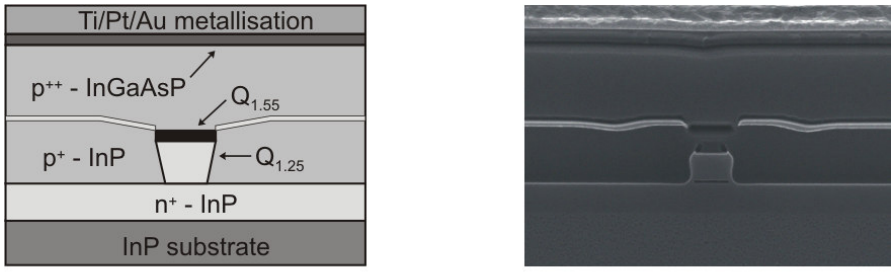

Fig. 4.1: Schematic view of the UL-SOA layer structure (a) and the photograph of the amplifier cross-section (b).

The ultra-long SOAs are characterised by high device gain. The total single-pass gain G at a given wavelength is generally described as [134]

$$G = exp\left(\int_0^L (\Gamma g(z) - \alpha_{int})dz\right) \tag{4.1}$$

where Γ is the confinement factor, g is the material gain coefficient, α_{int} are the internal losses of the device, and L is the cavity length of the SOA. Generally, very low reflectivities on the facets are required (typically smaller than 10^{-5}, [155]) in order to prevent the lasing of the devices. If the reflectivity is not low enough, ripples are observed in the gain spectra. Furthermore, too large facet reflectivities reduce the gain bandwidth, and the output saturation power [135]. Using a double layer TiO_2/SiO_2 antireflection (AR) coating, suppression of the reflectivities down to 10^{-4} is possible [137]. In case of ultra-long semiconductors, a further improvement was achieved by introducing tilted facets (the waveguides are penetrating the facet with an off-axis angle). The average reflectivity decreases when increasing the facet angle. However, the coupling efficiency between the chip and the optical fibre degrades for large facet angles due to the asymmetry of the far field pattern. The UL-SOA waveguides investigated in this work were angled by 12° relative to the crystal axis, resulting in 42° fibre coupling angle. A photograph of a 4 mm UL-SOA chip mounted on a heatsink (the angular shift relative to the coupled fibre tapers is clearly visible) and of the device packaged in a module is shown in Fig. 4.2.

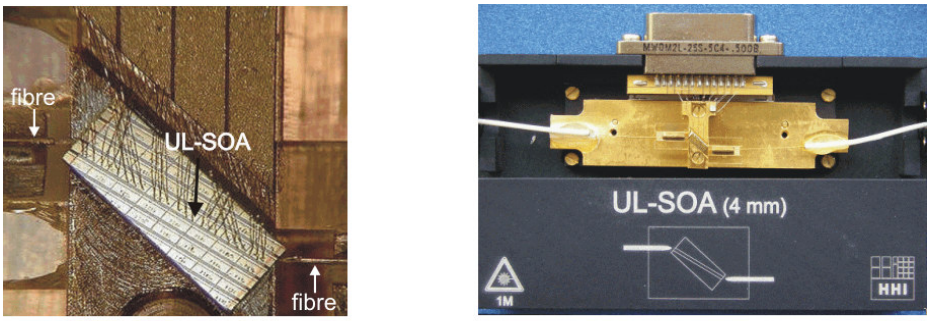

Fig. 4.2: Chip of the 4 mm UL-SOA with tilted facets (12° off axis) (a) and the open module of the packaged device (b).

A polarisation insensitive operation is required for optical signal processing. Basically, the transmitted waves in an SOA cavity experience different amplifications regarding their polarisation states, depending on the confinement factor of the guided mode and on the material gain of the SOA. Due to technological fabrication, an identical confinement for TE and TM is not possible [136]. Thus a strained bulk active layer is used, which introduces an anisotropy to the gain. The gain can be matched separately for TE and TM by fine-tuning of the strain, resulting in a polarisation insensitive SOA.

More detailed information to the semiconductor heterostructure, processing technique and SOA design optimisation can be found in [137] and references therein.

4.1.2 Small signal gain analysis

In this section, the basic analysis of the 2 mm and 4 mm ultra-long SOAs regarding polarisation sensitivity, small signal gain and saturation behaviour is performed. It was mentioned that the long semiconductor devices require special design of the end facets, in order to prevent unwanted lasing inside the active medium. The ASE spectrum behind the 4 mm UL-SOA without any external signal (driven by 800 mA DC bias) is depicted in Fig. 4.3a (red curve). It is clearly visible that in spite of anti-reflection coating and tilted facets, Fabry-Pérot modes distort the ASE spectrum in a range of more than 20 nm around the peak wavelength. Due to the strong internal gain, the maximum peak-to-peak amplitude of the ripple is up to 9 dB high. However, the internal lasing can be effectively eliminated when an external signal saturates the long amplifier (Fig. 4.3, green curve). In this case, a CW signal at 1550 nm was launched into the UL-SOA at a power level of 0 dBm. A suppression of the ripple from 9 dB down to 1 dB was achieved. It should be noted that the ultra-long SOAs are exclusively considered for optical signal processing and are, thus, typically operated in the highly saturated regime. Hence, the fabricated devices fulfil requirements regarding internal reflections and can be used for experimental investigations.

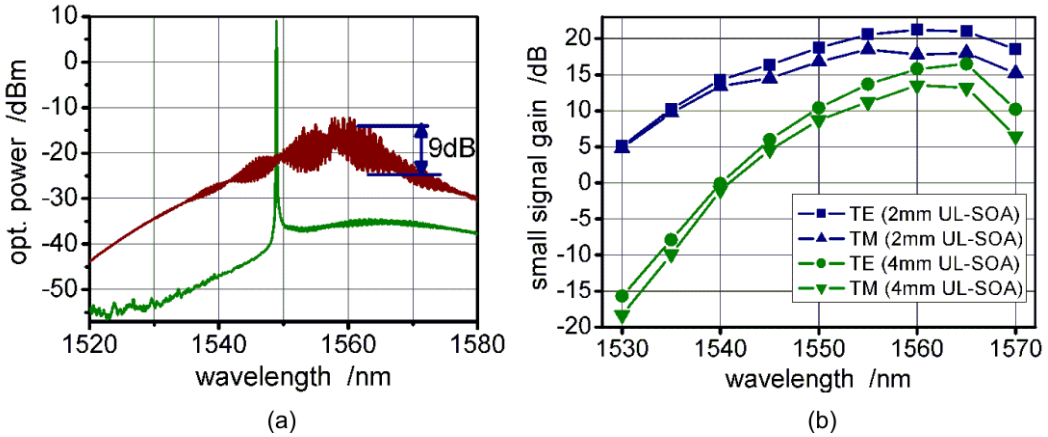

Fig. 4.3: ASE spectrum behind the 4 mm UL-SOA (I_{SOA} = 800 mA) without and with an external CW signal (P_{CW} = 0 dBm) (a) and the small signal gain of 2 mm and 4 mm long amplifiers for TE and TM modes as a function of the wavelength (b).

In the following, the gain spectrum for the TE and TM polarisations were measured behind the 2 mm and 4 mm amplifiers (Fig. 4.3b). The UL-SOAs were driven by a bias current of 200 mA/mm. The power level of the input CW signal was set to –15 dBm. The maximum gain evaluated for the 2 mm UL-SOA and for the 4 mm UL-SOA was 21 dB and 16 dB, respectively. The reduced gain in case of the longer amplifier is related to the higher fibre-chip losses. It can be seen that the amplification of the TE and TM modes show similar evolution in the measured wavelength spectrum. The polarisation sensitivity varies between 0.1 dB and 4 dB. In spite of the proper design of the SOA heterostructure, the gain peak (~1560 nm) is shifted by around 10 nm towards longer wavelengths. A gain maximum at 1550 nm would be preferable for system experiments, in order to exploit the UL-SOA bandwidth more effectively in the C-band. The gain bandwidth is narrower for the 4 mm UL-SOA. The bandwidth narrowing in cascaded SOAs or when increasing the SOA length is a well-known effect [138] (for the ASE spectra of the measured SOAs see Appendix C).

The integrated power of the amplified spontaneous emission at the UL-SOAs output and the small signal gain as a function of current density was measured (Fig. 4.4). For the calculation of the current density, the experimentally evaluated active region width of 0.9 µm was considered (100 mA bias current (1 mm SOA) corresponds to 1.11×10^8 A/m^2). A fast increase of the ASE power by tuning the current density from 0.14×10^8 A/m^2 to 0.83×10^8 A/m^2 is obvious from Fig. 4.4a. Further increase of the current density leads to stronger depletion of free carriers by the ASE itself, resulting in saturation of the output power at +11 dBm and +8 dBm in case of the 2 mm and 4 mm UL-SOA, respectively. The measured curves for small signal gain at 1550 nm show similar tendency (Fig. 4.4b). The gain saturation at low currents is mainly due to the strong impact of ASE in the long devices. A nearly constant small signal gain of around 11 dB (4 mm UL-SOA) and up to 20 dB (2 mm UL-SOA) was achieved behind the devices when increasing the current density from 0.28×10^8 A/m^2 up to 2.22×10^8 A/m^2.

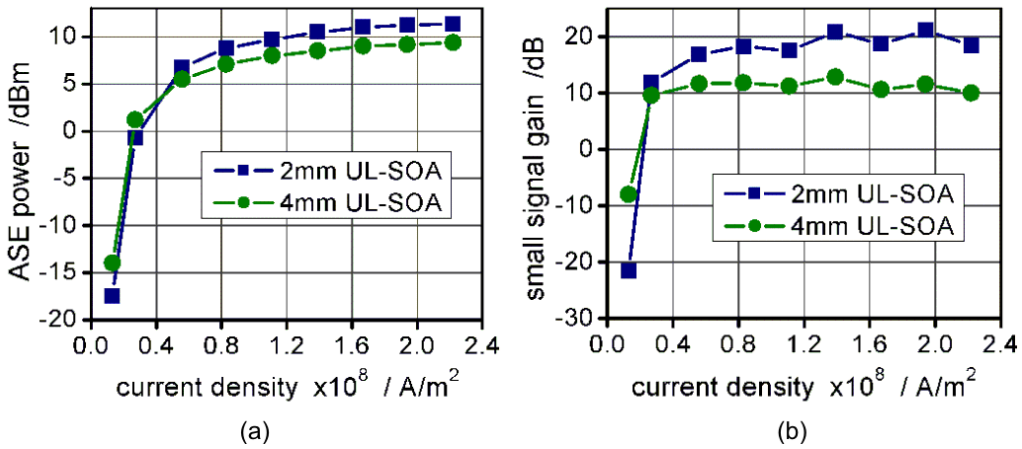

Fig. 4.4: Integrated ASE power (a) and the small signal gain (SSG) at 1550 nm (b) measured at the output of the 2 mm and 4 mm UL-SOA as a function of the amplifier current density ($1.1x10^8$ A/m^2 corresponds to 100 mA/mm).

4.1.3 Impact of the holding beam on signal amplification

In the following, the signal amplification versus input power was investigated without and with a holding beam (also referred to assist light). In optical signal processing, the use of a holding beam is an effective technique for the stabilisation of pattern dependent gain modulation as well as for increasing the speed potential of SOAs [90], [91]. Therefore, the impact of the assist light on the amplification of the optical signal was analysed for the long devices. The current density of the UL-SOAs was kept fixed at $2.22x10^8$ A/m^2; the power was measured in the fibre using an optical spectrum analyser (1 nm resolution bandwidth). Figure 4.5 summarises the results. Without the holding beam, a linear transfer function for small input powers (1550 nm) can be observed in a range up to –8 dBm (2 mm UL-SOA) and –4 dBm (4 mm UL-SOA). Due to the gain saturation, any further increase of the input power results in nearly constant output power levels of +9 dBm (2 mm UL-SOA) and +7 dBm (4 mm UL-SOA). In case of the holding beam (1560 nm, P_{hol} = +8 dBm), a linear power transfer function can be observed in the whole measured range. However, the CW signal does not experience any amplification behind the amplifiers.

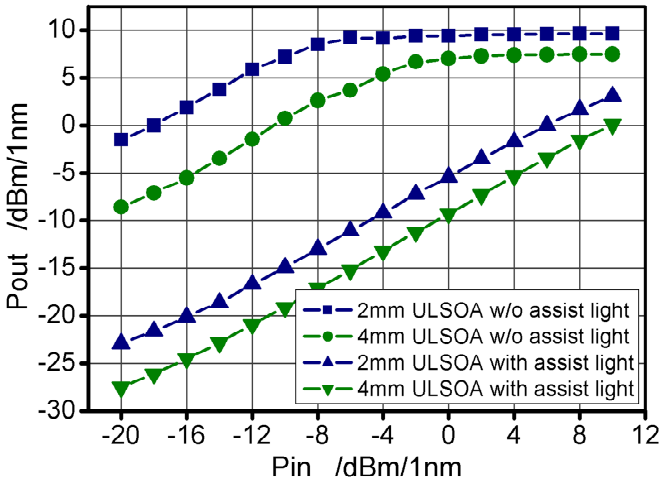

Fig. 4.5: Power transfer function of the CW signal at 1550 nm for 2 mm and 4 mm long semiconductor amplifiers without and with an additional holding beam (1560 nm, P_{hol} = +8 dBm).

In the following, the small signal gain as a function of the CW (1550 nm) input power was evaluated (Fig. 4.6). The gain is constant at low input powers and decreases for higher power levels. The measured input saturation power (3 dB gain suppression) was –6 dBm for the 2 mm and –1 dBm in case of the 4 mm UL-SOA. Injecting the strong assist light additionally into the amplifier (1560 nm, P_{hol} = +8 dBm), the signal gain is lower than the coupling losses. The negative net gain remains nearly constant in the whole measured range when increasing the CW power level (around 5 dB for the 2 mm UL-SOA and 9 dB in case of the 4 mm UL-SOA).

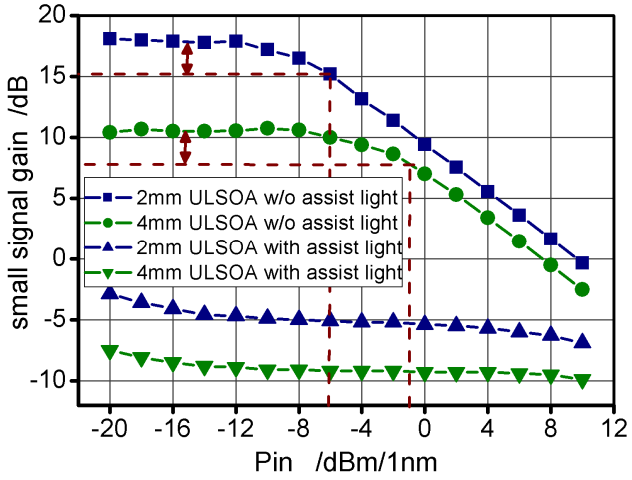

Fig. 4.6: Small signal gain versus input power level of the CW signal (1550 nm) for the UL-SOAs (2 mm, 4 mm) without an additional external light and by gain compression due to a holding beam (1560 nm, P_{hol} = +8 dBm).

In summary, the maximum measured fibre-to-fibre gain (1560 nm) of the fabricated ultra-long SOAs was 21 dB (2 mm) and 16 dB (4 mm). Both UL-SOAs show efficient gain saturation at low current densities. The saturation power levels were –6 dBm and –1 dBm for the 2 mm and 4 mm UL-SOA, respectively. Linear signal amplification was evaluated after applying a holding beam, however, without fibre-to-fibre net gain. The static characterisation proves the suitability of both devices for further dynamic analysis.

4.2 Gain dynamics of ultra-long SOAs

In the previous section, the UL-SOA gain analysis was done for CW operation. In the following, the temporal evolution of the gain after injecting a short optical pulse into the UL-SOA is investigated. First, the inter-band and intra-band effects in semiconductor amplifiers are discussed. The gain compression and recovery processes in the SOAs of different lengths are evaluated using a pump-probe technique based on XGM wavelength conversion at 10 GHz. The impact of the SOA length as well as power level and pulse width of the control signal on SOA gain dynamics is studied. For better understanding of the physical effects, numerical simulations are performed additionally to the experiments.

4.2.1 Inter-band versus intra-band effects

Generally, the SOA gain dynamics are characterised by inter-band and intra-band effects. The first correlates with carrier transitions between valence and conduction band, while the second effects modify the carrier energy distribution within one band [85] – [87].

The characteristic time constant for inter-band carrier modulation process is denoted as effective carrier lifetime τ_{eff}. This time constant (typically in a range of 100 ps) defines the gain recovery time after saturation of the SOA by an injected optical signal and is generally a limiting factor for XGM based high-speed signal processing. The value of the carrier lifetime depends strongly on the SOA type and on the operation conditions.

The gain of the semiconductor material is determined by the free carrier density N in the bands. Thus, the time evolution of the gain associated with the inter-band transitions is directly linked to variations of N. The involved dynamics are usually described by the rate equation [132]:

$$\frac{\partial N}{\partial t} = \frac{I}{qV} - R_{spon} - R_{stim} - R_{ASE} \tag{4.2}$$

The first term on the right hand side represents the rate of injected electrons into the active layer of the SOA. I is the bias current, q the electron charge, and V the active region volume. The other terms take into account the carrier loss caused by various radiative and non-radiative recombination processes: R_{spon} is the spontaneous recombination rate, R_{stim} and R_{ASE} represent the carrier recombination stimulated by the signal and spontaneously emitted photons, respectively.

The spontaneous recombination rate can be expressed as [134]

$$R_{spon} = A_N N + B_N N^2 + C_N N^3 \tag{4.3}$$

A_N, B_N, and C_N, are the defects, spontaneous radiative, and Auger recombination coefficients.

The stimulated recombination rate describes the impact of stimulated emission and absorption and can be written as [130]

$$R_{stim} = v_g g S \tag{4.4}$$

where S is the local signal photon density, v_g is the group velocity of the signal, and g is the local gain coefficient (difference between the rate of stimulated emission and absorption).

The R_{ASE} is related to the carrier recombination stimulated by spontaneously emitted photons, which are not included in the signal photon density S.

The presence of photons in SOA active region accelerates the dynamics of N, because of the increase of R_{stim} and R_{ASE} with increased photon density. The effective carrier lifetime is than defined as [138]

$$\frac{1}{\tau_{eff}} = \frac{\partial\left(R_{spon} + R_{stim} + R_{ASE}\right)}{\partial N} \tag{4.5}$$

In case of short SOAs with low input optical power (below saturation power), the value of τ_{eff} is mostly determined by R_{spon}. The R_{ASE} is dominant for long SOAs with weak input power signals and the R_{stim} becomes the main term when the injected optical power is large enough to saturate the SOA gain.

An increase of bias current reduces the effective lifetime, because of the increase of N, which leads to larger R_{spon}, R_{stim}, and R_{ASE}. Furthermore, τ_{eff} can be reduced by applying a holding beam [90], [91], resulting in an increase of the stimulated recombination rate (R_{stim}), however, by simultaneous N reducing. Finally, the carrier recovery processes can be accelerated, when enhancing the SOA length. This is due to the higher R_{ASE} in the long amplifiers [86]. The impact of the amplifier length on the inter-band gain dynamics will be investigated in more detail in the following sections of this chapter.

The gain dynamics due to intra-band effects is characterised by much shorter time constants (fs range) [127]. In contrary to the inter-band transitions, the intra-band effects change only the distribution of the free carriers within the band. Fig. 4.7 qualitatively shows the main processes related to the intra-band effects. Injecting an optical beam into the amplifier, the electrons in excited states are depleted because of the stimulated emission processes. The optical pulse stimulates carriers to recombine around a narrow range of energies corresponding to the pulse photon energy, resulting in a deviation from the Fermi distribution (Fig. 4.7b). This process is called spectral hole burning (SHB). At the same time, due to the high photon density in the active region, two photon absorption (TPA) occurs, causing electron transfer from the valence band to a high energy level of the conduction band. Furthermore, free carrier absorption effect (FCA) causes carriers excitation to higher energies within the same band.

The Fermi-Dirac distribution is restored via carrier-carrier scattering, which is typically on the 100 fs time scale [85] (Fig. 4.7c). The stimulated emission has removed carriers with energy lower than the average carrier energy in the band. Moreover, the TPA and FCA also contribute to the increase of the average energy. As a result, the effective carrier temperature is higher than the lattice temperature. The distribution cools down via a phonon emission to its original value (Fig. 4.7d). The time scale of this process is in sub-picoseconds range. A quasi-equilibrium Fermi-Dirac distribution at the lattice temperature is established. From this point on, the state of the amplifier is characterised by the total carrier density. The original carrier density is restored by electrical pumping within a time up to some hundreds of ps, depending on the SOA and on the operation conditions.

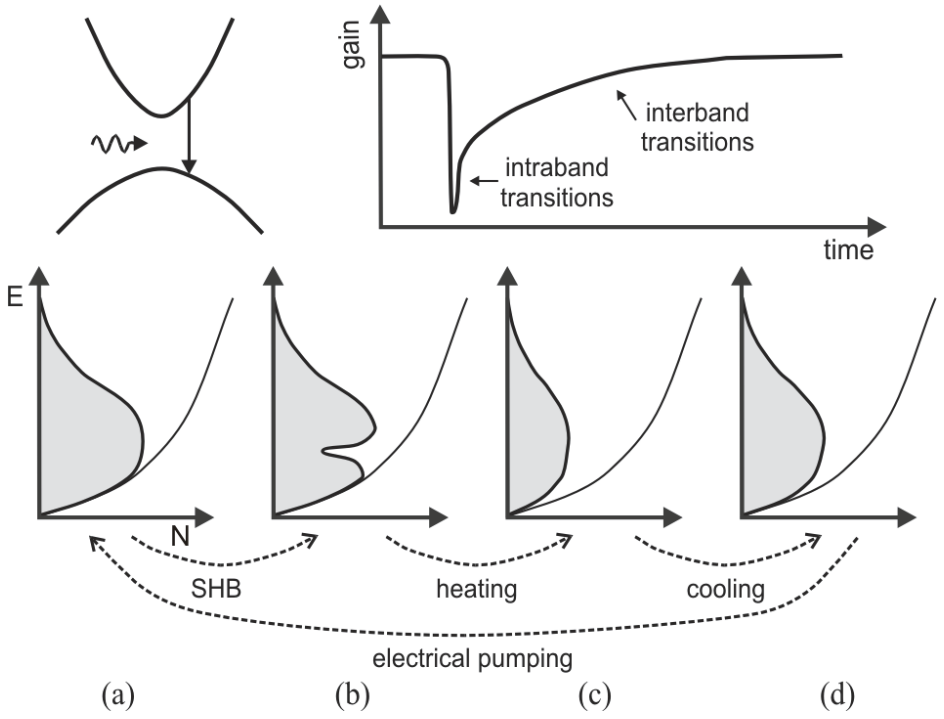

Fig. 4.7: Temporal evolution of the carrier distribution (carrier density N vs. carrier energy E) in the conduction band induced by a short optical pulse [138].

Detailed theoretical analyses of the SOA gain dynamics for calculating nonlinear pulse propagation in active semiconductor waveguides can be found in [93] – [96] and references herein.

Usually, the inter-band gain effects in SOAs are preferred for optical-signal processing. In this case both gain modulation (XGM) and phase modulation (XPM) caused by variations of the carrier density can be exploited. The signal processing based on XGM effects is simple and, thus, very attractive. However, the relatively slow time constants (~100 ps) limit the applications to a bit rate of around 10 Gbit/s. The bit rate can be further enhanced (up to 40 Gbit/s) when phase effects are exploited. In this case, more sophisticated architectures based on differential operation of an interferometric structure (see Chapter 2) are required. Although the ultra-fast intra-band gain dynamics combine simplicity (XGM) with high speed potential (beyond 160 Gbit/s), they are relatively weak in the conventional amplifiers [127]. In the following it will be demonstrated, how the efficiency of the intra-band effects can be increased when enhancing the SOA length.

4.2.2 Experimental analysis of gain effects in short and long SOAs

In the following experiments, the gain dynamics of SOAs of several lengths are investigated using a pump-probe technique with high timing resolution. The scheme of the experimental set-up is depicted in Fig. 4.8. Two signals were simultaneously injected into the analysed optical amplifier: a control signal comprising short pulses generated by a tuneable mode locked laser (TMLL) at a repetition rate of 10 GHz (2 ps FWHM) and a continuous wave (CW) probe signal generated by an external cavity laser. The emission wavelength of the pump source was kept unchanged at 1560 nm, while the probe wavelength was tuned in a range from 1540 nm to 1555 nm. The input average power levels were controlled by inline power-meters. The short MLL pulses saturate the SOA gain, resulting in a depletion of free carriers. The modulated carrier density leads to an amplitude variation of the co-propagated CW signal. Hence, gain saturation and recovery processes are directly impressed to the CW light. The CW wavelength was separated at the SOA output by a 3 nm band-pass filter and the XGM converted signal was analysed by an optical sampling oscilloscope (OSO). The time resolution of the proposed measurement technique is determined by the pulse width of the control signal as well as by the resolution bandwidth of the OSO, which was in this case 750 GHz (Agilent 86119A). Thus, the nonlinear dynamics of the amplifier gain can be directly evaluated.

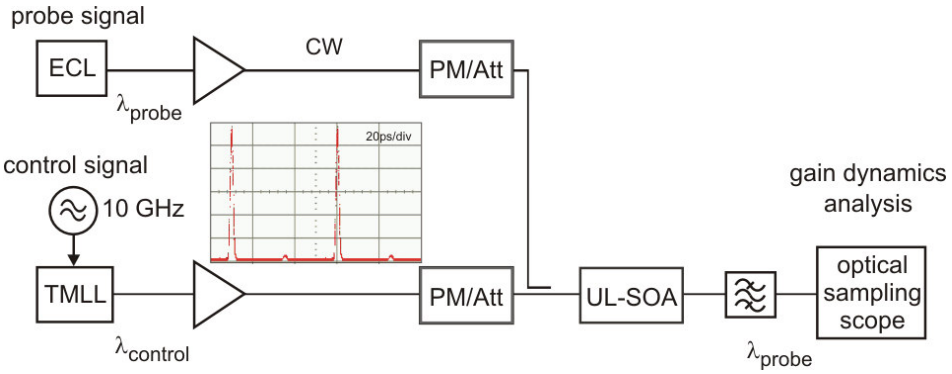

Fig. 4.8: Measurement set-up for SOA gain dynamics analysis using a pump-probe technique at 10 GHz.

The measured temporal evolution of the XGM modulated probe signal behind the optical amplifier is depicted in Fig. 4.9. The left diagram is related to the 0.5 mm long SOA, while the right plot corresponds to the 4 mm UL-SOA. The amplifiers were driven by a bias current of 200 mA/mm and the wavelength of the CW signal was set to 1550 nm in this case. The input average power levels (measured in the fibre in front of the amplifier) were adjusted to +3 dBm for the control and –2 dBm for the probe signal, respectively. Both curves show similar behaviour. The SOA gain drops down instantaneously due to the carrier depletion induced by the short pump pulse. The gain recovers in two steps. The fast recovery is related to the intra-band effects. After establishing a quasi-equilibrium carrier distribution, the slow recovery process governed by inter-band transitions restores the unsaturated gain.

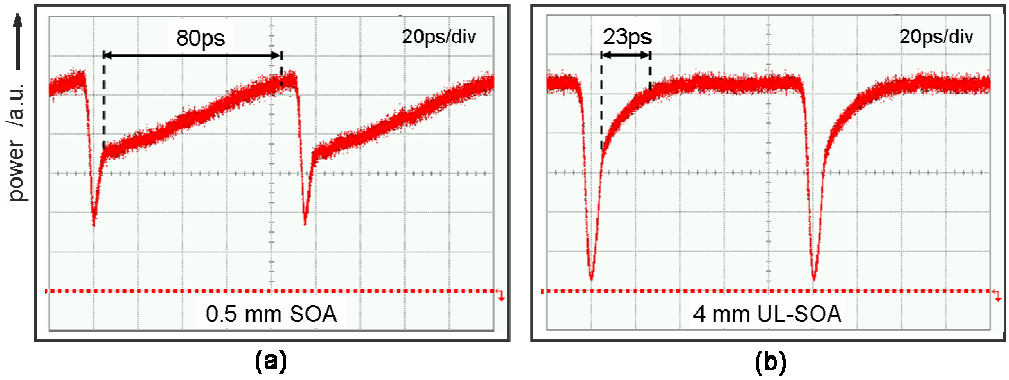

Fig. 4.9: Temporal evolution of the probe signal (λ_{probe} = 1550 nm, P_{probe} = -2 dBm) behind the 0.5 mm SOA (a) and 4 mm UL-SOA (b) indicating the gain dynamics of both amplifiers induced by 10 GHz short control pulses of 2 ps FWHM (λ_{contol} = 1560 nm, $P_{control}$ = +3 dBm).

The difference between the two measured curves is related to the total gain compression, which is clearly higher in case of the 4 mm UL-SOA (Fig. 4.9b). The strong gain saturation indicates an effective exploitation of the fast nonlinearities with the SOA length. Furthermore, the gain recovers to the unsaturated regime much faster for the long amplifier than for the 0.5 mm SOA.

The impact of the SOA length on the intra-band recovery processes was analysed in more detail. Here, the ratio between the fast (R_f) and slow (R_s) gain recovery (Fig. 4.10a) as a function of the SOA length was evaluated for three different wavelength correlations between the control and probe signal. The results are summarised in Fig. 4.10b. The influence of intra-band effects is clearly dominant in case of longer devices. Considering the 5 nm spectral separation, the evaluated R_f / R_s ratio for different SOA lengths is 0.9 (0.5 mm), 2.2 (2 mm), 5 (4 mm), and 13.2 (8 mm). The fast gain recovery is more than twice larger than the slow recovery part for 2 mm UL-SOA and even 13 times larger in case of the 8 mm UL-SOA. The ultra-fast effects clearly dominate the gain recovery in the long amplifiers. Thus, the UL-SOAs provide effective exploitation of intra-band gain dynamics needed for high-speed system applications.

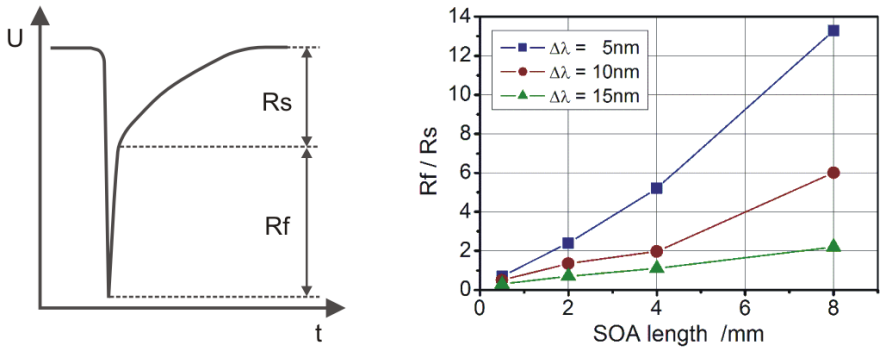

Fig. 4.10: Denotation of the linear magnitudes related to fast (R_f) and slow (R_s) gain recovery (a), and the R_f / R_s ratio as a function of the SOA length for three spectral separations between the control (1560 nm) and the probe signal (1555 nm – 1545 nm) (b).

It should be noted that the effectiveness of the ultra-fast intra-band gain effects is spectrally limited. From Fig. 4.10b is obvious that for the 10 nm spectral distance between the control and probe signal, the R_f / R_s ratio is already reduced to a value of 6 for the 8 mm and to a value of 2 in case of the 4 mm, respectively. For higher wavelength separations the impact of the fast gain recovery is even smaller.

However, comparing both transmission curves of the XGM converted signal behind the 0.5 mm SOA and 4 mm UL-SOA (Fig. 4.9), one can notice that the total gain recovery (including inter-band transitions) is much faster for the longer devices too. The gain recovery time can be estimated from the temporal evolution of the gain curve and will be defined in this work as a relaxation time due to inter-band transitions until 10 % of the unsaturated probe level. A shortening of the gain recovery constants from 80 ps (0.5 mm) down to 23 ps (4 mm) can be observed from Fig. 4.9. Thus, the ultra-long SOAs provide also the possibility of exploitation of inter-band XGM/XPM signal processing at much higher bit rates as it is in conventional SOAs. It should be noticed that while the spectral usage of intra-band processes is limited to several nm only, the effects based on inter-band transitions can be exploited in the whole SOA gain spectrum. More detailed investigation on the UL-SOA gain dynamics under different operation conditions was performed using numerical simulations and the results are discussed in the following section.

4.2.3 Numerical simulation on UL-SOA gain dynamics

The dynamic behaviour of the SOA gain effects was studied numerically using commercially available simulation software for photonic systems VPIcomponentMaker^{TM} [156]. The VPI environments enable detailed analysis, evaluation and design of optical components, circuits and networks [157] - [162]. In this work, the SOA model developed by VPI was employed. The longitudinal and spectral dynamics of the SOA were simulated using a segmented transmission line laser model (TLLM) [163]. For more details relating the TLLM see Appendix B. The parameter values used in the SOA model were adapted to the fabricated devices and are listed in Appendix B.

In order to compare the simulated results with the experiment, the SOA gain characteristics were derived by an identical technique, based on XGM pump-probe analysis at 10 GHz. The wavelengths of the pulsed control signal and of the CW probe signal were set to 1560 nm and 1550 nm, respectively. The peak power levels of the control and probe signals were set to +10 dBm and –2 dBm, respectively, the SOA current density was set to 2.75×10^8 A/m^2 and was kept fixed throughout all the simulations. First, the SOA gain compression and relaxation characteristics were investigated for control pulses with a width of 2 ps, as used in the experiments. The temporal evolution of the probe signal behind the 4 mm UL-SOA is depicted in Fig. 4.11a. The simulation show strong amplifier gain compression followed by relaxation due to intra-band and inter-band effects. The obtained results match very well with the measured ones.

Short control pulses are preferable for pump-probe measurements in order to study the recovery processes after a short excitation. However, in case of 40 Gbit/s RZ PRBS streams, the typical width of the data pulses is 12.5 ps (50 % duty cycle). Hence, in the following, the SOA gain dynamics were modeled using the pump-probe technique for 12.5 ps control pulses (Fig. 4.11b, upper trace). The temporal gain evolution behind the 4 mm UL-SOA is shown in Fig. 4.11b (lower trace). In contrary to the short pulses

(Fig. 4.11a), where the fast intra-band effects dominated the gain compression, one can notice that for the 12.5 ps pulses the gain dynamics is mainly determined by inter-band transitions. However, the gain recovery time due to the carrier relaxation is nearly the same in both cases.

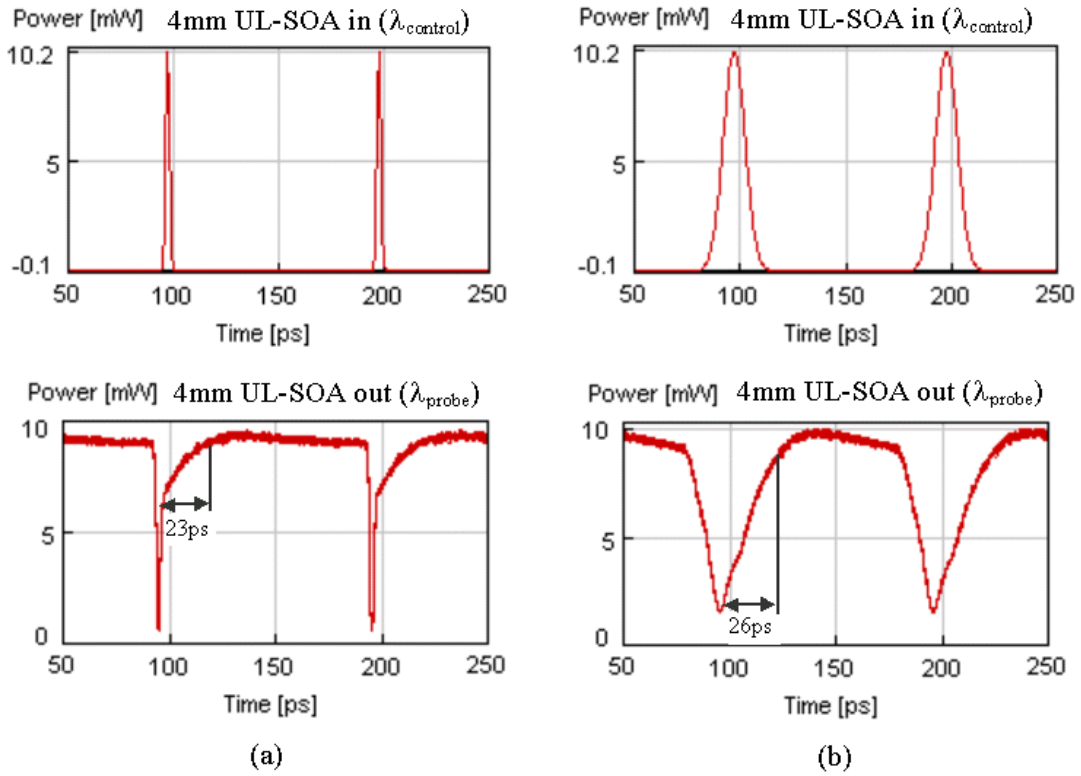

Fig. 4.11: Simulated gain dynamics of the 4 mm UL-SOA by pump-probe technique for two FWHM of the control pulses: 2 ps (a) and 12.5 ps (b). $\lambda_{control}$ = 1560 nm, $P_{control}$ = +10 dBm, λ_{probe} =1550 nm, P_{probe} = -2 dBm.

In the next analysis, the gain recovery time and the total gain compression were simulated as a function of the SOA length. The results for the two different control pulse widths (2 ps and 12.5 ps) are summarised in Fig. 4.12. The gain recovery time constant decreases nearly exponentially with the SOA length. The simulated time constants drop down from around 84 ps for the 0.5 mm SOA to less than 10 ps for the 8 mm long SOA. The total gain compression (also shown in Fig. 4.12) increases with the SOA length. It is obvious that the gain suppression is more effective for short control pulses (up to 12.2 dB) than in case of the 12.5 ps pulses (up to 9 dB). This is due to the additional contribution of intra-band effects to the gain compression in case of the 2 ps pulses.

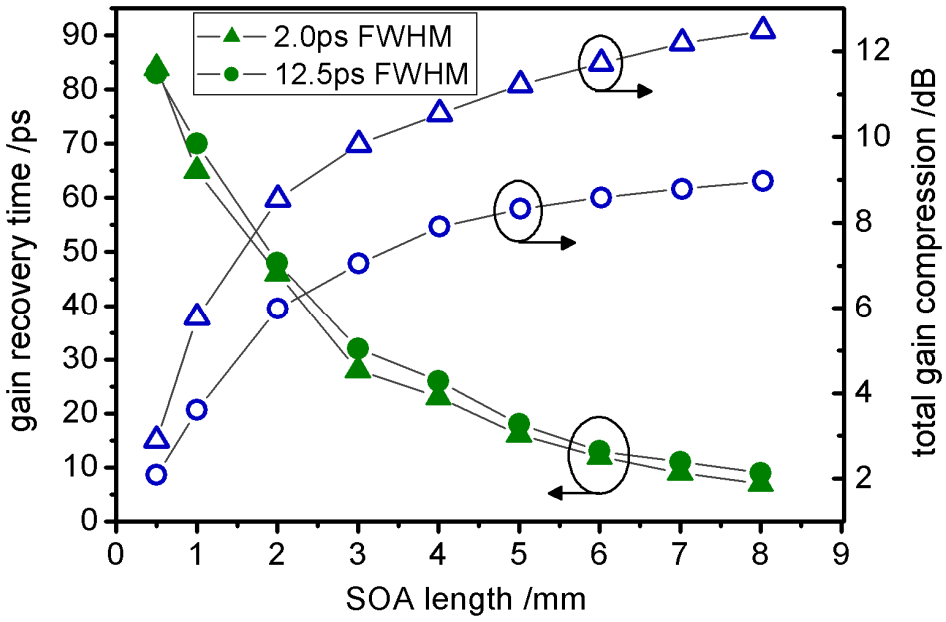

Fig. 4.12: Simulated gain recovery time and total gain compression as a function of the SOA length for two different pulse widths (2 ps, 12.5 ps FWHM) of the control signal. SOA current density: $2.75x10^8$ A/m^2, $\lambda_{control}$ = 1560 nm, $P_{control}$ = +10 dBm, λ_{probe} =1550 nm, P_{probe} = -2 dBm.

In the next simulation, the impact of the control peak power on the gain compression and gain recovery was investigated. The set-up and the operation conditions remained identical as described previously. The analysis was performed for 0.5 mm and 4 mm optical amplifiers and for two different pulse FWHM of the control signal: 2 ps and 12.5 ps. The results for short control pulses are summarised in Fig. 4.13a. It can be seen that for the 4 mm UL-SOA the gain is much stronger compressed already at moderate power levels. At the peak power level of the control signal of +10 dBm, a gain compression of 2.8 dB and 10.2 dB was evaluated for the 0.5 mm SOA and 4 mm UL-SOA, respectively. However, the gain recovery time does not depend on the control power. Time constants of 85 ps (0.5 mm SOA) and 23 ps (4 mm UL-SOA) were evaluated in the whole range. Hence, it is not possible to speed up the gain recovery of a short amplifier simply by increasing the power level of the optical control signal. The same simulation was performed also for the 12.5 ps control pulses (Fig. 4.13b). For the longer SOA, even faster increase of the total gain compression with the pulse power was obtained when comparing to the previous simulation (2 ps pulses). This is due to the reduced free carriers caused by stronger stimulated emission. The gain recovery time remains unchanged for the 0.5 mm SOA. Due to the stronger gain compression in the 4 mm device, the recovery time constants slightly increase when increasing the power level of the control signal.

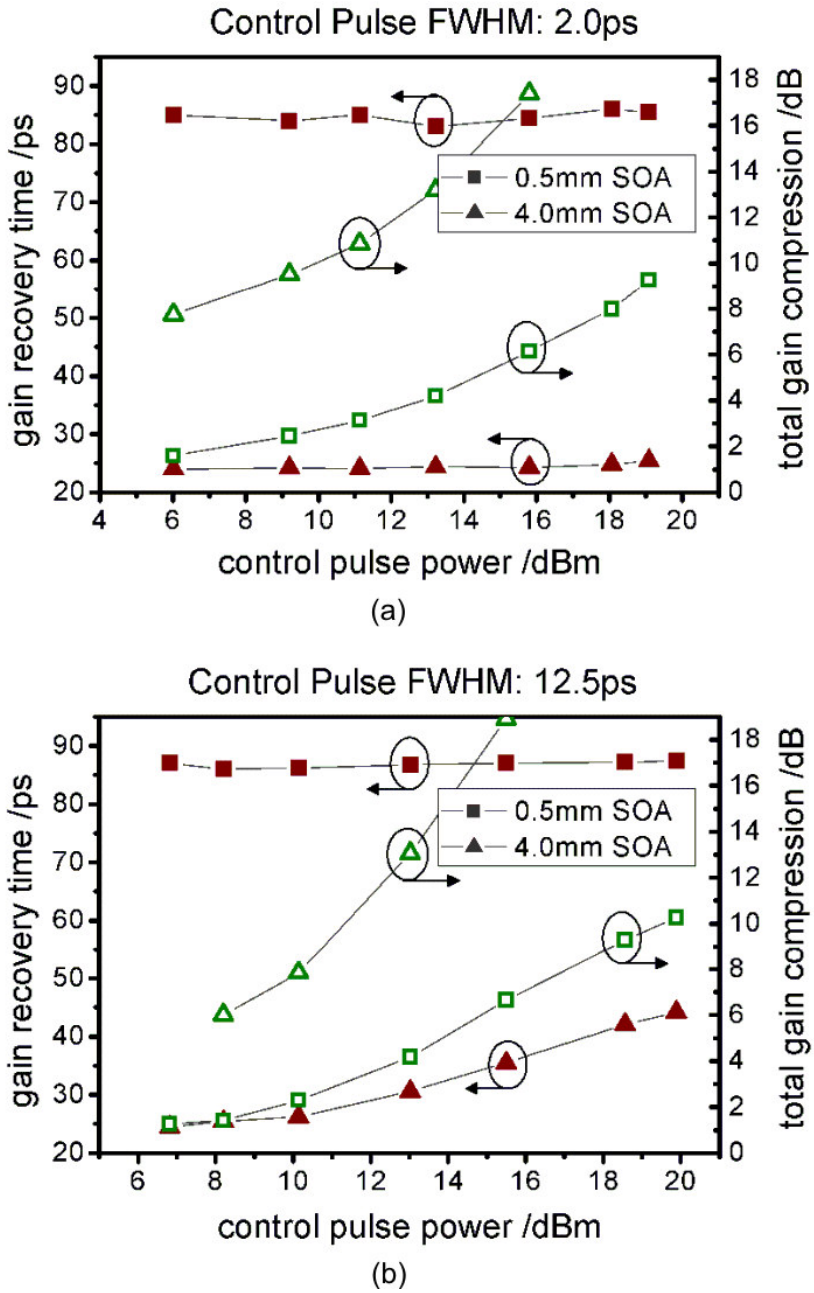

Fig. 4.13: Gain recovery time and gain compression as a function of peak power level of the control signal simulated for 0.5 mm and 4 mm amplifier and for 2 ps (a) and 12.5 ps (b) FWHM of the control pulses.

In summary, experimental analysis as well as modelling demonstrates acceleration of SOA gain dynamics with the amplifier length. Gain recovery time constants of 80 ps and 23 ps were measured for 0.5 mm SOA and 4 mm UL-SOA, respectively. The impact of intra-band effects on gain compression increases with the SOA length. However their effectiveness reduces for spectral separation higher than 10 nm between the control and probe signal. Gain recovery induced mainly by carrier relaxation was observed for 12.5 ps

control pulses. The inter-band effects are much faster in long SOAs compared to the conventional amplifiers. A total gain recovery down to 10 ps was simulated for an 8 mm UL-SOA. Finally, higher peak power of control pulses leads to stronger gain saturation (more effective for longer SOAs) but it has no impact on the recovery time. The short gain recovery time constants based on inter-band transitions can be exploited in long amplifiers for signal processing at much higher bit rates (40 Gbit/s). Furthermore, the ultra-fast intra-band effects indicate high-speed potential (up to 160 Gbit/s) of the UL-SOAs.

4.3 XGM effects in ultra-long SOAs for high-speed signal processing

The pump-probe measurements have shown that the inter-band gain effects can be effectively accelerated in ultra-long SOAs. The target is to exploit the UL-SOAs for the regeneration of 40 Gbit/s signals. In this section, the amplifier gain dynamics induced by 40 GHz periodical control signal is studied first. The investigations are performed for different operation conditions and amplifier lengths. Saturation effects in UL-SOAs are exploited for the generation of a short gain window. In the following, the impact of the gain window on a co-propagating weak 40 GHz sinusoidal signal is investigated. Re-timing and re-shaping of jittered periodical signals is demonstrated. Finally, the critical behaviour of UL-SOA gain dynamics operated in 40 Gbit/s PRBS data streams is analysed and the role of a holding beam on gain stabilisation is pointed out.

4.3.1 Impact of SOA length on gain window induced by 40 GHz sinusoidal signals

In the following numerical investigations, the gain dynamics of the SOAs are analysed by means of XGM wavelength conversion of a 40 GHz sinusoidal control signal to a CW probe signal. The amplitude modulations of the XGM converted signal behind the SOA directly correlates with the clock induced gain variations of the amplifier. In order to describe the SOA gain characteristics for different operation conditions, a term “gain window” is introduced in this work (similar to the “switching window” used for characterisation of interferometric structures, see Chapter 2). The shape of the generated gain window is described by the pulse form (FWHM, ER) of the XGM converted periodical signal.

The simulation was performed for 0.5 mm SOA and 4 mm UL-SOA devices. The wavelengths of the control and probe signal were set to 1560 nm and 1550 nm, respectively. The power level of the CW signal was kept fixed at 0 dBm, the average power of the modulated signal was set to –2 dBm and +13 dBm, respectively. In Fig. 4.14a, the pulse traces of the XGM converted signals at the 0.5 mm SOA and at 4 mm UL-SOA output for the control power of -2 dBm are depicted. It can be seen that the moderate power level of the clock signal is not high enough to saturate the 0.5 mm SOA and, thus, to sufficiently modulate the CW signal. As a result, the amplitude of the CW light is only slightly affected at the amplifier output. The interactions between the clock and the CW beam caused by XGM effects are stronger for the 4 mm UL-SOA. The

amplification of the clock signal due to higher gain in the long SOA leads to more effective carrier depletion. The impact of cross gain modulation on the probe CW signal is more obvious when increasing the clock power to +13 dBm (Fig. 4.14b). In this case, the extinction ratio of the converted signal is extended from 0.5 dB to around 3 dB for the 0.5 mm SOA. In case of the 4 mm ultra-long SOA, the sinusoidal input signal is converted to short pulses with FWHM below 6 ps and an extinction ratio of around 14 dB. The pulse shape of the converted signal defines the gain window induced by the clock signal during the propagation through the amplifier. Hence, the XGM effects at 40 GHz are much stronger in the long SOA than it is in the short one.

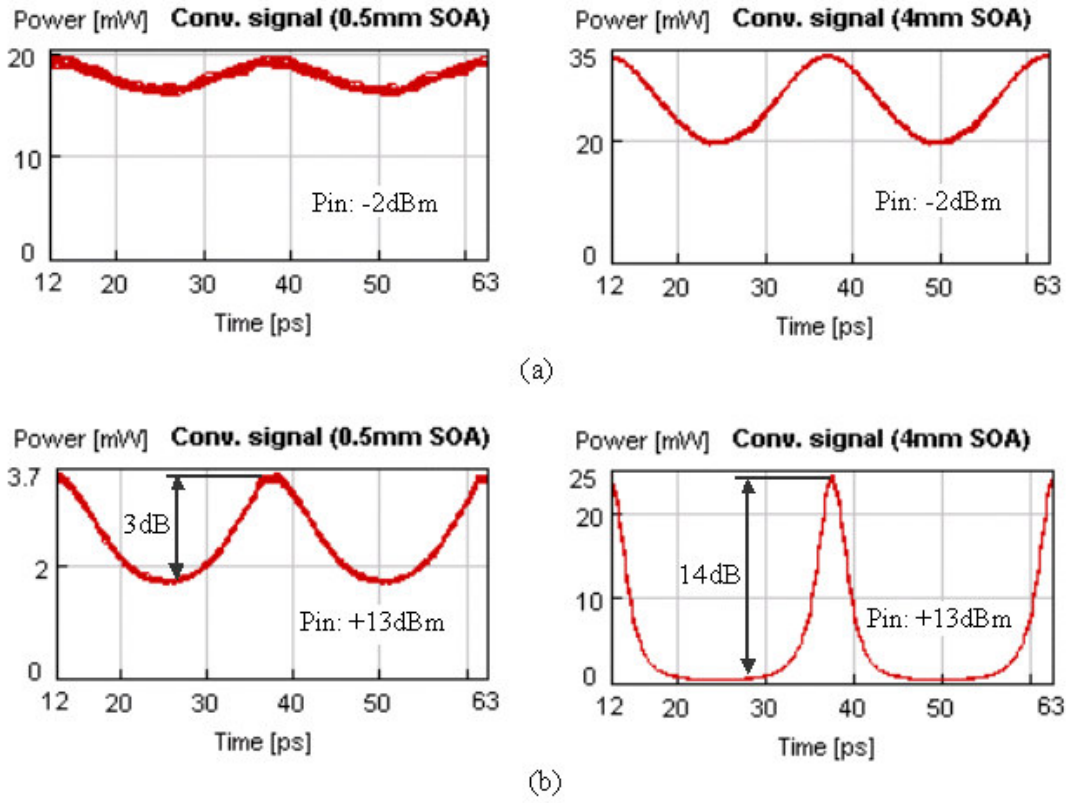

Fig. 4.14: Analysis of the gain window based on XGM wavelength conversion of a 40 GHz sinusoidal control signal to a CW probe signal in 0.5 mm and 4 mm UL-SOA for two different average power levels of the control signal: -2 dBm (a) and +13 dBm (b). $\lambda_{control}$ *= 1560 nm,* λ_{probe} *=1550 nm,* P_{probe} *= -2 dBm,* I_{SOA} *=200 mA/mm.*

In the following, the generation of the short gain window in ultra-long SOAs is investigated in more detail. Figure 4.15a shows the sinusoidal 40 GHz control signal (+13 dBm) and the CW probe signal (0 dBm) at the input of the 4 mm UL-SOA. The traces of both signals behind the optical amplifier are depicted in Fig. 4.15b. It is obvious that the pulse shape of the sinusoidal signal is highly deformed after propagation through the UL-SOA. Because of strong gain compression, the marks of the control signal are limited at the saturation power level, resulting in a pulse broadening. Due to the effective cross gain modulation and fast recovery processes in the UL-SOA, the modified shape of the input control signal is inversely transformed on the co-propagating CW signal.

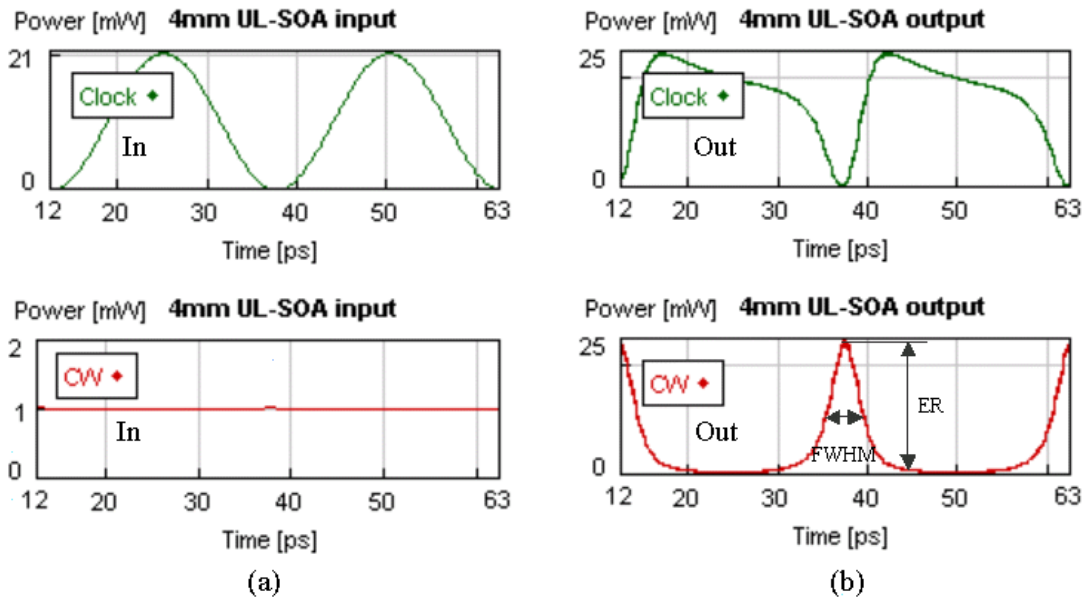

Fig. 4.15: 40 GHz sinusoidal clock control signal (+13 dBm, 1560 nm) and CW probe signal (0 dBm, 1550 nm) at the 4 mm UL-SOA input (a) and the pulse shape of both signals after propagating through the optical amplifier (b).

In the next simulations, the characteristics of the gain window are studied for different operation conditions. First, the FWHM (indicating width of the gain window) and the extinction ratio (indicating the contrast ratio of the gain window) of the XGM converted 40 GHz pulses as a function of the average power level of the sinusoidal control signal at the amplifier input are evaluated. The power level of the input CW probe signal was kept fixed at 0 dBm. Figure 4.16 summarises the results for two SOA lengths (0.5 mm and 4 mm). It can be seen that, in case of both SOAs, the width of the gain window (FWHM probe out) decreases when increasing the control power. However, the absolute values of the FWHM differ significantly when comparing the two amplifier lengths. In case of the 0.5 mm SOA, a power level of +16 dBm leads to a nearly identical FWHM between the input and the converted pulses. On the other hand, pulse compression down to 5 ps due to strong gain saturation and fast gain recovery in the 4 mm UL-SOA can be observed. The pulse widths correlate directly with the extinction ratio of the XGM converted signal. Even in case of the strong control signal (+16 dBm), the modulation depth of the probe signal behind the 0.5 mm amplifier does not exceed 4 dB. The effective gain suppression caused by the control signal propagating through the 4 mm UL-SOA leads to an ER increase up to 15 dB at the amplifier output.

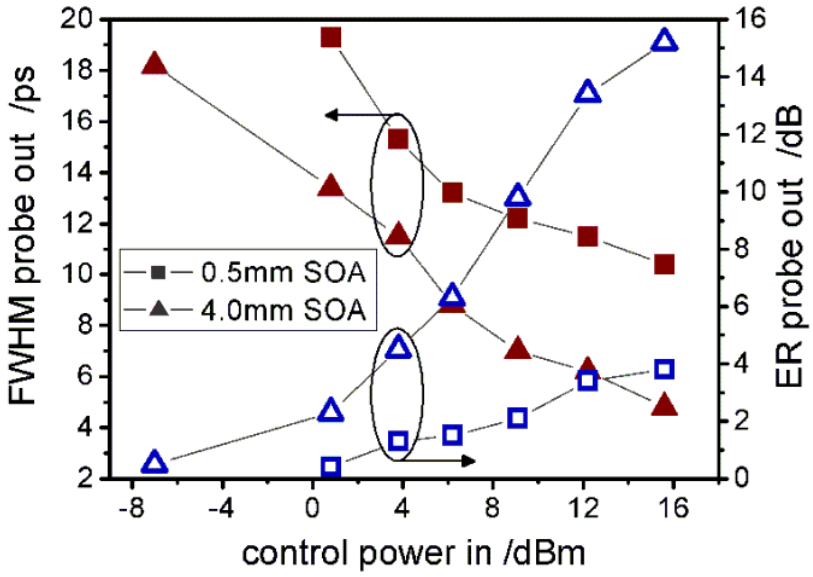

Fig. 4.16: Pulse FWHM and extinction ratio of the probe signal (defining the generated SOA gain window) behind the 0.5 mm SOA and 4 mm UL-SOA as a function of the average power level of the 40 GHz sinusoidal control signal at the amplifier input (P_{probe}= 0 dBm).

It has been shown that the shape of the gain window directly depends on the power level of the sinusoidal control signal (FWHM = 12.5 ps). The influence of the pulse width of the control signal on the generated gain window is investigated in the following simulation. The results for two SOA lengths (0.5 mm, 4 mm devices) are summarised in Fig. 4.17. In the simulation, the FWHM of the input control pulses was increased from 4 ps up to 18 ps and the corresponding FWHM and ER of the XGM converted signal was evaluated. The peak power levels of the control and probe signal at the amplifier input were kept fixed at +11 dBm and 0 dBm, respectively. From the numerical investigations follows, the width of the gain window (FWHM probe out) decreases when broadening the control pulses. This is due to inverse character of the XGM conversion. For both amplifiers, the simulated curves are almost parallel to each other in the whole range. However, the generated gain window is about 4 ps narrower in case of the ultra-long SOA. The modulation depth of the gain window (ER probe out) is much smaller at the 0.5 mm SOA output than behind the 4 mm UL-SOA because of different saturation degrees of both amplifiers. This is the reason why there is only a slight ER decrease (from 2 dB to 0.5 dB) in case of the short amplifier. Due to stronger carrier density modulation in the UL-SOA, the ER decreases from 13.5 dB down to 5 dB when broadening the control pulses. Notice that, in contrary to the amplitude change of the control signal showing in the previous simulation, narrower gain window leads to reduced output ER. In case of broad control pulses, the SOA gain modulation is smaller than for the short ones (longer saturation of the amplifier gain), resulting in reduction of the contrast ratio of the converted signal.

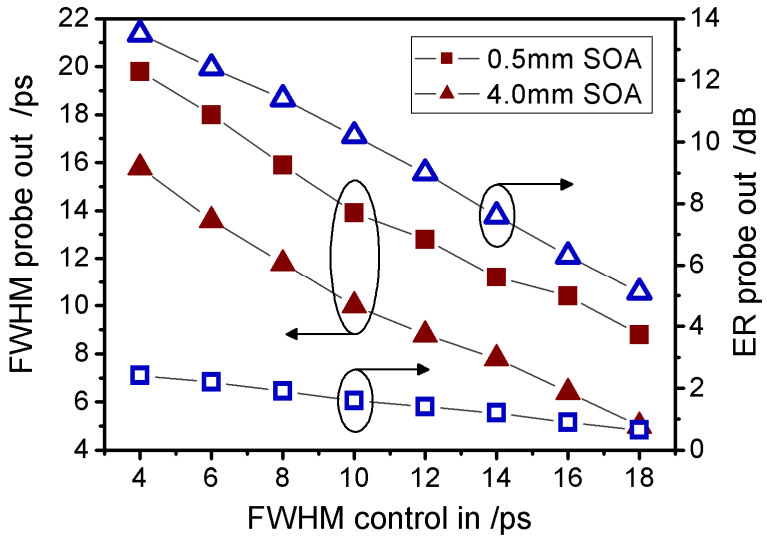

Fig. 4.17: Dependence of the pulse width and extinction ratio of the probe signal at the 0.5 mm and 4 mm amplifier output (defining the generated gain window) on the FWHM of the 40 GHz control pulses for fixed input peak powers ($P_{control}$= +11 dBm, P_{probe}= 0 dBm).

Figure 4.18 shows the evolution of both parameters (FWHM, ER) of the converted signal as a function of the SOA length. In the simulation, the average power levels of the 40 GHz control and of the CW probe signal at the SOA input were set to +13 dBm and 0 dBm, respectively. As expected, the FWHM of the gain window decreases and the modulation depth increases when enhancing the length of the semiconductor amplifier. The FWHM (ER) of the XGM converted pulses saturates to 3 ps (16 dB) for SOAs longer than 6 mm.

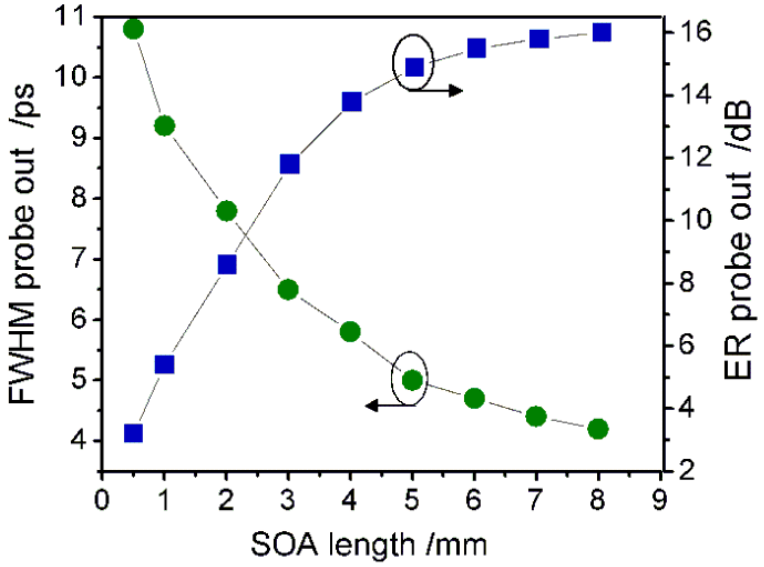

Fig. 4.18: FWHM and extinction ratio of the XGM converted signal (defining the generated SOA gain window) as a function of the SOA length for fixed average input powers of the control an probe signal ($P_{control}$= +13 dBm, P_{probe}= 0 dBm).

It is obvious that the shape of the gain window, which is generated by the periodical signal propagated through the amplifier, can be controlled by combination of several parameters. The FWHM of the gain window reduces and the contrast ratio increases with the amplifier length as well as when increasing the power level of the control signal. Broader control pulses result in narrowing of the gain window but reduce the modulation depth behind the SOA.

4.3.2 Signal re-timing and re-shaping by periodical UL-SOA gain modulation

In the previous section, the CW probe signal was used for analysis of the SOA gain modulation induced by the periodical 40 GHz control signal. Here, it will be demonstrated, how the gain window can be exploited for shaping of periodical signals. In this configuration, two signals simultaneously co-propagate through the amplifier: the 40 GHz control signal (generating the gain window) and a 40 GHz sinusoidal probe signal. In order to locate the ´ones´ of the probe signal in the transmission part of the gain window, the two signals are delayed by half a period to each other. Figure 4.19a depicts the pulse traces of both signals at the SOA input. The relative time position between the control and probe signal is clearly visible. Additionaly, the probe signal was intentionally degraded by timing jitter, in order to investigate the effect of the gain window. Based on the previous analysis, the average power levels of the control clock (1560 nm) and of the probe clock signal (1550 nm) were set to +10 dBm and to 0 dBm, respectively. The simulation was performed for a 0.5 mm and for a 4 mm UL-SOA driven by a bias current of 200 mA/mm. Figure 4.19b depicts the pulse form of the probe signal behind the 0.5 mm SOA (upper diagram) and behind the 4 mm UL-SOA (lower diagram). In case of the short amplifier, the signal interactions due to XGM effects are relatively weak. The corresponding gain window is characterised by FWHM of 12.3 ps and ER of 2 dB (see Fig. 4.16). Thus, the probe signal at the 0.5 mm SOA output follows the timing variations and shows only a slight improvement in the jitter. However, the re-shaping and re-timing effects are clearly visible, when applying the 4 mm UL-SOA. In this case, the stable control signal saturates the gain and effectively modulates the carrier density of the semiconductor amplifier. The resulted short gain window (7.2 ps FWHM, 10.5 dB ER) can be exploited for carving of the weak probe pulses. Hence, the timing fluctuations of the probe signal are clearly suppressed at the output of the UL-SOA.

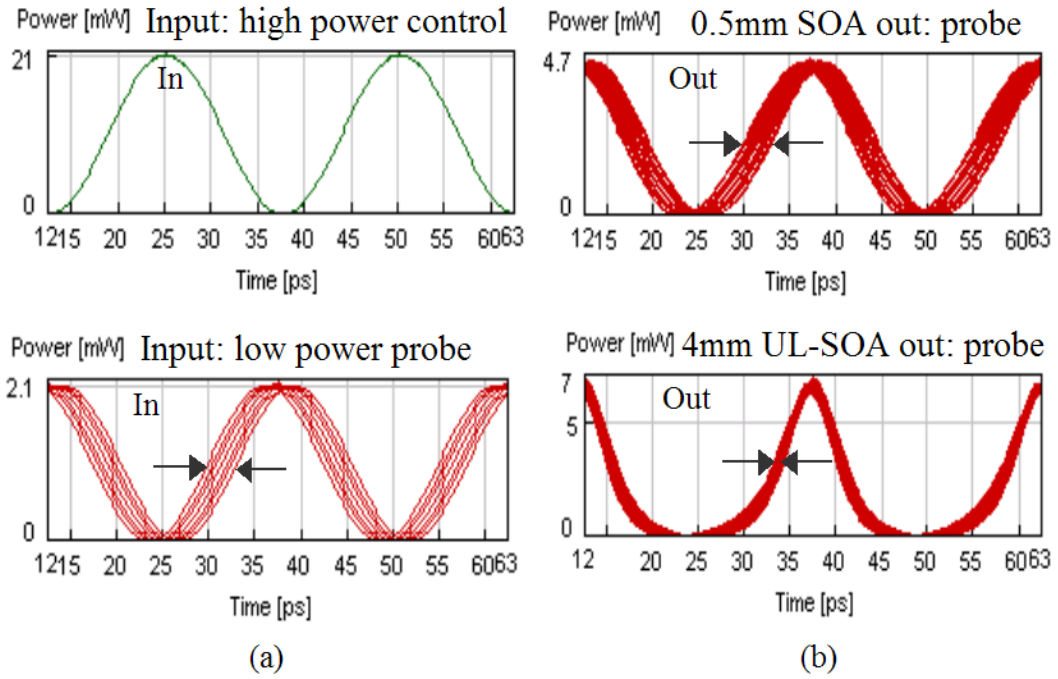

Fig. 4.19: Simulated curves of the sinusoidal 40 GHz high power control signal (+10 dBm, 1560 nm) and jittered 40 GHz weak probe signal (0 dBm, 1550 nm) in front of the optical amplifier (200 mA/mm bias current) (a) and the pulse shape of the probe signal behind the 0.5 mm SOA (upper trace) and 4 mm UL-SOA (lower trace) (b).

The impact of the gain window on the jitter reduction of the weak probe signal was investigated in more detail. In the following simulation, the timing stability of the 40 GHz probe signal was continuously degraded before injecting (together with the ideal 40 GHz sinusoidal control signal) into the 4 mm UL-SOA and the corresponding RMS-jitter of the probe signal at the amplifier output was evaluated. The average input power of the probe signal was kept constant at 0 dBm, while the average input power of the control signal was set to +11 dBm, +4 dBm, and –3 dBm, respectively. This corresponds to different FWHM of the gain window generated in the long SOA: 6.5 ps, 10.5 ps, and 15.2 ps, respectively (see Fig. 4.16). Figure 4.20 summarises the results on this simulation. It can be seen that the narrower the gain window, the more effective jitter improvement can be achieved. In case of the 6.5 ps window, the jitter of the probe signal behind the amplifier does not exceed 300 fs even for an input jitter of 1400 fs. However, there is no improvement in the timing stability, when the gain window is broader than the pulse width (including the timing instabilities) of the sinusoidal probe signal (GW: 15.2 ps in Fig. 4.20). It should be noted that the jitter reduction function results in modification of the shape of the output pulses (see Fig. 4.19b) and generally a compromise has to be found between the re-timing efficiency and the width of the output probe pulses.

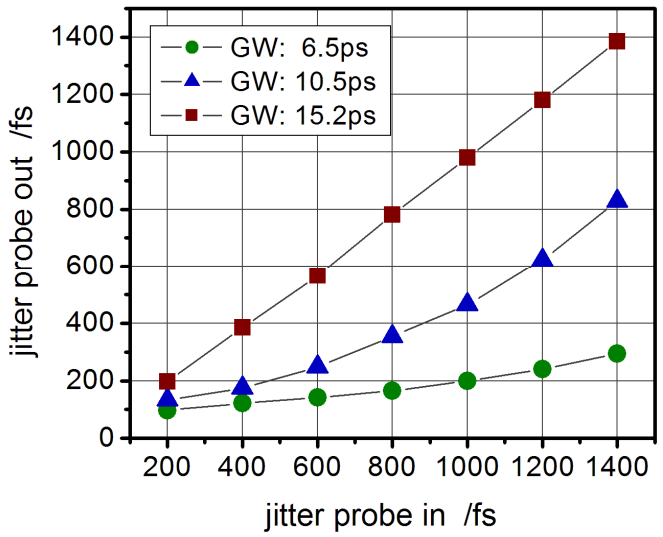

Fig. 4.20: The RMS-jitter of the 40 GHz probe signal at the 4 mm UL-SOA output as a function of the input RMS-jitter (P_{probe}= 0 dBm) for three different gain windows (GW).

The jitter reduction function of the probe clock signal in a periodically modulated 4 mm UL-SOA was also investigated for different widths of the control pulses at the 4 mm UL-SOA input: 6.5 ps, 12.5 ps, and 18.5 ps. In this simulation, the peak power of the control signal was kept fixed at +7 dBm. The results are summarised in Fig. 4.21. It has been shown in the previous section that broader control pulses result in narrowing of the gain window (Fig. 4.17). Thus, the most effective re-timing was obtained for control pulses of 18.5 ps FWHM. In case of the narrow control pulses (6.5 ps FWHM), a jitter improvement was obtained only for higher timing degradations (RMS-jitter > 1000 fs). Due to the relatively high power of the input control signal, the saturation effects partially reduce the gap between the pulses, resulting in jitter improvement function.

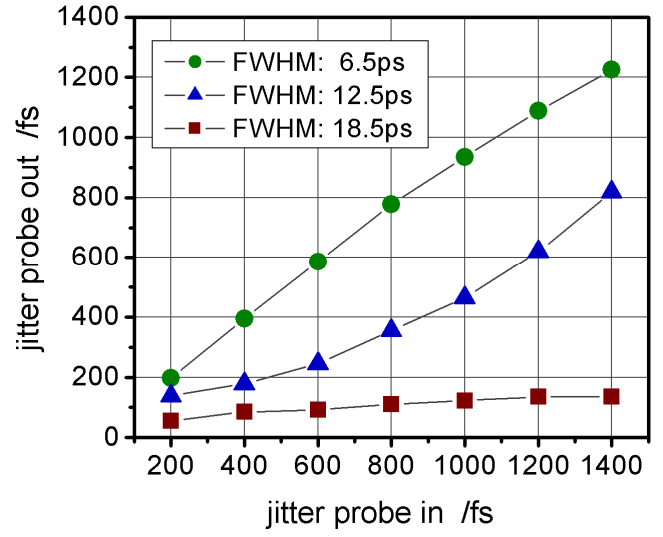

Fig. 4.21: The RMS-jitter of the 40 GHz probe signal at the 4 mm UL-SOA output as a function of the input RMS-jitter (P_{probe}= 0 dBm) for three different FWHM of the control pulses (constant peak power of $P_{control}$= +7 dBm).

In summary, the modelling results have shown that the gain effects induced by a 40 GHz periodical control signal are much more effective when increasing the SOA length. Based on the XGM wavelength conversion in the amplifier, a gain window was evaluated for different operation conditions. The pulse width of the XGM converted control signal was compressed in the 4 mm UL-SOA down to 5 ps ($P_{control}$ = +13 dBm). Simultaneously, the extinction ratio of the generated pulses increased up to 16 dB, indicating a high degree of SOA gain suppression. Furthermore, broadening the control pulses from 12.5 ps to 18 ps results in narrowing of the gain window in the 4 mm UL-SOA from 8 ps to 5 ps and simultaneous ER reducing from 9 dB to 5 dB. The fast gain modulation in ultra-long SOAs by the dominant control clock can be exploited for carving of weak periodical signals. Effective jitter reduction function of the optically clocked 4 mm UL-SOA was demonstrated. The RMS-jitter of the sinusoidal probe signal was reduced from 1400 fs down to around 800 fs for a 10.5 ps gain window and down to 300 fs in case of a 6.5 ps gain window width. Similar results were obtained when broadening the control pulses (pulses of 18.5 ps FWHM lead to jitter reduction down to 200 fs) in spite of reduced contrast ratio of the gain window in this case. Thus, the modulation depth has an inferior effect when short gain window with steep edges (fast gain recovery needed) is guaranteed.

4.3.3 PRBS signal degradation caused by pattern dependent gain modulation in UL-SOAs

In the previous sections the gain saturation and recovery processes in amplifiers of different lengths were discussed and the gain dynamics of the SOAs induced by 40 GHz periodical signals were investigated. Finally, in this section, the behaviour of the ultra-long amplifiers operated in 40 Gbit/s PRBS data streams is analysed and a comparison with SOAs of a conventional length (0.5 mm) is given.

In the following experiment, the influence of the SOA gain dynamics on the quality of 40 Gbit/s 2^{31}-1 PRBS RZ signals is studied. Again, two SOA lengths were considered: 0.5 mm SOA and 4 mm UL-SOA driven by a bias current of 200 mA/mm. The eye diagram of the high quality RZ data signal at the amplifier input is depicted in Fig. 22a. The quality criteria of the signals are determined by the timing stability (RMS-jitter) and by eye signal-to-noise ratio (eye S/N, for definition see Appendix D). The average power level of the data signal (1550 nm, RMS-jitter: 340 fs, eye S/N: 20.2) was set to –8 dBm before injecting into the amplifier. The measured eye diagram of the data signal behind the 0.5 mm device is shown in Fig. 4.22b. The short SOA operates in linear regime, leading to a nearly identical signal quality at the SOA output (RMS-jitter: 389 fs, eye S/N: 19.1). However, the PRBS data stream is strongly degraded behind the 4 mm UL-SOA, as it is obvious form Fig. 4.22d. Due to the gain saturation effects, the bits are differently amplified depending on the previous PRBS history. The carrier density follows the envelope of the PRBS signal. A mark experiences a higher gain after consecutive spaces than a mark that propagates inside a bit sequence of logical ´ones´. Thus, the data signal is distorted by strong power fluctuations leading to a timing jitter of 1300 fs. At the same time, the eye S/N decreases down to 4.1. Figure 4.18c shows the simulated eye diagram of the 40 Gbit/s PRBS signal behind the 4 mm amplifier, indicating similar behaviour as observed in the experiment.

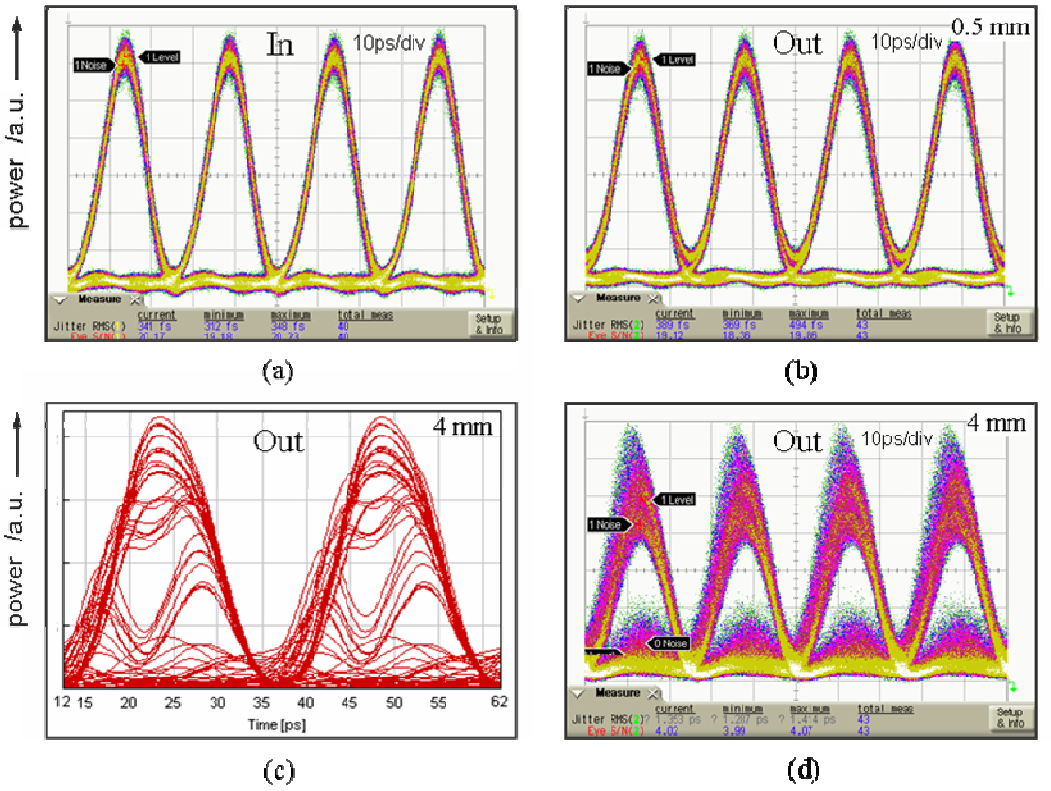

Fig. 4.22: Eye diagrams of the ideal 40 Gbit/s PRBS 2^{31}-1 RZ signal (λ_{data} = 1550 nm) before injecting into the amplifier (P_{in}=-8 dBm) (a), after propagating through the 0.5 mm SOA (b) and behind the 4 mm UL-SOA (c-modeling, d-experiment).

The timing jitter and eye signal to noise ratio of the data signal at the SOA output (0.5 mm, 4 mm devices) were measured for different input data average powers. The results are summarised in Fig. 4.23. In case of the 4 mm UL-SOA, the RMS-jitter as well as the eye S/N factor have their optimum for a limited power dynamic range between -12 dBm and -6 dBm. If the power level is smaller, degradations due to ASE are dominant. On the other side, for power levels higher than 0 dBm, the data signal is distorted mainly by strong amplitude fluctuations. However, even for the optimised configuration the quality of the PRBS signal after propagating through the amplifier (RMS jitter: 1170 fs, eye S/N: 6.2) is not comparable with the original signal (RMS jitter: 340 fs, eye S/N: 20.2). The data signal at the 0.5 mm SOA output shows clearly different behaviour. The jitter variation is much smaller in a wide power range of more than 10 dB; the eye S/N remains relatively high (beyond 16), until degradations due to patterning effects occur (saturated regime). Obviously, there is no advantage of long optical amplifiers directly operated in PRBS data streams.

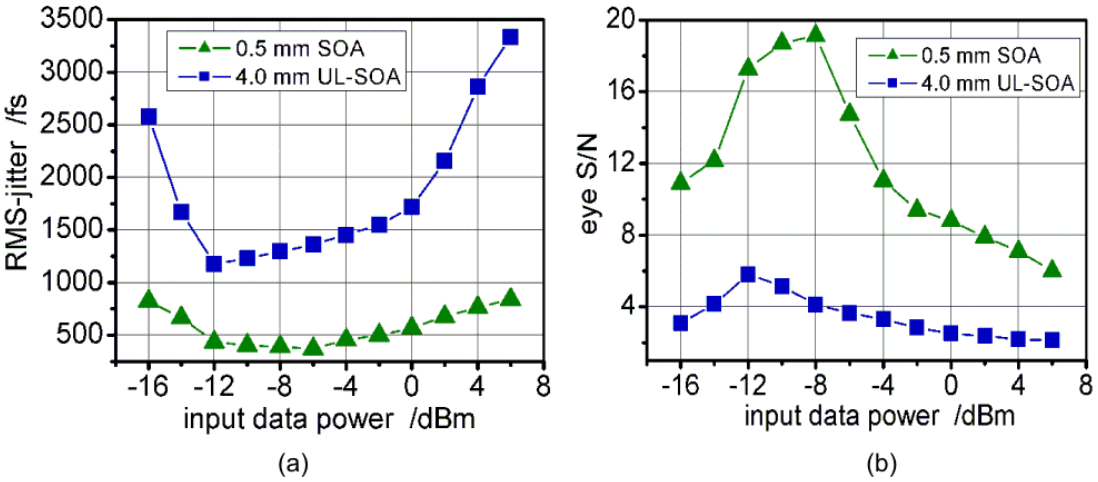

Fig. 4.23: RMS-jitter (a) and eye S/N (b) of the data signal at the output of the 0.5 mm SOA and 4 mm UL-SOA as a function of the average power level of the ideal PRBS 2^{31}-1 RZ signal (340 fs RMS-jitter, 20.2 eye S/N).

In order to prevent the strong signal degradations caused by the pattern dependent gain modulation of the long SOAs, the gain has to be saturated independently of the PRBS pattern. This can be achieved by a second signal, which propagates the amplifier together with the data signal and acts as a holding beam. The simulation shows (Fig. 4.24a) that the patterning effects are reduced when a CW signal (1560 nm, P_{CW} = +2 dBm) was launched into the 4 mm ultra-long SOA additionally to the 40 Gbit/s data signal (1550 nm, P_{data} = -8 dBm). However, even for an ideal input signal some distortions can be observed behind the UL-SOA. Figure 4.24b depicts the experimentally evaluated eye diagram of the data signal behind the 4 mm UL-SOA. The measurements confirm the modelling results. The RMS-jitter of the output data signal increased from 340 fs (ideal data in) to around 560 fs, the eye S/N factor reduces down to a value of 8.8, which is mainly due to residual amplitude fluctuations.

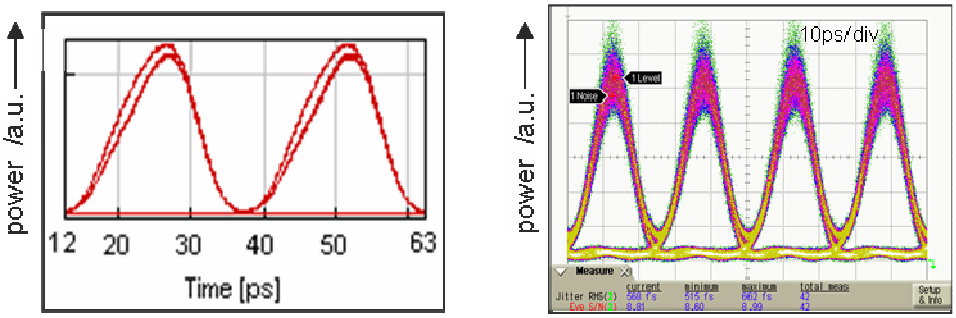

Fig. 4.24: Simulated (a) and measured (b) eye diagrams of the 40 Gbit/s PRBS data signal behind the 4 mm UL-SOA stabilised by an additional CW holding beam (P_{data} = -8 dBm, P_{CW} = +2 dBm).

In summary, the behaviour of ultra-long SOAs operated in PRBS data streams has been shown and a direct comparison with SOAs of a conventional length (0.5 mm) was performed. The numerical as well as experimental results indicate the key problem of the long devices for direct processing of 40 Gbit/s PRBS signals. Even at low power levels, strong signal degradations due to gain saturation effects were observed (RMS jitter increase from 340 fs to 1170 fs, eye S/N reduction from 20.2 down to 6.2). The different amplification of the data bits with dependence on the previous PRBS history leads to strong degradations behind the UL-SOAs. The distortions can be partially suppressed after applying an additional holding beam (RMS-jitter: 560 fs, eye S/N: 8.8). However, the quality of the original data signal cannot be achieved.

4.4 Conclusions

The gain dynamics of ultra-long semiconductor optical amplifiers provide very attractive features for high-speed all-optical signal processing. Based on the pump-probe measurements, the impact of intra-band effects on gain compression as well as recovery processes is much more effective in the long SOA devices compared to the conventional amplifiers with a length below 1 mm. Furthermore, the inter-band transitions are effectively accelerated when enhancing the SOA length. Gain recovery time constant of 23 ps was measured for the 4 mm UL-SOA and a recovery even below 10 ps was evaluated by numerical simulations in case of the 8 mm long SOA. Hence, in contrary to conventional SOAs (~100 ps recovery time), the inter-band gain effects (XGM, XPM) of the ultra-long SOAs provide a speed potential for signal processing at 40+ Gbit/s.

The exploitation of periodically modulated UL-SOAs for signal processing was studied in detail by numerical simulations. In this case, the SOA gain modulation was induced by a dominant 40 GHz optical clock signal. Due to strong gain saturation and fast recovery processes of the UL-SOAs, a short gain window is generated in the long device. The gain window can be effectively narrowed when increasing the clock power level and SOA length, respectively. The impact of the gain window in the periodically modulated UL-SOA was further exploited for re-shaping and re-timing of 40 GHz weak sinusoidal signals, intentionally degraded by timing fluctuations. An effective jitter reduction function from 1400 fs down to 300 fs was achieved in the optically clocked 4 mm amplifier. The behaviour of the UL-SOAs operated in 40 Gbit/s PRBS RZ streams was also analysed. In this case, the pattern dependent gain saturation results in strong degradation of the data quality behind the amplifier. The distortions caused by gain dynamics of the long amplifier can be partially eliminated by means of a CW holding beam, however with a still reduced signal quality compared to a conventional SOA.

The analysis has revealed a completely new potential of the ultra-long SOAs for high-speed all-optical signal processing. In case of PRBS data signals, the UL-SOA has to be stabilised by an external signal independently on the pattern sequence, in order to exploit the pronounced intra-band and fast inter-band effects in the long devices. In the proposed configuration, the dominant clock signal is used for gain stabilisation and simultaneous pulse carving. A periodically modulated UL-SOA has been identified as the key technique for both all-optical 3R regeneration schemes developed in frame of this thesis, as it will be demonstrated in the following chapters.

5 Optically Clocked 3R Regenerator: OC-3R

The target of this work is to develop an all-optical 3R architecture for spectrally efficient DWDM long-haul transmission systems that can be deployed in the fibre link as a 3R regenerative amplifier without the necessity of any wavelength monitoring function. In order to guarantee high integration degree, mechanical and thermal stability, the proposed scheme has to comprise exclusively compact semiconductor devices providing sufficient bandwidth for high-speed signal processing (40 Gbit/s and beyond).

The knowledge on UL-SOA gain dynamics as well as on the gain window generation induced by a periodical signal propagated through the long device was effectively exploited in the design of the novel wavelength preserving 3R scheme, the 'Optically Clocked' 3R regenerator (OC-3R).

First, the set-up and the basic characteristics of the OC-3R scheme operated in ideal 40 Gbit/s PRBS RZ data streams are presented. The impact of power levels for different data-clock wavelength combinations is pointed out. Furthermore, the demands on the UL-SOA length and on the quality of the clock signal for effective regeneration of distorted PRBS signals is analysed. The robustness of the optical regenerator is investigated by eye analysis and by BER measurements. Finally, the functionality of the OC-3R architecture is demonstrated in system experiments. The ability of the optical 3R regenerator for mitigation of chromatic and polarisation mode dispersion as well as for operation in 40 Gbit/s packet data streams are discussed.

5.1 Basic characteristics of the OC-3R regenerator

5.1.1 OC-3R set-up and performance for ideal data streams

The operation principle of the wavelength preserving 'Optically Clocked' 3R regenerator exploits the saturation effects and fast gain dynamics of ultra-long SOAs discussed in the previous chapter. The set-up of the proposed all-optical OC-3R regenerator is sketched in Fig. 5.1. Basically, it comprises an optical clock (e.g. PhaseCOMB-laser) and an UL-SOA. The principle of operation is as follows. The degraded 40 Gbit/s PRBS RZ signal is split off at the regenerator input. A part of the data signal is injected into the self-pulsating laser used for all-optical clock recovery. The PhaseCOMB-clock synchronises to the injected PRBS signal and emits a sinusoidal pulse stream. The second part of the data signal is delayed by half a bit period relative to the synchronised clock. Thus, the data signal propagates through the long amplifier within the gain window induced by the periodical clock (see section 4.3.1). The strong gain saturation due to the dominant clock together with fast XGM effects in the UL-SOA leads to amplitude equalising and effective carving of the distorted weak data pulses. The clock is filtered out behind the UL-SOA. The data signal is regenerated in the amplitude and time without any wavelength conversion.

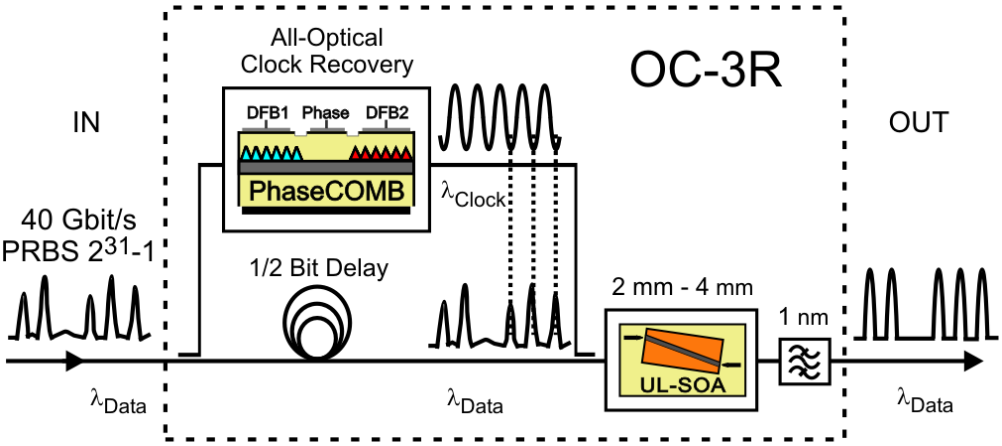

Fig. 5.1: Principle set-up of the 'Optically Clocked' 3R regenerator (OC-3R).

First, the performance of the OC-3R regenerator is investigated for ideal 40 Gbit/s RZ signals. Figure 5.2 depicts the simulated eye diagrams of the data signal (1550 nm, P_{data} = -2 dBm) at the regenerator input (upper trace) and behind the OC-3R (lower trace). The dominant 40 GHz clock signal (1560 nm, P_{clock} = +6 dBm) defines the gain dynamics in the long amplifier (4 mm UL-SOA). Thus, the distorting patterning effects (see section 4.3.3) are effectively suppressed and the high quality data signal pass through the optically clocked UL-SOA without any addition of amplitude noise and timing jitter. In the experiment, the 40 Gbit/s PRBS 2^{31}-1 RZ signal (1550 nm) was propagated through the 4 mm UL-SOA (200 mA/mm bias current) together with the clock signal recovered by the PhaseCOMB-laser (1560 nm). The average power levels of the data and clock in front of the amplifier (measured in fibre) were set to -2 dBm and +6 dBm, respectively. The resulted eye diagrams (Fig. 5.2b) match well with the simulated ones. For any incoming data bit, the UL-SOA gain history is defined by the preceding strong clock pulse and not by the data pattern.

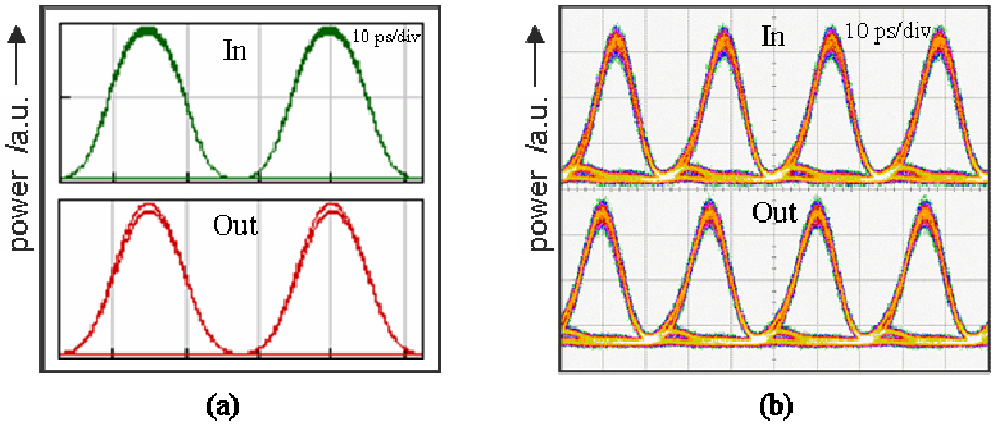

Fig. 5.2: Eye diagrams of the ideal 40 Gbit/s PRBS 2^{31}-1 RZ signal (1550 nm) at the OC-3R input (upper traces) and behind the regenerator (lower traces) evaluated by modelling (a) and in the experiment (b). The average power levels of the optical signals at the 4 mm UL-SOA input were set to P_{data} = -2 dBm, P_{clock} = +6 dBm.

From the system point of view, low power consumption, polarisation insensitive operation and wide wavelength range are important additional features of an optical regenerator. In the following experiments, the OC-3R performance was investigated for ideal data signals, in order to identify the typical behaviour of the proposed architecture. Figure 5.3 shows the ASE spectrum of the 4 mm UL-SOA applied in the regenerator, indicating the location of the clock signal (1560 nm) and of the data signal for three different wavelengths: 1540 nm, 1550 nm, and 1558 nm respectively. In order to effectively use the saturation conditions in the UL-SOA, which have to be defined by the periodical signal, the clock wavelength was located close to the gain maximum of the semiconductor amplifier. One can notice that the SOA gain differs in the investigated wavelength range for more than 10 dB (the data signal experiences different gain at 1558 nm compared to 1540 nm). The timing jitter of the output data signal was evaluated in order to quantify the typical operation conditions of the OC-3R regenerator.

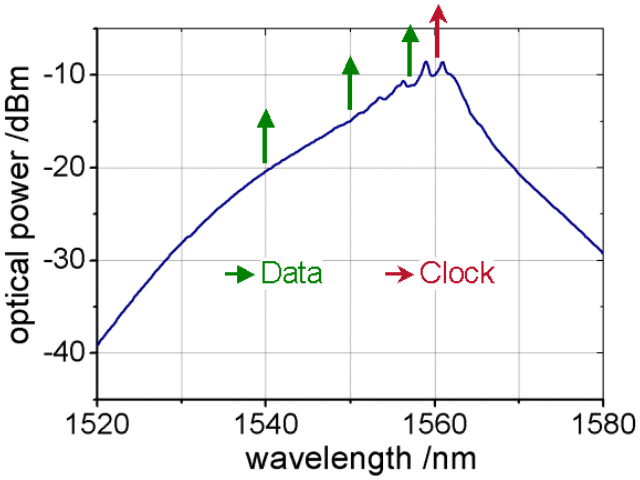

Fig. 5.3: ASE spectrum of the 4 mm UL-SOA (200 mA/mm bias current) indicating spectral location of the 40 GHz clock signal and of the three wavelengths used for the 40 Gbit/s PRBS data signal.

5.1.1.1. Data and clock power analysis in the OC-3R scheme

In the following, the power relations between the 40 Gbit/s PRBS 2^{31}-1 RZ signal and 40 GHz clock in the OC-3R scheme are studied. First, the average power level of the high quality data signal (380 fs RMS-jitter) was continuously varied from -18 dBm up to +4 dBm (measured in the fibre in front of the UL-SOA) and the RMS-jitter of the data signal at the OC-3R output was evaluated using a sampling oscilloscope with precision time base. The average power level of the clock signal was set to +4 dBm and was kept fixed during the measurement. The results are summarised in Fig. 5.4a. It can be seen that for the data wavelengths of 1558 nm and 1550 nm, a power level of only –6 dBm leads already to error-free operation of the OC-3R regenerator. In case of the short wavelength data signal (1540 nm), an input power of at least 0 dBm is required, which is related to the smaller gain at this operation point. At the low power levels (below -16 dBm) the regenerative potential of the OC-3R scheme is limited by the fibre-chip losses of the UL-SOA, resulting in signal degradation due to reduced OSNR behind the regenerator.

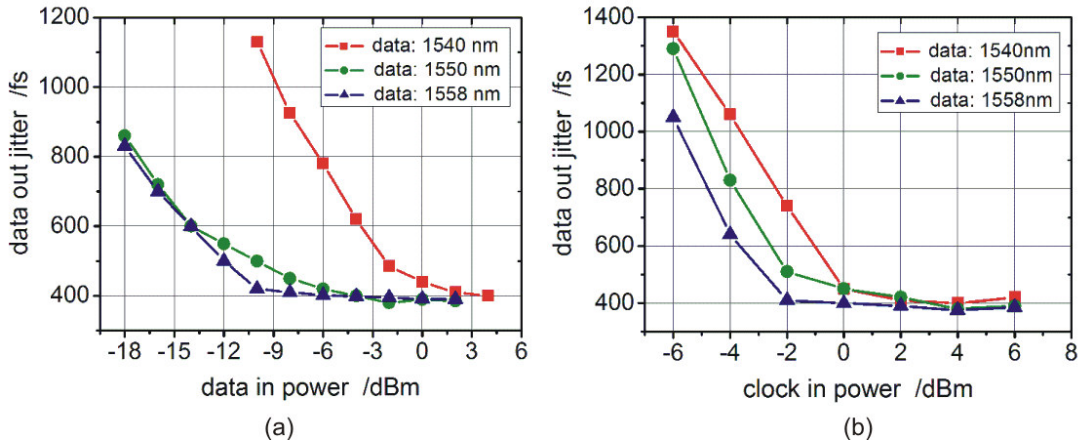

Fig. 5.4: RMS-jitter of the 40 Gbit/s PRBS 2^{31}-1 RZ signal behind the OC-3R regenerator as a function of the input average data power (P_{clock} =+4 dBm, λ_{clock} = 1560 nm) (a) and of the average clock power (P_{data} = 0 dBm) (b) for three data wavelengths (λ_{data} = 1540 nm, 1550 nm, 1558 nm, 380 fs RMS-jitter).

In the following, the requirements for the clock power level in the OC-3R scheme are analysed. Here, the average power level of the 40 Gbit/s PRBS signal was kept constant at 0 dBm. The amplitude of the clock signal was continuously increased from –6 dBm up to +6 dBm. Also in this case, the corresponding RMS-jitter of the output data signal was evaluated. Figure 5.4b shows the results on this measurement. An average clock power of -2 dBm only results in a high quality data signal behind the OC-3R, when both data and clock are located close to the UL-SOA gain maximum (1558 nm – 1560 nm),. A further increase of the clock amplitude has no influence on the timing stability of the data signal. It should be noted that the clock power defines directly the gain window in the UL-SOA (see section 4.3.1) and, thus, the regenerative efficiency of the OC-3R. In the experiments described here, a high quality data signal was applied at the regenerator input and hence no additional re-shaping induced by the gain window was necessary. Generally, a dominant clock power (narrower gain window with higher contrast ratio) is required in order to guarantee quality improvement of the data signal at the regenerator output. The increased data RMS-jitter for low clock powers is related to the patterning effects caused by the PRBS induced gain dynamics of the ultra-long SOA.

5.1.1.2. Polarisation sensitivity of the OC-3R scheme

In the next experiment, the polarisation dependence of the OC-3R scheme is investigated. The average power levels of the data signal (1550 nm) and of the clock (1560 nm) in front of the 4 mm UL-SOA were set to 0 dBm and +4 dBm, respectively. The polarisation state of the PRBS signal was controlled before injecting into the regenerator. Two extreme cases were considered; the parallel data-clock polarisation and the case, where the data signal was orthogonally polarised relative to the clock signal. The relative data-clock polarisation was determined using an optical spectrum analyser by means of new FWM products. The eye diagram of the 40 Gbit/s data signal behind the OC-3R for identical data – clock polarisation is shown in Fig. 5.5a. Subsequently, the polarisation of the data signal was rotated by 90 degree. The resulted eye diagram of the output signal is shown in Fig. 5.5b. A decrease in the amplitude of around 30 % can be noticed. Figure 5.5c shows the output

signal for orthogonal data – clock polarisation after readjusting the average power level in front of the receiver, indicating identical signal quality compared to the previous configuration. Hence, the OC-3R scheme does not require any explicit polarisation monitoring. The regenerative performance of the optically clocked scheme is based on fast gain effects that are generally polarisation insensitive. The amplitude changes observed in this experiment are related to the polarisation dependence of the UL-SOA gain (see section 4.1.2) and can be further eliminated by proper design of the semiconductor heterostructure.

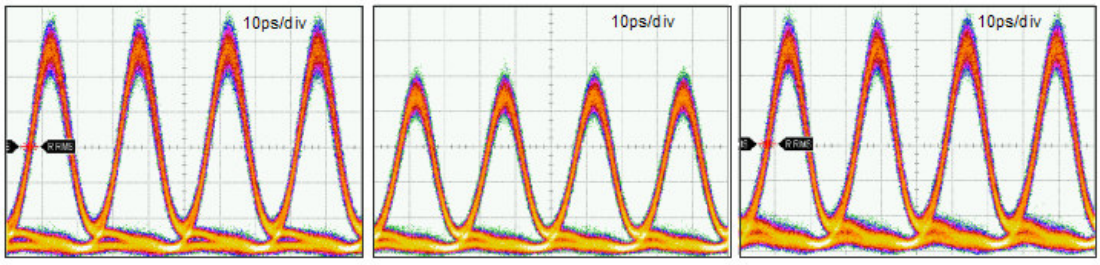

Fig. 5.5: Eye diagrams of the 40 Gbit/s data signal behind the OC-3R regenerator for identical data – clock polarisations (a) and for orthogonal data – clock polarisation before (b) and after readjusting the power level at the receiver (c).

In summary, the typical operation conditions of the OC-3R scheme were demonstrated by processing of ideal PRBS 2^{31}-1 RZ data streams. It has been shown that power relations between the data and clock signal are directly related to the gain spectrum of the ultra-long SOA. The carrier density of the amplifier has to be modulated by the dominant periodical clock signal in order to prevent data distortions due to patterning effects. The input power level of the data signal is less critical (more than 10 dB dynamic range), when the wavelength is located around the SOA gain peak. Based on the first analysis, the OC-3R regenerator shows potential for polarisation insensitive operation in a wide wavelength range of more than 20 nm.

5.2 Requirements for UL-SOA and Clock in the OC-3R scheme

In the following, requirements for the key devices of the OC-3R scheme operated in degraded data streams are numerically analysed using VPIcomponentMaker^{TM}. In the simulation, the 40 Gbit/s PRBS 2^{31}-1 RZ signal was intentionally degraded by amplitude fluctuations of around 3 dB before injecting into the optical regenerator. The parameter values of the SOA model were extracted from the simulations performed in the previous chapter and are given in Appendix B. First, the impact of the SOA length on regenerative performance of the OC-3R architecture is discussed. Furthermore, the basic prerequisites on the periodical clock signal for effective signal regeneration are demonstrated.

5.2.1 Impact of the SOA length

5.2.1.1. Re-shaping effect versus SOA length

Suppression of bit-to-bit amplitude fluctuations in the OC-3R regenerator for different SOA lengths was numerically analysed. In the simulation, the degraded 40 Gbit/s RZ PRBS data signal (λ_{data} = 1550 nm, P_{data} = 0 dBm, Fig. 5.6a) was injected bit interleaved to the ideal 40 GHz sinusoidal clock signal (λ_{clock} = 1560 nm, P_{clock} = +10 dBm) into the semiconductor amplifier. The simulation was performed for different SOA lengths between 0.5 mm and 8 mm. The quality of the data signal at the regenerator output was evaluated by eye diagrams (Fig. 5.6b-f). It is obvious that the SOA length directly determines the quality improvement of the data signal processed in the OC-3R regenerator. The longer the SOA, the more effective is the suppression of the amplitude fluctuations, resulting in improved eye opening at the regenerator output. The dominant clock signal stabilises the carrier density modulation in the long amplifiers, the patterning effects caused by the degraded data signal are effectively equalised. Furthermore, the generated gain window shapes the data pulses, leading to suppression of the timing jitter behind the OC-3R regenerator. Comparing the signal quality corresponding to the 4 mm and to the 8 mm UL-SOA, the eyes are nearly identical. From a practical point of view (considering e.g. power consumption, suppression of internal reflections, temperature stability), the amplifier should be as short as possible. Hence, a 4 mm UL-SOA was selected for further experimental analysis.

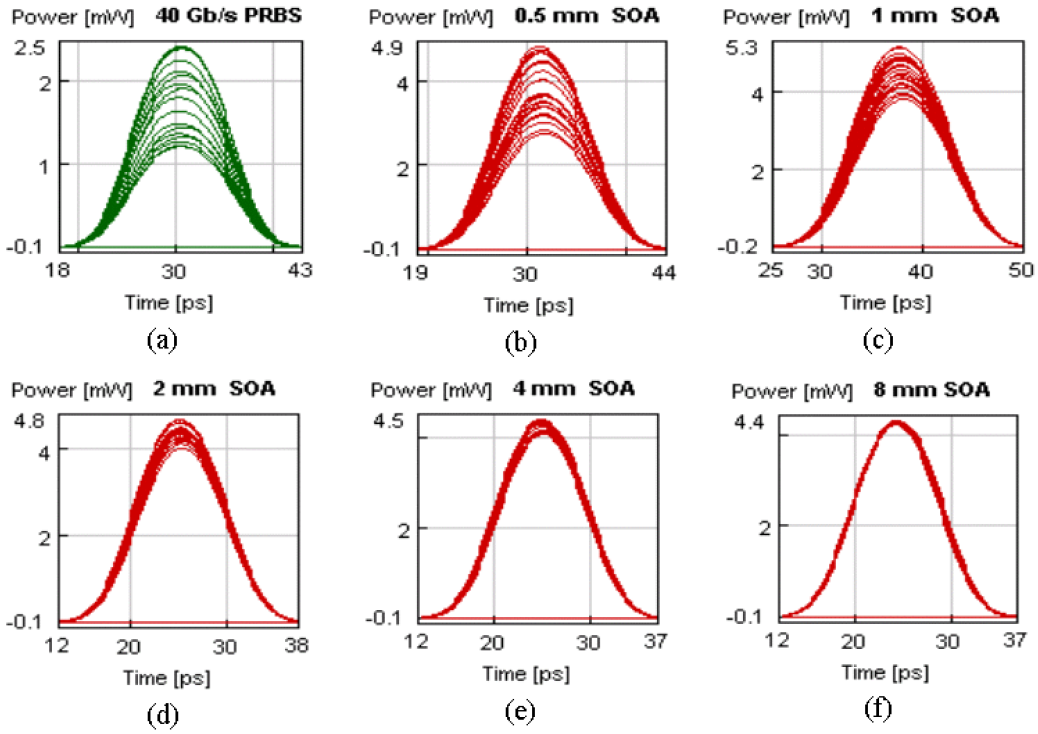

Fig. 5.6: Degraded 40 Gbit/s PRBS signal at the UL-SOA input (a) and the corresponding output signals behind the OC-3R regenerator for different UL-SOA lengths (b-f). (P_{data} = 0 dBm, λ_{data} = 1550 nm, P_{clock} = +10 dBm, λ_{clock} = 1560 nm.)

In the following, the jitter reduction function of the OC-3R architecture is evaluated numerically for different SOA lengths. The RMS-jitter of the degraded 40 Gbit/s RZ input signal (P_{data} = 0 dBm) and of the ideal 40 GHz clock (P_{clock} = +10 dBm) was 1680 fs and 100 fs, respectively. Figure 5.7 shows the RMS-jitter of the data signal behind the OC-3R regenerator as a function of the SOA length. The jitter values are extracted from the eye diagrams depicted in the previous simulation. The periodical clock signal propagates the SOA between two data pulses, resulting in re-timing and re-shaping of the distorted PRBS signal. The principle of signal interactions due to saturation effects and fast cross gain modulation in UL-SOAs has been already discussed in section 4.3.2. It is obvious that the jitter reduction effect is relatively small for short interaction lengths (200 µm, 500 µm SOAs) and increases when enhancing the length of the semiconductor amplifier. For devices longer than 4 mm the gain dynamics in the UL-SOA is stabilised by the clock signal predominantly and the RMS-jitter remains nearly unchanged.

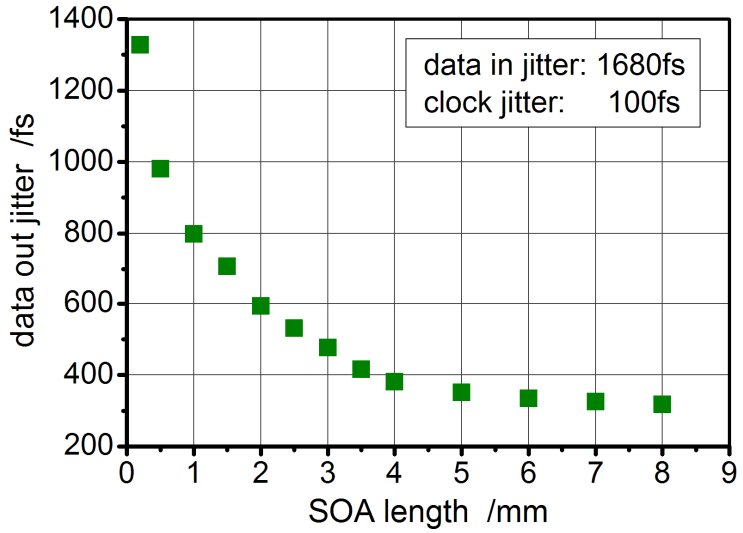

Fig. 5.7: RMS-jitter of the 40 Gbit/s data signal behind the OC-3R regenerator for different amplifier lengths. (P_{data} = 0 dBm, λ_{data} = 1550 nm, P_{clock} = +10 dBm, λ_{clock} = 1560 nm).

5.2.1.2. Impact of data extinction ratio in the OC-3R scheme

Up to now, the investigations were performed for RZ data signals with an extinction ratio (ER) higher than 25 dB. It has been shown that degradations in amplitude and time domain can be effectively eliminated behind the OC-3R regenerator. The following simulation shows behaviour of the OC-3R when processing PRBS signals with reduced extinction ratio. Figure 5.8a depicts the eye diagram of a 40 Gbit/s RZ data signal (1550 nm) with an ER of around 10 dB only. The eye diagrams of the data signal behind the OC-3R regenerator are shown in Fig. 5.8b-d for different SOA lengths (0.5 mm, 4 mm, 8 mm devices). The average power level of the clock signal (1560 nm) was set to +10 dBm before injecting into the amplifier. It can be seen that the reduced ER is not improved behind the regenerator. In case of the 0.5 mm SOA (Fig. 5.8b), the data signal pass through the device without any significant changes. For the 4 mm and 8 mm amplifiers

(Fig. 5.8c,d), the impact of the gain window induced by the dominant clock signal can be observed, reducing the zero level out of the bit slots. The XGM effects exploited in the optically clocked long amplifier do not provide any threshold function needed for suppression of data distortions at the space level. An extended 3R circuit based on the OC-principle, which performs additional ER improvement, will be briefly introduced in section 5.3.4. The theoretical background of this concept can be further found in [175].

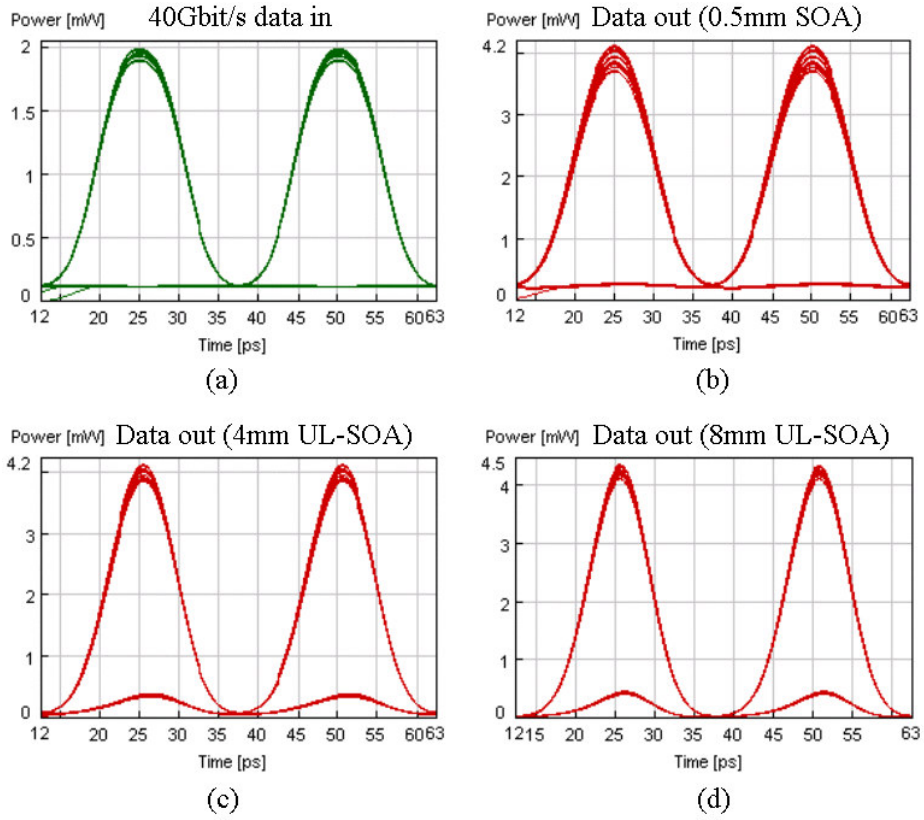

Fig. 5.8: 40 Gbit/s PRBS signal with reduced extinction ratio (ER = 10 dB) at the OC-3R input (a) and the eye diagrams of the corresponding signal behind the regenerator for different SOA lengths: 0.5 mm (b), 4 mm (c), and 8 mm (d). (P_{data} = 0 dBm, λ_{data} = 1550 nm, P_{clock} = +10 dBm, λ_{clock} = 1560 nm).

Figure 5.9 summarises the results on ER investigations for the 4 mm UL-SOA. In the simulation, the 40 Gbit/s PRBS signal was continuously degraded by reduced extinction ratio and the corresponding ER of the data signal behind the OC-3R was evaluated. The average power levels (wavelengths) of the data and clock signals at the amplifier input were set as specified in the previous simulation. From Fig. 5.9 can be seen that the output data ER is nearly identical with the input data ER when reducing the ER of the original PRBS signal down to 12 dB. Further reduce of the input ER leads to slightly faster ER degradation of the data signal at the regenerator output. Thus, the OC-3R regenerator (comprising exclusively a clock recovery stage and an ultra-long SOA) assumes processing of PRBS signals with sufficiently high extinction ratio (ER > 20 dB). The OC-3R can preserve the data ER, however an improvement cannot be achieved.

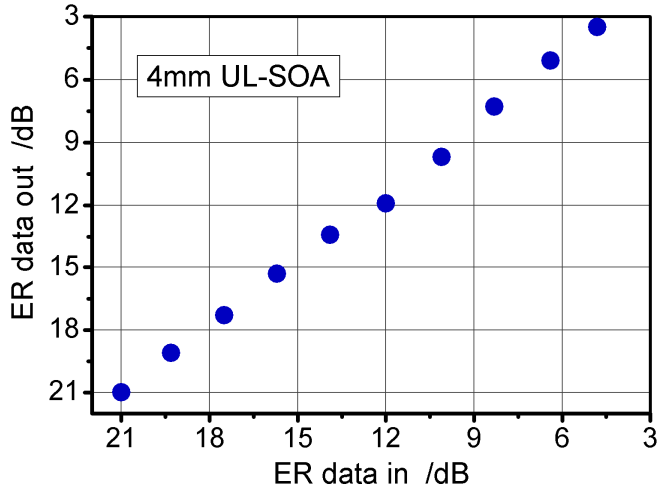

Fig. 5.9: Extinction ratio of the data signal behind the OC-3R regenerator comprising a 4 mm UL-SOA (I_{SOA} = 200 mA/mm) as a function of the input PRBS data ER. (P_{data} = 0 dBm, λ_{data} = 1550 nm, P_{clock} = +10 dBm, λ_{clock} = 1560 nm).

5.2.2 Demands on the clock parameters

Experimental results have shown (see section 5.1.1.2) that a dominant clock guarantee processing of ideal data signals without any additional degradation. In this section the impact of the clock signal on the regenerative efficiency of the OC-3R operated in degraded PRBS data streams is numerically studied in more detail.

In the following simulation, the jitter as well as extinction ratio of the 40 Gbit/s data signal (1550 nm) behind the OC-3R regenerator was evaluated for different power levels of the ideal clock signal (100 fs RMS-jitter). The data signal was intentionally degraded before injecting into the regenerator. The amplitude fluctuations of 3 dB (Fig. 5.6a) lead to an RMS-jitter of 1680 fs; the data extinction ratio was reduced down to 10 dB (Fig. 5.8a). The data average power level in front of the 4 mm UL-SOA (200 mA/mm) was set to 0 dBm. Figure 5.10 summarises the results. The importance of the clock power level is clearly visible. Increasing the clock average power from +3 dBm to +10 dBm causes an improvement of the output data RMS-jitter from 800 fs down to 400 fs. As discussed in section 4.3.1, the clock power determines directly the FWHM of the gain window generated in the long amplifier. A clock average power level of +3 dBm results in gain window width of 12 ps, the FWHM of the window reduces down to 6 ps for P_{clock} = +13 dBm (see Fig. 4.16), leading to even more effective carving of the degraded data signal.

The extinction ratio of the data signal at the OC-3R output can be also influenced by the power of the clock (filled triangles in Fig. 5.10). The more is the UL-SOA saturated by the clock, the higher data ER can be obtained. When the clock signal is not strong enough (e.g. P_{clock} = +3 dBm), the reduced data ER degrades at the OC-3R output from 10 dB down to 4.8 dB. The original extinction ratio can be preserved behind the long amplifier only for dominant clock power levels (more than +10 dBm in this case).

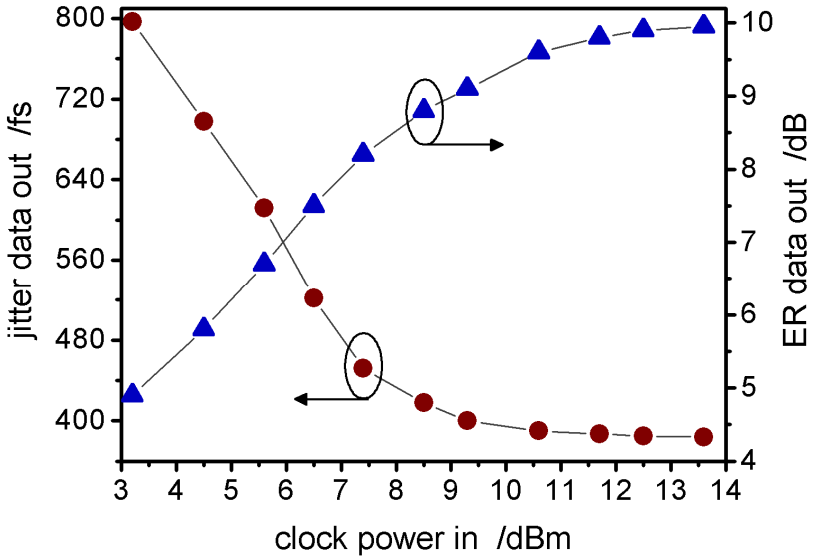

Fig. 5.10: RMS-jitter and extinction ratio of the degraded 40 Gbit/s PRBS data signal (1680 fs RMS-jitter, 10 dB ER) behind the OC-3R regenerator as a function of the clock average power level at the 4 mm UL-SOA input. (P_{data} = 0 dBm, λ_{data} = 1550 nm, λ_{clock} = 1560 nm).

It was demonstrated that the dominant clock signal is a prerequisite for regenerative performance of the OC-3R scheme. It should be noted that the absolute values of the clock power depend on the degree of data degradation, which the regenerator has to compensate for. Thus the regeneration efficiency of the OC-3R can be controlled directly by the clock power. In the following, the further influence of the clock on the data quality improvement is numerically analysed. The results are compared to the typical parameters of the self-pulsating PhaseCOMB all-optical clock. The simulations were performed for a 4 mm ultra-long SOA, the average power levels of the 40 Gbit/s PRBS signal (1550 nm) and 40 GHz clock signal (1560 nm) were set to 0 dBm and +10 dBm, respectively.

5.2.2.1. Relative data-clock delay

In order to show the importance of the relative time position between the data and clock pulses in the OC-3R scheme, the performance of the regenerator was investigated for two extreme cases. First, the degraded data signal and the ideal clock signal were launched simultaneously into the UL-SOA (Fig. 5.11a). The data pulses and the clock pulses propagate through the amplifier in the same time slots, which is equivalent to a holding beam configuration. Although the gain is strongly saturated by both signals, the carrier density in the long amplifier follows the amplitude fluctuations of the distorted PRBS signal. Thus, no signal regeneration can be observed behind the OC-3R. The unwanted dynamics of carrier density are effectively eliminated, when the data and clock pulses are interleaved to each other (Fig. 5.11b). The periodical gain modulation due to the dominant clock signal shapes the data pulses, which propagate within the gain window, resulting in a reduction of timing jitter and amplitude fluctuations at the regenerator output. Furthermore, because of the fast recovery time constants in the UL-SOA, the gain is compressed between two data pulses only. Thus, the data signal experiences at the regenerator output around 3 dB higher gain compared to the previous configuration.

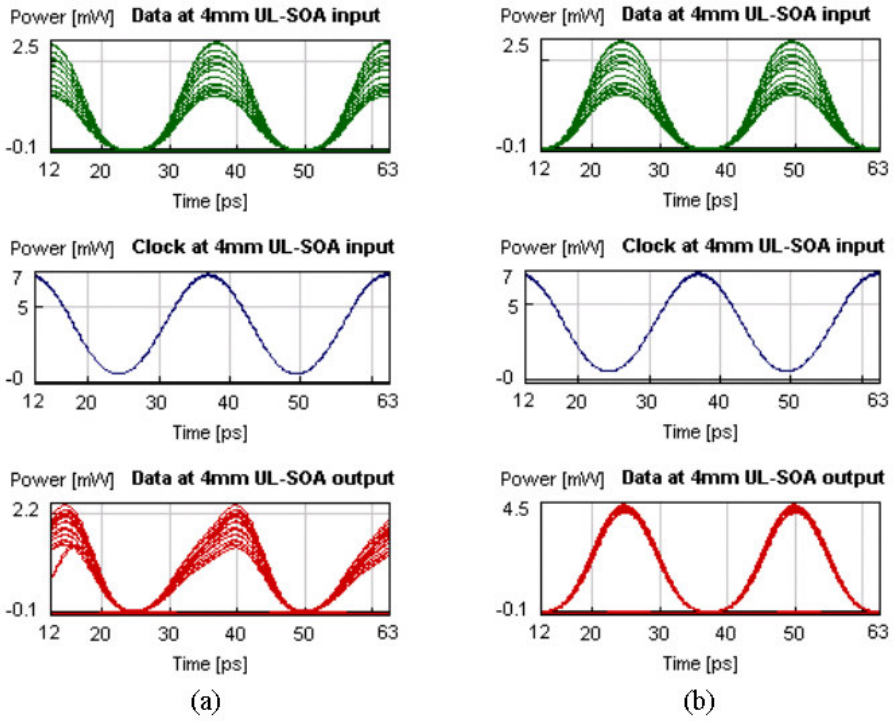

Fig. 5.11: Impact of the relative time position between the data and clock pulses on the regenerative performance of the OC-3R scheme. The degraded 40 Gbit/s PRBS signal and ideal 40 GHz clock propagate the 4 mm UL-SOA in the same time slots (a) and interleaved by 12.5 ps to each other (b).

5.2.2.2. Extinction ratio of the clock signal

In the following simulation, the impact of the clock ER on regenerative performance of the OC-3R architecture is analysed. The strongly degraded PRBS signal with an RMS-jitter of 1680 fs (Fig. 5.6a) and the sinusoidal clock signal (100 fs RMS-jitter) were injected interleaved by 12.5 ps into the 4 mm UL-SOA. Figure 5.12b summarises the dependence between the clock ER and the output data RMS-jitter. It can be seen that the regenerative function of the OC-3R scheme is less effective (higher jitter at the regenerator output) when decreasing the ER of the clock signal. In case of the reduced clock ER, the amplitude fluctuations are only partially suppressed; the re-shaping function due to fast XGM effects in the long amplifier cannot be fully exploited. An extinction ratio of 0 dB corresponds to the configuration, when a CW holding beam is used for stabilisation of the UL-SOA gain dynamics. As discussed in section 4.1.3, the UL-SOA shows nearly linear behaviour when applying a CW holding beam. Thus, the data signal is only linearly attenuated in this case, without any quality improvement at the regenerator output. Figure 5.12a depicts the eye diagram of the regenerated data signal for the clock with an ER of 3 dB. The typical extinction ratio of the clock signal generated by the PhaseCOMB-laser is higher than 6 dB. This is a sufficient value for an efficient quality improvement of the degraded PRBS signals.

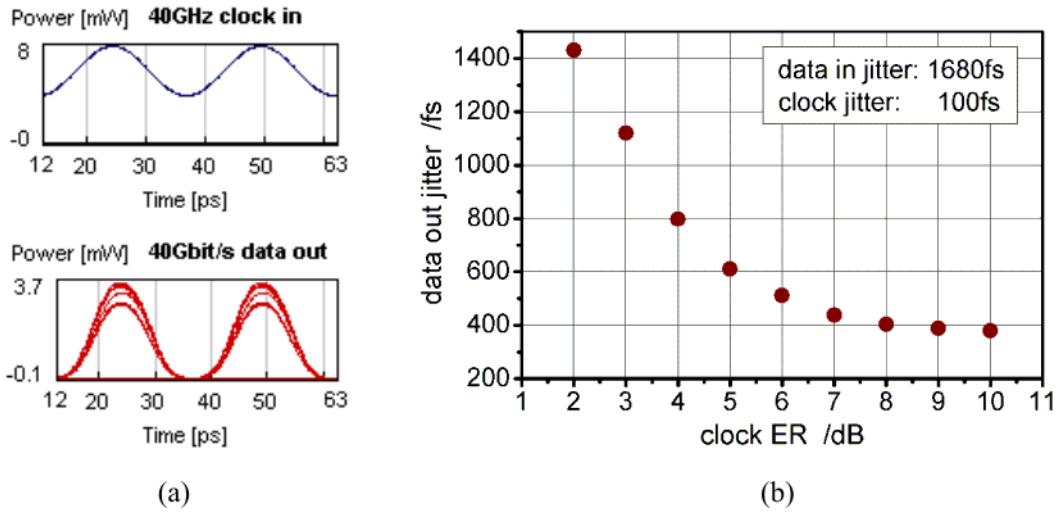

Fig. 5.12: Eye diagrams of the 40 GHz clock signal (ER = 3 dB) and the corresponding 40 Gbit/s PRBS signal at the OC-3R output (a) and the calculated data RMS-jitter behind the regenerator as a function of the clock extinction ratio (b). (P_{data} = 0 dBm, λ_{data} = 1550 nm, P_{clock} = +10 dBm, λ_{clock} = 1560 nm).

5.2.2.3. Clock timing stability

In the simulations discussed previously, the regenerative function of the OC-3R architecture was simulated for an ideal clock signal with a nearly negligible timing jitter. In a realistic scenario, however, the optical clock signal is characterised by a finite timing stability. In the following analysis, the 40 GHz clock signal was continuously distorted by timing fluctuations before injecting into the 4 mm ultra-long SOA and the corresponding RMS-jitter of the output data signal was extracted. Also here, the 40 Gbit/s PRBS RZ input signal was strongly degraded by amplitude fluctuations (Fig. 5.6a), leading to a timing jitter of 1680 fs. The results are summarised in Fig. 5.13. Figure 5.13a shows the degraded clock signal with an RMS-jitter of 820 fs (upper trace) and the corresponding data signal at the regenerator output with a RMS-jitter of around 600 fs (lower trace). The signal quality behind the regenerator for other jitter values of the clock is shown in Fig. 5.13b. The regenerative function of the OC-3R scheme is based on periodical modulation of the UL-SOA gain, without any wavelength conversion to the clock signal. Thus, the clock RMS-jitter defines the timing stability of the PRBS signal indirectly by the width of the generated gain window. For a low clock jitter (below 400 fs), the data improvement is limited by ASE of the amplifier. In case of highly jittered clock (more than 1000 fs) the degrading influence of the instable gain window can be observed. The RMS-jitter of the synchronised self-pulsating PhaseCOMB-laser is typically between 400 fs and 650 fs. Hence, an effective regenerative performance of the OC-3R architecture can be expected.

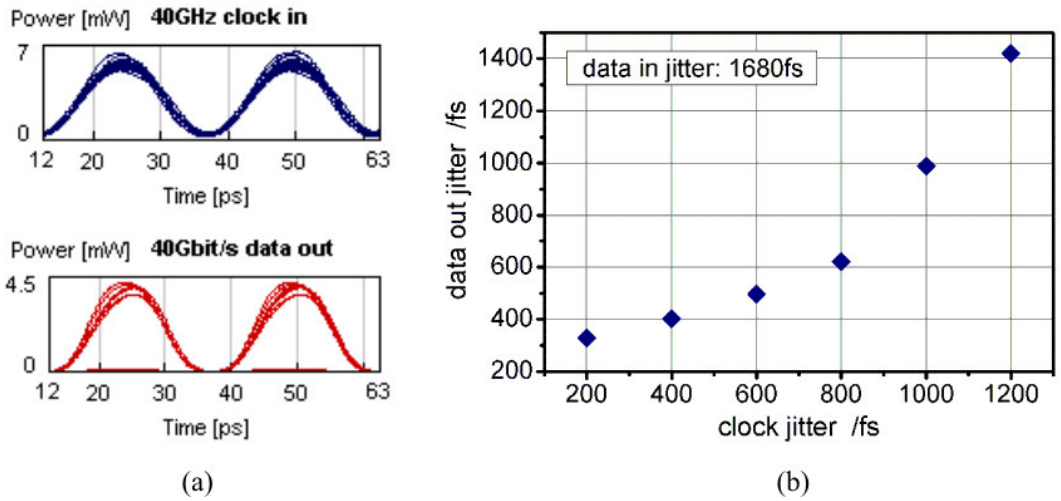

Fig. 5.13: 40 Gbit/s PRBS signal at the OC-3R output for degraded input data signal (1680 fs RMS-jitter) and 40 GHz clock signal (820 fs RMS-jitter) (a), the RMS-jitter of the data signal behind the regenerator for different timing stabilities of the clock signal (b).

5.2.2.4. FWHM of the clock pulses

As discussed in Chapter 2, there are several possibilities for generation of an optical clock signal. Depending on the applied recovery technique (e.g. TMLL, PhaseCOMB, AFL), the clock pulses can be characterised by different FWHM. The impact of width of the control pulses on re-timing of periodical 40 GHz signals in the long amplifier was discussed in section 4.3.2. Here, the influence of the clock pulse width on the regenerative functionality of the OC-3R scheme operated in degraded 40 Gbit/s PRBS data streams is studied. Three different configurations were simulated (Fig. 5.14). First, the data signal was propagated through the UL-SOA together with short clock pulses of 6.5 ps FWHM (Fig. 5.14a). Although the amplitude fluctuations of the degraded data signal are partially suppressed behind the regenerator, the eye diagram indicates some additional distortions at the zero level of the output PRBS signal. Because of the relatively long gap between the data and clock pulses and fast recovery processes in the ultra-long SOA, the gain is not saturated enough in case of a bit sequence of consecutives spaces. This leads to power fluctuations at the space level. Figure 5.14b shows the configuration, when applying a sinusoidal clock signal (12.5 ps FWHM at 40 GHz) in the OC-3R scheme. The improvement in signal quality compared to the previous case is clearly visible. The last simulation (Fig. 5.14c) demonstrates the performance of the OC-3R architecture for a clock pulses broadened up to 18.5 ps. The UL-SOA gain is saturated for a time period longer than the gap between the two RZ pulses, resulting in a suppression of amplitude fluctuations. Even for the short time interval between the clock pulses, the fast carrier density modulation additionally leads to an effective carving of the data pulses. Hence, similar results to the previous case were obtained. The simulations show that short clock pulses (large gain window in the UL-SOA) are less suitable for signal quality improvement in the OC-3R scheme. The sinusoidal waveform of the self-pulsating PhaseCOMB-lasers can be effectively exploited in the OC-3R regenerator.

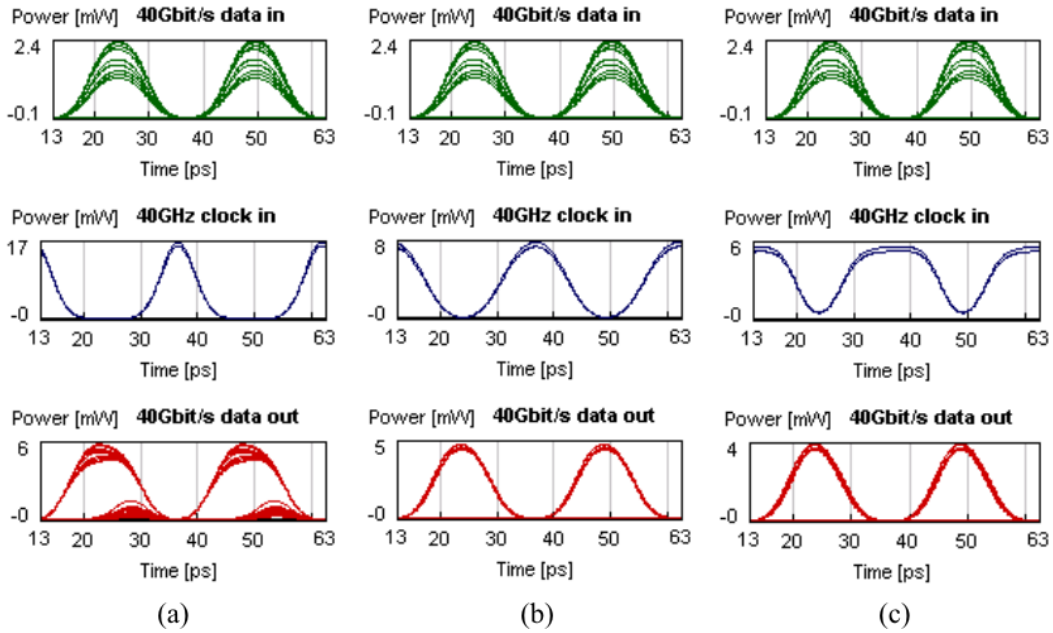

Fig. 5.14: Regenerative performance of the OC-3R scheme for different FWHM of the 40 GHz clock pulses: 6.5 ps (a), 12.5 ps (b) and 18.5 ps (c). (P_{data} = 0 dBm, λ_{data} = 1550 nm, P_{clock} = +10 dBm, λ_{clock} = 1560 nm).

In summary, the design rules of the key components of the OC-3R regenerator were investigated by numerical simulations. First, the influence of the SOA length was analysed. Effective power equalising and jitter reduction of degraded 40 Gbit/s RZ PRBS signals was achieved in amplifiers longer than 4 mm. Furthermore, it has been shown that the periodical clock signal defines the regenerative efficiency of the OC-3R scheme. The power level as well as the pulse form of the clock controls the saturation effects and gain window in the long amplifier. The dominant clock (P_{clock} > 10 dBm) results in effective pulse carving and improved extinction ratio (up to ER of the data in) of the degraded data signals. Based on the simulations, an ER of more than 6 dB, RMS-jitter below 650 fs and sinusoidal shape of the clock signal guarantee a regenerative signal processing of distorted PRBS data streams. The results show suitability of the self-pulsating PhaseCOMB-lasers as well as of the 4 mm UL-SOAs for their implementation in the all-optical OC-3R regenerator.

5.3 Experimental analysis of the OC-3R regenerative performance

Based on the modelling results discussed in the previous section, the OC-3R regenerator was assembled and experimentally investigated. The key devices are the 4 mm UL-SOA and the self-pulsating PhaseCOMB-clock. The performance of the OC-3R scheme was studied by operation in degraded 40 Gbit/s RZ data streams. Figure 5.15 sketches the experimental set-up (for the complete scheme see Appendix E1). The 40 Gbit/s RZ PRBS

2^{31}-1 data signal (50 % duty cycle) was generated using a tuneable external cavity laser (ECL) followed by two modulators for encoding of the clock and data information. Hence, the emission wavelength of the data signal can be flexibly tuned in the whole C-band. In order to investigate the regenerative potential of the OC-3R scheme, the quality of the data signal was intentionally distorted in a degradation unit before injecting into the regenerator. The degradation stage (shown in Appendix E3) provides controlled inducing of timing jitter and amplitude fluctuations to the high quality PRBS signal as well as noise loading, which results in degradation of the OSNR. The signal analysis was performed using an electrical sampling oscilloscope (eye diagrams), optical spectrum analyser (wavelength and power analysis) and finally by bit error ratio measurements.

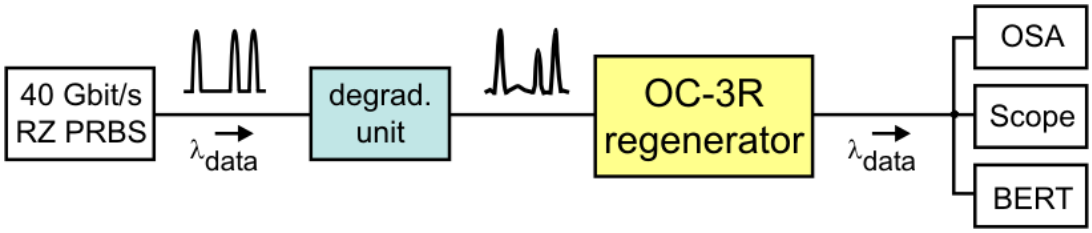

Fig. 5.15: Principle scheme for experimental performance investigation of the OC-3R architecture operated in degraded 40 Gbit/s PRBS 2^{31}-1RZ data streams.

The eye diagram of the intentionally distorted 40 Gbit/s PRBS signal (1550 nm) behind the degradation unit is depicted in Fig. 5.16a. Strong patterning effects result in RMS-jitter of more than 1300 fs. The average power level of the data signal before injecting into the optical regenerator was set to +2 dBm. The RMS-jitter of the 40 GHz sinusoidal clock signal (1560 nm, average power level of +8 dBm) used for generation of the gain window in the semiconductor amplifier was 490 fs. In order to experimentally verify the importance of the SOA length on the OC-3R regenerative performance, the measurement was performed for a 0.5 mm SOA and a 4 mm UL-SOA, respectively. Both amplifiers were driven by a bias current of 200 mA/mm. The eye diagrams of the corresponding data signals behind the regenerator are depicted in Fig. 5.16b,c. It has been already shown by numerical simulations that the interaction length between the data and clock pulses propagated through the amplifier determines directly the degree of signal regeneration. This behaviour is obvious also in the experiment. The amplitude fluctuations are only partially suppressed and the timing jitter remains higher than 1000 fs, when the OC-3R comprises the 0.5 mm SOA (Fig. 5.16b). However, a significant signal quality improvement in case of the 4 mm ultra-long SOA (Fig. 5.16c) was achieved. The RMS-jitter of the data signal is reduced from 1330 fs down to 680 fs. Furthermore, effective elimination of the patterning effects leads to an eye opening enhancement behind the regenerator. Thus, the experimental results on the OC-3R performance confirm the numerical simulations.

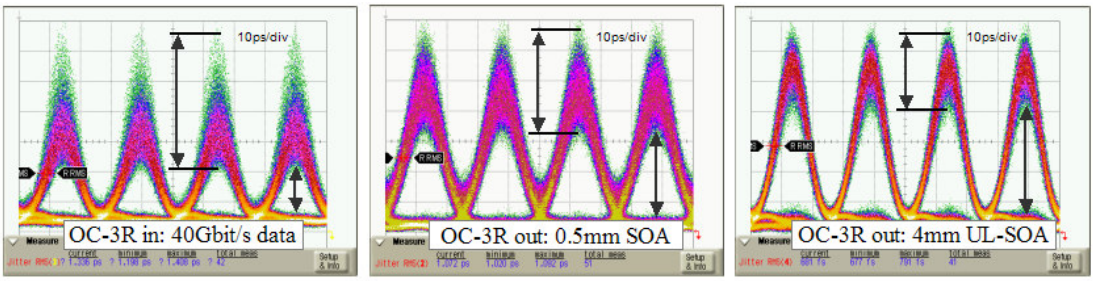

Fig. 5.16: Eye diagram of the strongly degraded 40 Gbit/s PRBS 2^{31}-1 RZ signal (a) and the measured eye diagrams behind the OC-3R regenerator comprising a 40 GHz PhaseCOMB all-optical clock and a 0.5 mm SOA (b) and a 4 mm UL-SOA (c). P_{data} = +2 dBm, λ_{data} = 1550 nm, P_{clock} = +8 dBm, λ_{clock} = 1560 nm, I_{SOA} = 200 mA/mm.

5.3.1 Equalising of amplitude fluctuations

Slow power fluctuations of the transmitted data flows can be expected in the optical networks. Therefore, the equalising effect of the OC-3R regenerator was investigated in more detail. In order to identify the impact of the gain spectrum of the 4 mm UL-SOA (shown in Fig. 5.3), the analysis was performed for different wavelength combinations between the data and clock signal. The data wavelength was set to 1540 nm, 1550 nm, and 1558 nm respectively, while the wavelength of the sinusoidal clock was kept fixed at 1560 nm. In the second configuration, the data-clock wavelengths were 1560 nm-1550 nm. Throughout the whole measurement, the average power level of the clock signal remained constant and was set to +8 dBm. The power of the input RZ PRBS signal (measured using an optical spectrum analyser with a 1 nm resolution bandwidth) was continuously increased and the corresponding power level of the output data signal was evaluated. Figure 5.17 summarises the results. Comparing the shadow areas at the x-axis (input power variation) and the y-axis (output power variations), the equalising effect of the OC-3R is clearly visible. When the data and clock are located close to the gain peak of the 4 mm UL-SOA (Fig. 5.17a, b), the increase of the data power at the regenerator input from –2 dBm to +2 dBm causes only a marginal amplitude changes (1.1 dB (a) and 0.6 dB (b)) behind the OC-3R. The equalising behaviour is less effective for the short wavelength data signal (1540 nm). This is due to the smaller gain saturation at the shorter wavelengths. However, optimising the fibre-chip losses and shifting the gain maximum of the UL-SOA to 1550 nm, even higher equalising efficiency in a wider wavelength range can be expected.

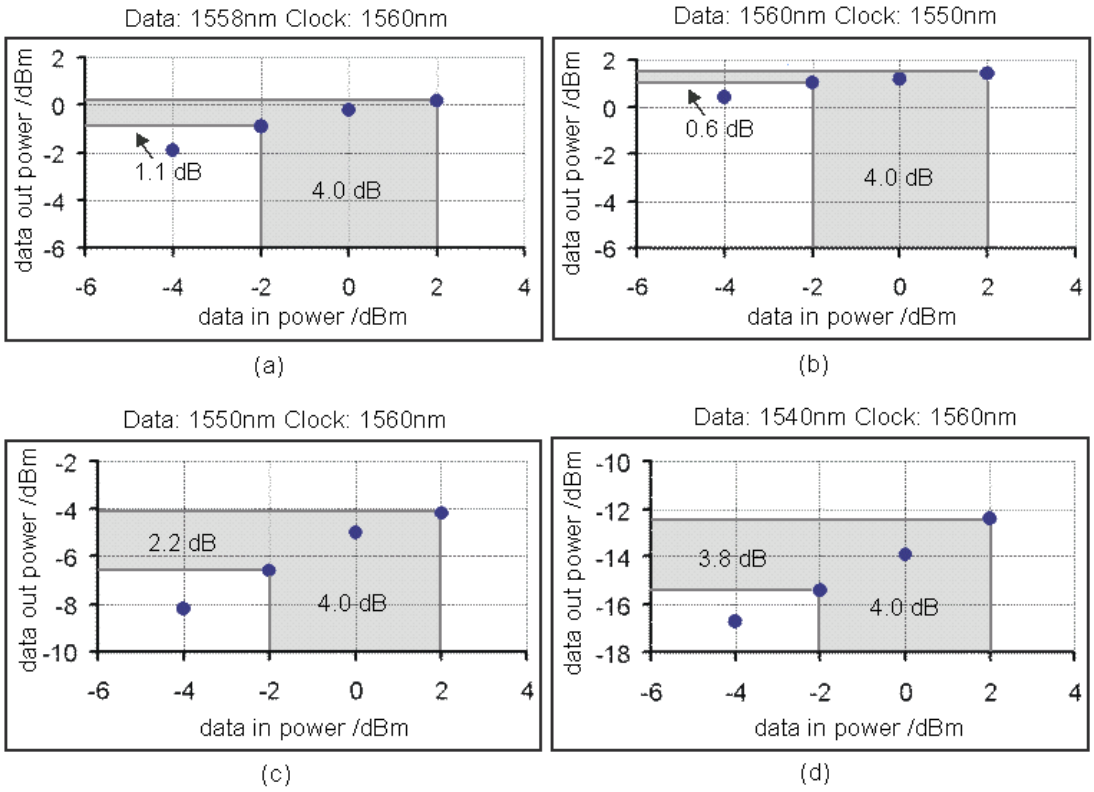

Fig. 5.17: Power equalising in the OC-3R regenerator comprising the 4 mm UL-SOA (200 mA/mm bias current, see Fig. 5.3 for the ASE spectrum) for different data-clock wavelength combinations. The average clock power was fixed at P_{clock} = +8 dBm.

In the previous analysis it was demonstrated that the OC-3R regenerator effectively equalises slow power fluctuations. Another type of distortions in high-speed transmission systems are related to bit-to-bit amplitude variations originated mainly from non-linear characteristics of fibres and semiconductor devices. Hence, equalising of fast amplitude fluctuations in the optical regenerator was also investigated. The 40 Gbit/s PRBS 2^{31}-1 RZ signal was additionally degraded by strong patterning effects (bit-to-bit amplitude fluctuations) and launched together with the 40 GHz clock signal into the 4 mm UL-SOA. The average power levels of the data and clock signals were set to +2 dBm and +8 dBm, respectively. In Fig. 5.18, the pattern of the distorted data signal at the regenerator input (upper traces) and the PRBS sequence behind the OC-3R (lower traces) are shown for two data-clock wavelength configurations: 1550 nm – 1560 nm and 1560 nm – 1550 nm. Due to the high gain saturation and short recovery constants of the ultra-long amplifier, the bit-to-bit amplitude fluctuations are effectively suppressed from 2.5 dB to only 0.5 dB at the regenerator output in case of both wavelength combinations.

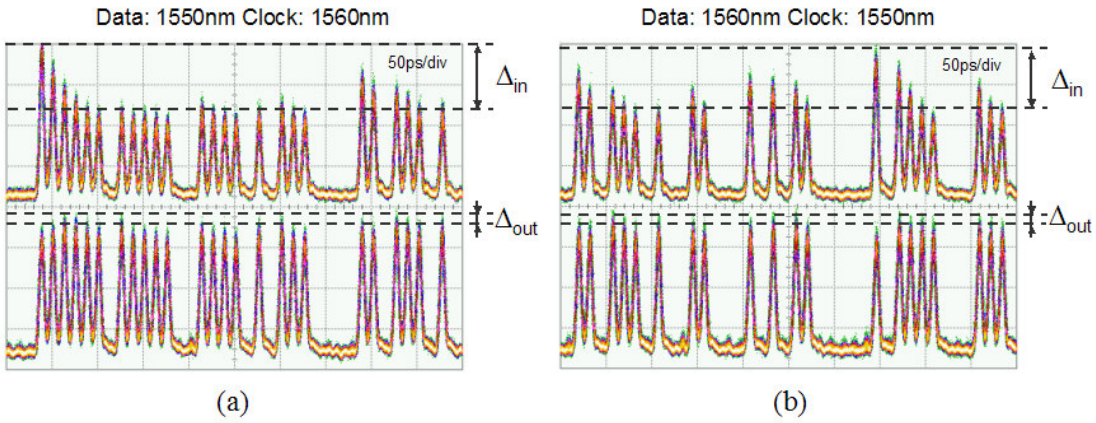

Fig. 5.18: Effective suppression of bit-to-bit amplitude fluctuations in the OC-3R regenerator for two data-clock wavelength combinations (1550 nm – 1560 nm, 1560 nm – 1550 nm). Upper traces: PRBS 2^{31}-1 RZ signal distorted by patterning effects (Δ_{in} =2.5 dB), lower traces: bit pattern of the data signal behind the optical regenerator (Δ_{out} =0.5 dB). P_{data} = +2 dBm, P_{clock} = +8 dBm.

5.3.2 Re-timing function of the OC-3R architecture

Preserving of the timing stability of the optical signals is a key issue in high-speed transmission systems. Thus, regenerative function in the time domain is an important task for a 3R regenerator. In the following, the jitter reduction function of the optically clocked 3R scheme was evaluated by the histogram function of the electrical sampling oscilloscope in more detail. The RMS-jitter of the input 40 Gbit/s PRBS 2^{31}-1 RZ signal was extracted for different degradation degrees (induced in the degradation unit by amplitude fluctuations) and the corresponding timing jitter of the data signal behind the OC-3R was measured. The average power level of the clock signal (400 fs RMS-jitter) was set to +8 dBm. The clock wavelength was kept constant at 1560 nm, while the data wavelength was set to: 1558 nm, 1550 nm, and 1540 nm, respectively. For a clock wavelength of 1550 nm, the data signal was located to 1560 nm. The resulting jitter transfer characteristics are summarised in Fig. 5.19. It can be seen that the jitter remains clearly reduced behind the regenerator for all wavelength combinations in the whole measured range when comparing to the input data jitter. Increasing the data RMS-jitter from 400 fs up to 800 fs leads to a small jitter increase (below 50 fs) at the OC-3R output. The gain window induced in the 4 mm UL-SOA by the dominant clock signal causes effective carving of the jittered data pulses. For stronger data degradations, the output jitter increases too, however a significant jitter improvement (e.g. from 1200 fs to around 600 fs) in case of all investigated correlations was achieved.

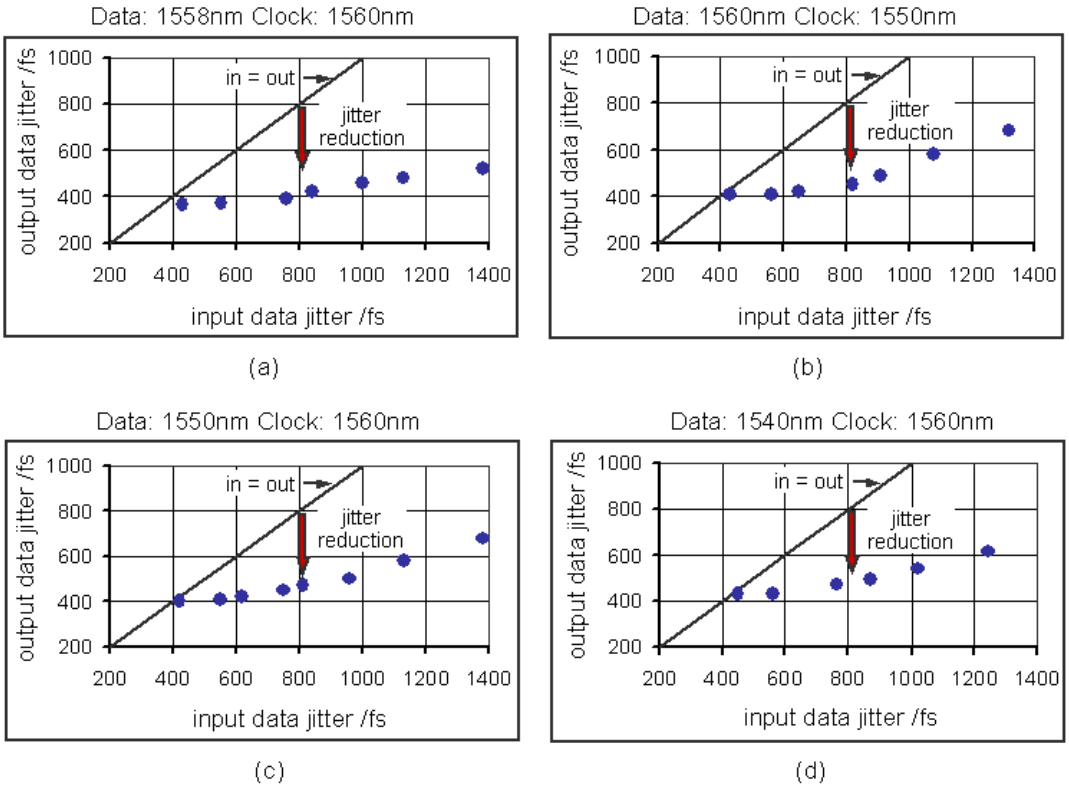

Fig. 5.19: Jitter reduction function of the OC-3R regenerator for different data-clock wavelength correlations. P_{data} = +2 dBm P_{clock} = +8 dBm, I_{SOA} = 200 mA/mm.

5.3.3 BER analysis of the OC-3R regenerative performance

In the previous sections, the regenerative performance of the OC-3R scheme was investigated by eye diagrams. The improvement of timing stability and effective suppression of amplitude fluctuations was demonstrated for different data-clock wavelength combinations. In this chapter, the functionality of the OC-3R regenerator is characterised by bit error ratio (BER) measurements. The schematic of the BER receiver is depicted in Appendix E4. In the following experiments, the wavelength of the degraded 40 Gbit/s PRBS 2^{31}-1 RZ signal was kept constant at 1550 nm, while the clock wavelength was set to 1560 nm and 1540 nm, respectively. The average power levels of the data signal and clock in front of the 4 mm UL-SOA (ASE spectrum shown in Fig. 5.3) was set to 0 dBm and +8 dBm, respectively.

5.3.3.1. BER versus received power

The results on BER as a function of the average power level at the receiver are summarised in Fig. 5.20. The back-to-back curve of the distorted data signal behind the degradation unit (Appendix E3) is shown by filled squares. The BER curves of the PRBS signal behind the OC-3R are depicted by filled dots and triangles, respectively. A negative penalty of 2 dB was achieved (relative to the back-to-back curve) at the OC-3R output for the

1550 nm-1560 nm data-clock combination. In case of the short wavelength clock (1540 nm, filled triangles), the regenerative performance of the OC-3R is less effective. The data quality is nearly preserved at BER of 10^{-9}; a negative penalty of 1 dB was obtained at 10^{-3} BER. In this configuration, the clock wavelength is located 20 nm out of the UL-SOA gain maximum. Hence, the periodical modulation of the carrier density is not strong enough in order to sufficiently shape the degraded data pulses.

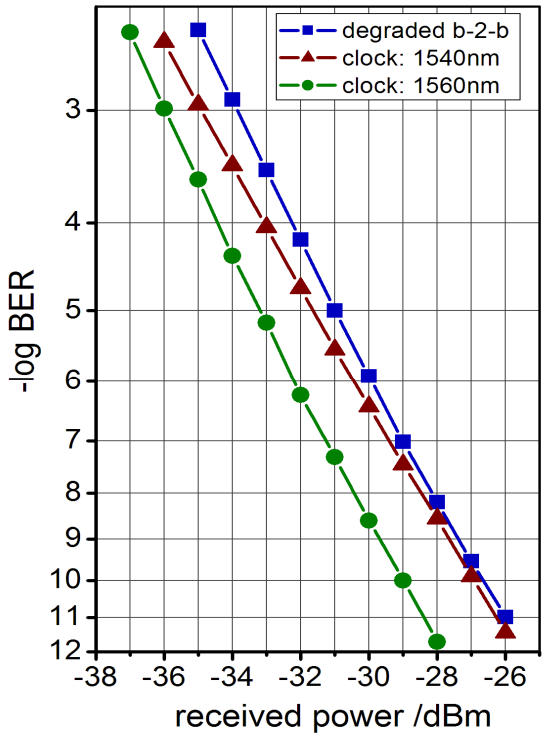

Fig. 5.20: BER measurements of the degraded 40 Gbit/s PRBS 2^{31}-1 RZ signal (filled squares) and the BER curves of the regenerated data signal at the OC-3R output for two data-clock wavelength combinations: 1550 nm – 1560 nm and 1550 nm – 1540 nm. (P_{data} = 0 dBm, P_{clock} = +8 dBm).

5.3.3.2. Dynamic range

In the following experiment, the dynamic range of the OC-3R was evaluated by BER measurements. The average data power was varied from -6 dBm up to +3 dBm, while the average clock power level was kept constant at +8 dBm. The sensitivity (received power at BER of 10^{-9}) was measured at fixed decision threshold level of the BER receiver. Figure 5.21 summarises the results. In case of the 1560 nm clock, the BER sensitivity of -28 dBm remained nearly unchanged when increasing the data power from -2 dBm up to +3 dBm. A 1 dB-penalty was measured for an input power level as low as -4.5 dBm, resulting in a dynamic range of 7.5 dB. This is related to the high gain in the long amplifier and effective pulse carving caused by the gain window. The estimated dynamic range is smaller (around 5 dB for 1 dB penalty) in case of the 1540 nm clock signal. An optimum in

the power level between 0 dBm and +2 dBm can be observed for this configuration. This is because of impact of patterning effect for stronger signals (the gain dynamics in the UL-SOA are determined by the PRBS signal) and, on the other site, due to the data degradation by amplified spontaneous emission for weaker data signals.

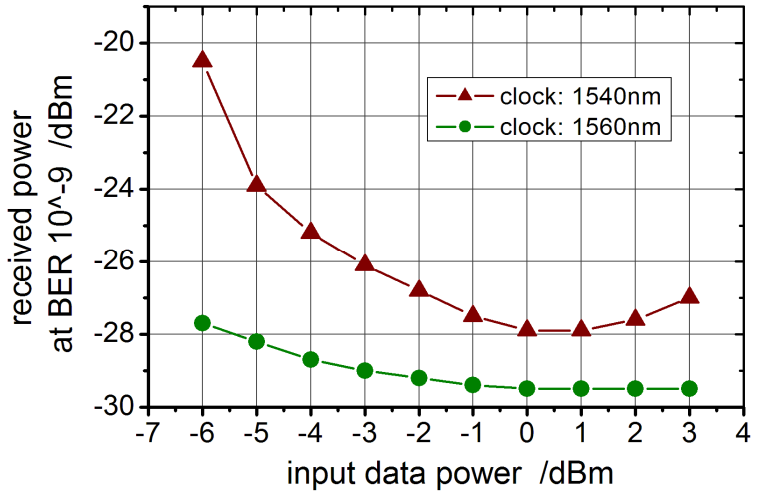

Fig. 5.21: Received power at BER of 10^{-9} as a function of the average data power at the OC-3R input for two data-clock wavelength combinations: 1550 nm – 1560 nm and 1550 nm – 1540 nm. The average clock power level was kept fixed at +8 dBm.

5.3.3.3. Tolerance to the decision timing

The bit error ratio analysis regarding timing stability of the degraded PRBS signal and after propagation through the optically clocked 3R regenerator was performed. The decision marker of the BER receiver was continuously detuned from its optimum time position and the corresponding received power at BER of 10^{-9} was evaluated. The jitter reduction function of the OC-3R scheme is obvious mainly for the data-clock wavelength combination of 1550 nm-1560 nm (Fig. 5.22). The suppression of timing fluctuations behind the regenerator leads to an enhanced detuning range from 4.8 ps up to 6.2 ps (for a 1 dB-power penalty). As expected, the influence of the periodical modulation of SOA gain is less effective, when the clock signal (1540 nm) was located outside the gain peak (1560 nm) of the semiconductor amplifier, resulting in improvement of the detuning range of around 0.2 ps only.

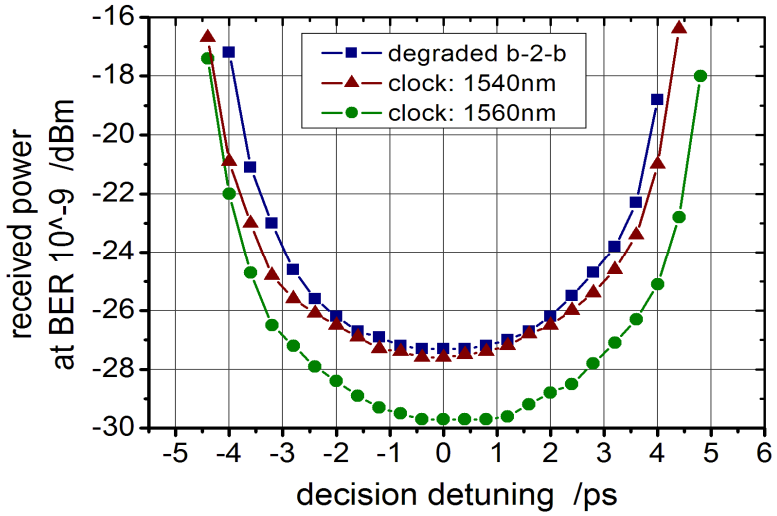

Fig. 5.22: Received power at BER of 10^{-9} as a function of the decision marker detuning in the BER receiver for 1550 nm – 1560 nm and 1550 nm – 1540 nm data-clock wavelength combinations. (P_{data} = 0 dBm, P_{clock} = +8 dBm).

5.3.3.4. Impact of the OSNR on BER

The OC-3R is a wavelength-preserving scheme without signal conversion to a new wavelength. This is an advantageous feature when considering an in-line optical 3R regenerator without need of any wavelength controlling function. However, the XGM effects exploited in the UL-SOA for signal regeneration do not provide any decision function (as discussed in section 5.2.1), in order to suppress the accumulated noise. In the following, the impact of the OSNR degradation on the performance of the OC-3R scheme was evaluated. The degraded 40 Gbit/s PRBS 2^{31}-1 RZ signal was strongly attenuated (down to -35 dBm) and amplified to a constant average power level of 0 dBm before injecting into the regenerator. The noise loading (OSNR reduction) can be controlled by varying the data attenuation. The data signal OSNR was evaluated using an optical spectrum analyser.

The received power level at the BER of 10^{-9} was measured as a function of the data OSNR. The results for the 1550 nm – 1560 nm data – clock wavelength combination are summarised by filled dots in Fig. 5.23. The data signal at the OC-3R output follows nearly linearly the penalty of the input data signal down to an OSNR of 27 dB/0.1nm. In this range the regenerative ability of the OC-3R scheme remains unchanged. However, there is a relatively fast penalty increase for OSNR below 26 dB/0.1nm. The regenerative performance is more critical in case of the second wavelength configuration (1550 nm data, 1540 nm clock, filled triangles in Fig. 5.23). Here, the spontaneous emission is even more amplified, resulting in noise addition to the degraded data signal.

Thus, the OC-3R regenerator can effectively improve the quality of the data signals degraded by amplitude and timing jitter, when the input data OSNR remains higher than 27 dB/0.1nm. The ASE at the UL-SOA output can be filtered out by a narrowband optical band pass filter. However, an additional compensation stage for noise suppression (e.g. a saturable absorber) would be preferable, in order to guarantee a better robustness of the OC-3R architecture.

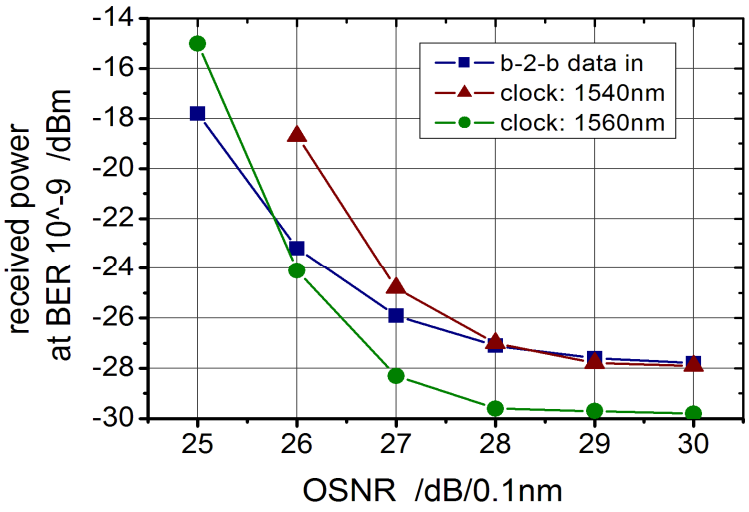

Fig. 5.23: Impact of the data OSNR on regenerative functionality of the OC-3R scheme for two data-clock wavelength combination: 1550 nm – 1560 nm and 1550 nm – 1540 nm. (P_{data} = 0 dBm, P_{clock} = +8 dBm).

5.3.4 Optically clocked saturable absorber

The reduced OSNR leads to signal degradation in the time and amplitude domain as well as to distortions in the zero power level. It has been shown that the OC-3R is well suited for effective suppression of amplitude fluctuations and timing jitter, which are critical distortions in high-speed (40 Gbit/s and beyond) DWDM systems. An OSNR improvement in a pass-through regeneration scheme using a saturable absorber (SA) has been already reported [68]. The SA is characterised by a very low transmission for small data power levels, which is followed by nonlinear increase of the transmission when exceeding a threshold power value (transparency regime). The potential of an absorber for noise suppression at the space level was simulated. In the modelling, the 40 Gbit/s PRBS RZ signal, intentionally degraded in the zero amplitude (Fig. 5.24a), was directly injected into an 80 µm long saturable absorber. The eye diagram of the signal at the absorber output is shown in Fig. 5.24b. It is obvious that the zero distortions are effectively suppressed. However, strong patterning effects, due to pattern dependent absorption modulation, additionally degrade the data signal.

The key idea for avoiding the pattern degradations is to apply the same technique as in case of the UL-SOA, the optically clocked scheme [175]. Figure 5.24c shows the data signal behind the SA when propagating bit interleaved with the periodical clock signal. The zero distortions are effectively suppressed without affecting the timing and amplitude stability of the original signal. Hence, the optically clocked principle can be used for stabilisation of gain dynamics in ultra-long SOAs as well as absorption dynamics in SAs. The experimental proof of the concept was not possible because of the lack on a saturable absorber with sufficiently fast absorption recovery characteristic.

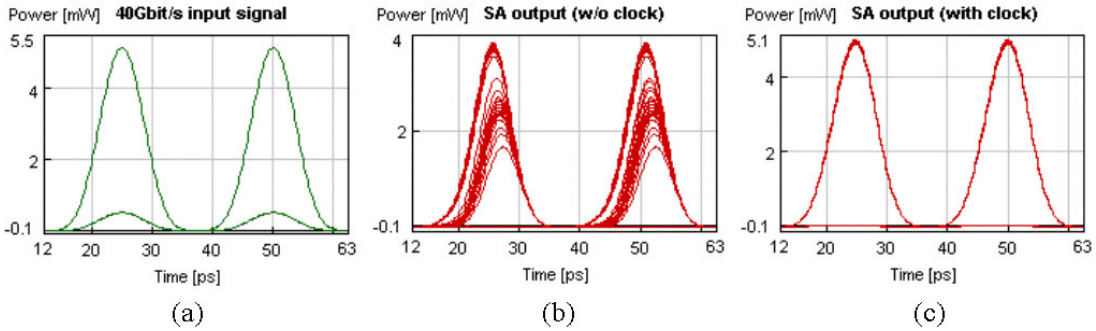

Fig. 5.24: Simulated 40 Gbit/s PRBS RZ signal intentionally distorted in the zero power level (a), eye diagrams of the data signal behind a 80 µm saturable absorber (b) and after stabilisation of the absorption dynamics by a periodical 40 GHz clock signal (c).

In summary, experimental analysis on the regenerative performance of the OC-3R architecture proves the modelling results performed in the previous sections. The quality of the strongly degraded 40 Gbit/s PRBS RZ signals can be effectively improved behind the regenerator when enhancing the SOA length from 0.5 mm to 4 mm. Due to the gain saturation and fast XGM effects in the UL-SOA, slow power variations (up to 4 dB) as well as bit-to-bit amplitude fluctuations (up to 2 dB) were effectively equalised behind the OC-3R scheme for different wavelength combinations between the data and clock signal. Suppression of timing fluctuations from 1200 fs down to around 600 fs was obtained, showing an effective jitter reduction function of the proposed regenerator. The efficiency in the compensation of signal distortions correlates directly with the gain spectrum of the applied ultra-long SOA. Generally, a dominant clock is needed with a wavelength located close to the gain maximum of the amplifier. The regenerative functionality of the OC-3R was verified by BER measurements. A 2 dB negative penalty, 7 dB dynamic range and 1.4 ps enhancement of the timing window was demonstrated. The first simulation results show that the signal distortions at the zero power level due to reduced OSNR can be compensated in an optically clocked saturable absorber.

5.4 System applications of the OC-3R scheme at 40 Gbit/s

In the previous sections the regenerative performance of the OC-3R architecture was analysed in detail. The optical regenerator was investigated in order to identify the best configuration (device characteristics) and operation conditions (power levels, data-clock wavelengths). In this section, the performance of the accordingly optimised OC-3R regenerator is experimentally evaluated for processing of 40 Gbit/s PRBS RZ data streams degraded by residual chromatic and polarisation mode dispersion. Furthermore, the ability of the proposed scheme for operation in 40 Gbit/s packet data streams is discussed. The regenerator comprises a PhaseCOMB-laser (λ_{clock} = 1560 nm) for all-optical clock recovery and a 4 mm ultra-long SOA (ASE spectrum shown in Fig. 5.3).

5.4.1 OC-3R for dispersion compensation

Chromatic dispersion (CD) as well as polarisation mode dispersion (PMD) is degrading the performance of ultra long haul 40 Gbit/s transmission links and can result in severe system outages [139]. Several individual compensation techniques have been applied to overcome these impairments [140]. Especially the temporal and statistical drift of PMD characteristics is a serious obstacle distorting the quality of transmitted optical signals. 3R regenerators have been considered to be an attractive approach for mitigation of the PMD since the costs for developing and installing of additional PMD compensators can be avoided in this case [141]. Hence, the performance of the OC-3R all-optical regenerator for mitigation of PMD and CD degradations at 40 Gbit/s was explicitly analysed.

The experimental set-up is sketched in Fig. 5.25. First, the 40 Gbit/s PRBS 2^{31}-1 RZ data signal (1552 nm) was injected into a dispersion emulator. The PMD emulator comprises a polarisation controller and a polarisation maintaining fibre (Newport, F-SPPC-15) with average differential group delay (DGD) of 10.2 ps (corresponding to 40 % bit deviation from the pulse width at 40 Gbit/s). The splitting ratio of the data power level between the fast and slow polarisation axis of the fibre can be continuously tuned by rotating the quarter wave and half wave plate of the polarisation controller. In case of the CD emulator, a 2 km long SMF-fibre with accumulated CD of 35 ps/nm was applied, in order to simulate non-perfect slope compensation. The dispersion distorted PRBS signals were launched into the OC-3R. The input/output signal quality was analysed and compared using a wide-bandwidth electrical sampling oscilloscope with precision time base reference module and by BER tester.

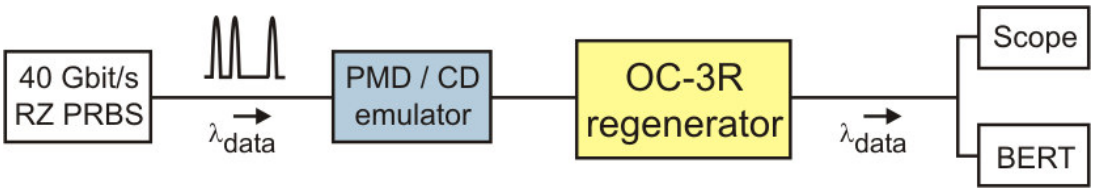

Fig. 5.25: Experimental set-up for performance analysis of the OC-3R regenerator operated in 40 Gbit/s PRBS data streams intentionally distorted by PMD and CD dispersion, respectively (λ_{data} = 1552 nm, λ_{clock} = 1560 nm).

5.4.1.1. PMD and CD compensation: eye analysis

Figure 5.26a depicts the eye diagram of the data signal behind the PMD emulator (10.2 ps DGD). The pulses are broadened from 12 ps to around 21 ps (930 fs RMS-jitter). The quality of the data signal behind the OC-3R regenerator is clearly improved, as it is obvious from the eye diagram shown in Fig. 5.26b. In the 4 mm UL-SOA, the data pulses are effectively reshaped by the sinusoidal clock signal of the synchronised PhaseCOMB all-optical clock (1560 nm, 520 fs RMS-jitter) to an RZ signal of 50% duty cycle (FWHM of 12.5 ps). Furthermore, the amplitude fluctuations are suppressed and the RMS-jitter of the regenerated signal is reduced down to 550 fs.

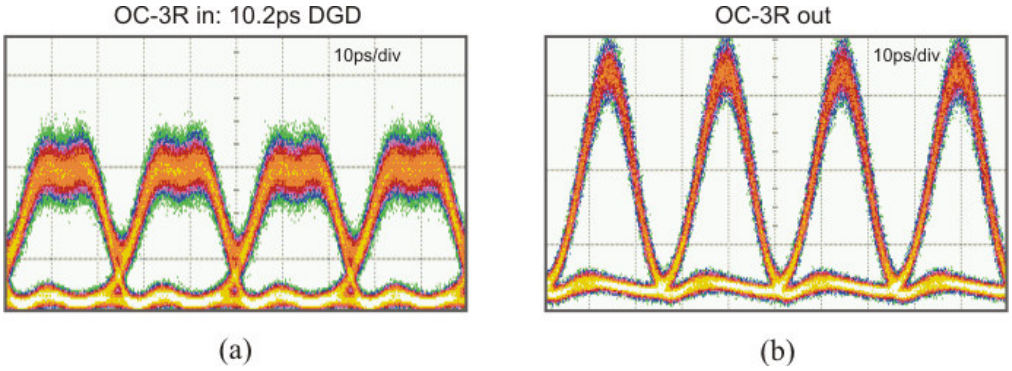

Fig. 5.26: Eye diagrams of the PMD distorted (10.2 ps DGD, 930 fs RMS-Jitter) 40 Gbit/s PRBS 2^{31}-1 RZ signal at the OC-3R input (a) and behind the optical regenerator (550 fs RMS-Jitter) (b). λ_{data} = 1552 nm, λ_{clock} = 1560 nm.

In the following, the adaptive compensation of PMD distorted signals was analysed in more detail. The eye diagrams of the 40 Gbit/s input data signal for different splitting ratios between the fast and slow axis of the data pulses (generated by rotating the signal polarisation in front of the PMD emulator) are depicted in Fig. 5.27 (upper traces). Figure 5.27 (middle traces) shows the corresponding eye diagrams of the PRBS signal at the regenerator output. For all polarisation states, clearly opened eyes were obtained, always stable in amplitude and shape. In order to explain the timing shift of the output signal, the recovered clock signal behind the PhaseCOMB-laser is depicted in the lowest diagrams of Fig. 5.27. Due to the effective carving function in the UL-SOA, the timing position of the regenerated data pulses correlates with the position of the clock pulses. Hence, in the evaluated range, the OC-3R improves the signal quality independently of the input data polarisation state. It should be noted that the PMD was adaptively compensated from 0 ps up to 10.2 ps without any change of the OC-3R operation conditions.

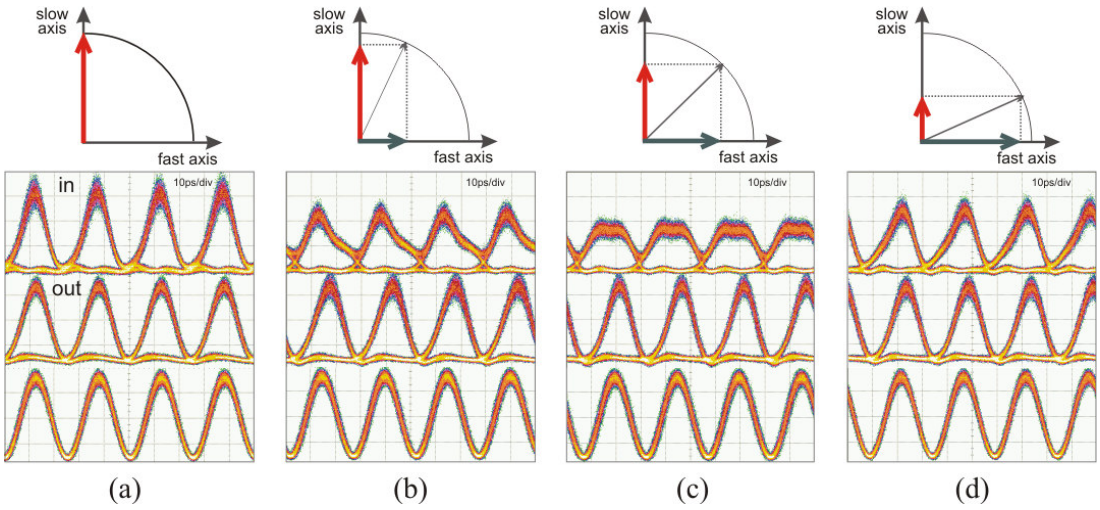

Fig. 5.27: Adaptive PMD compensation (10.2 ps DGD) by the OC-3R regenerator for different power splitting ratios between the fast and slow polarisation axis of the data pulses. Upper traces: 40 Gbit/s PRBS RZ signal at the regenerator input, middle traces: data signal behind the OC-3R, lower traces: clock recovered by the PhaseCOMB-laser.

In the next analysis, the impact of non-ideal compensation of the chromatic dispersion on regenerative performance of the OC-3R scheme is investigated. Figure 5.28 depicts the 40 Gbit/s PRBS signal behind the 2 km SSMF fibre (accumulated dispersion of 35 ps/nm). The eye diagram of the regenerated signal behind the optical regenerator is shown in Fig. 5.28b. Also in this case, the amplitude fluctuations are effectively suppressed and the broadened pulses are reshaped to around 50 % duty cycle.

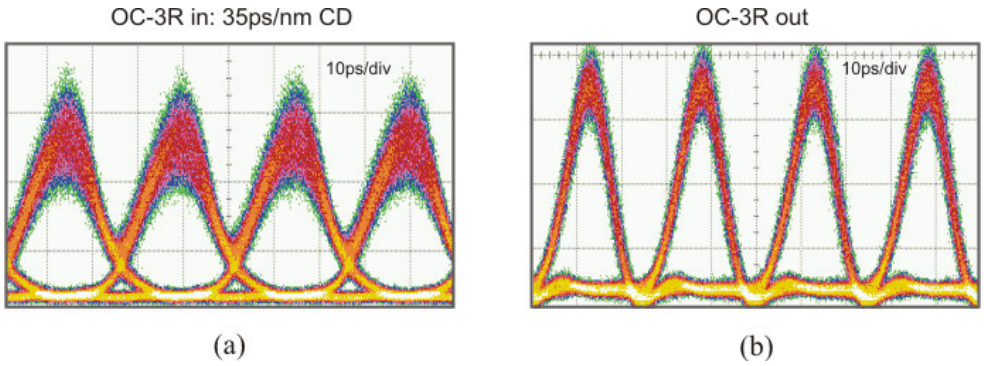

Fig. 5.28: Eye diagrams of the 40 Gbit/s RZ signal after transmission through a 2 km SSMF (35 ps/nm accumulated dispersion) (a) and the regenerated signal behind the OC-3R regenerator (b).

The mitigation of the PMD as well as CD distorted PRBS signals in the proposed OC-3R regenerator is limited by the maximum FWHM of the data pulses. The pulses are shaped in the long amplifier due to the gain window induced by the periodical clock signal. The PhaseCOMB-laser directly synchronises to RZ-like PRBS data streams only. Thus, at 40 Gbit/s, the distorted data pulses should not exceed FWHM of around 22 ps. However, the PhaseCOMB-laser recovers clock information from NRZ data signal, if a pre-processing circuit is additionally used (see Ref. 25 in Appendix G). In this case, even more broadened data pulses due to fibre dispersion can be compensated in the all-optical regenerator.

5.4.1.2. PMD and CD compensation: BER analysis

In order to confirm the results on the eye-analysis, the impact of distortions induced by dispersion on the OC-3R performance was investigated using bit error ratio measurements (Fig. 5.29a,b). The solid squares belong to the back-to-back measurement for an ideal signal in front of the PMD/CD emulator. The data signal, intentionally degraded by average DGD of 10.2 ps (Fig. 5.29a) and by accumulated CD of 35 ps/nm (Fig. 5.29b), is denoted by solid triangles. Finally, the measured BER curves of the data signal behind the regenerator are denoted by solid dots. It is obvious that a negative penalty higher than 2 dB at a BER of 10^{-9} without any indication on error floor down to a BER of 10^{-12} was obtained for PMD as well as for CD degraded data signals at the regenerator output. The output curves are very close to the initial high quality data signal. Thus, the BER measurements prove the suitability of the OC-3R scheme for regeneration of dispersion distorted data signals.

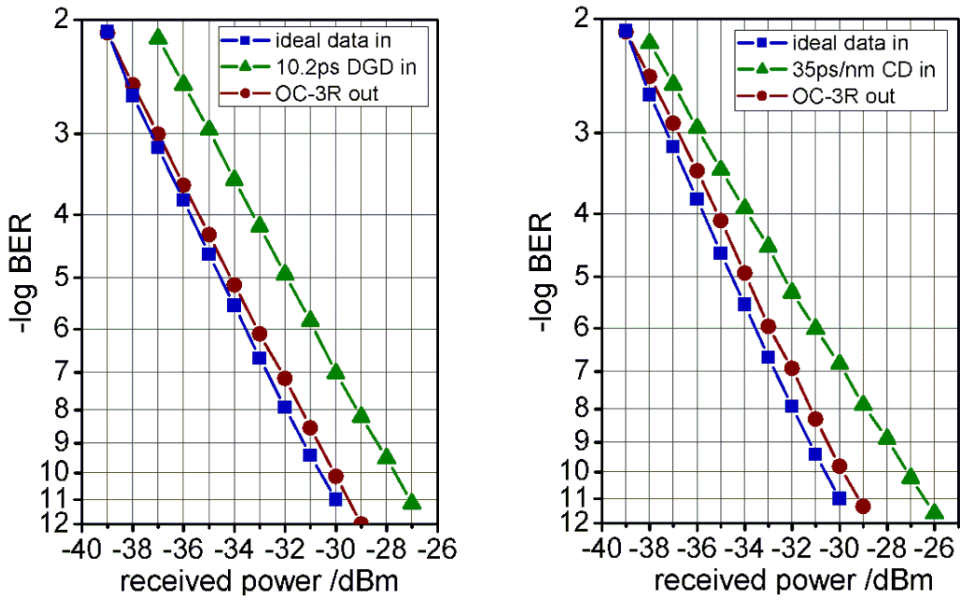

Fig. 5.29: BER curves of the ideal 40 Gbit/s PRBS 2^{31}-1 RZ signal (squares), data signal behind the CD/PMD emulator (triangles) and of the regenerated signal at the OC-3R output for PMD (a) and CD (b) signal distortions.

In summary, the investigations show that the OC-3R scheme is well suited even for operation in dispersion degraded PRBS data streams. It should be noted that an optical regenerator could improve the signal quality (pulse shape, timing jitter), when the broadening of the data pulses does not exceed overlapping of the neighbouring pulses. Hence, conventional compensation techniques of chromatic dispersion (e.g. DCF modules) cannot be generally replaced by an optical 3R regenerator. However, the 3R regenerator can compensate for the residual dispersion, a critical issue mainly in high-speed multi-channel DWDM systems (because of the SSMF dispersion slope). The statistical character of PMD leads to high requirements for an effective compensation technique. In this case, the instantaneous polarisation state of the optical signal has to be controlled adaptively. An adaptive mitigation of the PMD up to 10.2 ps was achieved in the OC-3R regenerator.

5.4.2 OC-3R operated in asynchronous data packet streams

Communication networks with burst and packet switching have to be taken into account in the next generation network scenarios for improving the system granularity. The main advantage of optical packet switching nodes is related to high flexibility in bandwidth usage [142], [143]. Considering these scenarios, all-optical 3R regenerators have to improve the quality of data bits encapsulated in short packets, leading to additional requirements for the regeneration schemes. Ultra-fast synchronisation to the incoming PRBS packets is one of the main prerequisite for processing of packet data streams. Furthermore, as the data packets can originate from different sources, the transmitted wavelength is not predefined. Hence, the incoming packets are uncorrelated in time and wavelength to each other.

The capability of the OC-3R regenerator for operation in 40 Gbit/s PRBS packet data streams was analysed. The scheme of the regenerator is sketched in Fig. 5.30. It is obvious that the basic architecture is identical with the scheme used for synchronous data streams. The only difference is related to an additional delay line (t_D) for proper adjustment of the lengths between the data path and clock path inside the regenerator. It is important that the UL-SOA is already stabilised by the strong sinusoidal clock pulses before the first data bit of the PRBS packet arrives. At the same time, the UL-SOA has to be stabilised even for the time, when the last bit of the PRBS packet propagates the amplifier. Thus, an asymmetrical locking characteristic of the optical clock is required. The relative time difference between the data path and clock path depends directly on synchronisation behaviour of the PhaseCOMB-clock.

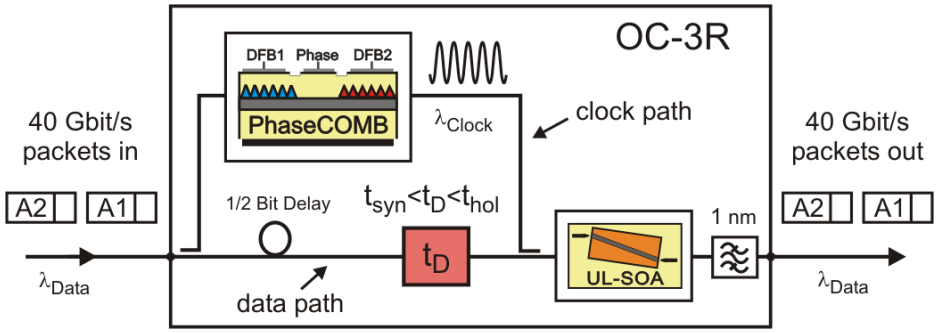

Fig. 5.30: Scheme of the OC-3R regenerator for operation in asynchronous 40 Gbit/s PRBS RZ packet streams.

5.4.2.1. Operation of the PhaseCOMB-clock in packet streams

The locking characteristics of the PhaseCOMB-laser operated in short data packet streams were investigated in more detail. Triggering of an optical regenerator for processing of short PRBS packets is a critical issue. Generally, a preamble with synchronisation bits has to be added to each packet [143]. However, the degraded preamble must be swapped by a new one after the regeneration stage, resulting in sophisticated logical circuits. Figure 5.31a shows a 40 Gbit/s PRBS packet (3000 bits) at 1550 nm (upper trace) and the according clock signal behind the self-pulsating laser (lower trace) measured in the average mode of the sampling oscilloscope. The average function does not change the amplitude of a synchronised signal, while the amplitude of a non-synchronised signal converges to the zero level. The instantaneous increase of the clock amplitude at the packet head shows ultra-fast locking and the slow decrease of the amplitude at the packet end indicates a long holding of the synchronisation after the end of the packet.

The synchronisation behaviour of the PhaseCOMB-laser was analysed by evaluating the timing stability of the clock pulse trace. The fast decrease of the RMS-jitter after injecting the data packet into the SP-laser (t_{ON}) is clearly visible from Fig. 5.31b. Depending on the average data power level, the PhaseCOMB is already synchronised to the incoming PRBS packet in frequency and phase within a time scale between 3 ns and 4 ns. On the other side, the synchronised state is preserved for longer than 27 ns (4 ps RMS-Jitter, Fig. 5.31c) after the last data bit leaves the laser cavity (t_{OFF}). In this case, the data power dependency can be neglected. It should be noted that the smallest RMS-jitter (around 1 ps) was limited by intrinsic timing stability of the sampling oscilloscope.

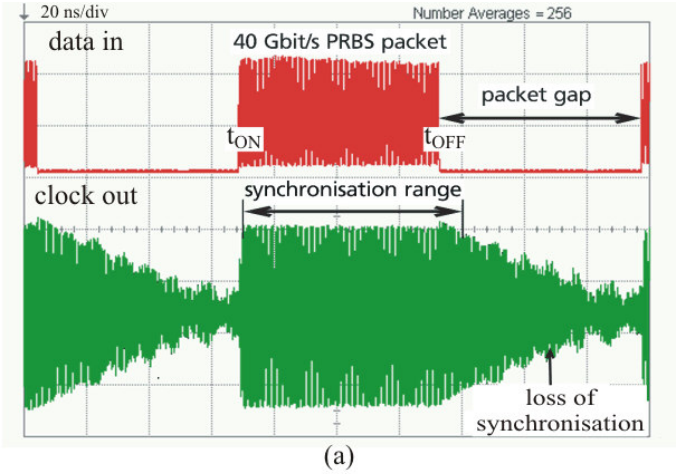

(a)

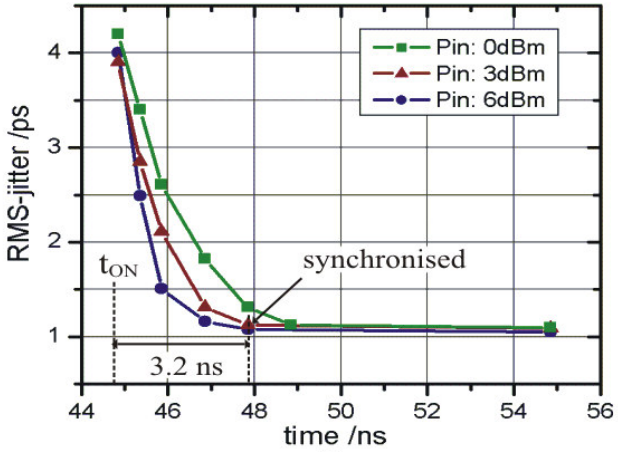

(b)

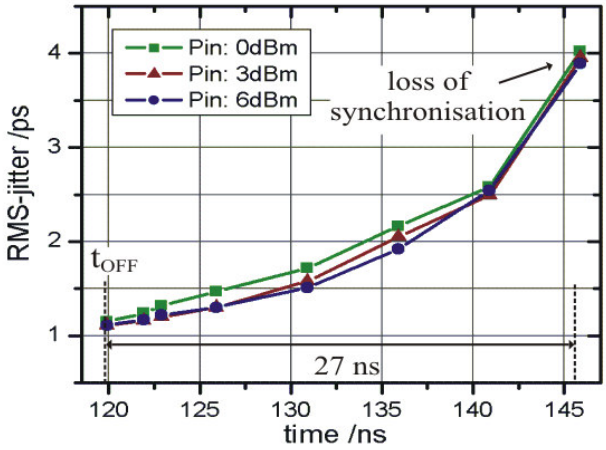

(c)

Fig. 5.31: (a) 40 Gbit/s short PRBS packet (upper trace) and the synchronisation behaviour of the PhaseCOMB-clock (lower trace). Measured clock RMS-jitter indicating locking time to the injected PRBS packet (b) and holding of the synchronisation after the data packet lefts the optical clock (c) for different average data power levels (0 dBm, 3 dBm, 6 dBm).

5.4.2.2. OC-3R for processing of asynchronous packets

The asymmetric locking characteristics of the PhaseCOMB-laser can be exploited in the OC-3R scheme for regeneration of asynchronous packets without any additional preamble. An error-free processing of all data bits can be expected for proper adjustment of the timing delay between the data and clock path (Fig. 5.32). Short PRBS packets (3000 bits) at 1550 nm were generated and injected into the 3R regenerator. The impact of improper adjustment of the t_D delay on the processed bits is visible from Fig. 5.32a. If the data pulses reach the UL-SOA earlier than the synchronised clock ($t_D < t_{syn}$), the first data bits are distorted by the uncorrelated SOA gain variations. On the other hand, if the data-clock delay is longer than the holding time of the PhaseCOMB-clock ($t_D > t_{hol}$), the bits at the packet end propagate the amplifier together with the unsynchronised clock signal, again resulting in data degradations. Next, the synchronisation behaviour of the PhaseCOMB-clock was considered and the delay t_D was set to 5 ns. The results for this configuration are depicted in Fig. 5.32b showing the PRBS packet at the input and output of the regenerator. It is obvious that the first bit as well as the last bit of the injected data packet is processed in the OC-3R without any distortions.

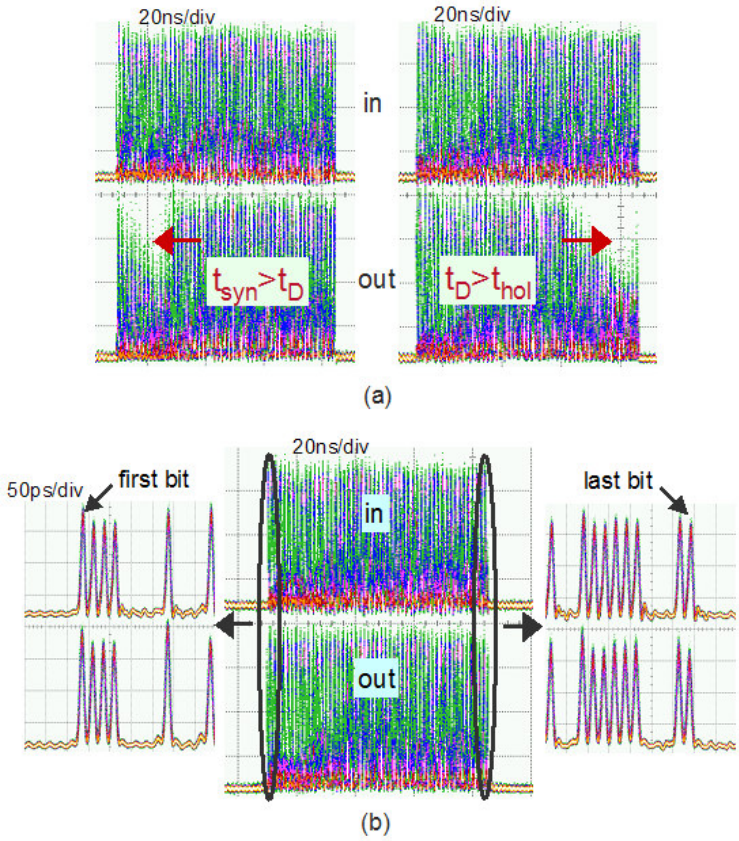

Fig. 5.32: Short PRBS packet (3000 bits) at the OC-3R input (upper traces) and output (lower traces). (a) Data - clock delay (t_D) does not correlate with the PhaseCOMB synchronisation behaviour, (b) properly adjusted data-clock delay (t_D = 5 ns).

5.4.2.3. Asynchronous packet processing at two wavelengths

In the following experiment, the performance of the OC-3R is analysed by operation in a stream of data packets with alternating wavelength and various guard band lengths. Two 40 Gbit/s packet streams at 1550 nm and 1555 nm with a time duration of 50 ns were generated. The data packets were relatively delayed to each other, multiplexed, and alternatively launched into the optical regenerator (Fig. 5.33). The guard band between the data packets (Δt) was set to 10 ns. The data packets were analysed using a sampling oscilloscope.

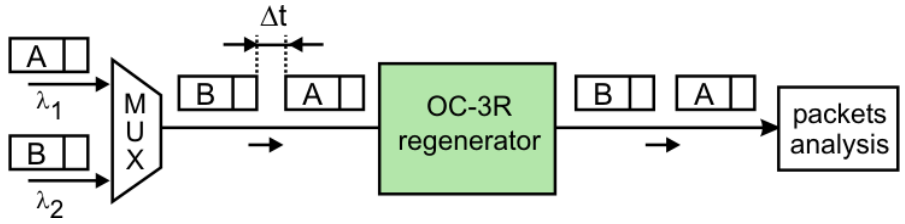

Fig. 5.33: Set-up for performance analysis of the OC-3R regenerator operated in asynchronous WDM packet streams (λ_1 = 1550 nm, λ_2 = 1555 nm).

The results are shown in Fig. 5.34a. The PhaseCOMB-clock synchronises alternatively ultra-fast to the incoming data packets (Fig. 5.34a middle trace). Thus, the packet streams are processed in the OC-3R without any bit losses behind the regenerator (Fig. 5.34a lower trace). Note that the time span of the sampling oscilloscope does not resolve the individual bits. The free-running oscillation of the unsynchronised clock is depicted as a continuous dark noise band, while for the locked state bright vertical lines can be observed. In Fig. 5.34b, the first bits of the two data packets at OC-3R input and output are resolved. The second packet was delayed by half a bit period relative to the first packet, resulting in an asynchronous packet flow. This corresponds to the worst case of the bit correlation. Nevertheless, no distortions are visible at the output of the regenerator. Thus, the OC-3R scheme is well suited even for operation in asynchronous packet data streams at different wavelengths.

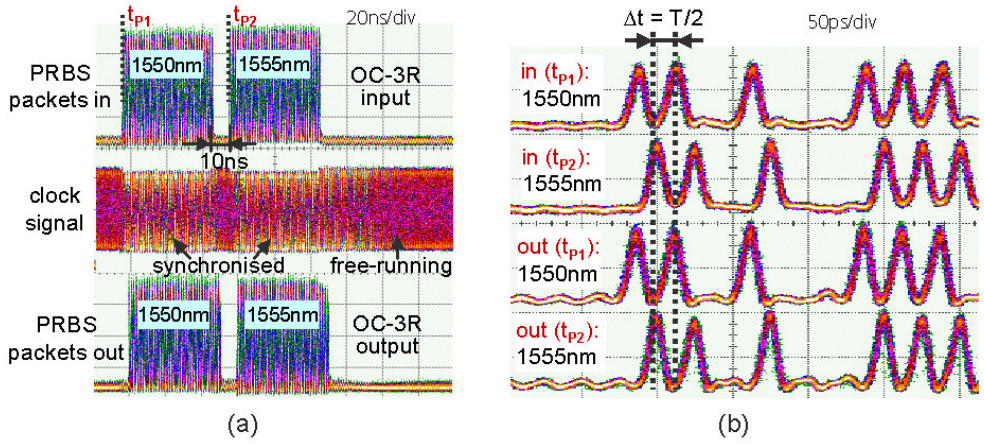

Fig. 5.34: Processing of short PRBS packets at two wavelengths (10 ns guard band) in the OC-3R regenerator (a), start of the packets (delayed by half a bit period to each other) at the input and output of the OC-3R demonstrating asynchronous operation (b).

In summary, the performance of the optically clocked 3R regenerator has been investigated for processing of 40 Gbit/s asynchronous packet data streams. The ultra-fast locking (down to 3 ns) and the long synchronisation holding time of the PhaseCOMB-laser based clock recovery are the key features for preamble free packet processing without bit losses. The OC-3R was successfully applied for regeneration of PRBS packets at alternating wavelengths with a small guard band of 10 ns. No bit distortions were observed even for the most critical relative time position between the consecutive packets. Thus, the OC-3R regenerator fulfils the requirements for future dynamic reconfigurable asynchronous all-optical WDM networks.

5.5 Conclusions

In this chapter, the first 3R scheme developed in frame of this thesis was introduced, the wavelength preserving 'Optically Clocked' 3R regenerator. The OC-3R is basically a very simple and compact architecture comprising only two functional components, the PhaseCOMB all-optical clock and the periodically modulated ultra-long SOA. The quality restoration of distorted PRBS data signals is performed without any wavelength conversion as well as necessity of wavelength monitoring function. This makes the OC-3R scheme attractive for deployment in long-haul transmission links as a 3R regenerative amplifier.

The operation principle and the regenerative performance of the OC-3R operated in 40 Gbit/s PRBS RZ data streams have been evaluated by numerical simulations and experimental analysis. The signal regeneration is based on shaping of degraded data pulses during propagation through an UL-SOA, which is periodically modulated by a dominant clock signal. The data and clock have to be delayed by half a bit period relative to each other before injecting into the amplifier. The influence of the device parameters on the regeneration efficiency of the OC-3R was demonstrated and the optimised operation conditions were defined. An SOA length of at least 4 mm was identified as one of the prerequisite for effective suppression of strong amplitude fluctuations and timing jitter of the degraded data signals. The clock parameters, extracted from the numerical analysis, correlate very well with typical values of the self-pulsating PhaseCOMB-laser, proving the suitability of the all-optical clock for operation in the proposed regeneration scheme. It has been shown that the regeneration efficiency increases for higher clock power levels. The clock determines the shape of the gain window generated in the UL-SOA (jitter improvement) as well as the saturation conditions in the long amplifier (power equalising). Hence, the clock wavelength should be located close to the UL-SOA gain peak, while the data wavelength can be flexibly tuned within the whole C-band. Based on the experimental results, suppression of bit-to-bit amplitude fluctuations from 2 dB down to 0.5 dB and of the RMS-jitter from 1300 fs down to 600 fs was achieved at the regenerator output. The signal quality improvement has been finally proven by BER measurements showing a 2 dB negative penalty. The XGM effects of the periodically modulated UL-SOA do not provide a decision function for elimination of distortions at the zero level. The extended architecture proposed in this work exploits a saturable absorber for ER improvement and noise suppression. The modelling has shown that the optically clocked technique can be used for avoiding of patterning effects in the SA.

The performance of the OC-3R scheme was analysed in different system experiments. An adaptive PMD compensation in a range from 0 ps up to 10.2 ps (40 % bit deviation from the pulse width at 40 Gbit/s bit rate) was demonstrated. Furthermore, pulse broadening and amplitude fluctuations due to residual chromatic dispersion of 34 ps/nm could be effectively suppressed behind the optical regenerator. Finally, the operation of the OC-3R in packet switched networks was considered. The asymmetric locking behaviour of the PhaseCOMB-clock has been exploited for preamble free processing of 40 Gbit/s packet data streams without loss of any bits.

The proposed wavelength preserving OC-3R scheme fulfils the main prerequisites for successful implementation in spectrally efficient 40 Gbit/s DWDM transmission systems as a cost effective in-line 3R regenerator. The semiconductor devices can be further integrated to a compact array for performing a pass-through 3R regeneration of all DWDM channels in the fibre link. The knowledge of the optically clocked principle was exploited in the second 3R architecture, developed as a 3R flexible wavelength converter for optical cross-connects. The operation principle and the performance of this regeneration scheme are presented in the following chapter.

6 Alternating Data-Clock 3R Regenerator: ADC-3R

Optical switching nodes with regenerative wavelength conversion are needed for degradation-free signal routing as well as in order to avoid wavelength collision in the future reconfigurable transparent networks. In the conventional wavelength converting 3R schemes, the data information is encoded onto the wavelength of the clock signal. Hence, optical clock devices with emission wavelength covering any DWDM channel defined by the ITU have to be fabricated.

The 'Alternating Data-Clock' 3R regenerator (ADC-3R) is a novel semiconductor based 3R architecture developed in the frame of this work that fundamentally performs λ-conversion independently on the clock wavelength. Similar to the previous regeneration scheme (OC-3R), fast inter-band gain processes in a periodically modulated ultra-long SOA are exploited for all-optical signal processing. In the ADC-3R, the output wavelength is determined by a CW laser source and can be flexibly tuned in the whole C-band, while the clock at a fixed wavelength defines the timing stability of the converted data pulses.

In this chapter, the scheme and the operation principle of the ADC-3R regenerator is presented. The effectiveness of the ADC wavelength conversion is first investigated for high quality 40 Gbit/s PRBS RZ signals by numerical simulations and experimental analysis. The impact of frequency chirping in UL-SOAs on extinction ratio improvement of the converted signals is demonstrated. In the second part, the regenerative behaviour of the ADC-3R is analysed for different operation conditions as well as data degradations.

6.1 Basic characteristics of the ADC-3R regenerator

In this section, the principle of the ADC wavelength conversion is schematically described and the key prerequisites are defined. In the ADC scheme, both the XGM and XPM effects in the UL-SOA and a concatenated processing filter are exploited. The frequency chirp of periodical signals induced by the long amplifiers is experimentally evaluated for different operation conditions. The impact of frequency detuning of a BP-filter on the quality of the ADC wavelength converted signal is demonstrated.

6.1.1 Scheme and principle of ADC wavelength conversion

Figure 6.1 depicts the set-up of the 'Alternating Data-Clock' 3R regenerator. The similarity of the ADC-3R architecture to the OC-3R scheme is obvious. Also in this case, the PhaseCOMB all-optical clock (Chapter 3) and ultra-long SOA (Chapter 4) are the key components of the proposed regenerator. Additionally, a CW laser and a processing filter extend the functionality of the ADC-3R scheme. In the regenerator, three signals

simultaneously co-propagate the UL-SOA: the 40 Gbit/s PRBS RZ signal, the synchronised clock signal (bit interleaved to each other) and the CW beam. Here, the data information is first encoded by means of strong cross gain modulation into the CW wavelength. Behind the UL-SOA, the converted signal passes through a processing filter in order to exploit cross phase effects induced by carrier density modulation in the long amplifier. A wavelength converted 40 Gbit/s PRBS signal with improved quality is obtained at the output of the ADC-3R.

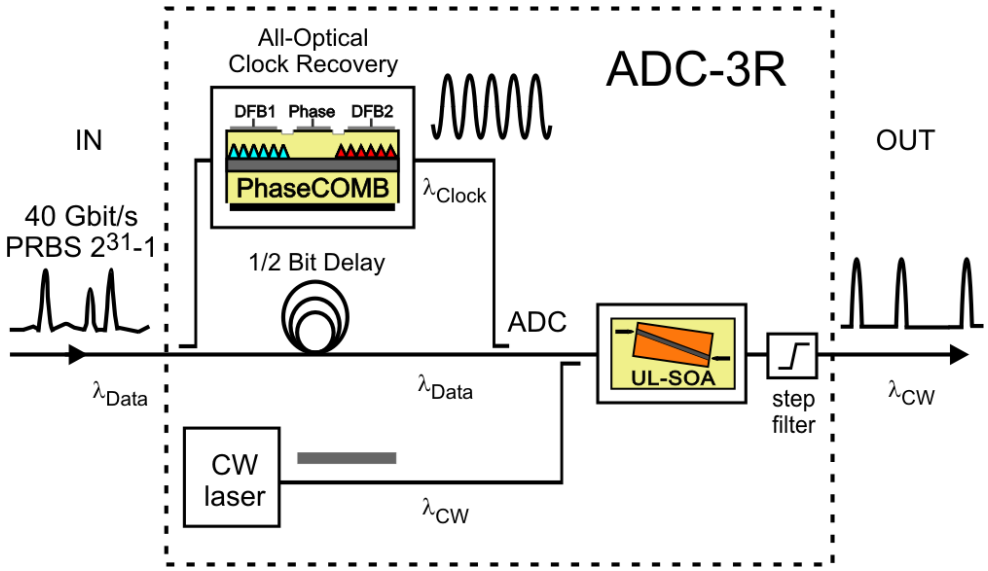

Fig. 6.1: Scheme of the 'Alternating Data-Clock' 3R regenerator (ADC-3R) showing the main building blocks.

The operation principle of the ADC wavelength conversion is schematically depicted in Fig. 6.2. As mentioned previously, the PRBS RZ signal and the periodical clock signal are delayed by half a bit period relative to each other. In contrary to the OC-3R scheme, where the dominant clock controls the weak data signal, the average power levels of the data and clock are nearly identical in the ADC-3R. A new combined signal, referred as ADC in this work, is derived from the envelope of both interleaved signals. The amplitude of the combined ADC signal remains constant, if consecutive marks are present in the PRBS word and drops down between two adjacent clock pulses in case of a space. Hence, the ADC signal is inverted in the logic compared to the original data signal. The logical ones appear as zeros and vice versa. In the UL-SOA, the information of the ADC signal is encoded by means of XGM onto the new CW signal. The gain dynamics of the amplifier is defined exclusively by the dominant ADC signal that controls the amplitude of the weak CW beam. Notice that the pulse shape as well as the timing stability of the converted PRBS signal are determined by two adjacent clock pulses and are nearly independent of the quality of the data signal. Thus, the ADC principle provides a 3R regenerative wavelength conversion of distorted PRBS RZ data streams to a flexible wavelength defined by the CW signal.

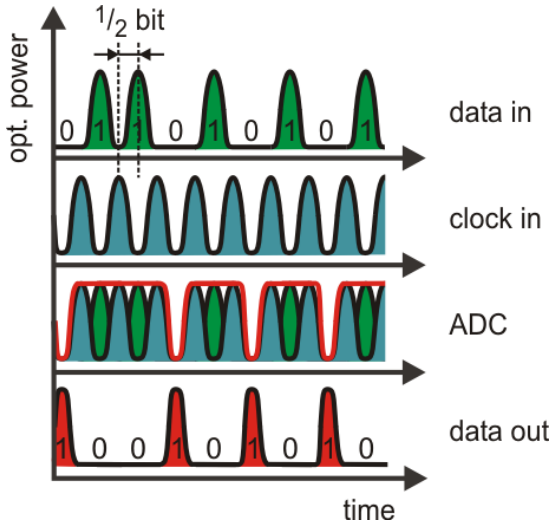

Fig. 6.2: Operation principle of the XGM based ADC wavelength conversion.

In the following experiment, wavelength conversion of high quality data streams in the ADC-3R scheme is performed. A 40 Gbit/s RZ PRBS 2^{31}-1 signal (590 fs RMS-jitter, Fig. 6.3a) was converted from 1550 nm to 1555 nm. Figure 6.3b shows the 40 GHz pulse trace of the synchronised self-pulsating PhaseCOMB-clock (1560 nm, 500 fs RMS-jitter). The average power level of the data and clock before splitting together was set to +4 dBm and +5 dBm, respectively. The combined ADC signal was encoded to a weak CW beam (1555 nm, P_{CW} = -3 dBm) in a 4 mm UL-SOA (800 mA bias current, ASE spectrum shown in Fig. 5.3). Behind the amplifier, the CW wavelength was filtered by a 1 nm tuneable BP-filter. The eye diagram of the converted PRBS signal is depicted in Fig. 6.3c. Due to the fast XGM effects in the UL-SOA, a clearly open eye without any patterning effects was obtained at the ADC-3R regenerator output. Notice that the RMS-jitter of the converted signal (490 fs) correlates with the jitter of the periodical clock. The extinction ratio is slightly reduced at the regenerator output. As mentioned previously, phase variations induced by carrier density modulations can be further exploited in a processing filter for improved wavelength conversion. Obviously, the conventional 1 nm BP-filter used in the experiment does not provide sufficient functionality. In order to identify the demands on transmission characteristics of the processing filter, chirp effects in ultra-long SOAs were studied in more detail.

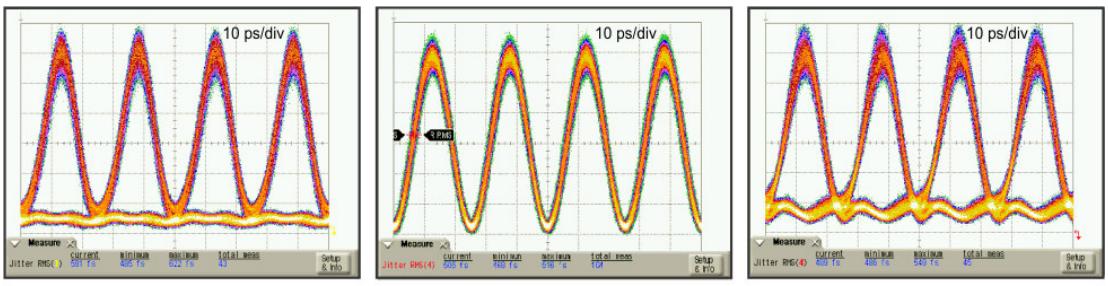

(a) (b) (c)

Fig. 6.3: Eye diagrams of the 40 Gbit/s data signal (590 fs RMS-jitter, 1550 nm) (a), recovered clock signal behind the PhaseCOMB-laser (500 fs, 1560 nm) (b), and the wavelength converted signal at the ADC-3R output (490 fs, 1555 nm) (c).

6.1.2 Signal chirping induced by UL-SOAs

In the ADC scheme, encoding of the data information on the co-propagated CW signal is based on XGM effects in UL-SOAs. The modulation of the refractive index due to inter-band transitions results in phase variation of the CW beam. The total phase-to-gain changes in the SOA can be expressed by a coupling factor α_{eff}, also referred as a chirp parameter [167]. Considering XGM interactions between a modulated control signal and a CW probe signal, the effective α-factor is defined as [168]:

$$\alpha_{eff} = -\frac{1}{2}\frac{\Delta\Phi_{tot}}{\ln\left(\frac{G_{\max}}{G_{\min}}\right)} \tag{6.1}$$

where G_{min} and G_{max} are the minimum and maximum gain values associated with the interband gain recovery and $\Delta\Phi_{tot}$ is the total phase shift of the probe signal induced by the control signal in the SOA, which is related to the waveguide length L and the mean refractive index changes $\Delta\bar{n}$

$$\Delta\Phi_{tot} = \frac{2\pi L}{\lambda}\Delta\bar{n} \tag{6.2}$$

where λ is the wavelength of the probe signal. The effective α-factor increases with the SOA length due to combination of nonlinear gain compression and propagation effects (carrier density is not constant over the amplifier length) in the long devices [169].

The frequency chirp of the optical signal behind the SOA is defined as the frequency deviation relative to the beam optical frequency, which is caused by the phase changes of the output signal

$$\Delta\nu(t) = -\frac{1}{2\pi}\frac{\partial\phi}{\partial t} \tag{6.3}$$

From the equation (6.3) follows that every phase variation at the amplifier output (due to e.g. SPM or XPM) is always accompanied by a certain amount of chirp. The relation between the frequency chirp and the chirp parameter is [138]

$$\Delta\nu(t) = \frac{1}{4\pi}\left(\frac{\partial\alpha_{eff}(t)}{\partial t}ln\left(P(t)/P_{in}\right) + \frac{\alpha_{eff}(t)}{P(t)}\frac{\partial P(t)}{\partial(t)}\right) \tag{6.4}$$

where P_{in} is the input power level of the probe signal and $P(t)$ is the power variations of the probe signal associated with SOA gain changes. Since the dependence of α_{eff} on the input power of the probe signal is relatively small when the signal wavelength, bias current and SOA length are fixed, the α_{eff} can be considered as a constant. In this case the equation (6.4) reduces to

$$\Delta\nu(t) = \frac{\alpha_{eff}}{4\pi P(t)}\frac{\partial P(t)}{\partial(t)} \tag{6.5}$$

where P(t) is the time dependent probe beam output power. The equation (6.5) indicates that the chirp is not only dependent on the α_{eff} but also on the dynamics of $P(t)$. Hence, large α_{eff} and fast changes of $P(t)$ enhance the frequency chirp of the modulated signal.

Generally, there are two types of frequency chirp: A positive chirp where the output pulses undergo blue shift during the rising edge and red shift during the falling edge and vice

versa for a negative chirp. The magnitude of the maximum chirp variation is referred as maximum chirp excursion or peak-to-peak chirp [113]. In the following, the influence of the ultra-long SOAs on the frequency chirping of 40 GHz periodical signals is experimentally investigated for different operation conditions.

6.1.2.1. Measurement of the frequency chirp

The basic issue in measuring the frequency chirp is the ability to detect the optical frequency or optical phase variations of the investigated signal and to distinguish them from the power variations. Since the photodetector is not sensitive to the optical phase, a FM/AM converter is usually needed. Several methods have been developed for measuring the frequency chirp of the modulated light source. Most of them use optical filters as frequency discriminators e.g. a Fabry-Pérot etalon [115], a waveguide grating router [116], or a Mach-Zehnder interferometer [117] – [119].

In the following experiments, the chirp characteristics of the optical signals were measured using a commercial system from Agilent Technologies. The signal analysis was performed by an optical spectrum analyser (OSA, Agilent 8614B with TRC option) combined with a digital communication analyser (DCA, Agilent 86100 A/B). The measurement was based on time resolved spectroscopy (TRS). Thus, a temporal distribution of the frequency shift of the analysed modulated signals was evaluated. A detailed description to the measurement technique can be found in [123]. It has to be noted that the system was calibrated for bit rates up to 10 Gbit/s only. In order to prevent high peak errors, the measurement was performed for 40 GHz periodical signals instead of PRBS data streams. As a reference, the frequency chirp of the synchronised PhaseCOMB-laser was measured. The peak-to-peak chirp of the clock signal after propagation through the SOAs of different lengths (0.5 mm, 2 mm and 4 mm) was evaluated for different operation conditions. The resolution bandwidth of the OSA filter was set to 1 nm; the 10 nm spectral window was sampled in 0.5 nm steps around the central wavelength of the measured signal.

6.1.2.2. Peak-to-peak chirp analysis

The chirp pulse trace of the synchronised self-pulsating PhaseCOMB-clock is depicted in Fig. 6.4a. It is obvious that the peak-to-peak frequency chirp of the optical clock is below 10 GHz. The small chirp value is due to the beating type oscillation of the PhaseCOMB-clock (see Chapter 3). The periodical clock signal was then injected at average power level of +3 dBm into the investigated amplifiers (200 mA/mm bias current). Behind the 0.5 mm SOA, the peak-to-peak chirp already increased from 10 GHz up to 30 GHz (Fig 6.4a). Figure 6.4b shows the chirp pulse traces of the sinusoidal signal at the 2 mm and 4 mm UL-SOA output. Due to the stronger carrier induced phase modulation, the evaluated peak-to-peak chirp was 52 GHz and 57 GHz for the 2 mm and 4 mm amplifier, respectively. The frequency chirp increases with the SOA length and is nearly twice as high in case of the 4 mm UL-SOA compared to the amplifier with a conventional length of 0.5 mm.

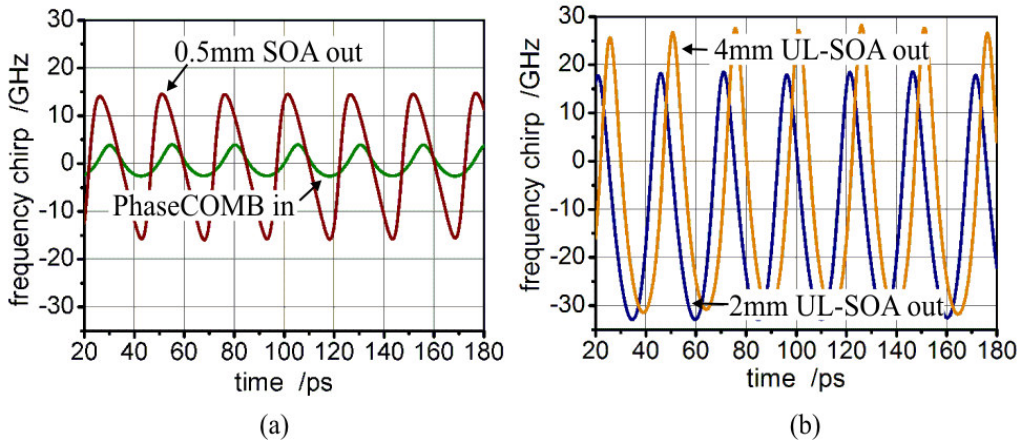

Fig. 6.4: Measured frequency chirp traces of the synchronised PhaseCOMB-clock at the input and output of the 0.5 mm SOA (a) and behind the 2 mm and 4 mm UL-SOAs (b). P_{clock} = +3 dBm, λ_{clock} = 1560 nm, I_{SOA} = 200 mA/mm.

In the ADC-3R regenerator, the UL-SOA is operated in a highly saturated regime. Therefore, the maximum chirp excursion behind the 2 mm and 4 mm amplifiers was measured as a function of the input power level. Figure 6.5a summarises the results. The increased power leads to stronger carrier density modulation. Thus, the sinusoidal signal experiences higher phase changes. A faster increase of the frequency chirp can be observed for the 4 mm amplifier. At P_{in} = +8 dBm, a difference of more than 10 GHz was measured when comparing both amplifiers. This is due to stronger gain saturation in the longer device. The smaller peak-to-peak chirp for lower input powers (below 0 dBm) in case of the 4 mm UL-SOA is related to different quality of fibre-chip coupling between both amplifiers (see section 4.1). Figure 6.5b shows the chirp dependence of the 40 GHz clock signal (P_{in} = +3 dBm) on the UL-SOA current density. The frequency fluctuations increase with higher current density. However, due to carrier depletion induced by amplified spontaneous emission, both curves saturate at a nearly constant levels.

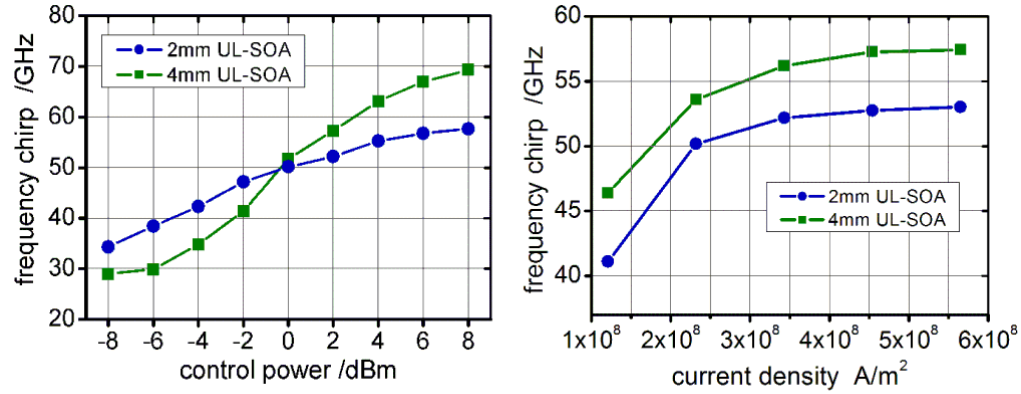

Fig. 6.5: Measured peak-to-peak chirp of the control clock signal for two UL-SOA lengths as a function of the input power level (a) and amplifier current density, P_{in} = +3 dBm (b).

6.1.3 Exploitation of the frequency chirp for improved ADC wavelength conversion

The high frequency chirp (phase modulation) induced by the long amplifiers can be exploited for data wavelength conversion in an interferometric scheme. In this section, the focus will be given on a band-pass filter with sharp frequency response, as a compact and very simple structure for optical signal processing. The ADC wavelength conversion and the impact of the BP-filter were simulated using VPIphotonics^{TM} in more detail.

In the first approach, the ADC conversion based only on the XGM in the 4 mm UL-SOA (I_{SOA} = 200 mA/mm) is numerically analysed for different power levels of the CW signal. Figure 6.6a depicts the eye diagrams of the ideal 40 Gbit/s PRBS RZ signal (1550 nm, upper trace) and of the ADC converted data signal (1555 nm, lower trace) behind the UL-SOA. The average power levels of the input data signal, clock (1560 nm) and of the CW signal (1555 nm) at the amplifier input were set to +6 dBm, +6.5 dBm, and –5 dBm, respectively. Comparing both eye diagrams, the only difference in the quality of the data signals is related to reduced extinction ratio behind the UL-SOA down to 5.5 dB. The ER value of the converted signal directly depends on the input CW power, as it is obvious from Fig. 6.6b. The maximum extinction ratio of 6 dB was achieved for CW amplitude smaller than -7 dBm. The data ER decreases when increasing the CW power and is below 2 dB for the input power of +8 dBm.

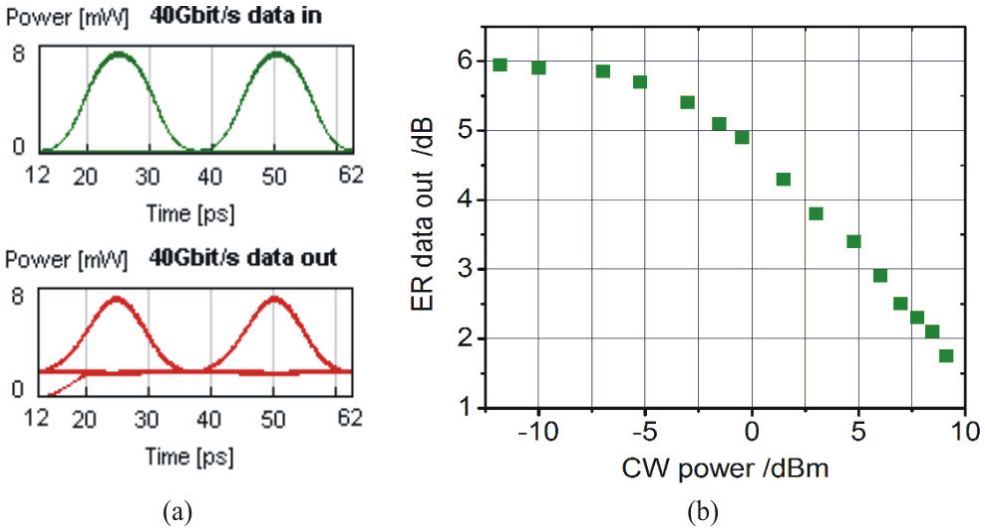

(a) (b)

Fig. 6.6: (a) ADC XGM wavelength conversion of a 40 Gbit/s PRBS RZ signal (1550 nm to 1555 nm) in a 4 mm UL-SOA (P_{data} = +6 dBm P_{clock} = +6.5 dBm P_{CW} = -5 dBm, λ_{clock} = 1560 nm, I_{SOA} = 200 mA/mm), (b) extinction ratio of the converted data signal as a function of the CW power level at the UL-SOA input.

In the following simulation, a trapezoid band-pass filter was additionally concatenated behind the 4 mm UL-SOA and the impact of frequency detuning between the CW signal and the center frequency of the BP-filter on the converted data signal was investigated. Figure 6.7 depicts the transfer function of the BP-filter. The FWHM of the filter was set to 200 GHz (sufficiently wide for 40 Gbit/s RZ signals); the filter steepness was optimised to around 3 dB/10 GHz. For identical frequencies (middle eye diagram in Fig. 6.7), high

quality RZ signal with ER of around 6 dB was detected at the regenerator output (comparable to the case without any filter). Tuning the filter by 150 GHz towards shorter frequencies, pulse broadening as well as degradations in timing stability and ER can be observed behind the BP-filter (Fig. 6.7, right hand side eye diagram). However, the extinction ratio of the converted signal can be effectively enhanced, when the filter transmission spectrum was shifted towards longer frequencies. Frequency shift of 150 GHz leads to an ER improvement from 6 dB to more than 13 dB at the regenerator output (Fig. 6.7, left hand side eye diagram). As already shown, the gain modulations are accompanied by phase changes due to frequency chirping of the UL-SOA. The phase modulation corresponds to a blue-shifted chirp (longer frequencies) on the leading edge of the converted pulses and a red-shifted chirp (shorter frequencies) on the trailing edge. Tuning the central frequency of the output BP-filter, either the red-shifted or blue-shifted spectral components can be suppressed. In case of the ADC wavelength conversion, an improvement can be achieved, when blue-shifted components are selected, which are governed by fast carrier depletion effects. The almost rectangular shape of the trapezoid filter allows effective blocking of the CW signal and provides transparency already for small chirp values.

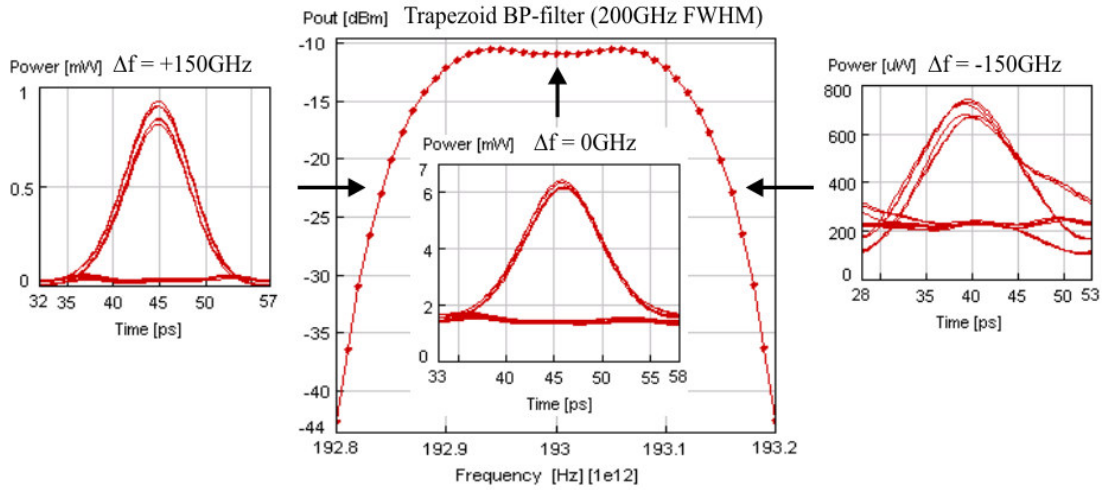

Fig. 6.7: Transmission spectrum of the trapezoid band-pass filter (200 GHz FWHM, 3 dB /10 GHz steepness) and the eye diagrams of the ADC converted 40 Gbit/s PRBS signal (4 mm UL-SOA) for different detuning of the filter centre frequency relative to the CW beam: Δf = -150 GHz, 0 GHz, +150 GHz. (P_{data} = +6 dBm, λ_{data} = 1550 nm, P_{clock} = +6.5 dBm, λ_{clock} = 1560 nm, P_{CW} = -7 dBm, λ_{CW} = 1555 nm, I_{SOA} = 200 mA/mm).

Figure 6.8 summarises the results of the previous simulation. For comparison, the influence of a commercial BP-filter with a Bessel power transmission characteristic (200 GHz bandwidth, 1 dB/10 GHz steepness) was also considered. The central frequency of the band-pass filters at the 4 mm UL-SOA output was tuned in a wide range from –170 GHz up to +170 GHz relative to the emission wavelength of the CW laser and the ER of the converted signal was evaluated. The average power level of the 40 Gbit/s data signal, 40 GHz clock and CW was kept fixed at +6 dBm, +6.5 dBm and –7 dBm, respectively. It is obvious that an ER improvement can be achieved only when the BP-filter is detuned towards longer frequencies. In case of the Bessel filter, the ER increases

nearly linearly with the positive detuning and an improvement from 6 dB to 9 dB can be observed at +170 GHz frequency shift. Different behaviour shows the configuration with the trapezoid BP-filter. The ER of the converted signal remains almost unchanged inside the transmission spectrum of the filter. However, relative strong ER increase can be observed at the filter edge (frequency shift higher than +100 GHz) and an extinction up to 17 dB was achieved for the maximum frequency shift.

At the same time, the average output power level of the converted signal was evaluated at the ADC-3R output for different filter detuning. From Fig. 6.8 is clearly visible that the ER improvement by frequency detuning is closely coupled with additional insertion losses. This is due to partly suppression of the data modulation spectrum behind the BP-filter. When comparing both configurations, the losses are more critical for the trapezoid BP-filter (6 dB difference at +170 GHz detuning). Thus, there is a trade off between the ER enhancement (filter steepness) and the output power level of the converted data signal.

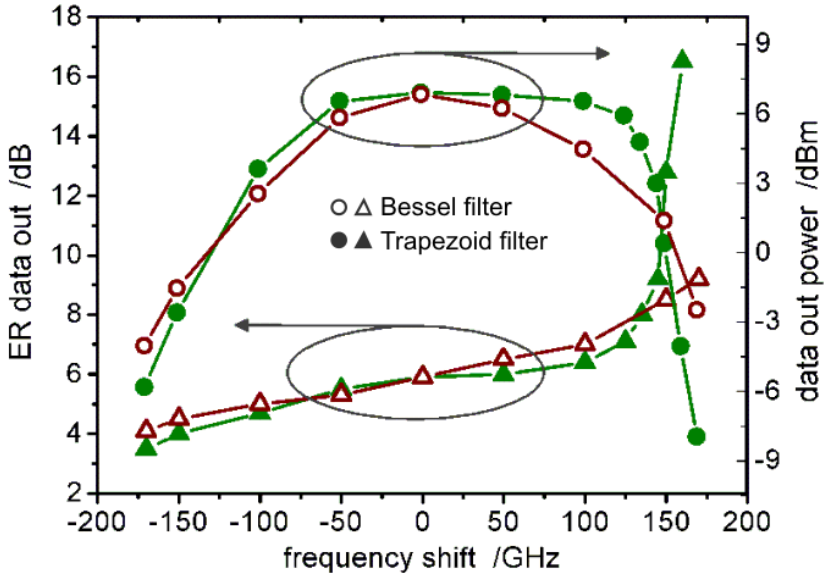

Fig. 6.8: Extinction ratio and average power level of the converted 40 Gbit/s PRBS RZ data signal at the ADC-3R output as a function of frequency detuning of the 200 GHz FWHM BP-filter (Bessel (1 dB /10 GHz), trapezoid (3 dB /10 GHz)) relative to the CW wavelength.

In summary, the optically clocked principle was exploited in the ADC-3R regenerator for effective wavelength conversion of 40 Gbit/s PRBS RZ data streams. In the ADC scheme, the clock signal determines the timing stability of the converted signal. The output wavelength is defined by the CW signal and can be flexibly tuned independently of the clock wavelength. The wavelength conversion based on XGM effects in UL-SOAs result in high quality output signals, however, with reduced extinction ratio. Furthermore, XPM effects can be exploited for improved conversion efficiency. The peak-to-peak frequency chirp increased from 30 GHz up to 57 GHz when enhancing the SOA length from 0.5 mm to 4 mm. In the optimised ADC-3R architecture comprising a BP-filter with step-like transmission characteristic, an effective ER improvement of the converted signal from 6 dB up to 17 dB was demonstrated.

6.2 Design optimisation of the ADC-3R scheme operated in degraded PRBS streams

The ADC-3R scheme shows good performance for operation in ideal 40 Gbit/s data streams. However, the purpose of this work was to develop a wavelength converter with regenerative features. In this section, the potential of the ADC-3R for regeneration of strongly distorted PRBS signals is numerically investigated in more detail. Throughout all simulations, the wavelengths of the PRBS signal, clock and CW were set to 1550 nm, 1560 nm, and 1555 nm, respectively. The SOA bias current was set to 200 mA/mm.

First, ADC wavelength conversion of degraded data signals by means of XGM effects in the 4 mm UL-SOA is discussed and the interactions between the optical signals are analysed at the bit level. The impact of the SOA length and of the processing filter on the quality improvement of the converted signals is demonstrated. In the second part, the basic requirements for the periodical clock signal in the ADC-3R are pointed out.

6.2.1 Impact of signal distortions on ADC wavelength conversion

The ADC wavelength conversion of degraded PRBS signals exploiting XGM effects in a 4 mm UL-SOA was investigated. In the simulation, an ideal sinusoidal 40 GHz clock signal (P_{clock} = +6.5 dBm) was launched together with a 40 Gbit/s PRBS RZ data signal (P_{data} = +6 dBm), strongly distorted by amplitude fluctuations and timing jitter, and a weak CW signal (P_{CW} = -4 dBm) into the amplifier. A 3 nm band-pass filter, tuned to the wavelength of the CW signal, was placed behind the UL-SOA. The eye diagrams of the degraded PRBS signal and of the converted 40 Gbit/s data signal at the ADC-3R output are depicted in Fig. 6.9a, b. It is clearly visible that the strong amplitude fluctuations as well as the timing jitter are effectively suppressed behind the regenerator. The XGM wavelength conversion results in extinction ratio reduction of the output data signal, as already shown in the previous section. Furthermore, comparing the eye diagrams for the ideal data streams (Fig. 6.6a), some additional distortions at the zero level can be observed, which reduce the eye opening of the new signal behind the ADC-3R regenerator.

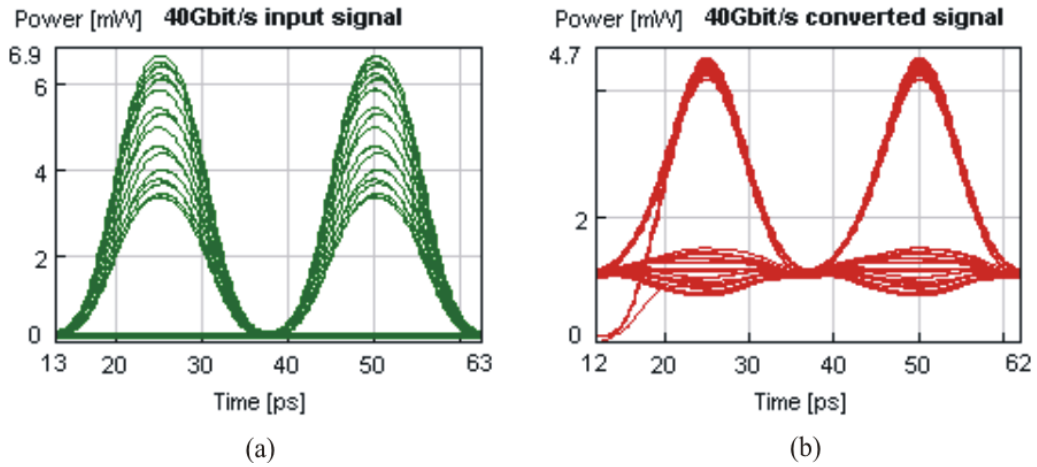

Fig. 6.9: Eye diagrams of the degraded 40 Gbit/s PRBS RZ signal (a) and of the ADC wavelength converted data behind the ADC-3R regenerator comprising a 4 mm UL-SOA and a 3 nm BP-filter tuned to the CW wavelength (b). P_{data} *= +6 dBm,* λ_{data} *= 1550 nm,* P_{clock} *= +6.5 dBm,* λ_{clock} *= 1560 nm,* P_{CW} *= -4 dBm,* λ_{CW} *= 1555 nm,* I_{SOA} *= 200 mA/mm.*

The origin of the distortions is obvious from the pattern diagrams of the optical signals at the UL-SOA input and output, respectively (Fig. 6.10). The principle of the ADC scheme is based on continuous SOA gain saturation when the data and clock pulses are simultaneously present in the amplifier. It is assumed that the amplitudes of both signals are nearly identical (Fig. 6.2). However, in case of degraded signals, the amplitude of the data pulses strongly fluctuates, resulting in fluctuations of the amplitude difference between the data and clock (Fig. 6.10a). Figure 6.10b depicts the temporal evolution of the three signals behind the UL-SOA. It is obvious that the pulses of the converted signal appear in the time slots between two adjacent clock pulses. Due to the UL-SOA gain saturation, the marks of the new signal are effectively fixed at a constant power level. The fluctuations of the degraded input signal are also partially suppressed. However, interactions between the distorted data and the clock signal during propagation through the amplifier lead to additional encoding of the bit pattern onto the clock. The resulted differences in the data-clock amplitudes (Δx in Fig. 6.10b) induce power variations at the space levels of the converted signal.

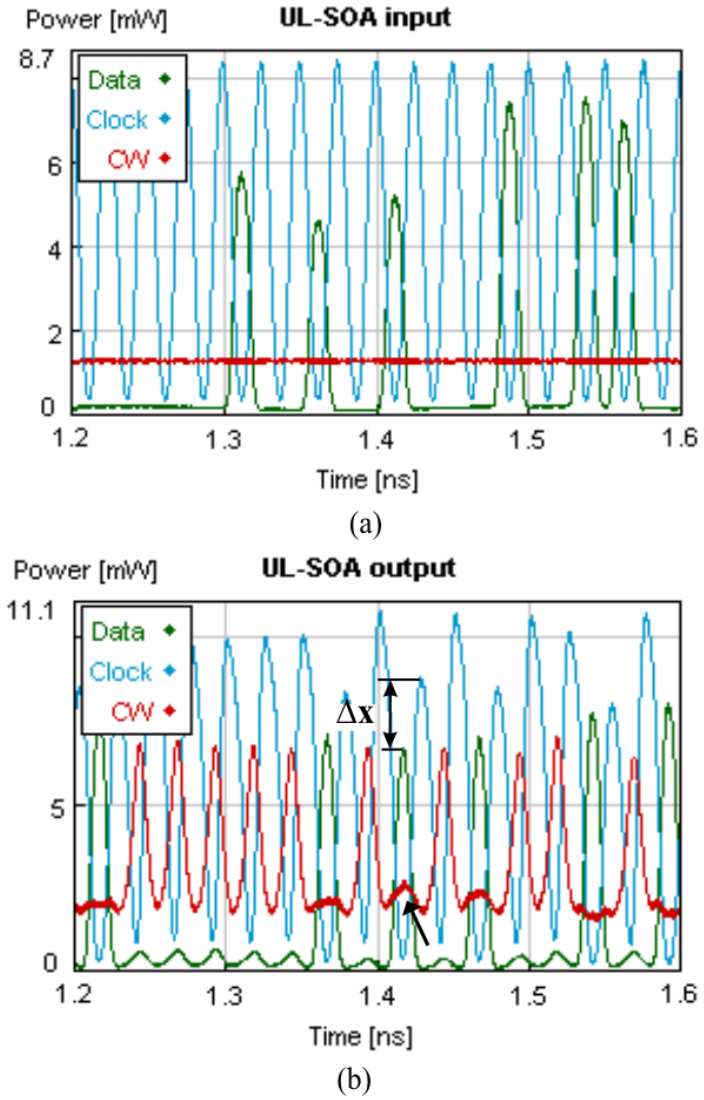

Fig. 6.10: ADC wavelength conversion of degraded 40 Gbit/s PRBS signals. Pulse traces of the optical signals (data, clock. CW) at the 4 mm UL-SOA input (a) and after propagation through the long amplifier showing the influence of amplitude differences between the data and clock (Δx) on the zero distortion of the converted signal (b).

6.2.2 Regenerative potential of the ADC scheme

Reduced ER and residual distortions of the converted signal caused by XGM effects in the ultra-long SOA degrade the regenerative behaviour of the ADC-3R scheme. Thus, an additional optimisation of the proposed architecture is required. In the following, the performance of the ADC-3R regenerator is evaluated for different SOA lengths and the impact of the processing filter is discussed.

6.2.2.1. Role of the SOA length

As mentioned previously, the ADC scheme exploits strong gain saturation and fast recovery processes in UL-SOAs. In the following simulation, the impact of the SOA length on the regenerative efficiency of the ADC wavelength conversion is analysed in more detail. The simulation was performed for three different amplifier lengths: 1 mm, 4 mm and 8 mm UL-SOA. The degradation of the 40 Gbit/s PRBS corresponds to the signal shown in Fig. 6.9a. The eye diagrams of the ADC converted data signal behind the three amplifiers are depicted in Fig. 6.11. In case of the 1 mm SOA (Fig. 6.11a), the modulation depth as well as the fast gain recovery part are relatively weak in order to effectively transform the data information into the new wavelength. Due to the slow inter-band transitions in the short amplifier, the broadened eye of the converted signal is degraded in the extinction ratio and in the timing jitter. Figure 6.11b,c shows the eye diagrams of the converted signal behind the 4 mm and 8 mm UL-SOA, respectively. In this case, the quality improvement is clearly visible. The timing jitter and amplitude fluctuations are effectively suppressed. Although there is only a small difference in the quality of the converted signal when comparing the two amplifiers, the distortions at the zero level are more reduced and the extinction ratio is more improved behind the 8 mm UL-SOA. This is because of stronger gain saturation, resulting in smoothing of the amplitude differences between the signals. However, from a practical point of view, the 4 mm UL-SOA seems to be a good compromise for further experimental investigations.

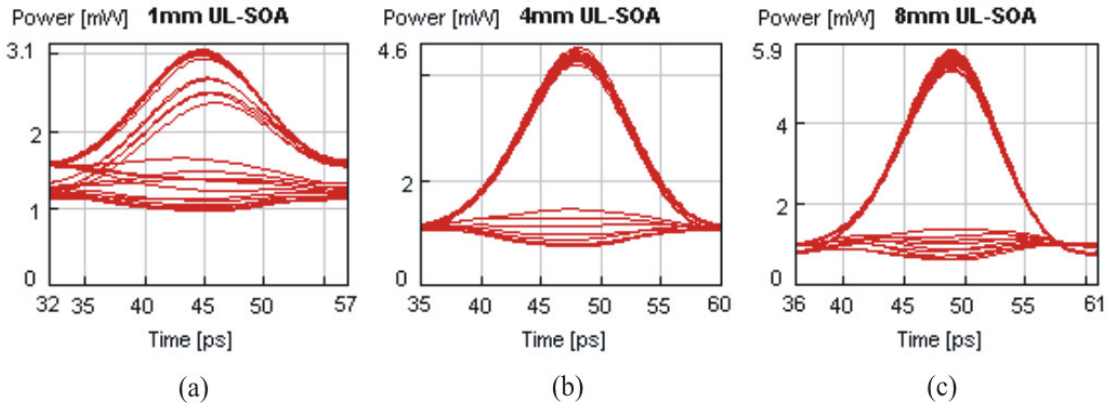

Fig. 6.11: Eye diagrams of the ADC wavelength converted 40 Gbit/s data signals (degraded input data shown in Fig. 6.9a) for different SOA lengths: 1 mm (a), 4 mm (b) and 8 mm (c). P_{data} = +6 dBm, λ_{data} = 1550 nm, P_{clock} = +6.5 dBm, λ_{clock} = 1560 nm, P_{CW} = -4 dBm, λ_{CW} = 1555 nm, I_{SOA} = 200 mA/mm.

6.2.2.2. Impact of the frequency detuned BP-filter

It has been shown in the section 6.1.3 that the ER of the output signal can be significantly improved, when exploiting the processing filter detuned towards longer frequencies relative to the CW wavelength.

In the following simulation, the impact of the trapezoid BP-filter (200 GHz FWHM, 3 dB/10 GHz steepness) in case of degraded data streams was studied. The average power levels of the data signal, clock and CW were set to +6 dBm, +6.5 dBm and –5 dBm before injecting into the 4 mm UL-SOA. The detuning between the filter and the CW wavelength was continuously varied and the quality of the converted data signal was evaluated by eye S-N parameter. This parameter simultaneously captures amplitude fluctuations at marks and spaces as well as the extinction ratio of the converted signal (equation in Fig. 6.12b). Figure 6.12 summarises the results. It is obvious that the eye S-N of the wavelength-converted signal is even smaller than the eye S-N of the input degraded PRBS signal, when the converted signal do not interact with the steep slope of the concatenated BP-filter. An improvement can be seen for detuning larger than 120 GHz. Further frequency detuning leads to an improved signal quality behind the ADC-3R regenerator. An eye S-N up to 9 was evaluated in case of a 160 GHz filter shift. The corresponding eye diagram of the converted 40 Gbit/s signal is depicted in Fig. 6.12a. Effective suppression of amplitude fluctuations and timing jitter as well as an improved extinction ratio is clearly visible. Furthermore, the residual distortions at the zero bit level are significantly reduced when comparing to the output signal without additional filter processing (Fig. 6.9b). Thus, the combination of the periodically modulated UL-SOA (re-shaping, re-timing function) and the steep processing filter (ER improvement, zero equalising) in the ADC-3R architecture results in an all-optical 3R regenerative wavelength conversion of degraded 40 Gbit/s PRBS RZ signals.

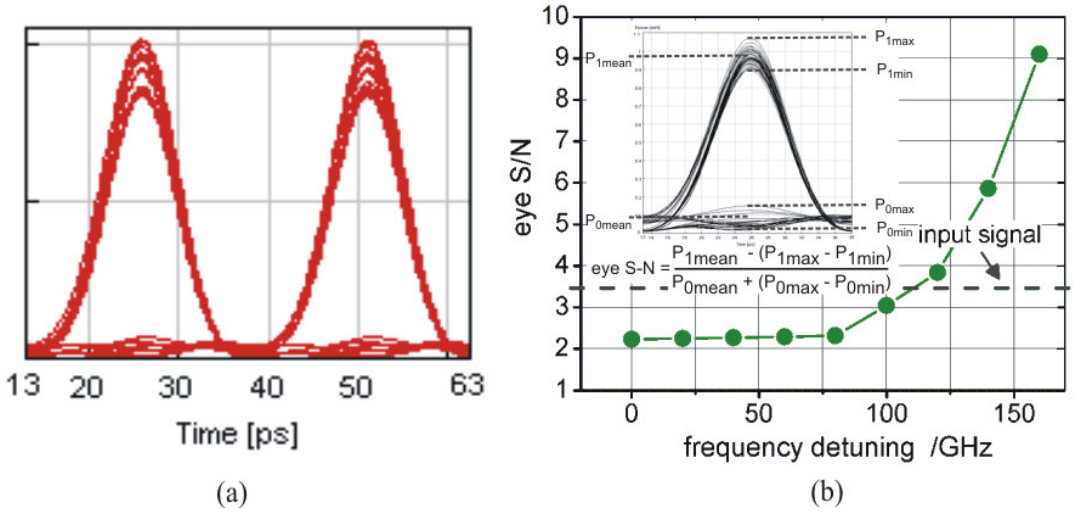

Fig. 6.12: Eye diagram of the ADC-converted 40 Gbit/s PRBS signal (4 mm UL-SOA) for a 160 GHz frequency detuned trapezoid filter (200 GHz FWHM, 3 dB/10 GHz) (a) and the eye S-N parameter of the output signal as a function of filter detuning relative to the CW wavelength (b). (Degraded input data signal shown in Fig. 6.9a).

6.2.3 Clock requirements for the regenerative ADC conversion

In the ADC-3R architecture, the pulse shape and timing stability of the converted data signal depends directly on the quality of the periodical clock signal. Hence, basic requirements on the clock signal for a regenerative wavelength conversion has to be evaluated. In the following, the performance of the ADC-3R regenerator operated in degraded 40 Gbit/s PRBS data streams (1550 nm) was numerically analysed for different quality of the 40 GHz clock signal (1560 nm). Based on the simulation results, the regenerative potential of the ADC-3R comprising a self-pulsating PhaseCOMB-laser can be estimated. The typical parameters of the PhaseCOMB-clock are (see Chapter 3): ER > 6 dB, RMS-jitter < 650 fs, and FWHM ~ 12.5 ps. In the simulations, a 4 mm UL-SOA (800 mA bias current) concatenated with a 200 GHz trapezoid BP-filter (3 dB/10 GHz steepness) detuned by 160 GHz relative to the CW wavelength (1555 nm) was utilised.

6.2.3.1. Clock extinction ratio

First, the impact of the extinction ratio of the ideal 40 GHz clock (100 fs RMS-jitter) is analysed. In order to define the limits of the ADC regeneration, the clock ER was varied from 2 dB up to 10 dB and the corresponding RMS-jitter of the converted PRBS signal was evaluated. The RMS-jitter of the degraded data signal was 1680 fs. Figure 6.13b summarises the results. The highest RMS-jitter of 1700 fs (2 dB clock ER) corresponds to the jitter of the input data signal. In this case, the relatively strong CW component of the clock signal saturates the amplifier gain, however the amplitude fluctuations and timing jitter are suppressed only partially. Further increase of the clock extinction ratio results in jitter improvement of the converted signal. From the simulations follows, the data jitter can be reduced down to 400 fs, when the clock ER exceeds 8 dB. It should be noticed that due to strong patterning effects of the degraded data signal (Fig. 6.9a), a jitter reduction near to an ideal clock signal cannot be achieved even in the case of 10 dB clock ER. Figure 6.13a shows the eye diagram of the ADC converted data signal for a clock ER of 3 dB.

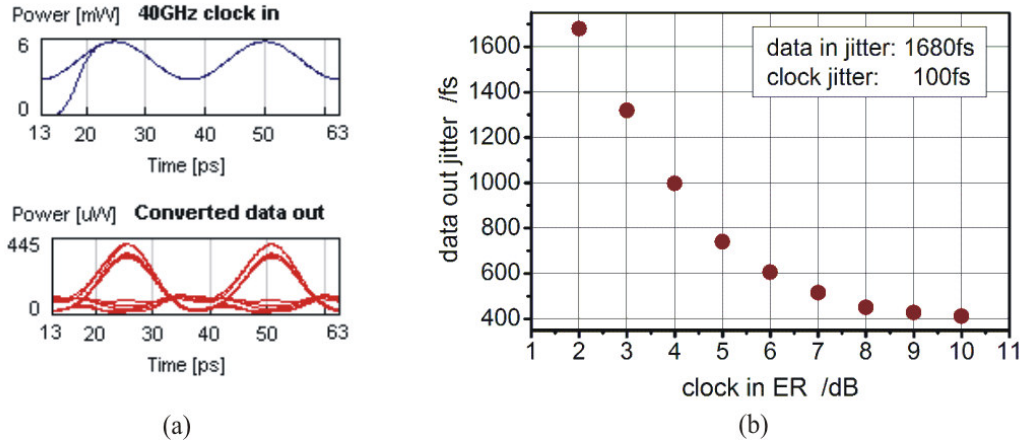

Fig. 6.13: (a) ADC converted 40 Gbit/s PRBS RZ signal (lower trace) for a clock signal of 3 dB ER (upper trace), (b) RMS-jitter of the converted data signal as a function of the 40 GHz clock ER.

6.2.3.2. Clock timing stability

The timing jitter of the clock signal is one of the most critical parameter of an optical 3R regenerator. In the following, the relation between the clock jitter and the RMS-jitter of the ADC converted signal are modelled. The results are summarised in Fig. 6.14b. Although the output data jitter remains in the whole range higher than the clock jitter, a faster data jitter increase for stronger degraded clock can be observed. The timing fluctuations can be halved at the regenerator output when the clock jitter amounts 700 fs. However, no regenerative wavelength conversion can be guaranteed, when the clock RMS-jitter exceeds 900 fs, as it is visible from the eye diagram depicted in Fig. 6.14a.

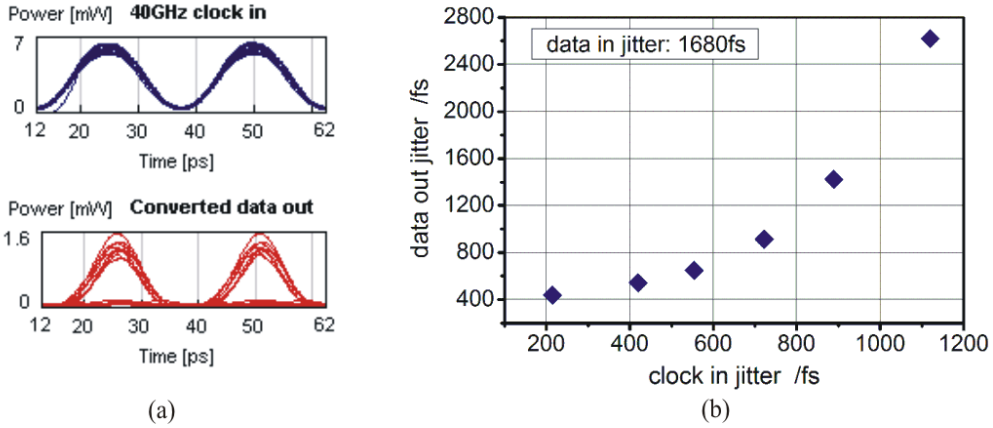

Fig. 6.14: (a) Eye diagrams of the converted 40 Gbit/s PRBS signal (lower trace) for a clock RMS-jitter of 900 fs (upper trace), (b) RMS-jitter of the output data signal as a function of the clock RMS-jitter in the ADC-3R regenerator.

6.2.3.3. FWHM of the clock pulses

Finally, the performance of the ADC-3R regenerator was simulated for three different pulse widths of the optical clock. First, a periodical signal with short pulses (6.5 ps FWHM) was propagated together with the degraded PRBS signal and the CW through the 4 mm UL-SOA (Fig. 6.15a). The pulses of the converted signal are obviously broadened at the regenerator output. This is because of the marks generation in the time slot between two clock pulses. However, the SOA gain is not stabilised sufficiently in this case, resulting in amplitude fluctuations. Furthermore, additional distortions at the zero level can be observed. Figure 6.15b shows the performance of the ADC-3R architecture by applying a sinusoidal clock signal. A regenerative wavelength conversion is achieved behind the regenerator, as discussed in the previous sections. The third simulation was performed for clock pulses with a FWHM of 18.5 ps (Fig. 6.15c). Except for a narrower pulse width, there is no difference in the signal quality compared to the previous configuration comprising a sinusoidal clock signal. Due to the effective gain saturation and fast XGM effects in the long amplifier, the stable periodical signal shapes the distorted data pulses, resulting in an effective power equalising and jitter reduction function. Thus, a regenerative wavelength conversion can be performed in the ADC-3R regenerator for clock signals with sinusoidal or even wider pulse form.

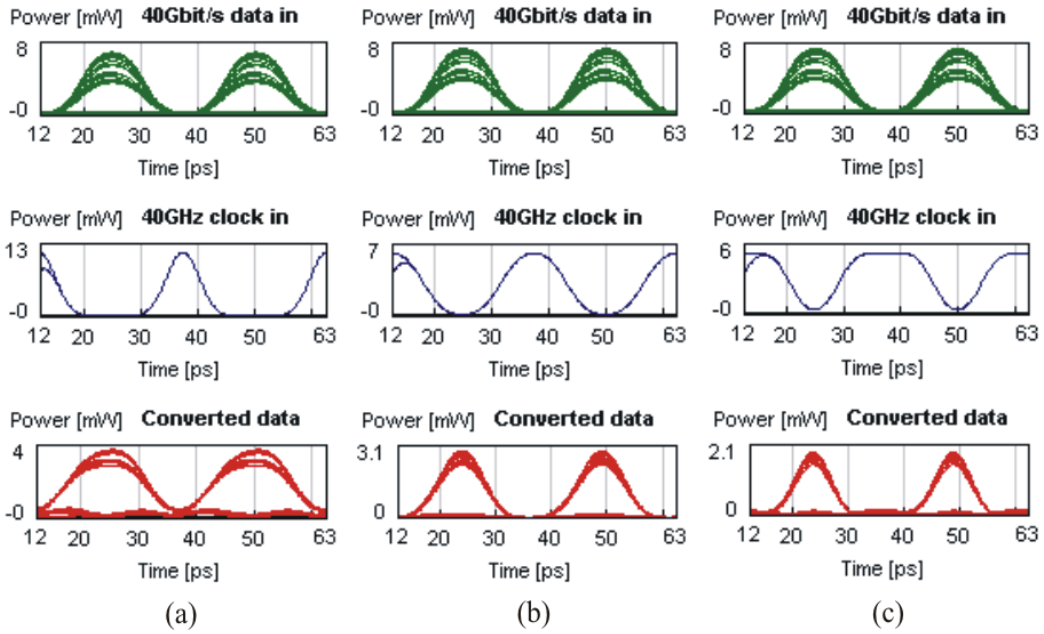

Fig. 6.15: Regenerative ADC wavelength conversion of degraded 40 Gbit/s data signal for different FWHM of the 40 GHz clock signal: 6.5 ps (a), 12.5 ps (b), and 18.5 ps (c).

In summary, signal degradations due to strong amplitude fluctuations and timing jitter can be effectively suppressed behind the ADC-3R regenerator. However, the signal interactions induced by XGM effects in ultra-long SOAs lead to distortions at the zero level of the converted signal. An improved wavelength conversion was demonstrated when increasing the amplifier length (up to 8 mm). Further improvement in the signal quality can be obtained when exploiting phase modulation in a concatenated processing filter. Eye S-N increase from 2.2 up to 9 has been shown for frequency detuning of 160 GHz between the trapezoid filter and the CW wavelength. The optimised 3R architecture provides a complete signal regeneration of strongly distorted PRBS signals. Finally, the impact of clock features on the ADC-3R regenerative performance was investigated. The RMS-jitter of the clock signal was identified as the most critical parameter. An ER ≥ 7dB and FWHM ≥ 12.5 lead to effective suppression of signal degradations. The simulation results prove the suitability of the PhaseCOMB-clock for implementation in the ADC-3R regenerator.

6.3 Experimental analysis of the ADC-3R regenerative performance

In the following experimental investigations, the regenerative performance of the ADC architecture operated in 40 Gbit/s PRBS 2^{31}-1 RZ degraded data streams was studied. The set-up is sketched in Fig. 6.16 (for the complete scheme see Appendix E2). The quality of the ideal data signal can be controlled in a degradation unit, enabling intentional signal

degradation in the amplitude and time domain (Appendix E3). The distorted PRBS signal was injected into the ADC-3R regenerator comprising the PhaseCOMB-clock and the 4 mm UL-SOA (200 mA/mm bias current) with tuneable Bessel BP-filter (1 nm FWHM). The quality of the wavelength-converted signal was analysed by an electrical sampling oscilloscope with precision time base and by BER measurements.

First, the robustness of the ADC-3R is demonstrated. The influence of slow amplitude fluctuations and timing jitter (relative data-clock position) is investigated. Furthermore, the impact of bit-to-bit data distortions is analysed. The quality of the data signal behind the ADC-3R is evaluated for different wavelength combinations of the data, clock and CW signal.

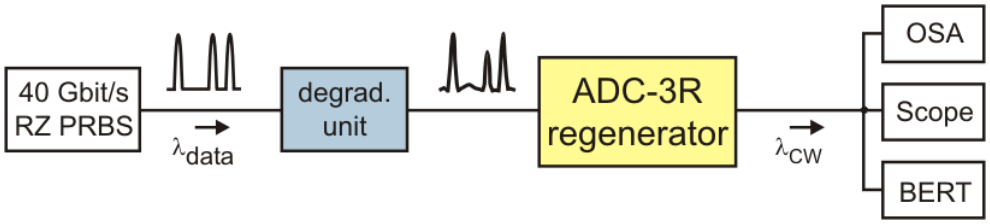

Fig. 6.16: Experimental set-up for performance analysis of the ADC-3R regenerator operated in 40 Gbit/s PRBS 2^{31}-1 RZ degraded data streams.

6.3.1 Robustness of the ADC-3R scheme against data distortions

The robustness of the ADC-3R regenerator against distortions in the amplitude and time domain was experimentally studied. The wavelengths of the data signal, clock and CW were set to 1555 nm, 1560 nm and 1550 nm, respectively. First, the impact of slow power variations was investigated. The average power level of the PRBS signal was continuously increased from –1 dBm up to +5 dBm and the quality of the converted signal was monitored using a sampling oscilloscope. During the measurements, the average power levels of the 40 GHz clock and of the CW signal were kept fixed at +5 dBm and –2 dBm, respectively. Figure 6.17a shows the input signal and the converted signal for two extreme cases. The upper diagram corresponds to the low input power (–1 dBm), while in the lower diagram the data signal was increased by 6 dB. In both cases, the quality of the converted signal remains nearly unchanged. Due to the high gain in the 4 mm UL-SOA, the data amplitude saturates to a fixed power level, resulting in a large dynamic range. However, slightly improved regeneration can be observed for lower data power (Fig. 6.17a, upper diagram). In this case, the dominant clock leads to stable pulse shaping at the ADC-3R output. The impact of the continuous data power increase can be clearly noticed in Fig. 6.17b. Here, the integration function of the sampling oscilloscope was used. It is obvious that the strong amplitude variations of the data signal (upper trace) in an extremely wide range (up to 6 dB) influence the eye opening of the converted signal (lower trace) only marginally.

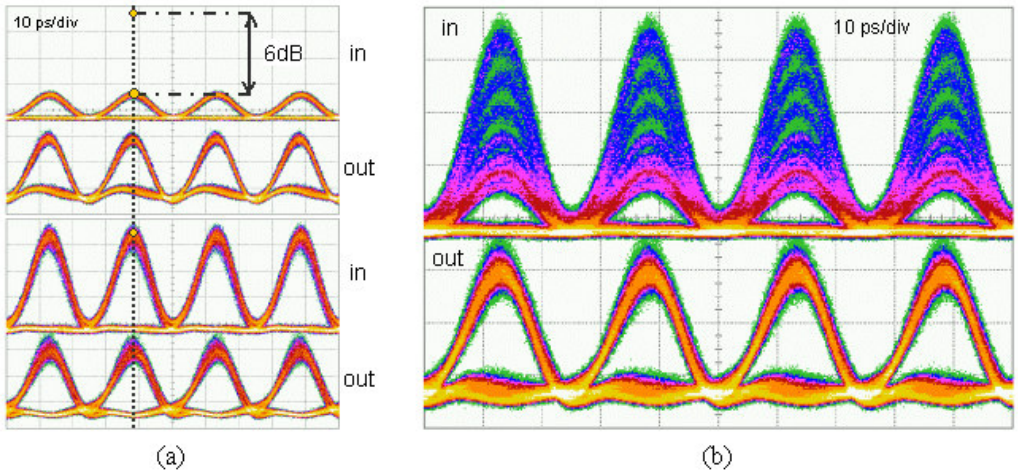

Fig. 6.17: (a) Eye diagrams of the PRBS 2^{31}-1 RZ signal at the ADC-3R input and behind the regenerator for P_{data} = -1 dBm (upper diagram) and P_{data} = +5 dBm (lower diagram), respectively, (b) impact of slow data power variations of 6 dB (upper trace) on the quality of the ADC converted signal (lower trace). λ_{data} = 1555 nm, λ_{clock} = 1560 nm, λ_{CW} = 1550 nm, P_{clock} = +5 dBm, P_{CW} = -2 dBm.

In the following, the impact of timing variations on the quality of the ADC wavelength converted signal is demonstrated. The power levels of the data, clock and CW signal in front of the 4 mm UL-SOA were set to +3 dBm, +5 dBm and –2 dBm, respectively. First, the relative position between the data and clock pulses was delayed exactly half a bit period to each other. The data signal was then continuously detuned by ±3 ps from its optimum timing position. The measurement results are depicted in Fig. 6.18. From the integrated view is clearly visible that the pulse shape of the converted signal (Fig. 6.18b lower trace) is not affected by the strong timing shift of the input signal (Fig. 6.18b upper trace). This is because the timing position of the converted signal is exclusively defined by the stable clock. However, some distortions can be observed in the zero level. The origin of these distortions is more obvious from Fig. 6.18a, where the eye diagrams of both signals for two extreme detuning positions are depicted. The envelope of the interleaved data-clock pulses (combined ADC signal) determines the zero level of the converted signal. The relative data-clock time shift leads to a short gap between both pulses. Due to fast cross gain modulation effects in the ultra-long SOA, the resulted gain variations influence amplitude of the co-propagated CW beam. Hence, a small ripple can be noticed in the space level of the converted signal. However, it should be noted that the investigation was performed for an extremely wide data-clock detuning. In the realistic systems timing fluctuations below 3 ps can be expected, demonstrating sufficient robustness of the ADC-3R against distortions in the time domain.

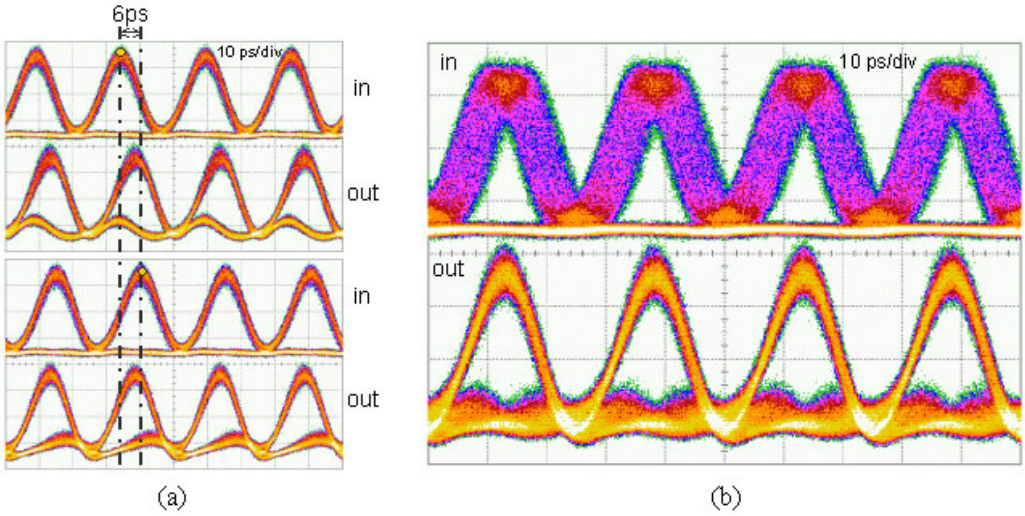

Fig. 6.18: (a) Eye diagrams of the PRBS data signal at the ADC-3R input and behind the regenerator for data-clock detuning of +3 ps (upper diagram) and –3 ps (lower diagram), respectively, (b) impact of the continuous data time shift in a range of 6 ps (upper trace) on the timing stability of the converted signal (lower trace). λ_{data} *= 1555 nm,* λ_{clock} *= 1560 nm,* λ_{CW} *= 1550 nm,* P_{data} *= +3 dBm,* P_{clock} *= +5 dBm,* P_{CW} *= -2 dBm.*

6.3.2 Dynamic power equalisation and jitter reduction function

In the following, the regenerative wavelength conversion of the ADC-3R architecture is analysed in strongly degraded 40 Gbit/s PRBS 2^{31}-1 RZ data streams. The regenerative potential of the proposed scheme for suppression of bit-to-bit amplitude and timing fluctuations is demonstrated by eye diagrams and finally by BER measurements.

6.3.2.1. Bit-to-bit amplitude fluctuations

The high quality 40 Gbit/s PRBS signal was intentionally distorted in the degradation unit before injecting into the regenerator (Fig. 6.19a). Due to strong patterning effects, the amplitude fluctuations result in an RMS-jitter of around 1100 fs. The wavelength and the power levels of the optical signals were set as mentioned previously (λ_{data} = 1555 nm, λ_{clock} = 1560 nm, λ_{CW} = 1550 nm, P_{data} = +3 dBm, P_{clock} = +5 dBm, P_{CW} = -2 dBm). Figure 6.19b depicts the eye diagram of the corresponding ADC converted signal behind the regenerator. It is obvious that the amplitude fluctuations are effectively suppressed; the timing jitter is reduced down to 578 fs. The eye opening is clearly improved at the ADC-3R output. It should be noticed that a conventional tuneable 1 nm BP-filter was used behind the UL-SOA instead of a properly designed processing filter. Although the filter was detuned relatively to the CW wavelength, the small steepness (below 1 dB/10 GHz) does not completely suppress the zero distortions. Improved regeneration efficiency can be expected when a step-like filter (as shown in the modelling) will be applied.

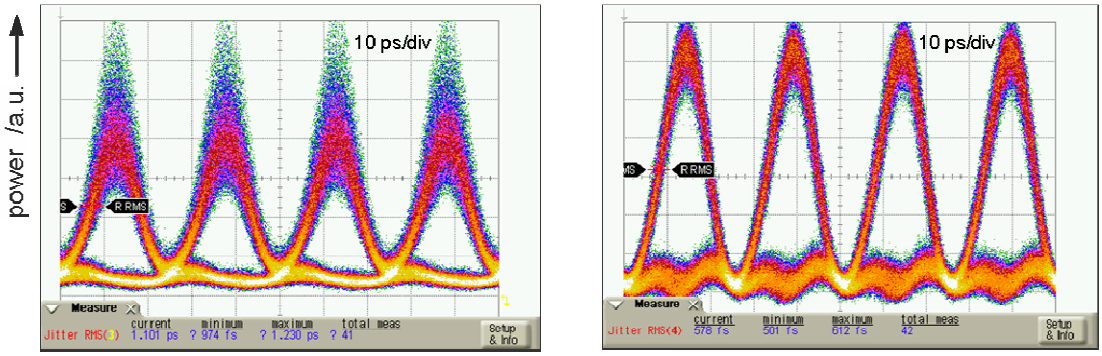

(a) (b)

Fig. 6.19: Eye diagram of the strongly degraded 40 Gbit/s PRBS signal (1555 nm, 1100 fs RMS-jitter) (a), and the wavelength converted data signal behind the ADC-3R regenerator (1550 nm, 578 fs RMS-jitter) (b). P_{data} = +3 dBm, P_{clock} = +5 dBm, P_{CW} = -2 dBm λ_{clock} = 1560 nm.

In the following, the suppression of bit-to-bit amplitude fluctuations in the ADC-3R is demonstrated (Fig. 6.20). The upper trace depicts the degraded PRBS pattern of the data injected into the regenerator, while the lower trace is related to the pattern of the converted signal. Comparing the input and the output pulse traces, the logical inversion behind the ADC-3R is clearly visible. The marks are converted to spaces and vice versa. Due to the high gain saturation in the UL-SOA, the strong amplitude fluctuations of 2 dB can be effectively suppressed to around 0.5 dB at the regenerator output.

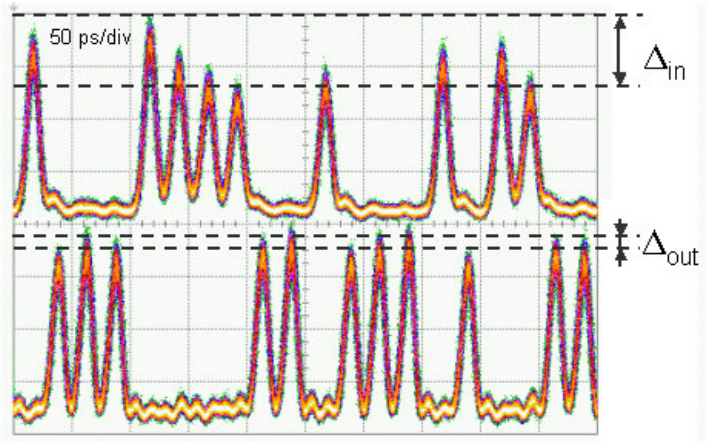

Fig. 6.20: Equalisation of the bit-to-bit amplitude fluctuations caused by patterning effects. Upper trace: input 40 Gbit/s PRBS RZ signal (1555 nm), lower trace: converted data signal (1550 nm) behind the ADC-3R regenerator.

6.3.2.2. Wavelength flexibility of the ADC-3R scheme

The ADC-3R was developed to provide flexible conversion to any wavelength defined by the CW signal. Hence, the regenerative performance of the proposed architecture was analysed for different wavelength combinations between the data, clock and CW signal. In order to quantify the functionality of the regenerator, the RMS-jitter of the converted signal

was measured as a function of the input data jitter. The clock wavelength was set to 1560 nm and 1540 nm, respectively. For each clock wavelength up-conversion (1550 nm to 1555 nm) and down-conversion (1555 nm to 1550 nm) was performed. The RMS-jitter of the input 40 Gbit/s PRBS RZ signal was varied from 600 fs up to 1390 fs. Figure 6.21 summarises the results. It is obvious that an effective jitter reduction function was obtained for all wavelength combinations. The evolution of the curves is nearly identical up to an input RMS-jitter of 900 fs. Further jitter increase leads to more efficient signal conversion towards shorter wavelengths (a typical feature for XGM based wavelength converters). Due to the stable clock signal (490 fs RMS-jitter), strong timing fluctuations (1300 fs RMS-jitter) could be reduced down to an RMS-jitter of 800 fs (up-conversion) and 700 fs (down-conversion) behind the ADC-3R regenerator.

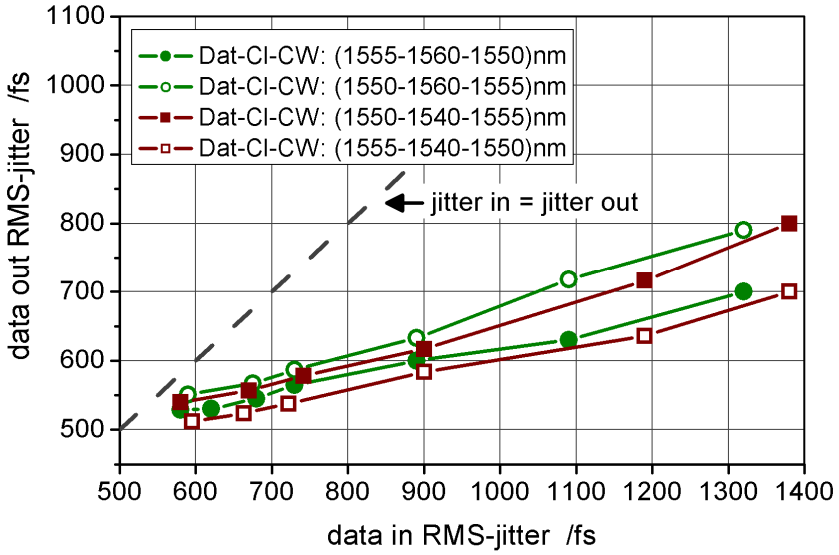

Fig. 6.21: RMS-jitter of the ADC converted 40 Gbit/s PRBS 2^{31}-1 RZ data signal as a function of the input data RMS-jitter for different wavelength combinations between the data, clock and CW signal.

6.3.2.3. BER analysis

Finally, the regenerative performance of the ADC-3R architecture was investigated by bit error ratio measurements. Also here, different wavelength combinations between the optical signals were considered. The evaluated BER as a function of received power at the bit error detector is shown in Fig. 6.22. The BER of the degraded input signal is depicted by filled triangles. It is clearly visible that the BER curves measured for the converted signals prove the eye diagram analysis. For all wavelength combinations, a negative penalty could be evaluated without any error floor down to a BER of 10^{-12}. An identical negative penalty of 2 dB at a BER of 10^{-9} was obtained for both clock wavelengths when a down-conversion (1555 nm to 1550 nm) was performed. In case of the up-conversion (1550 nm to 1555 nm), the ADC-3R regenerator shows better performance, when the clock wavelength was set to 1540 nm (-1.5 dB at 10^{-9} BER). Thus, the ADC-3R scheme provides a regenerative signal conversion to the shorter as well as to the longer wavelengths.

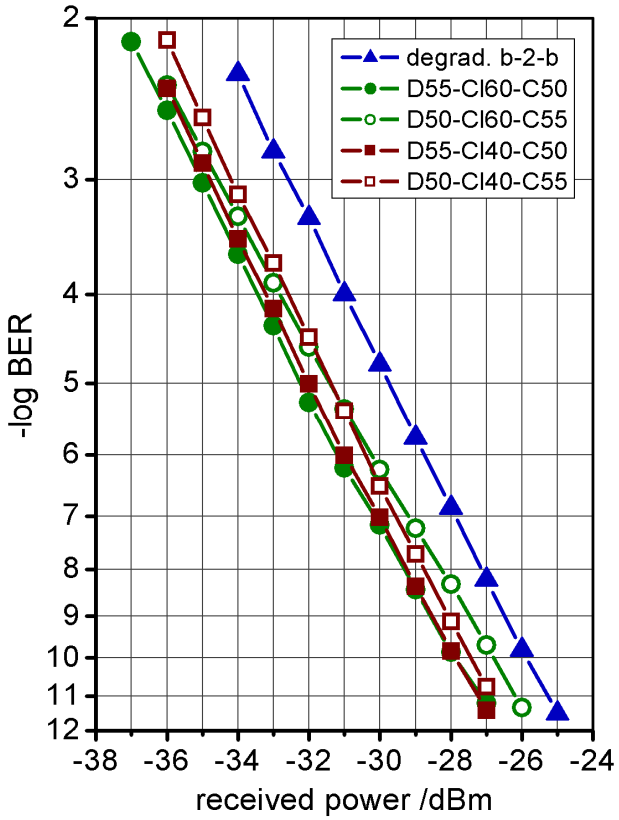

Fig. 6.22: BER curves of the degraded 40 Gbit/s PRBS 2^{31}-1 RZ signal (filled triangles) and of the converted data signal behind the ADC-3R regenerator for different wavelength combinations between the data, clock and CW signal.

In summary, the experimental investigations show robust operation of the ADC-3R regenerator. The saturation effects in the ultra-long SOA result in suppression of slow power variations in a wide dynamic range up to 6 dB. Due to the dominant impact of the clock in the ADC-3R scheme, a stable pulse shape of the converted signal was obtained for data detuning in the range of ±3 ps. The regenerative behaviour of the ADC-3R was analysed by operation in strongly degraded 40 Gbit/s PRBS 2^{31}-1 RZ data streams. Patterning effects (up to 2 dB bit-to-bit amplitude fluctuations) were effectively suppressed. A jitter reduction from 1300 fs down to 700 fs was demonstrated for different wavelength combinations. Finally, BER measurements were performed. A negative penalty of 2 dB (down-conversion) and 1.5 dB (up-conversion) was obtained behind the ADC-3R regenerator.

6.4 Conclusions

In this chapter, the wavelength converting 'Alternating Data-Clock' 3R regenerator developed in the frame of this thesis was presented. The ADC-3R is a compact semiconductor based architecture that effectively exploits fast inter-band gain dynamics of periodically modulated ultra-long SOAs. In contrary to a conventional 3R scheme, the data information is encoded to a wavelength defined by a free tuneable CW laser and not by a clock signal used for re-timing in the 3R circuit. Hence, flexible wavelength conversion within the whole C-band can be performed simply by adjusting the CW source to the ITU wavelength.

In the ADC-3R regenerator, the data pulses and the clock pulses are combined in the ADC signal (data and clock balanced in power, bit interleaved to each other) before injecting into the UL-SOA. The physical advantage of the ADC wavelength conversion is related to the inverse operation of the long SOA. The power level of the ADC signal remains constant in case of '1' bits (continuously saturated SOA) and drops down in case of a '0' bit, however only within a time slot between two clock pulses. Thus, the slow gain recovery effects that follow the PRBS envelope and usually degrade the XGM converted signals are eliminated in this scheme. Furthermore, the short recovery time and strong gain saturation of the UL-SOAs guarantee that the shape and timing of the output signal are defined by quality of the adjacent clock pulses (re-timing and re-shaping function in the ADC-3R). The XPM effects in the long amplifiers (frequency chirping) are further exploited in a concatenated processing filter for more efficient wavelength conversion. The optical filter improves the ER of the converted signals and, at the same time, acts as a decision stage for suppression of distortions at the zero power level.

The ADC-3R regenerator was characterised in 40 Gbit/s PRBS RZ data streams. Based on numerical simulations, effective suppression of amplitude fluctuations (from 3 dB down to 0.2 dB) and timing jitter (from 1680 fs down to 450 fs) of degraded data signals was achieved in the regenerator comprising SOA devices longer than 4 mm long and a stable sinusoidal clock signal (RMS-jitter < 500 fs). Due to the high frequency chirp generated in the UL-SOA (up to 70 GHz), an improvement of ER from 6 dB to 16 dB and of eye S-N from 3.5 up to 9 was demonstrated behind the frequency detuned trapezoid BP-filter (3 dB/10 GHz steepness). The performance of the ADC-3R scheme was finally proven experimentally by eye diagrams and BER measurements. Regenerative wavelength conversion of distorted 40 Gbit/s RZ data streams was achieved behind the all-optical 3R regenerator for different wavelength combinations (up-conversion, down-conversion).

The ADC-3R regenerator combines the main features important for operation in realistic high-speed optical networks. The flexible tuning of the output wavelength defined by the CW source performs signal routing and avoids wavelength collision in the optical switching nodes. The compact semiconductor devices can be further monolithically/hybrid integrated on a common platform, reducing the footprint and increasing the mechanical and thermal stability of the proposed scheme. Furthermore, pulses of a duty cycle close to 50 % make the ADC-3R suitable for deployment in spectrally efficient DWDM systems. As the ADC-3R comprises identical functional components as applied in the wavelength preserving OC-3R scheme, adaptive processing of PMD and CD distorted data signals as well as operation in asynchronous data packet flows can be performed.

7 Summary and outlook

In the framework of this thesis, two novel all-optical 3R regeneration schemes have been developed and evaluated by operation in 40 Gbit/s PRBS RZ data streams. Both 3R regenerators apply compact semiconductor devices, exploiting their nonlinearities for fast optical signal processing. The first 3R architecture is a wavelength and phase preserving regenerator that can act as a 3R regenerative amplifier in long-haul fibre transmission links, without necessity of any wavelength monitoring function. The second 3R scheme combines signal regeneration with wavelength conversion and has been designed for application in an optical switching node. The key functional components of the proposed schemes are the all-optical PhaseCOMB-clock and the ultra-long SOA.

The self-pulsating PhaseCOMB-laser for all-optical clock recovery is a well known device developed at FhG-HHI. In this work, the selected modules were characterised at optimised operation conditions in 40 Gbit/s data streams. The focus was given on the robustness of the optical clock as one of the most important feature for implementation in a 3R regeneration scheme. A stable sinusoidal clock signal (RMS-jitter below 500 fs) was recovered from PRBS data signals intentionally strongly distorted by reduced OSNR (down to 14 dB/0.1 nm) and by timing jitter of up to 1900 fs. Furthermore, the performance of the PhaseCOMB-clock was evaluated by processing of short PRBS packets. It could be demonstrated that the optical clock synchronises ultra-fast (~3 ns) to the incoming data packets and holds the synchronisation for longer than 10 ns. The asymmetric locking behaviour of the PhaseCOMB-clock was exploited in the design of the proposed 3R schemes for preamble free signal regeneration of asynchronous packet flows.

The second key functional component is the UL-SOA. Although conventional SOAs have been successfully applied in lot of experiments, the impact of device length as a parameter for optimising the nonlinearities has not been investigated consequently yet. The according studies have been performed in this work for the first time. Ultra-long amplifiers with a length between 2 mm and 8 mm were fabricated in the technology of FhG-HHI. The gain dynamics of UL-SOAs were studied numerically as well as experimentally using a pump-probe technique based on XGM wavelength conversion at 10 GHz. It could be demonstrated that the impact of ultra-fast (< 1 ps) intra-band effects on total SOA gain saturation effectively increases with the device length (by a factor of two in the 2 mm UL-SOA and even up to 13 times higher in the 8 mm UL-SOA compared to a conventional 0.5 mm SOA). The effective exploitation of the intra-band XGM proves the high speed potential (beyond 160 Gbit/s) of the ultra-long SOAs.

A very attractive feature identified in this work is related to acceleration of the inter-band transitions when increasing the SOA length. Based on the simulation results, the gain recovery time constants can be shortened significantly from 80 ps for a 0.5 mm SOA down to 10 ps evaluated in the 8 mm UL-SOA. A total gain recovery within 23 ps was experimentally measured in the 4 mm amplifier. Thus the 4 mm UL-SOA can be effectively exploited for XGM as well as XPM based signal processing even at 40 Gbit/s.

In the next step, the dynamic behaviour of the UL-SOAs controlled by a dominant 40 GHz periodical optical clock signal was analysed. Due to strong saturation effects and fast recovery processes in the UL-SOAs, the clock generates a short gain window while propagating through the long amplifier. The form of the gain window (FWHM, ER)

depends on the power level and pulse width of the clock signal as well as on the length of the SOA. Higher clock power and longer SOA device lead to shorter gain window with improved contrast ratio. For the 4 mm UL-SOA, gain window narrowing down to 5 ps and simultaneously an ER increase up to 16 dB was achieved. The impact of the gain window was exploited for re-shaping and re-timing of 40 GHz sinusoidal signals, intentionally degraded by timing fluctuations. In this case, the weak jittered signal was delayed by half a period relative to the dominant clock in order to propagate through the long amplifier within the gain window. Effective RMS-jitter reduction from 1400 fs down to 300 fs was demonstrated behind the periodically modulated 4 mm UL-SOA.

The novel technique based on periodical modulation of the ultra-long SOAs was successfully exploited in both 3R architectures developed in frame of this thesis, the 'Optically Clocked' 3R regenerator (OC-3R) and the 'Alternating Data-Clock' 3R regenerator (ADC-3R)

In the OC-3R regenerator, the signal quality improvement is performed simply by carving (jitter reduction) of the degraded data pulses in a periodically modulated UL-SOA that operates in highly saturated regime (power equalising). Hence, the wavelength and phase of the data signal remain preserved during the signal processing. In order to exploit the regenerative impact of the gain window, the weak data signal has to be injected into the UL-SOA bit interleaved to the dominant clock. The performance of the OC-3R scheme was characterised and optimised by operation in degraded 40 Gbit/s PRBS 2^{31}-1 RZ data streams. Based on the numerical studies, an effective regeneration can be achieved in the OC-3R comprising an UL-SOA with a length of at least 4 mm and a stable sinusoidal clock signal with RMS-jitter below 600 fs. It was demonstrated that the reduced extinction ratio of the input data signal could be preserved behind the OC-3R regenerator. ER improvement as well as distortions elimination at the zero power level can be further achieved in an optically clocked saturable absorber.

Experimental investigations have proven the regenerative functionality of the OC-3R scheme. Suppression of bit-to-bit amplitude fluctuations from 2 dB down to 0.5 dB and of the RMS-jitter from 1300 fs down to 600 fs was obtained for different data-clock wavelength combinations. A negative penalty of 2 dB (BER of 10^{-9}) was achieved for the regenerated 40 Gbit/s data signal behind the OC-3R. Based on the performed investigations, in the optimised configuration the dominant clock signal should be located near to the gain maximum of the UL-SOA, while the data wavelength can be flexibly tuned in the whole C-band. The OC-3R regenerator was successfully applied in several system experiments. An adaptive PMD compensation within a range from 0 ps up to 10.2 ps was demonstrated. Furthermore, pulse broadening and amplitude fluctuations due to residual chromatic dispersion of 34 ps/nm were effectively suppressed behind the optical regenerator. The asymmetric locking performance of the PhaseCOMB-clock was exploited in the OC-3R regenerator for preamble free processing of 40 Gbit/s packet data streams without loss of any bits.

In the second 3R scheme proposed in this work, the ADC-3R, simultaneous signal regeneration and wavelength conversion is performed. The operation principle is based on XGM and XPM interactions between the combined ADC signal and CW signal when propagating through the ultra-long amplifier. The combined ADC signal comprises the data and clock signal, which are delayed by half a bit period relative to each other and balanced in power. Thus, the converted data pulses are generated at the CW wavelength in the time slots between two stable clock pulses, resulting in re-timing and re-shaping

function of the novel 3R scheme. Furthermore, processing filter with a step-like transfer characteristic exploits the frequency chirping of the converted signals induced by the UL-SOA for improved efficiency of the ADC wavelength conversion. The ADC-3R regenerator was designed and characterised for processing of 40 Gbit/s PRBS 2^{31}-1 RZ data streams. Based on numerical simulations, suppression of strong amplitude fluctuations (from 3 dB down to 0.2 dB) and RMS-jitter (from 1680 fs down to 450 fs) was obtained behind the ADC-3R comprising a 4 mm UL-SOA. A converted data signals with improved ER (from 6 dB up to 16 dB) and eye S-N (from 3.5 up to 9) was obtained after applying a trapezoid BP-filter (3 dB/10 GHz steepness), detuned towards longer frequencies relative to the CW wavelength. The regenerative behaviour of the proposed 3R scheme was proven by experimental analysis. Effective suppression of slow variations in amplitude (up to 6 dB) and time (±3 ps) was demonstrated behind the ADC-3R regenerator. Furthermore, a negative penalty of 2 dB (down-conversion) and 1.5 dB (up-conversion) was measured at BER 10^{-9} for the ADC wavelength converted 40 Gbit/s data signals.

Both optical 3R regeneration schemes developed in frame of this thesis provide attractive features for implementation in realistic 40 Gbit/s transmission systems. The deployment of the OC-3R as an inline 3R regenerative amplifier can effectively improve the maximum transmission distances of long-haul fibre links. The ADC-3R regenerator can additionally perform signal routing and avoid wavelength collision in optical switching nodes of future transparent optical networks. Both schemes have been optimised for processing of RZ pulses of around 50 % duty cycle, which is an advantage when considering DWDM systems with high spectral efficiency. Furthermore, high nonlinearities at moderate power levels of the compact semiconductor devices guarantee cost effective operation as well as combine mechanical and thermal stability with integration possibility of the all-optical schemes on a common motherboard.

In outlook, the characteristics of the functional components can be subsequently optimised for improved performance of the proposed 3R architectures. Reducing the losses of the fibre-chip coupling in the UL-SOA (e.g. by integrated tapers) and shifting the gain maximum close to 1550 nm will contribute to higher efficiency and wider spectral usage of the exploited nonlinear effects. Based on the simulation results, an optically clocked saturable absorber can provide better robustness of the OC-3R regenerator against distortions at the space level. Furthermore, a specially designed processing filter with a steep (step-like) transmission characteristic can improve the wavelength conversion in the ADC-3R scheme. It has been shown that the PhaseCOMB-clock as well as the gain dynamics of the UL-SOAs (intra-band effects) provide high modulation bandwidth. Hence, ultra-fast processing of PRBS data streams at bit rates up to 160 Gbit/s can be fundamentally performed in the proposed 3R regeneration schemes. Finally, assembly and integration of the 3R circuits in compact line-cards will accomplish the requirements for a practicable solution in the reconfigurable all-optical DWDM networks.

8 Appendix

A Parameters of the SOA devices applied in the experimental investigations

0.5 mm SOA (AVT StdA-V3.0-040/05)

Parameter	Value	Unit
Device Chip Length	0.5e -03	m
Spontaneous Emission Peak Wavelength	1542e -09	m
Active Region Width	0.9e -06	m
Active Region Thickness	0.2e -06	m
Polarisation Dependent Gain	< 0.6	dB
Fibre-to-Fibre Maximum Gain	11.0	dB
Saturation Output Power	5.0	dBm

2 mm UL-SOA (AVT 110/04_GS)

Parameter	Value	Unit
Device Chip Length	2.0e -03	m
Spontaneous Emission Peak Wavelength	1561e -09	m
Active Region Width	0.9e -06	m
Active Region Thickness	0.2e -06	m
Polarisation Dependent Gain	< 4.0	dB
Fibre-to-Fibre Maximum Gain	19.0	dB
Saturation Output Power	9.0	dBm

4 mm UL-SOA (AVT 106/03_Eh)

Parameter	Value	Unit
Device Chip Length	4.0e -03	m
Spontaneous Emission Peak Wavelength	1567e -09	m
Active Region Width	0.9e -06	m
Active Region Thickness	0.2e -06	m
Polarisation Dependent Gain	< 4.0	dB
Fibre-to-Fibre Maximum Gain	11.0	dB
Saturation Output Power	7.0	dBm

B Transmission-Line Laser Model used for simulation of the SOA gain dynamics

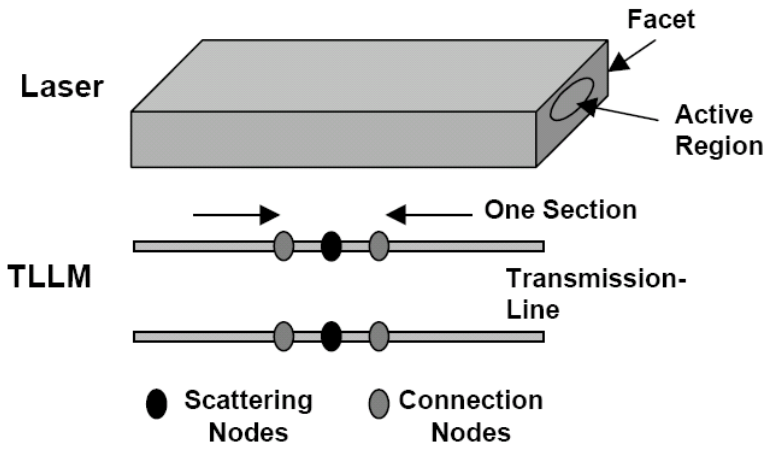

B1: Schematic of a semiconductor laser and its Transmission-Line Laser Model (TLLM), showing a node within a model section [172].

The analysis of semiconductor optical amplifiers using VPIcomponentMaker™ simulation tool is based on the Transmission-Line Laser Model (TLLM). In this model, the laser is divided into longitudinal sections, as shown in Figure B1. Each section contains scattering nodes representing the gain (stimulated emission), loss (scattering and absorption), noise (spontaneous emission), grating coupling, and index changes that optical waves experience while passing through the section. The nodes of adjacent sections are connected by transmission-lines, which represent the waveguide-propagation delay. The output of the model is a stream of optical field samples separated by the model time step. The optical spectrum can be easily calculated by taking a Fourier transform of the samples. Thus, the TLLM allows the full dynamics of semiconductor lasers to be efficiently simulated, including the spectral dynamics. The TLLM model is able to predict:

- Nonlinearities during analogue modulation
- Evolution of lasing spectra during modulation
- CW spectra performance and purity (multi-mode, single-mode, noise floors)
- Optical noise (intensity noise spectra, Amplified Spontaneous Emission)
- RF noise (Relative Intensity Noise, excess noise due to feedback, chaos)
- Effect of external optical components, optical injection
- Modulation response (IM, FM, magnitude and phase)

The parameters of the SOA model used for the numerical investigations in this work were compared and adapted to the typical behaviour of the devices fabricated at FhG-HHI. The main values are listed in Tab. B2.

Parameter	Value	Unit
Active region width	0.9e-06	m
Active region thickness	0.2e-06	m
Confinement factor	0.3	
Group effective index	3.7	
Left facet reflectivity	1.0e-04	
Right facet reflectivity	1.0e-04	
Optical coupling efficiency	1.0	
Fixed internal loss	4000	1/m
Differential refractive index	-1.11e-26	m^3
Chirp reference carrier density	2.3e+24	1/m
Current injection efficiency	1.0	
Linear recombination coeff.	1.0e+08	1/s
Bimolecular recombination coeff.	1.0e-16	m^3/s
Auger recombination coeff.	1.0e-41	m^6/s
Linear material gain coeff.	3.0e-20	m^2
Transparency carrier density	1.5e+24	1/m^3
Nonlinear gain coefficient	1.0e-23	1/m^3
Nonlinear gain time constant	200e-15	s
Gain peak frequency	0.0	Hz
Gain peak freq. carrier dependence	0.0	Hz*m^3
Gain coefficient spectral width	1.0e+15	Hz
Gain coef. spectral width carrier depend.	0.0	Hz*m^3
Population inversion parameter	2	
Spontaneous emission peak frequency	0.0	Hz
Spont. emission freq. carrier dependence	0.0	Hz*m^3
Spont. emission spectral width	1.0e+15	Hz
Spont. emission spect. width carrier dep.	0.0	Hz*m^3
Initial carrier density	1.0e+24	1/m^3

B2: Parameter values used in the SOA model for numerical investigations.

C ASE spectra of the SOA devices fabricated at FhG-HHI

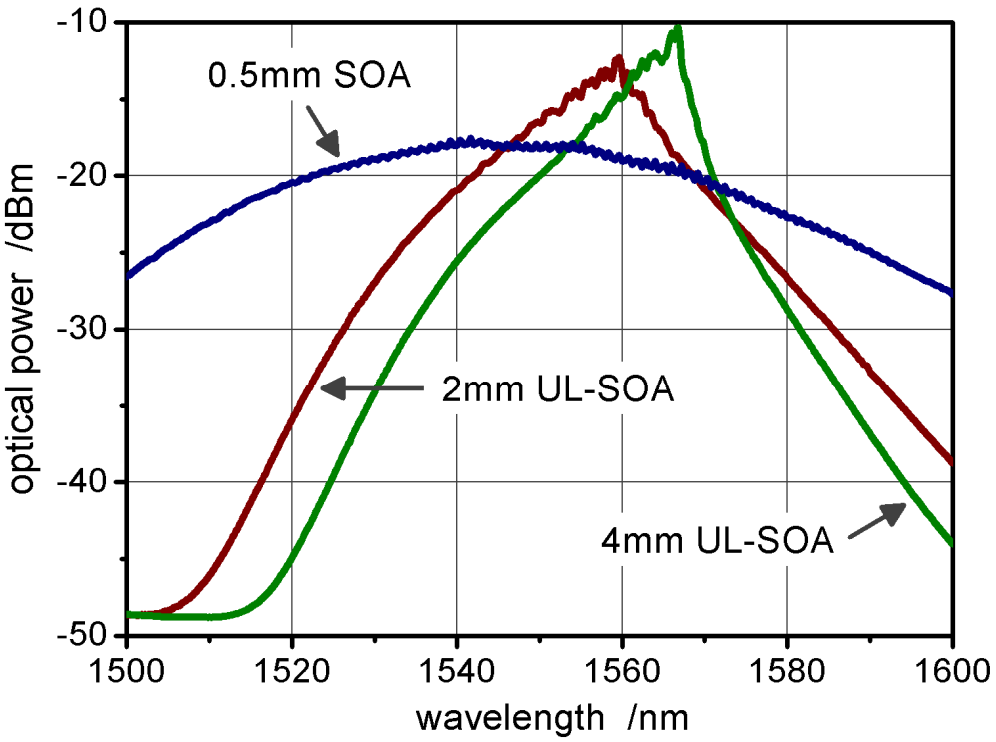

C1: ASE spectra of the SOA devices applied in the experimental investigations referred in this work (I_{SOA} = 200 mA/mm).

D Waveform characterisation using Agilent 86100B Infiniium DCA

The Agilent 86100B Infiniium DCA wide-bandwidth oscilloscope was used in the experimental investigations for characterisation of the optical waveforms. An automatic measurement of the timing jitter and eye signal-to-noise ratio (eye S/N) was exploited, in order to quantify the quality of the 40 Gbit/s data signals. In the following, the definition of both parameters is given [173].

Jitter: RMS and Peak-to-peak

The timing jitter is a measure of the instability of a signal from its ideal time position. In an RZ signal, jitter is manifested as a broadening in both the rising and falling edges of the eye. To characterise the jitter, histograms are constructed on the first edge from the left of the screen. The *peak-to-peak jitter* is determined by finding the difference between the extreme data points of the histogram. The *RMS jitter* is determined by calculating the standard deviation σ of the histogram (Fig. D1).

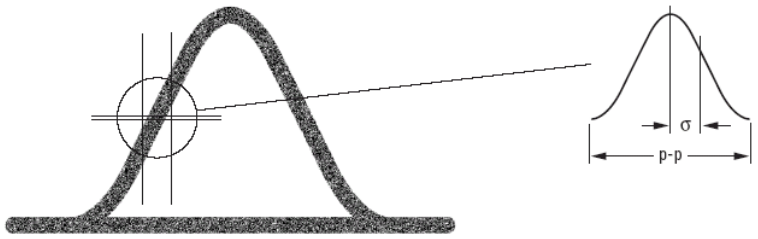

D1: Eye diagram of an RZ signal indicating measurement of the peak-to-peak jitter and RMS-jitter.

Eye signal-to-noise ratio

The eye S/N parameter is a measure of the actual eye opening. The "signal" is the information power of the signal indicated by the difference between the '1' and '0' level, The "noise" is the combined standard deviations of the '1'level spread and the '0' level spread (Fig. D2). The measurement is constructed as: *(1 level – 0 level)/*$(\sigma_1 + \sigma_0)$

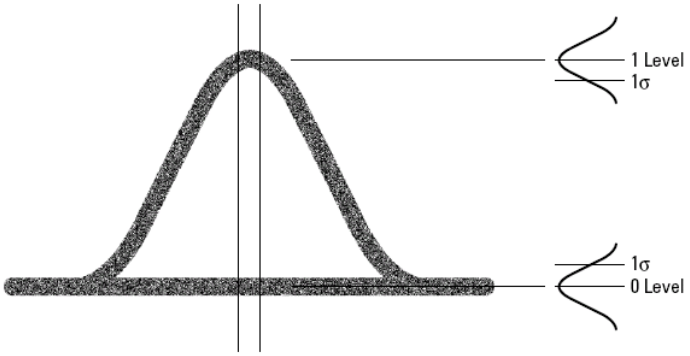

D2: Eye diagram of an RZ signal indicating measurement of the eye signal-to-ratio parameter (eye S/N).

E Experimental set-ups

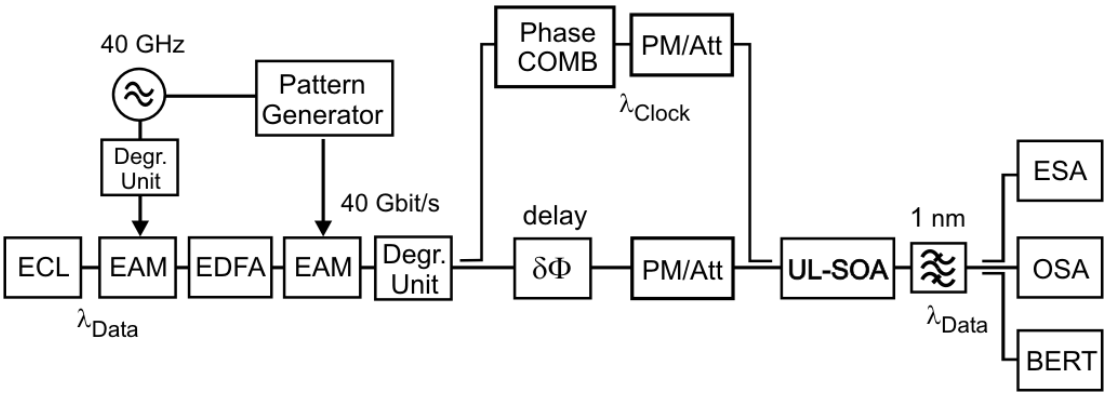

E1: Experimental set-up for performance analysis of the OC-3R regenerator.

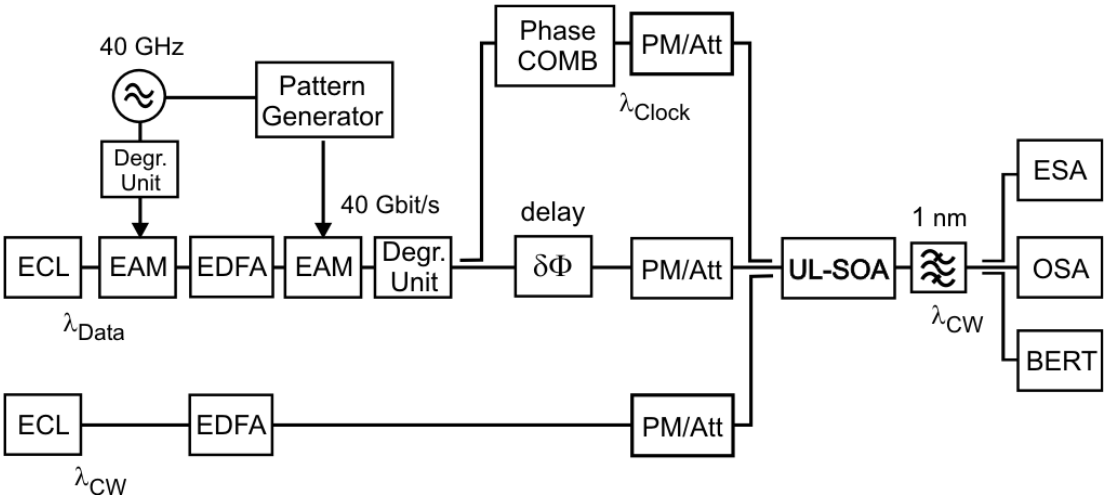

E2: Experimental set-up for performance analysis of the ADC-3R regenerator.

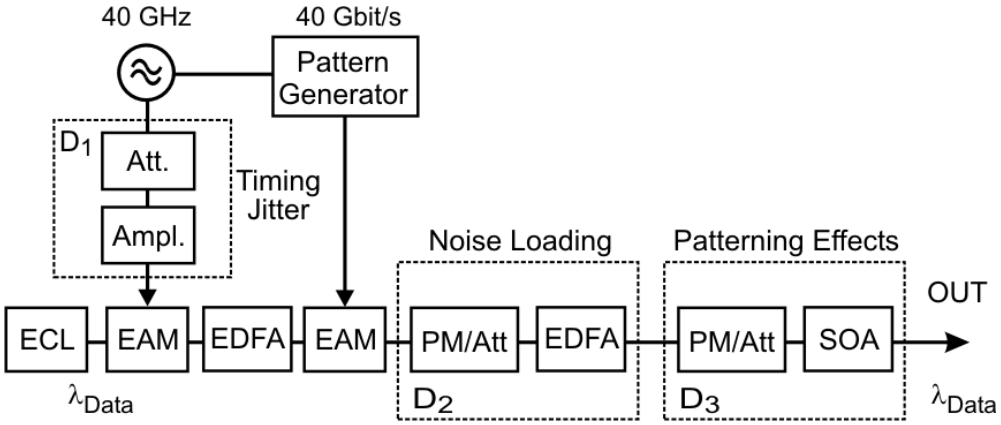

E3: Set-up of the degradation unit enabling intentional inducing of different types of distortions (D_1, D_2, D_3) into the 40 Gbit/s PRBS RZ data signal.

D_1 – addition of timing jitter to the 40 GHz el. clock signal used for pulse carving.

D_2 – degradation of the data OSNR by strong signal attenuation and re-amplification.

D_3 – generation of bit-to-bit amplitude fluctuations caused by patterning effects in SOA.

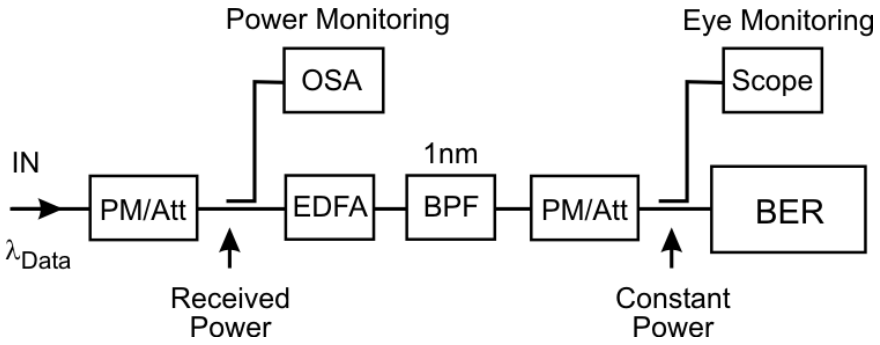

E4: Set-up of the bit error ratio receiver indicating the location of the evaluated received power for the BER estimation.

F List of Abbreviations and Symbols

3R	re-amplification, re-timing, re-shaping
ADC-3R	alternating data-clock 3R
AFL	active feedback laser
AM	amplitude modulation
AR	anti reflection
ASE	amplified spontaneous emission
ATT	attenuator
BER	bit error ratio
BP	band-pass
CD	chromatic dispersion
CW	continuous wave
DC	direct current
DCF	dispersion compensating fibre
DEMUX	demultiplexer
DFB	distributed feedback laser
DGD	differential group delay
DI	delayed interferometer
DQS	dispersive Q-switching
DSF	dispersion shifted fibre
DWDM	dense wavelength division multiplexing
EAM	electro-absorption modulator
ECL	external cavity laser
EDFA	erbium doped fibre amplifier
ER	extinction ratio
ESA	electrical spectrum analyser
FP	Fabry-Pérot
FSR	free spectral range
FWHM	full width at half of maximum
FWM	four wave mixing
GVD	group velocity delay
IFWM	intra-channel FWM
IXPM	intra-channel XPM
KFL	Kerr fibre modulator
MLL	mode locked laser
MLLD	mode locked laser diode
MOD	modulator
MOVPE	metalorganic vapour phase epitaxy
MQW	multi quantum well
MUX	multiplexer
MZI	Mach-Zehnder interferometer
NOLM	nonlinear optical loop mirror
NRZ	non return-to-zero
OC-3R	optically clocked 3R

O/E	optical/electrical
OPLL	optical phase locked loop
OSA	optical spectrum analyser
OTDM	optical time division multiplexing
OXC	optical cross-connect
PhaseCOMB	phase controlled mode beating
PIC	photonic integrated circuit
PM	power monitor
PMD	polarisation mode dispersion
PMF	polarization maintaining fibre
PRBS	pseudo-random bit sequence
RF	radio frequency
RMS	root mean square
RW	ridge waveguide
RZ	return-to-zero
SA	saturable absorber
SDH	synchronous digital hierarchy
SI	Sagnac interferometer
SLALOM	Semiconductor laser amplifier in a loop mirror
SOA	semiconductor optical amplifier
SONET	synchronous optical network
SP	self-pulsation
SPM	self-phase modulation
SSB	single side band
SMF	single mode fibre
TE	transverse electrical
TM	transverse magnetical
TOAD	terahertz optical asymmetric demultiplexer
UL-SOA	ultra-long semiconductor optical amplifier
UNI	ultrafast nonlinear interferometer
VCO	voltage controlled oscillator
WDM	wavelength division multiplexing
XGM	cross gain modulation
XPM	cross phase modulation

G Publications and Talks

1 C. Bornholdt, J. Slovak, M. Möhrle, B. Sartorius, ”Application of a 80 GHz All-Optical Clock in a 160 km Transmission Experiment,” in Proc. of OFC`02, paper TuN6, 2002.

2 C. Bornholdt, B. Sartorius, J. Slovak, M. Möhrle, R. Eggemann, D. Rohde, G. Grosskopf, “60GHz Millimetre-Wave Broadband Wireless Access Demonstrator for the Next Generation Mobile Internet,” in Proc. of OFC`02, paper TuV4, 2002.

3 G. Grosskopf, B. Sartorius, C. Bornholdt, B. Kuhlow, G. Przyrembel, S. Zinal, D. Rohde, R. Eggemann, J. Slovak, M. Möhrle, ”60 GHz-Millimetre-Wave Generation and Beam-Forming in Hybrid-Fibre-Radio Systems for Broadband-Wireless Access,” in Proc. of URSI`02, paper D1.O.2, 2002.

4 C. Bornholdt, J. Slovak, B. Sartorius, “Novel All-Optical 3R Regenerator Concept Demonstrated at 40 Gbit/s,” in Proc. of ECOC`02, post-deadline paper PD 4.8, 2002.

5 B. Sartorius, C. Bornholdt, J. Slovak, H. P. Nolting, ”Novel 3R Architecture with Wavelength Flexible Output,” in Proc. of ECOC`02, paper 6.3.3, 2002.

6 B. Sartorius, S. Bauer, C. Bornholdt, M. Mörle, H. P. Nolting and J. Slovak, “All-Optical Clock Recovery for Signal Processing and Regeneration,” in Proc. of LEOS Summer Topical 2002, invited paper TuO1, 2002.

7 J. Slovak, C. Bornholdt, B, Sartorius, H. P. Nolting, ”Novel All-Optical 3R Regenerator at 10 Gbit/s,” in Proc. of CLEO`03, paper CJ2-2-MON, 2003.

8 J. Slovak, C. Bornholdt, B. Sartorius, M. Möhrle, H. P. Nolting, “All-Optical 3R Regenerator Applying Compact Semiconductors for Clock Recovery and Decision,” in Proc. of ECIO`03, paper WeB3.4, 2003.

9 C. Bornholdt, J. Slovak, M. Möhrle, B. Sartorius, “Jitter Analysis of All-Optical Clock Recovery at 40 GHz,” in Proc. of OFC`03, paper MF 97, 2003.

10 T. Tekin, C. Bornholdt, J. Slovak, M. Schlak, B. Sartorius, J. Kreissl, S. Bauer, Ch. Bobbert, W. Brinker, B. Maul, Ch. Schmidt, H. Ehlers, “Semiconductor Based True All-Optical Synchronous Modulator for 3R Regeneration,” in Proc. of ECOC`03, paper We4.P.119, 2003.

11 S. Bauer, O. Brox, C. Bornholdt, J. Slovak, J. Kreissl, B. Sartorius, “Self-Pulsating Multi-Section DFB Lsers and their Applications,” in Proc. of LEOS`03, paper ME1, 2003.

12 J. Slovak, C. Bornholdt, U. Busolt, G. Braman, Ch. Schmidt, H. Ehlers, H. P. Nolting, B. Sartorius, “Optically Clocked Ultra Long SOAs: A Novel Technique for High Speed 3R Signal Regeneration,” in Proc. of OFC`04, paper WD4, 2004.

13 J. Slovak, C. Bornholdt, U. Busolt, G. Bramann, H. P. Nolting, B. Sartorius, “Dynamic behavior of optically clocked 4mm UL-SOA at 40 Gbit/s,” in Proc. of Integrated Optics and Photonic Integrated Circuits, SPIE`04, Vol. 5451, pp. 147-155, 2004.

14 C. Bornholdt, J. Slovak, B. Sartorius, “Semiconductor-based all-optical 3R regenerator demonstrated at 40 Gbit/s,” El. Letters, Vol. 40, No. 3, pp.192-194, 2004.

15 H. P. Nolting, S. Bauer, C. Bornholdt, J. Slovak, B. Sartorius, “High Speed Self-Pulsating Lasers for 3R Regeneration,” in Proc. of OAA`04, 2004.

16 C. Bornholdt, J. Slovak, H. J. Thiele, and B. Sartorius, “Optical versus Electrical Clock Recovery at 40 Gbit/s,” in Proc. of ECOC`04, paper We4.P.08, 2004.

17 J. Slovak, C. Bornholdt, B. Sartorius, ”All-Optical 3R Regenerator for Asynchronous Data Packets at 40 Gbit/s,” in Proc. of ECOC`04, paper We2.5.7, 2004.
18 J. Slovak, C. Bornholdt, B. Sartorius, “Wavelength-Preserving All-Optical 3R Regenerator, ”Communications Scientific Letters of the University of Zilina, , pp. 84-88, December 2004.
19 C. Bornholdt, J. Slovak, Ch. Schmidt, B. Sartorius, “Mitigation of PMD at 40 Gb/s Using an Optically Clocked 3R Regenerator,” in Proc. of OFC`05, paper OTuO6, 2005.
20 B. Sartorius, S. Bauer, C. Bornholdt, H. P. Nolting, M. Schlak, J. Slovak, H. J. Wünsche, “Signal processing in SOAs – Beyond the limits of carrier relaxation,” in Proc. of OAA`05, invited paper SuB5, 2005.
21 C Bornholdt, J. Slovak, B. Sartorius, M. Schlak, Ch. Schmidt, “Optical phase comb generator using pulse compression in ultra-long semiconductor amplifiers,” in Proc. of ECOC`05, paper Tu.1.5.6, 2005.
22 J. Slovak, T. Tekin, C. Bornohldt, B. Sartorius, E. Lach, M, Schmidt, S. Vorbeck, R. Leppla, “Self-pulsating laser based all-optical clock recovery applied in 421 km field experiment for 170.6 : 42.7 Gbit/s OTDM demultiplexing,” in Proc. of ECOC`05, paper Th.3.1.3, 2005.
23 B. Sartorius, C. Bornholdt, J. Slovak, M. Schlak, Ch. Scmidt, A. Marculescu, P. Vorreau, S. Tsadka, W. Freude, J. Leuthold, “All-Optical DPSK Wavelength Converter Based on MZI with Integrated SOAs and Phase Shifters,” in Proc. of OFC`06, paper OWS6, 2006.
24 J. Slovak, C. Bornholdt, S. Bauer, J. Kreissl, M. Schlak, and B. Sartorius “Novel Concept for All-Optical Clock Recovery from NRZ Format PRBS Data Streams,“ in Proc. Of OFC`06, paper OthS6, 2006.
25 J. Slovak, C. Bornholdt, J. Kreissl, S. Bauer, M. Biletzke, M. Schlak, and B. Sartorius “Bit Rate and Wavelength Transparent All-Optical Clock Recovery Scheme for NRZ Coded PRBS Signals,” Photon. Technol. Lett., Vol. 18, No. 7, pp. 844 – 846, April 2006.

G1 Patents

B. Sartorius, C. Bornholdt, J. Slovak,
“Wellenlängen-erhaltender optischer Signalregenerator“

Deutsches Patent DE 103 44 319.3, International: Aktenzeichen PCT/DE2004/002003, Veröffentlichungsnummer WO2005/029734.

9 Bibliography

1 B. Mikkelsen, C. Rassmussen, P. Mamyshev, F. Liu, S. Dey, F. Rosca, "Deployment of 40 G/s systems: Technical and cost issues," in Proc of OFC`04, paper ThE6, 2004.

2 A. Jourdan, F. Bakhti, L. Berthelon, Bruyere, M. Chbar, D. Chiaroni, C. Drion, G.J. Eilenberger, M. Garnot, F. Masetti, P.A. Pierrer, and M. Renaud, "Key building blocks for high-capacity WDM photonic transport networks," J. of Select. Area in Communications, Vol. 16, No. 7, pp. 256 – 259, 1998.

3 A. H. Gnauck, G. Raybon, S. Chandrasekhar, J. Leuthold, C. Doerr, L. Stulz, A. Agraval, S. Banerjee, D. Grosz, S. Hunsche, A. Kung, A. Mardhelyuk, D. Maywar, M. Movassaghi, X. Wei, D. M. Gill, "2.5 Tb/s (64x42.7 Gb/s) Transmission Over 40x100 km NZDSF Using RZ-DPSK Format and All-Raman-Amplified Spans," in Proc of OFC`02, post deadline paper PD FC2, 2002.

4 C. Rasmussen, T. Fjelde, J. Bennike, F. Liu, S. Dey, B. Mikkelsen, P. Mamyshev, P. Serbe, Y. Akasaka, D. Harris, D. Gapnstev, P. R. Hall, "DWDM 40G transmission over trans-Pacific distance (10,000 km) using CSRZ-DPSK, enhanced FEC and all-Raman amplified 100 km UtraWave fiber spans," in Proc of OFC`03, post deadline paper PD 18, 2003.

5 T. Ono, Y. Yano, K. Fukuchi, T. Ito, H. Yamazaki, Y Yamaguchi, and K. Emura, "Characteristics of Optical Duobinary Signals in Terabit/s Capacity, High-Spectral-Efficiency WDM Systems," J. of Lightwave Technology, Vol. 16, pp. 788-797,1998.

6 J. M. Kahn and K. Ho, "Advanced modulation and signal processing techniques for 40 Gb/s optical transmission systems," in Proc of SPIE`04, paper 4872-04, 2004.

7 O. Lecrec, B. Dany, , D. Rouvillain, P. Brindel, E. Desurvire, C. Duchet, A. Shen, F. Devaux, A. Coquelin, M. Goix, S. Bouchoule, L. Fleury, and P. Nouchy, "Simultaneously regenerated 4 x 40Gbit/s dense WDM transmission over 10,000km using single 40GHz INP Mach-Zehnder modulator, " Electronics Letters, Vol. 36, No. 18, pp. 1574 - 1575, 2000.

8 N. Shinomiya, T. Hoshida, Y. Akiyama, H. Nakashima, T. Terahara, M. Miyabe and N. Nakayama, "Translucent Photonic Networking Dimensioning for Equipment Cost Minimization," in Proc of OFC`04, paper FH6, 2004.

9 D. Breuer and K. Petermann, "Comparison of NRZ- and RZ-Modulation Format for 40-Gb/s TDM Standard-Fiber Systems," Photonics Technology Letters, Vol. 9, No. 3, March 1997.

10 H. Sunnerud, M. Karlsson, and P. A. Andrekson, "A Comparison Between NRZ and RZ Data Formats with Respect to PMD-Induced System Degradation," IEEE Photonics Technology Letters, Vol. 13, No. 5, May 2001.

11 A. Hodzic, "Investigations of high bit rate optical transmission systems employing a channel data rate of 40 Gb/s," PhD thesis, Technische Universität Berlin, 2004.

12 G.P. Agrawal, "Fiber optics communication systems," ISBN 0-471-17540-4, John Wiley and Sons Inc. 3. Edition, 2002.

13 ITU-T Recommendation G.691 Series G: Transmission systems and media, digital systems and networks – Optical interfaces for single channel STM-64, STM-256 and other SDH systems with optical amplifiers, October 2000.

14 A. Pizzinat, A. Dchiffini, F. Albeti, F. Matera, A.N. Pinto, and P. Almeida, “40 Gb/s systems on G.625 fibres: Comparison between periodic and all-at-the-end dispersion compensation,“ Journal of Lightwave Technology. Vol. 20, No. 9, pp. 1673 – 1679, Sepetember 2002.

15 Y. Li, Ch. Kim, G. Li, Y. Kaneko, R.L. Jungerman, and O. Buccafusca, “Wavelength and polarization insensitive all-optical clock recovery from 96-Gb/s data by using a two-section gain-coupled DFB laser,“ Photonics Technology Letters, Vol. 15, No. 4, pp. 590 – 592, April 2003.

16 Y. Li and G. Li, “80 Gbit/s all-optical clock recovery using two-section gain-coupled DFB laser,” Electron. Letters Vol. 38, No. 15, pp. 892 – 893, July 2002.

17 B. Sartorius, M. Möhrle, S. Reichenbacher, H. Preier, H.-J. Wünsche, and U. Bandelow, “Dispersive self-Q-switching in self-pulsating DFB lasers,” J. of Quantum Electronics, Vol. 33, No. 2, pp. 211 – 218, February 1997.

18 C. Bornholdt, S. Bauer, M. Möhrle, H.P. Nolting, and B. Sartorius, “All optical clock recovery at 80 GHz and beyond,” in Proc. of ECOC`01, Th.F.1.2, 2001.

19 H. P. Nolting, S. Bauer, C. Bornholdt, J. Slovak, B. Sartorius, “High Speed Self-Pulsating Lasers for 3R Regeneration,” Optical Amplifiers and Their Applications OAA`04, 2004.

20 H. Yokoyama, Y. Hamashito, H. Kurita, I. Ogura, T. Shimizu, R. Kuribayashi, M. Shirane, and H. Yamada, “Highly reliable mode-locked semiconductor lasers and their applications,” in Proc. of CLEO`01, WJ1, 2001.

21 H. Kurita, T. Shimizu, and H. Yoikoyama, “All-optical clock extraction at bit rates up to 80 Gbit/s with monolithic mode-locked laser diodes,” in Proc of CLEO`97, CtuJ5, 1997.

22 R. Ludwig, W. Pieper, E. Jahn, N. Agrawal, A. Ehrhardt, L. Küller, and H.G. Weber, “10 GHz all-optical clock recovery using a mode-locked semiconductor laser in a 40 Gbit/s, 100-km transmission experiment,” in Proc. of OFC`96, WH2, 1996.

23 L. Wang, Y. Su, A, Agarwal, and P. Kumar, “Polarization insensitive widely tunable all-optical clock recovery based on AM mode-locking of a Fibre Ring Laser,” Photonics Technology Letters, Vol. 12, No. 2, pp. 211 – 213, February 2000.

24 W. A. Pender, T. Widdowson and A. D. Ellis, “Error free operation of a 40 Gbit/s all-optical regenerator,” Electron. Letters, Vol. 32, No. 6, pp. 567-569, 1996.

25 X. Zhou, Ch. Lu, P. Shum, H.H.M. Shalaby, T.H.Cheng, and P. Ye, “A performance analysis of an all-optical clock extraction circuit base on Fabry-Pèrot filter,” J. of Lightwave Technology, Vol. 19, No. 5, pp. 603 – 612, May 2001.

26 C. Bintjas, K. Yiannopoulos, N. Pleros, G. Theophilopoulos, M. Kalyvas, H. Avramopoulos, and G. Guekos, “Clock recovery circuit for optical packets,” Photonics Technology Letters, Vol. 14, No. 9, pp. 1363 – 1365, September 2002.

27 G. Contestabile, A. D`Errico, M. Presi, and E. Ciaramella, “40-GHz all-optical clock extraction using a semiconductor-assisted Fabry-Pérot filter,” Photonics Technology Letters, Vol. 16, No. 11, pp. 2523 – 2525, November 2004.

28 T. Saito; Y. Yano, and N. Henmi, ”Optical TDM 20 Gb/s-105 km transmission employing newly proposed optical PLL timing extraction,” Photonics Technology Letters, Vol. 6, No. 4, pp. 555 – 557, April 1994.

29 O. Kamatani and S. Kawanishi, “Ultrahigh-speed clock recovery with phase locked loop based on four-wave mixing in a traveling-wave laser diode amplifier,” J. of Lightwave Technology, Vol. 14, No. 8, pp. 1757 – 1766, August 1996.

30 T. Yamamoto, L.K. Oxenlowe, C. Schmidt, C. Schubert, E. Hilliger, U. Feiste, J. Berger, R. Ludwig, and H.G. Weber, "Clock recovery from 160Gbit/s data signals using phase-locked loop with interferometric optical switch based on semiconductor optical amplifier," Electron. Letters, Vol. 37, No. 8, pp. 509 – 510, April 2001.
31 C. Boerner, V. Marembert, S. Ferber, C. Schubert, C. Schmidt-Langhorst, R. Ludwig, and H.G. Weber, "320 Gbit/s clock recovery with electro-optical PLL using a bidirectionally operated electroabsorption modulator as phase comparator," in Proc. of OFC`05, OtuO3, 2005.
32 C. Boerner, C. Schubert, C. Schmidt, E. Hiliger, V. Marembert, J. Berger, S. Feber, E. Dietrich, R. Ludwig, and H.G. Weber, "160 Gbit/s clock recovery with electro-optical PLL using a bidirectionally operated electroabsorption modulator as phase comparator," in Proc. of OFC`03, FF3, 2003.
33 W. A. Pender, P. J. Watkinson, E. J. Greer and A. D. Ellis, "10 Gbit/s all-optical regenerator," Electron. Letters, Vol. 31, No. 18, pp. 1587-1588, 1995.
34 W. A. Pender, T. Widdowson and A. D. Ellis, "Error free operation of a 40 Gbit/s all-optical regenerator," IEEE Electron. Letters, Vol. 32, No. 6, pp. 567-569, 1996.
35 J. Suzuki, T. Tanemura, K. Taira, Y. Ozeki, K. Kikuchi, "All-optical regenerator using wavelength shift induced by cross-phase modulation in highly nonlinear dispersion-shifted fiber," Photonics Technology Letters, Vol. 17, No. 2, 2005.
36 S. Bigo, O. Leclerc, and E. Desurvire, "All-optical fiber signal processing and regeneration for soliton communications," J. of Select. Topics in Quantum Electron., Vol. 3, No. 5, pp. 1208 – 1223, October 1997.
37 A. Bogoni, P. Ghelfi, M. Scaffardi, L. Poti, " NOLM-based 3 stage regenerator for 160 Gbit/s transmission systems," in Proc. of ECOC`03, Th2.5.6, 2003.
38 N. Chi, L. Oxenloeve, A. Siahlo, P. Jeppensen, "All-optical fiber signal processing based on balanced NOLM and imbalanced NOLM," in Proc. of ECOC`02, paper 6.3.5, 2002.
39 O. Leclerc, P. Brindel, D. Rouvillain, E. Pincemin, B. Dany, E. Desurvire, C. Duchet, E. Boucherez, and S. Bouchoule, "40Gbit/s polarisation-insensitive and wavelength-independent InP Mach-Zehnder modulator for all-optical regeneration," Electron. Letters, Vol. 35, No. 9, pp. 730 – 731, April 1999.
40 B. Lavigne, P. Guerbel, P. Brindel, E. Balmefrezol, B. Dagens, "Cascade of 100 Optical 3R Regenerators at 40Gbit/s Based on All-Active Mach Zehnder Interferometers," in Proc. of ECOC`01, paper We.F.2.6., 2001.
41 O. Leclerc, B. Dany, D. Rouvillian,, P. Brindel, E. Desurvire, C. Duchet, A. Shen, F. Devaux, A. Coquelin, M. Goix, S. Bouchoule, L. Fleury and P. Nouchy, "Simultaneously regenerated 4x40 Gbit/s dense WDM transmission over 10.000 km using single 40 GHz InP Mach-Zehnder modulator," Electron. Letters, Vol. 36, No.18, pp. 1574-1575, 2000.
42 J. Sarathy, "Design and applications of all-optical regenerators," in Proc of OFC`05, invited paper OthE1, 2005.
43 G. Lakshminarayana, J. Sarathy, B. Stefanov, R. Mu, T. Thai, D. Lowe, "A new architecture for counterpropagation-based photonic regeneration and reshaping," in Proc of OFC`05, OtuO4, 2005.
44 S. Fischer, M. Dülk, E. Gamper, W. Vogt, E. Gini, H. Melchior, W. Hunziker, D. Nesset and A. D. Ellis, "Optical 3R regenerator for 40 Gbit/s networks," Electron. Letters, Vol 35, No. 23, pp. 2047-2049, 1999.

45 O. Leclerc, P. Brindel, D. Rouvillain, E. Princemin, B. Dany, E. Desurvire, “40 Gbit/s polarization-independent, push-pull InP Mach-Zehnder modulator for all-optical regeneration,” in Proc. of OFC`99, post-deadline paper PD35, 1999.
46 B. Lavigne, E. Balmefrezol, P. Brindel, B. Dagens, R. Brenot, L. Pierre, J-L. Moncelet, D. de la Grandière, J-C. Remy, J-C. Bouley, B. Thedrez, and O. Leclerc, “Low input power all-optical 3R regenerator based on SOA devices for 42.66Gbit/s ULH WDM RZ transmissions with 23dB span loss and all-EDFA amplification,” in Proc of OFC`03, post-deadline paper PD15, 2003.
47 Y. Ueno, S. Nakamura, J. Sasaki, T. Shimoda, A. Furukawa, T. Tamanuki, T. Sasaki, and K. Tajima, ”Ultrahigh-speed all-optical data regeneration and wavelength conversion for OTDM systems,” in Proc. of ECOC`01, Th.F.2.1, 2001.
48 G. Gavioli and P. Bayvel, ”Novel, high-stability 3R all-optical regenerator based on polarization switching in a semiconductor optical amplifier,” in Proc. of ECOC`02, paper 7.3.2, 2002.
49 G. Gavioli, V. Mikhailov, B. Thomsen and P. Bayvel, “Investigation of transmission with cascaded all-optical 3R regenerators and variable inter-regenerator spacing,” Electron. Letters, Vol. 41, No. 3, 2005.
50 H. Chayet, S. Ben Ezra, N. Narkiss, S. Zadok, A. Sher, R. Zeibel, ”Compensation of chromatic dispersion by chirp control in all-optical regenerator based on asymmetric Sagnac loop,” in Proc. of OFC`05, OFK6, 2005.
51 I.D. Phillips, A.D. Ellis, H.J. Thiele, R.J. Manning, and A.E. Kelly, “40 Gbit/s all-optical data regeneration and demultiplexing with long pattern lengths using a semiconductor nonlinear interferometer,” Electron. Letters, Vol. 34, No. 24, 1998.
52 H. J. Thiele, A. D. Ellis, I. D. Phillips, “Recirculating loop demonstration of 40Gbit/s all-optical 3R data regeneration using a semiconductor nonlinear interferometer,” Electron. Letters, Vol. 35, No. 3, 1999.
53 J. Leuthold, B. Mikklsen, R. E. Behringer, G. Raybon, C. H. Joyner, and P. A. Besse, “Novel 3R regenerator based on semiconductor optical amplifier delayed-interference configuration,” Photonics Technology Letters, Vol. 13, No. 8, pp. 860-862, 2001.
54 J. Leuthold, M. Kauer, M. Duelk, “Power equalization and signal regeneration with delay interferometer all-optical wavelength converters,“ in Proc. of ECOC`02, paper 7.3.4, 2002.
55 J. Leuthold, R. Ryf, D. N. Maywar, S. Cabot, J. Jaques, and S. S. Patel, “Nonblocking all-optical cross connect based on regenerative all-optical wavelength converter in a transparent demonstration over 42 nodes and 16800 km,” J. of Lightwave Technology, Vol. 21, No. 11, pp. 2863-2870, 2003.
56 H. Chayet, S. Ben Ezra, N. Shachar, S. Tzadok, S. Tsadka, J. Leuthold, “Regenerative all-optical wavelength converter based on semiconductor optical amplifier and sharp frequency response filter,” in Proc. of OFC`04, ThS2, 2004.
57 J. Leuthold, D. Marom, S. Cabot, R. Ryf, P. Bernasconi, F. Baumann, J. Jaques, D. T. Neilson, C. R. Giles, “All-optical wavelength converter based on a pulse reformatting optical filter,” in Proc. of OFC`04, post-deadline paper PD41, 2004.
58 T. Otani, T. Miyzaki, and S. Yamamoto, “40 Gbit/s signal transmission using optical 3R regenerator based on electroabsorption modulators,” in Proc of OFC`00, ThP3-1, 2000.
59 E. S. Awad, P. S. Cho, Ch. Richardson, N. Moulton, J. Goldhar, “Optical 3R regeneration with all-optical timing extraction and simultaneous wavelength

conversion using a single electroabsorption modulator," in Proc. of ECOC`02, paper 6.3.2, 2002.
60 S. Hoejfeldt, S. Bischoff, and J. Moerk, "All-optical wavelength conversion and signal regeneration using an electroabsorption modulator," J. of Lightwave Technology, Vol. 18, No. 8, pp. 1121 – 1127, August 2000.
61 T. Otani, T. Miyazaki, and S. Yamamoto, "Optical 3R regenerator using wavelength converters based on electroabsorption modulator for all-optical network applications," Photonics Technology Letters, Vol. 12, No. 4, pp. 431-433, 2000.
62 E. S. Awad, P. S. Cho, Ch. Richardson, N. Moulton, J. Goldhar, "Optical 3R regeneration using a single EAM for all-optical timing extraction with simultaneous reshaping and wavelength conversion," Photonics Technology Letters, Vol. 14, No. 9, pp.1378 – 1380, September 2002.
63 T. Otani, T. Miyazaki, and S. Yamamoto, "40 Gb/s optical 3R regenerator using electroabsorption modulators for optical networks," J. of Lightwave Technology, Vol. 20, No. 2, pp. 195-200, 2002.
64 P. S. Cho, P. Sinha, D. Mahgerefteh and G. M. Carter, "All-optical regeneration at the receiver of 10-Gb/s RZ data transmitted over 30000 km using an electroabsorption modulator," Photonics Technology Letters, Vol. 12, No. 2, pp. 205-207, 2000.
65 K. Nishimura, M. Tsurusawa, and M. Usami, "Novel all-optical 3R regenerator using cross-absorption modulation in rf-driven electroabsorption waveguide," in Proc. of ECOC`01, WE.F.2.4, 2001.
66 H.F. Chou, Z. Hu, J. E. Bowers, D. J. Blumenthal, "Compact optical 3R regeneration using a travelling-wave electroabsorption modulator," Photonics Technology Letters, Vol. 17, No. 2, pp. 486-488, 2005.
67 T. Otani, M. Suzuki and S. Yamamoto, "40 Gbit/s optical 3R regenerator for all-optical networks," in Proc. of ECOC`01, We.F.2.1, 2001.
68 F. Öhman, S. Bischoff, B. Tromborg, and J. Moerk, "Noise and regeneration in semiconductor waveguides with saturable gain and absorption," J. of Quantum Electronics, Vol. 40, No. 3, pp. 245 – 255, March 2004.
69 C. Knöll, M. Gölles, Z. Bakonyi, G. Onishchukov, and F. Lederer, "Optimization of signal transmission by an in-line semiconductor optical amplifier-saturable absorber module," Opt. Communications, Vol. 187, No. 1, pp. 141 – 153, 2001.
70 L.J. Christiansen, L. Xu, K. Yvid, F. Öhman, L. Oxenlowe, and J. Moerk, "2R regeneration in concatenated semiconductor optical amplifiers and electroabsorbers," in Proc. of ECOC`04, Mo3.4.3, 2004.
71 M. Nakazawa, E. Yamada, H. Kubota, K. Suzuki, "10Gbit/s soliton data transmission over one million kilometers," Electr. Letters, Vol. 27, No. 14, pp. 1270 – 1272, 1991.
72 K. Suzuki, H. Kubota, A. Sahara and M. Nakazawa, "40 Gbit/s single channel optical soliton transmission over 70000 km using in-line synchronous modulation and optical filtering," Electron. Letters, Vol. 34, No. 1, pp. 103-104, 1998.
73 M. Nakazawa, K. Suzuki and H. Kubota, " Single-channel 80 Gbit/s soliton transmission over 10000 km using in-line synchronous modulation," Electron. Letters, Vol. 35, No. 2, pp 162-164, 1999.
74 G. Raybon, Y. Su, J. Leuthold, R. J. Essiambre, T. Her, C. Joergensen, P. Steinvurzel, K. Dreyer, K. Feder, "40 Gbit/s Pseudo-linear Transmission Over One Million Kilometers," in Proc. of OFC`02, PD paper FD10, 2002.

75 P. Brindel, O. Leclerc, D. Rouvillain, B. Dany, and E. Desurvire, “Experimental validation of new regeneration scheme for 40Gbit/s dispersion-managed long haul transmission,” in Proc. of OFC`00, TuD1, 2000.
76 O. Leclerc, P. Brindel, D. Rouvillain, B. Dany, R. Brenot, A. Labrousse, A. Coquelin, B. Dagens, “Regenerated long-haul transmission using all-optical SOA-MZI as loss-free synchronous modulator,“ in Proc. of OFC`01, WF6-1, 2001.
77 P. Brindel, B. Dany, O. Leclerc, E. Desurvire, “ “Black box” optical regenerator for RZ transmission systems,” Electron. Letters, Vol. 35, No. 6, 1999.
78 S. Bauer, “Nonlinear dynamics of semiconductor lasers with active optical feedback,” PhD thesis, Humboldt Universität Berlin 2005.
79 O. Brox “DFB-Laser mit integriert optischer Rückkoplung für die optische Signalverarbeitung,” PhD thesis, Technische Universität Berlin 2005.
80 O. Brox, S. Bauer, M. Radziunas, M. Wolfrum, J. Sieber, J. Kreissl, B. Sartorius, and H.J. Wünsche, “High-frequency pulsations in DFB lasers with amplified feedback,” J. of Quantum Electron., Vol. 39, No. 11, pp. 1381 – 1387, November 2003.
81 B. Sartorius, M. Möhrle, S. Reichenbacher, H. Preier, H.J. Wünsche, and U. Bandelow, “Dispersive self-Q-switching in self-pulsating DFB lasers,“ J. of Quantum Electron., Vol. 33, No. 2, pp. 211 – 218, February 1997.
82 M. Radziunas, H.J. Wünsche, B. Sartorius, O. Brox, D. Hoffmann, K. Schneider, and D. Marcenac, “Modelling self-pulsating DFB-lasers with integrated phase tuning section,“ J. of Quantum Electron., Vol. 36, pp. 1026 – 1035, September 2000.
83 M. Möhrle, B. Sartorius, C. Bornholdt, S. Bauer, O. Brox, A. Sigmund, R. Steingrüber, M. Radziunas, and H.J. Wünsche, „Detuned grating multisection-RW-DFB lasers for high-speed optical signal processing,“ J. on Selec. Topics in Quantum Electron., Vol. 7, No. 2, pp. 217 – 223, March/April 2001.
84 C. Bornholdt, S. Bauer, M. Möhrle, H.P. Nolting, and B. Sartorius, “All optical clock recovery at 80 GHz and beyond,” in Proc. of. ECOC`01, Th.F.1.2, 2001.
85 J. Moerk, M. L. Nielsen, T. W. Berg, “The Dynamics of Semconductor Optical Amplifiers, Modeling and Applications,” Optics and Photonics News, pp. 43 – 48, July 2003.
86 F. Girardin, G. Guekos and A. Houbavlis, “Gain Recovery of Bulk Semiconductor Optical Amplifiers”, IEEE Photonics Technology Letters, Vol. 10, No. 6, June 1998.
87 L. Occhi, Y. Ito, H. Kawaguchi, L. Schares, J. Eckner, and G. Guekos, “Intraband Gain Dynamics in Bulk Semiconductor Optical Amplifiers: Measurement and Simulations,” Journal of Quantum Electronics, Vol. 38, No. 1, January 2002.
88 M. Radziunas, H.J. Wünsche, B. Sartorius, O. Brox, D. Hoffmann, K. Schneider, D. Marcenac, “Modeling self-pulsating DFB-lasers with an integrated phase tuning section,“ J. of Quantum Electron., Vol. 36, No. 9, pp. 1026 – 1035, 2000.
89 H.J. Wünsche, M. Radziunas, S. Bauer, O. Brox, B. Sartorius, “Modeling of mode control and noise in self-pulsating PhaseCOMB lasers,” Journal of Sel. Top. Quantum Electron., Vol. 9, No. 3, pp. 857 – 864, 2003.
90 J. L. Pleumeekers, M. Kauer, K. Dreyer, Ch. Burrus, A. G. Dentai, S. Stunk, J. Leuthold, and Ch. H. Joyner, “Acceleration of gain recovery in semiconductor optical amplifiers by optical injection near transparency wavelength,” Photonics Technology Letters, Vol. 14, No. 1, pp. 12 – 14, January 2002.
91 M. Usami, M. Tsurusawa, and Y. Matsushima, “Mechanism for reducing recovery time of optical nonlinearity in semiconductor laser amplifiers,” Appl. Phys. Lett. Vol. 72, pp. 2657 – 2659, 1998.

92 S. Bischoff, M. L. Nielsen, and J. Moerk, “Improving the all-optical response of SOAs using a modulated holding signal,” Journal of Lightwave Technology, Vol. 22, No. 5, pp. 1303 – 1308, May 2004.
93 P. Borri, S. Scaffeti, J. Moerk, W. Langbein, J. M. Hvam, A. Mecozzi, and F. Martelli, “Measurement and calculation of the critical pulsewidth for gain saturation in semiconductor optical amplifiers,” Opt. Commun., Vol. 164, pp. 51 – 55, 1999.
94 K. L. Hall, G. Lenz, A. M. Darwish, and E. P. Ippen, ”Subpicosecond gain and index nonlinearities in InGaAsP diode lasers,” Opt. Commun., Vol. 111, pp. 589 – 612, Oct. 1994.
95 A. Mecozzi and J. Moerk, “Saturation effects in nondegenerated four-wave mixing between short optical pulses in semiconductor laser amplifiers,” Journal of Selected Topics in Quantum Electronics, Vol. 3, No. 5, pp. 1190 – 1207, Oct. 1997.
96 S. Diez, C. Schmidt, R. Ludwig, H. G. Weber, K. Obermann, S. Kindt, I. Koltchanov, and K. Petermann, “Four-Wave mixing in semiconductor optical amplifiers for frequency conversion and fast optical switching,” Journal of Selected Topics in Quantum Electronics, Vol. 3, No. 5, pp. 1131 – 1143, 1997.
97 J. Yu and P. Jeppesen, “Improvement of cascaded semiconductor optical amplifier gates by using holding light injection,” Journal of Lightwave Technology, Vol. 19, pp. 614 – 623, May 2001.
98 R. J. Manning, D. A. O. Davies, and J. K. Lucek, “Recovery rates in semiconductor laser amplifiers: Optical and electrical bias dependencies,” Electronics Letters, Vol. 30, No. 15, pp. 1233 – 1234, 1994
99 J. Leuthold, M. Mayer. J. Eckner, G. Guekos, H. Melchior, Ch. Zellweger, “Material gain of bulk 1.55 μm InGaAsP/InP semiconductor optical amplifiers approximated by a polynomial model,” Journal of Applied Physics, Vol. 87, No. 1, pp. 618 – 620, January 2000.
100 G. Hunziker, R. Paiella, K. J. Vahala, and U. Koren, “Measurement of the stimulated carrier lifetime in semiconductor optical amplifiers by four-wave mixing of polarized ASE noise,” Photonics Technology Letters, Vol. 8, No. 7, pp. 907 – 909, July 1997.
101 M. L. Nielsen, D. J. Blumenthal, and J. Moerk, “A transfer function approach to the small-signal response of saturated semiconductor optical amplifiers,” Journal of Lightwave Technology, Vol. 18, No. 12, pp. 2151 – 2156, December 2000.
102 A. Mecozzi, “Small signal gain theory of wavelength converters based on cross-gain modulation in semiconductor optical amplifiers,” Photonics Technology Letters, Vol. 8, pp. 1471 – 1473, 1996.
103 D. Marcenac and A. Mecozzi, “Switches and frequency converters based on cross-gain modulation in semiconductor optical amplifiers,” Photonics Technology Letters, Vol. 9, pp. 749 – 751, 1997.
104 F. Ginovart and J. C. Simon, “Semiconductor optical amplifier length effects on gain dynamics,” Journal of Physics D: Applied Physics, Vol. 36, pp. 1473 – 1476, 2003.
105 R. J. Manning and G. Sherlock, “Recovery of a p phase shift in ~12.5 ps in a semiconductor laser amplifier,” Electr. Letters, Vol. 31, No. 4, pp. 307 – 308, 1995.
106 F. Ginovart and J. C. Simon, “Theoretical analysis of a semiconductor optical amplifier based multi-stage wavelength converter,” LEOS 2004, Vol. 1, pp. 382 – 383, November 2004.
107 K. Obermann, T. Liu, K. Petermann, F. Girardin, G. Guekos, “Saturation of semiconductor optical amplifiers due to amplified spontaneous emission,” in Proc. of CLEO`98, CThM6, 1998.

108 A. Uskov, J. Moerk, and J. Mark, "Theory of short-pulse gain saturation in semiconductor laser amplifiers," Photonics Technology Letters, Vol. 4, No. 5, pp. 443 – 445, May 1992.
109 T. Saitoh and T. Mukai, "Gain saturation characteristics of traveling-wave semiconductor laser amplifier in short optical pulse amplification," J. of Quantum Electronics, Vol. 26, pp. 2086 – 2094, December 1990.
110 F. Ginovart and J. C. Simon, "Wavelength dependence of gain recovery time in a semiconductor optical amplifier based wavelength shifter," in Proc. of CLEO/Europe`03, pp. 181, June 2003.
111 I. Valiente, L. Lablonde, J. C. Simone, and L. Billes, "Effects of amplified spontaneous emission on gain recovery dynamics of semiconductor amplifiers," in Proc. of OAA`96, Monterey, pp. 224 – 227, 1996.
112 R. Inohara, K. Nishimura, M. Tsurusawa, and M. Usami, "Experimental analysis of cross-phase modulation and cross-gain modulation in SOA-injecting CW assist light," Photonics Technology Letters, Vol. 15, No. 9, pp. 1192 – 1194, 2003.
113 F. Koyama and K. Iga, "Frequency chirping in external modulators," Journal of Lightwave Technology, Vol. 6, pp.87 – 92, January 1988.
114 T. Watanable, N. Sakaida, H. Yasaka, F. Kano, and M. Koga, "Transmission performance of chirp-controlled signal by using semiconductor optical amplifier," Journal of Lightwave Technology, Vol. 18, No. 8, pp. 1069 – 1077, August 2000.
115 S. Tammela, H. Ludvigsen, T. Kajava, and M. Kaivola, "Time-resolved frequency chirp measurements using a silicon-wafer etalon," Photonics Technology Letters, Vol. 9, pp. 475 – 477, April 1997.
116 R. Monnard, C. R. Doerr, and C. R. Giles, "Real-time dynamic chirp measurements of optical signal," in Proc. of OFC`98, Vol. 2, pp. 120 – 121, 1998.
117 R. A. Saunders, J. P. King and I. Hardcastle, "Wideband chirp measurement technique for high bit rate sources," Electronics Letters, Vol. 30, No. 16, pp. 1336 – 1337, August 1994.
118 L. S. Yan, A. E. Willner, "Chirp measurement of electro-optic modulators using simple optical spectrum analysis," in Proc. of OFC`03, Vol. 1,pp. 70 – 71, 2003.
119 B. Kowalski, J. Debeau, and R. Boittin, "A simple and novel method for measuring the chirp parameter of an intensity modulated light source," Photonics Technology Letters, Vol. 11, No. 6, pp. 700 – 702, June 1999.
120 Ch. Laverdiène, A. Fekecs, and M. Têtu, "A new method for measuring time-resolved frequency chirp of high bit rate sources," Photonics Technology Letters, Vol. 15, No. 3, pp. 446 – 448, March 2003.
121 E. Peral, W. K. Marshall, and A. Yariv, "Precise measurement of semiconductor laser chirp using effect of propagation in dispersive fiber and application to simulation of transmission through fiber gratings," Journal of Lightwave Technology, Vol. 16, No. 10, pp. 1874 – 1878, October 1998.
122 www.u2t.com.
123 "Making time-resolved chirp measurements using the optical spectrum analyzer and digital communications analyzer" Agilent Application Note 1550-7.
124 H. Lee, H. Yoon, Y. Kim, And J. Jeong, "Theoretical study of frequency chirping and extinction ratio of wavelength-converted optical signals by XGM and XPM using SOA`s," Journal of Quantum Electronics, Vol. 35, No. 8, August 1999.
125 J. T. Hsieh, P. M. Gong, S. L. Lee, and J. Wu, "Analysis of frequency chirping of optical phase conjugate signals by four-wave mixing in light-holding SOA`s," in

Proc. of Microwave and Optoelectronics Conference, IMOC`03, Vol. 2, pp. 571 – 576, September 2003.
126 Y. Kim, H. Lee, S. Kim, J. Ko, and J. Jeong, "Analysis of frequency chirping and extinction ratio of optical phase conjugate signals by four-wave mixing in SOA`s," Journal of Selected Topics in Quantum Electronics, Vol. 3, No. 5, pp. 873 – 879, May/June 1999.
127 A. Uskov, J. Moerk, and J. Mark, "Wave Mixing in Semiconductor Laser Amplifiers Due to Carrier Heating and Spectral-Hole Burning," Journal of Quantum Electronics, vol. 30, No. 8, pp. 1769-1781, August 1994.
128 R. J. Manning, A. D. Ellis, A. J. Poustie, and K. J. Blow, "Semiconductor laser amplifiers for ultrafast all-optical signal processing," Journal of Opt. Soc. Am., Vol. 14, No. 11, pp. 3204 – 3216, November 1997.
129 G. P. Agrawal, N. K. Dutta, "Long Wavelength Semiconductor Lasers," Ch. 5, ISBN 0-442-20995-9 Van Nostrand Reinhold, New York (1986).
130 C. Schubert, "Interferometric gates for all-optical signal processing," PhD thesis, Technische Universität Berlin, 2004.
131 T. Durhuus, B. Mikkelsen, and C. Joergensen, "All-optical wavelength conversion by semiconductor optical amplifiers," Journal of Lightwave Technology, Vol. 14, pp. 942 – 954, 1996.
132 G. P. Agrawal, N. K. Dutta, "Semiconductor lasers," Kluwer Academic, Boston, 1993.
133 J. Leuthold, B. Mikkelsen, G. Raybon, C. H. Joyner, J. L. Pleumeekers, B. I. Miller, K. Dreyer and, R. Behringer, "All-optical wavelength conversion between 10 and 100 Gb/s with SOA delayed-interference configuration," Opt. and Quant. Electronics, Vol. 33, pp. 939 – 952, 2001.
134 E. Voges, K. Petermann, "Optische Kommunikationstechnik," Springer Verlag, Berlin Heidelberg, 2002.
135 Y. Yamamoto and T. Mukai, "Fundamentals of optical amplifiers," Optical Quantum Electronics, Vol. 21, pp. S1 – S14, 1989.
136 J. Y. Emery, P. Doussiere, L. Goldstein, F. Pommereau, C. Fortin, R. Ngo, N. Tscherptner, J. L. Lafragette, P. Aubert, F. Brillouet, "New, process tolerant, high performance 1.55 µm polarization insensitive semiconductor optical amplifier based on low tensile bulk GaInAsP," in Proc. of ECOC`96, WeD 2.3, pp. 165 – 168, 1996.
137 T. Tekin, "Monolithically integrated gain shifted Mach-Zehnder interferometer for all-optical demultiplexing," PhD thesis, Technische Universität Berlin 2004.
138 L. Occhi, "Semiconductor optical amplifiers made of ridge waveguide bulk InGaAs/InP: Experimental characterization and numerical modeling of gain, phase, and noise," PhD thesis, ETH Zurich 2002.
139 R. Freund, L. Molle, N. Hanik, A. Richter, "Design issues of 40 Gbit/s WDM-Systems for metro and core network application, " in Proc. of ECOC`04, Tu3.5.1, 2004.
140 F. Buchali, H. Bülow, "Adaptive PMD Compensation by Electrical and Optical Techniques, " J. of Lightwave Technology, Vol. 22, pp.1116 –1126, 2004.
141 M. Karlsson et al., "PMD compensation using 2R and 3R regenerators," in Proc. of ECOC`04, invited paper We1.4.2, 2004.
142 L. Dittman, "Optical Packet Networks – Conclusions from the IST DAVID Project," in Proc. of OFC`04, paper TuQ1, 2004.

143 D.J. Blumenthal, "All-Optical Label Swapping Networks and Technologies," J. of Lightwave Technology, Vol. 18, No. 12, pp. 2058 – 2075, 2000.
144 C. Joergensen, K.D. Danielsen, K.E. Stubkjaer, M. Chilling, K. Daub, P. Doussiere, F. Pommerau, P.B. Hansen, H.N. Poulsen, A. Kloch, M. Vaa, B. Mikkelsen, E. Lach, G. Laube, W. Idler, K. Wunstel, "All-optical wavelength conversion at bit rates above 10Gb/s using semiconductor optical amplifiers," J. of Selec. Topics in Quantum Electronics, Vol. 3, No. 5, pp.1168 – 1180, October 1997.
145 A.D. Ellis, A.E. Kelly, D. Nesset, D. Pitcher, D.G. Moodie, R. Kashyap, "Error free 100 Gb/s wavelength conversion using grating assisted cross-gain modulation in 2mm long semiconductor amplifier," Electron. Letters, Vol. 34, No. 20, pp. 1958 – 1959, 1998.
146 J. Leuthold, G. Raybon, Y. Su, R. Essiambre, S. Cabot, J. Jaques, M. Kauer, "40 Gbit/s transmission and cascaded all-optical wavelength conversion over 1000000 km," Electron. Letters, Vol. 38, No. 16, pp.890 – 892, August 2002.
147 M.F.C. Stephens, D. Nesset, R.V. Penty, I.H. White, M.J. Fice, "Wavelength conversion at 40 Gbit/s via four wave mixing in semiconductor optical amplifier with integrated pump laser," Electron. Letters, Vol.35, No. 4, pp. 420 – 421, March 1999.
148 O. Leclerc, B. Lavigne. E. Balmefrezol, P. Brindel, L. Pierre, D. Rouvillain, and F. Seguineau, "Optical Regeneration at 40 Gb/s and Beyond," Journal of Lightwave Technology, Vol. 21, No. 11, November 2003.
149 C. Schubert, J. Berger, S. Diez, H.J. Ehrke, R. Ludwig, U. Feiste, C. Schmidt, H.G. Weber, G. Toptchiyski, S. Randel, K. Petermann, "Comparison of interferometric all-optical switches for demultiplexing applications in high-speed OTDM systems," J. of Lightwave Technology, Vol.12, No. 5, pp. 618 – 624, April 2002.
150 J.H. Kim, Y.M. Jhon, Y.T. Byun, S. Lee, D.H. Woo, and S.H. Kim, "All optical XOR gate using semiconductor optical amplifiers without additional input beam," Photonics Technology Letters, Vol. 14, No. 10, pp. 1436 – 1438, October 2002.
151 F. Devaux, "All-optical 3R regenerators: Status and challenges," in Proc. of Semiconductor Laser Conference 2000, MA3, 2000.
152 B. Sartorius, "3R regeneration for all-optical networks," in Proc. of ICTON`01, Th.A.4, 2001.
153 F. Devaux, Y. Sorel, and J. F. Kerdiles, "Simple measurement of fiber dispersion and of chirp parameter of intensity modulated light emitter," J. of Lightwave Technology, Vol. 11, pp. 1937 – 1940, 1993.
154 G. Bramann, H. J. Wünsche, U. Busolt, C. Schmidt, M. Schlak, B. Sartorius, and H.P. Nolting, "Two-wave competition in ultralong semiconductor optical amplifiers," J. of Quantum Electronics, Vol. 41, No. 10, pp. 1260 – 1267, 2005.
155 R. Ludwig, "Experimentelle Untersuchungen an Halbleiterlaserverstärkern für die optische Nachrichtentechnik", PhD thesis, Technische Universität Berlin, Germany, 1993.
156 www.vpiphotonics.com
157 H.P Nolting and B. Sartorius, "Fast Clocked Decision – a novel ultra high speed switching technique," in Proc. of ECOC`02, paper 8.4.5, 2002.
158 B. Konrad, K. Petermann, J. Berger, R. Ludwig, C.M. Weinert, H. G. Weber, and B. Schmauss, "Impact of fiber chromatic dispersion in high-speed TDM transmission systems," J. of Lightwave Technology, Vol. 20, No. 12, invited paper, pp. 2129 – 2135, 2002.

159 A. Hodzic, B. Konrad, K. Petermann, "Alternative modulation formats in Nx40 Gb/s WDM standard fiber RZ-transmission systems," J. of Lightwave Technology, Vol. 20, No. 2, 2004.
160 S. Randel, "Analyse faseroptischer Übertragungssysteme mit Wellenlängenmultiplex bei 160 Gbit/s Kanaldatenrate," PhD thesis, Technische Universität Berlin, Germany, 2005.
161 M.T. Hill, E. Tangdionegga, H. de Waard, G.D. Khoe, and H.J.S. Dorren, "Carrier recovery time in semiconductor optical amplifiers that employ holding beams," Opt. Letters, Vol. 27, No. 18, pp. 1625 – 1627, 2002.
162 M. Premaratne, and A.J. Lowery, "Analytical characterisation of SOA-based optical pulse delay discriminator," J. of Lightwave Technology, Vol. 23, No. 9. pp. 2778 – 2787, 2005.
163 W.F. Hoefer, "The transmission-line matrix method – theory and applications," Trans. On Microwave Theory and Techniques, Vol. MTT-33 (10), 1985.
164 www.shf.biz.
165 A. M. Kanas, P. Likamwa, "Ultrafast all-optical switching not limited by the carrier lifetime in an integrated multiplequantum-well Mach-Zehnder interferometer," Journal of Optical Society of America, Vol. 14, No. 11, 1997.
166 D. Marcenac, A. Kelly, D. Nesset, and D. Davis, "Bandwidth enhancement of wavelegth conversion via cross-gain modulation by semiconductor optical amplifier cascade," Electron. Letters, Vol. 32, pp.1442 – 1443, 1995.
167 B. Kowalski, J. Debeau, and R. Boittin, "A simple and novel method for measuring the chirp parameter of an intensity modulated light source," Photonics Technology Letters, Vol. 11, No. 6, pp. 700 – 702, 1999.
168 L. Schares, C. Schubert, C. Schmidt, H.G. Weber, L. Occhi, and G. Guekos, "Phase dynamics of semiconductor optical amplifiers at 10-40 GHz," J. of Quantum Elect., Vol. 39, No. 11, 2003.
169 L. Occhi, R. Scollo, L. Schares, and G. Guekos, "Effective alpha factor in bulk semiconductor optical amplifiers of different lengths," in Proc. of 14th LEOS Annual Meeting, paper MM5, 2001.
170 T. Liu, K. Obermann, K. Petermann, F. Giradin, and G. Guekos, "Effects of saturation caused by amplified spontaneous emission on semiconductor optical amplifiers performance," Electron. Letters, Vol. 33, pp. 2042 – 2043, 1997.
171 R. J. Manning and D. A. O. Davies, "Three-wavelength device for all optical signal processing," Opt. Letters, Vol. 19, pp. 889 – 891, 1994.
172 VPIcomponentMaker™, "Overview of TLLM," Active Photonics User`s Manual, Chapter 5, pp. 53 – 103.
173 Agilent Technologies, "40 Gb/s and Return-to-Zero Measurements Using the Agilent 86100A Infiniium DCA," Product Note 86100-3.
174 B. Sartorius, "3R Regenerator mit flexibler Ausgangswellenlänge," Deutsches Patent DE 101 18 958 A1, Internat. No. WO 02/084900 A2.
175 B. Sartorius, C. Bornholdt, J. Slovak, "Wellenlängen-erhaltender optischer Signal-regenerator," Deutsches Patent DE 103 44 319.3, Internat. No. WO2005/029734.

Acknowledgements

The results presented in this thesis have been realised in the framework of my research activities at the Fraunhofer Institute for Telecommunications, Heinrich-Hertz-Institut (FhG-HHI) thanks to the support of a large number of people.

First of all, I would like to thank my project leader Dr. B. Sartorius for giving me the opportunity to work in this very exciting research field. I especially appreciate his willingness and openness for fruitful discussions and his continuous support during my whole time at the FhG-HHI.

Special thanks go to my advisor Prof. Dr. K. Petermann for granting me the opportunity to work on the topic of this thesis and for his valuable comments in the framework of the 'Optical Fibre Communication Seminar' as well as during the final stage of completing this dissertation. Further, I would like to thank Prof. Dr. J. Leuthold for co-examinations of this work and Prof. Dr. Ch. Boit for chairing the examination committee.

I would like to express my thanks to C. Bornholdt for introducing me to the world of optical measurement technique. I am grateful to him for sharing his many years of research experience with me and for supporting me in most of the experimental investigations presented in this dissertation.

I would like to thank Dr. H. P. Nolting for inviting me to participate in the research tasks at the FhG-HHI and for supporting me in the simulations presented in this thesis. Furthermore, I would also like to thank Prof. Dr. H. J. Wünsche and M. Schlak for fruitful discussions on the part concerning the SOA modelling.

I would like to express my gratitude to both my present and former colleagues at the FhG-HHI, especially Dr. T. Tekin, Dr. S. Bauer, Ch. Schmidt, M. Biletzke, Dr. U. Busolt, Dr. Ch. Bobbert, G. Bramann, Dr. O. Brox, H. Ding, M. Gravert, G. Sahin, W. Brinker, H. Ehlers, Dr. M. Möhrle, Dr. J. Kreissl, A. Sigmund, R. Stenzel, L. Molle, Ch. Caspar, Dr. R. Freund, V. Marembert, Dr. R. Ludwig, Dr. C. Schubert, Dr. C. Schmidt-Langhorst, Dr. M. Kroll, S. Ferber, and H.J. Ehrke.

I would also like to thank Prof. Dr. M. Dado for supervising the first years of my PhD studies at the University of Zilina and for giving me the opportunity to continue my research activities at the FhG-HHI.

Last but not least, I would like to take this opportunity to thank my parents and my brother, who always believed in me, and my girlfriend Bohdana, for her support, understanding, and patience.

Berlin, October 2006

Curriculum Vitae

Personal Data

Name:	Juraj Slovak
Date of birth:	May 20th, 1976
Nationality:	Slovakian
Contact:	juraj.slovak@gmail.com

Work Experience

2006 onwards	System engineer at Siemens PSE Optical Transmission Dept., Munich, Germany
2001 – 2006	Research scientist at Fraunhofer Institute for Telecommunications, Heinrich-Hertz-Institut (FhG-HHI) Optical Signal Processing Dept., Berlin, Germany

Education:

1994 – 2001	University of Zilina, Zilina, Slovak Republic Faculty of Electrical Engineering Department of Telecommunications
1990 – 1994	Grammar school, Zilina, Slovak Republic

Trainings:

1999	Deutsche Telekom AG, Technologiezentrum Darmstadt, Germany Modelling and optimisation of a DWDM optical fibre link Darmstadt–Berlin for 10 Gbit/s NRZ data transmission
1997	Study stay at FH-Dieburg, Germany